



## PhD thesis

Mads Dam Ellehøj

# Ice-vapor equilibrium fractionation factor

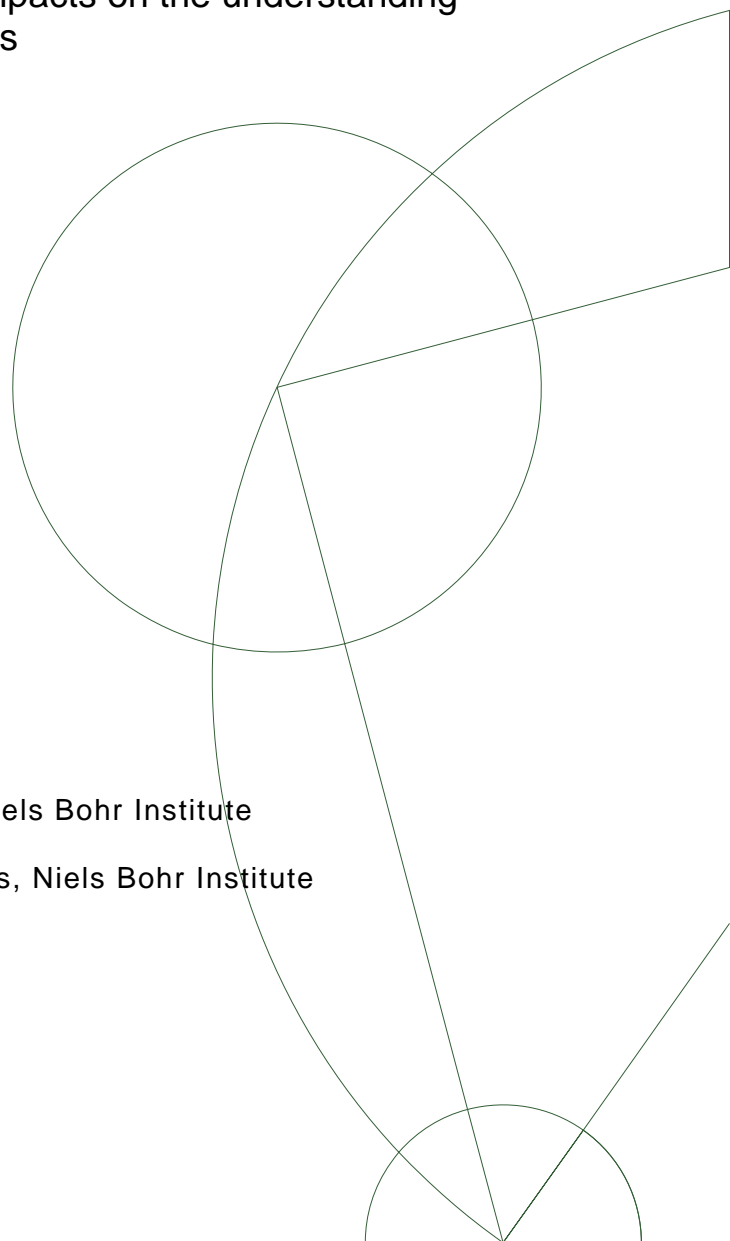
Experimental investigations and possible impacts on the understanding  
of the hydrological cycles on Earth and Mars

Academic advisors:

Sigfús J. Johnsen, Centre for Ice and Climate, Niels Bohr Institute

Morten Bo Madsen, Earth and Planetary Sciences, Niels Bohr Institute

Submitted: 01/11/10, Revised: 31/01/11



## Abstract

Since it controls the magnitude of the isotope fractionation during phase change the ice-vapor equilibrium fractionation factor  $\alpha$  is a core component in isotope models e.g. used to interpret ice core data for palaeoclimate studies.

In this work we successfully designed and built an experimental setup with the purpose of investigating the temperature dependency of  $\alpha$  and to improve the temperature range of earlier work. This experimental setup proved to perform as intended with good reproducibility of the data obtained with both a Picarro cavity ringdown spectrometer and a conventional IRMS system.

The results of the experiments show fractionation factors for  $\delta\text{D}$  and  $\delta^{18}\text{O}$ , with a temperature dependency well in accordance with theory for equilibrium fractionation, for temperatures between  $0^\circ\text{C}$  and  $-40^\circ\text{C}$ . The expressions for the results are:  $\ln(\alpha_{\delta\text{D}}) = 0.2133 - \frac{203.10}{T} + \frac{48888}{T^2}$  and  $\ln(\alpha_{\delta^{18}\text{O}}) = 0.0831 - \frac{49.192}{T} + \frac{8312.5}{T^2}$ . Compared to previous work, a significantly larger  $\alpha$  for  $\delta\text{D}$  is obtained while for  $\delta^{18}\text{O}$   $\alpha$  is larger for temperatures below  $-20^\circ\text{C}$  and slightly lower for temperatures above this.

A case study of condensation in the martian atmosphere show that the differences between Mars temperature (202 K) extrapolated  $\alpha$  from earlier work and this work not surprisingly cause significant changes in D/H ratios, and better knowledge of  $\alpha$  at martian temperatures is needed for proper understanding of the processes in the martian water cycle.

Investigations with a Rayleigh distillation model show that the differences between earlier work and this work cause significant changes in both magnitude and shape of an annual deuterium excess signal with offsets and variations of 5-10%, similar in magnitude to natural variations. This emphasizes the importance of  $\alpha$  for accurate studies of the processes in the hydrological cycle and underlines the significance of the differences between the results of this work and earlier work. The results of this work emphasize the need for better characterization of the basic parameters in the models used to investigate present and past climates, and should be considered in future evaluations of the ice-vapor processes in the hydrological cycle.

## Resumé

Da den kontrollerer størrelsen af isotopfraktioneringen ved faseovergange er is-damp ligevægts fraktionerings faktoren  $\alpha$  en hjørnesten i isotopmodeller, der bl.a. bruges til fortolkning af iskernedata i palæoklimastudier.

I disse undersøgelser blev en eksperimentiel opstilling bygget med det formål at undersøge temperaturafhængigheden af  $\alpha$ , samt for at udføre målinger ved lavere temperaturer end tidligere opnået. Opstillingen virkede som forventet med reproducerbare data ved målinger både med et Picarro cavity ringdown spektrometer samt med et konventionelt IRMS system.

Resultaterne af disse forsøg viser fraktioneringsfaktorerne for  $\delta D$  og  $\delta^{18}O$  for temperaturer mellem  $0^\circ C$  og  $-40^\circ C$  med en temperaturafhængighed i overensstemmelse med gældende teori for ligevægtsfraktionering. Resultaterne kan udtrykkes ved følgende afhængighed:  $\ln(\alpha_{\delta D}) = 0.2133 - \frac{203.10}{T} + \frac{48888}{T^2}$  og  $\ln(\alpha_{\delta^{18}O}) = 0.0831 - \frac{49.192}{T} + \frac{8312.5}{T^2}$ . Sammenlignet med tidligere resultater ses betydeligt højere  $\alpha$  for  $\delta D$ , hvorimod for  $\delta^{18}O$  er  $\alpha$  større for temperaturer under  $-20^\circ C$  og en smule lavere for temperaturer over denne temperatur.

Et simpelt studie af kondensation i atmosfæren på Mars viser at forskellene imellem ekstrapolerede  $\alpha$  (til 202 K) for tidligere resultater og disse resultater ikke overraskende viser betydelige ændringer i D/H forholdet og det er klart at mere viden om  $\alpha$  for Mars temperaturer er nødvendig for forståelsen af processerne i vandets cyklus på Mars.

Undersøgelser foretaget med en Rayleigh type model viser at forskellene imellem tidligere resultater og disse resultater resulterer i betydelige ændringer i størrelsen og formen af den årlige deuterium excess cyklus med forskelle på 5-10‰, hvilket er af samme størrelsesorden som naturlige ændringer. Dette viser vigtigheden af  $\alpha$  for præcise undersøgelser af processerne i den hydrologiske cyklus, samt fremhæver betydningen af forskellene imellem tidligere resultater og disse resultater. Disse resultater understreger nødvendigheden af bedre undersøgelser af de grundlæggende parametre i modeller brugt til at undersøge den nuværende samt tidligere klimaperioder og bør tages i betragtning ved fremtidige undersøgelser af is-damp processer i den hydrologiske cyklus.

# Preface

This PhD project was carried out at the Centre for Ice and Climate (CIC), Niels Bohr Institute, University of Copenhagen. The project was funded by the Faculty of Science, University of Copenhagen. The principal supervisor of the project was Sigfús J. Johnsen from CIC with Morten Bo Madsen from Earth and Planetary Science, Niels Bohr Institute as co-advisor. The change of environment was carried out at the NASA Phoenix Mars Mission Science Operations Centre, University of Arizona, USA.

## Outline

This PhD thesis contains 8 chapters that describe and discuss experimental investigations of the ice-vapor equilibrium fractionation factor as well as investigate the impacts of the obtained results on the understanding of essential processes in the hydrological cycle on Earth and Mars. The chapters will be structured in the following manner:

Chapter 1 gives a general background to isotope hydrology and isotopic fractionation, introduces previous work and discuss the theory behind the experimental setup which is introduced and discussed in Chapter 2. In Chapter 3 the obtained datasets as well as the needed calibrations are found. Chapter 4 discuss the equilibrium conditions in the two main components of the experimental setup; the vapor source and the ice-vapor equilibrium chamber. In Chapter 5 the results of the experimental work are presented, discussed and compared with previous results. The limitations and possible improvements of the experimental setup are also discussed here. Chapter 6 uses a case study to investigate the implications of the differences between the results of this work and previous results when extrapolating to Mars temperatures. Chapter 7 investigates the impact of the differences between the previous results and results from this work with a Rayleigh distillation model. Finally, Chapter 8 summarizes the main conclusions of this work.

The thesis was submitted November 1st 2010 and revised for typos on January 31st 2011.

## Acknowledgements

Many people have helped me with this work and I am very thankful to all of you. First, I would like to thank my supervisors: Sigfús, for being encouraging, insightful and for supporting me in this work. Morten, for great support, guidance and an always positive mind, especially during our time working with Phoenix with the rest of the great people in the Mars group.

I would like to thank the Centre for Ice and Climate for support and all the people there for the great social environment, both in Copenhagen and at the NEEM camp. A special thanks goes to Theo Jenk, Christo Buizert, Peter Sperlich, Vasileios Gkinis, Trevor Popp as well as Simon Sheldon for helping out and always keeping your stash open. Thanks should also go to the NBI workshop and Sven Pantmann for good service.

I owe many thanks to office-mate and friend Hans-Christian Steen Larsen for many thoughtful discussions, both on and off topic and for help with the experimental setup when it was mostly needed.

Last but definitely not least, I would like to thank Hanne as well as my family and friends for being patient and encouraging when this work was time consuming.

Mads Dam Ellehøj  
Copenhagen, November 2010

# Contents

<b>Abstract</b>	<b>i</b>
<b>Preface</b>	<b>i</b>
<b>1 Background</b>	<b>1</b>
1.1 Isotope hydrology . . . . .	1
1.1.1 The $\delta$ notation . . . . .	2
1.2 Isotope fractionation . . . . .	2
1.2.1 Equilibrium fractionation . . . . .	2
1.2.2 Temperature dependence of equilibrium fractionation factors . . . . .	3
1.2.3 Kinetic fractionation . . . . .	5
1.2.4 Rayleigh Fractionation . . . . .	7
1.3 Measuring the equilibrium fractionation factor . . . . .	9
1.4 Previous results . . . . .	11
<b>2 Experimental setup and instrumentation</b>	<b>15</b>
2.1 General setup design . . . . .	15
2.2 Picarro Wavelength Scanned Cavity Ringdown Spectrometer . . . . .	19
2.3 TC/EA GC-IRMS . . . . .	20
2.3.1 $H_3^+$ factor corrections . . . . .	22
2.3.2 $^{17}O$ Corrections . . . . .	23
2.3.3 Peak area dependencies . . . . .	23
2.3.4 Memory effects . . . . .	24
2.4 Connecting the experimental setup to the TC/EA . . . . .	26
2.5 Cryofocus . . . . .	27
2.6 The vapor source . . . . .	29

---

2.6.1	Temperature controlling of the vapor source . . . . .	31
2.7	Ice-vapor equilibrium chamber . . . . .	32
2.7.1	Temperature controlling of the equilibrium chamber . . . . .	33
2.7.2	Design of the equilibrium chamber . . . . .	33
2.8	Standard injection port . . . . .	36
2.9	Conclusion of this chapter . . . . .	37
<b>3</b>	<b>Dataset and calibrations</b>	<b>38</b>
3.1	Picarro datasets . . . . .	40
3.1.1	Typical measurements . . . . .	40
3.2	Picarro calibrations . . . . .	43
3.2.1	Picarro humidity calibration . . . . .	44
3.2.2	Picarro VSMOW calibration . . . . .	46
3.2.3	Uncertainty for the Picarro data . . . . .	49
3.2.4	The final Picarro dataset . . . . .	50
3.3	TC/EA-IRMS data . . . . .	51
3.3.1	Typical measurements . . . . .	51
3.3.2	IRMS VSMOW calibrations . . . . .	54
3.3.3	Uncertainty of the IRMS data . . . . .	57
3.3.4	Final IRMS dataset . . . . .	59
3.4	Conclusion of this chapter . . . . .	59
<b>4</b>	<b>Characterization of the experimental setup</b>	<b>62</b>
4.1	Characterization of the vapor source . . . . .	62
4.1.1	Temperature and humidity stability . . . . .	63
4.1.2	Isotopic composition of the vapor . . . . .	66
4.1.3	Changes in the isotopic composition of the vapor . . . . .	68
4.1.4	Rayleigh model for the vapor source . . . . .	69
4.1.5	Surface cooling investigations . . . . .	73
4.2	Ice-vapor equilibrium chamber . . . . .	76
4.2.1	Transients in the isotope values before equilibrium . . . . .	76
4.2.2	Stability in the equilibrium state . . . . .	79
4.2.3	General performance and limitations of the equilibrium chamber . . . . .	80
4.3	Conclusion . . . . .	84

<b>5</b>	<b>Results and discussion</b>	<b>85</b>
5.1	Uncertainties on the measured fractionation factor . . . . .	85
5.2	Initial conditions for the $\alpha$ calculations . . . . .	88
5.2.1	The impact of different $\delta_{vo}$ approaches on $\alpha$ . . . . .	88
5.2.2	The impact of surface cooling on $\alpha$ . . . . .	89
5.3	Presentation of the final dataset . . . . .	91
5.4	Fitting the data and comparison with theory . . . . .	94
5.5	Comparison with previous measurements and discussion . . . . .	99
5.5.1	The work of Merlivat and Nief (1967) and Majoube (1970) . . . . .	103
5.5.2	Summary of this section . . . . .	106
5.6	Experimental setup performance and improvements . . . . .	106
5.6.1	Setup . . . . .	107
5.6.2	Instrumentation . . . . .	108
5.7	Conclusion . . . . .	109
<b>6</b>	<b>Implications for the martian water cycle</b>	<b>112</b>
6.1	The Martian water cycle . . . . .	112
6.1.1	Phoenix Mars Lander . . . . .	116
6.2	Investigations with the results of this work . . . . .	116
6.3	Conclusion . . . . .	119
<b>7</b>	<b>Implications for isotope hydrology</b>	<b>120</b>
7.1	Effective fractionation factor . . . . .	123
7.2	Investigating precipitation . . . . .	124
7.2.1	Trajectories . . . . .	125
7.2.2	Impact on the modeling of an annual cycle . . . . .	127
7.3	Investigating the super saturation function . . . . .	128
7.4	Conclusion . . . . .	132
<b>8</b>	<b>Conclusions</b>	<b>133</b>
8.1	Equilibrium conditions in the setup . . . . .	133
8.2	Experimental results . . . . .	134
8.3	Impacts on processes in the hydrological cycle and future work . . . . .	135
	<b>List of Figures</b>	<b>137</b>

<b>List of Tables</b>	<b>143</b>
<b>Bibliography</b>	<b>145</b>

# Chapter 1

## Background

The aim of this PhD thesis is to investigate the temperature dependency of the ice-vapor equilibrium fractionation factor with experimental measurements.

The following chapter will give an introduction to the topics covered in this work. We will describe and discuss the theory behind the fractionation (equilibrium and kinetic) of the water isotopes and its temperature dependency. We will discuss previous measurements of the ice-vapor equilibrium fractionation factor and set up some theory behind the experimental work presented in the following chapters.

### 1.1 Isotope hydrology

Water is practically everywhere at the Earth's surface and atmosphere where it undergoes phase transitions, interacts with minerals and is a major component in complex metabolic processes necessary for life. The water isotopes undergo fractionation during these processes. The three main isotopic components of water are  $\text{H}_2^{16}\text{O}$ ,  $\text{HD}^{16}\text{O}$  and  $\text{H}_2^{18}\text{O}$  and their abundance are approximately 997680:320:2000 ppm (parts per million)(Dansgaard, 1964). Since the earliest measurements of isotopic abundance in the 1930s in Europe and Japan (Rankama, 1954) and by the Chicago school of Urey ((Nier, 1947; McKinney et al., 1950)), it has been observed that freshwater samples are depleted in the heavy isotopes, while the residue of evaporating waters (e.g. lakes) are enriched (Craig, 1961). A relationship between  $^{18}\text{O}$  abundance in precipitation and the cloud condensation temperature was found (Dansgaard, 1953) and correlations between the depletion of D and  $^{18}\text{O}$  were established, known as the meteoric water line and deuterium excess (Craig, 1961; Craig and Gordon, 1965; Dansgaard, 1964). The isotopic values of meteoric precipitation were found to correlate with temperature, altitude, latitude and proximity to the ocean (Dansgaard, 1964). Measurements of the isotopic composition of water have since then improved the understanding of the the governing processes of the water cycle and proved successful in

the reconstruction of the palaeoclimate through ice core records (Dansgaard et al., 1968). Many ice cores have been drilled in both Antarctica and Greenland (Johnsen et al., 2001; Jouzel et al., 2007; Petit et al., 1999) that have provided crucial knowledge about past climate changes and the behavior the climate system (Johnsen et al., 1992; Fischer et al., 1999; Blunier and Brook, 2001).

### 1.1.1 The $\delta$ notation

Measuring an absolute isotope ratio or abundance requires very accurate mass spectrometry and the results from absolute measurements are much harder to compare due to differences in methods and instrumentation. Furthermore the variations of the stable isotope concentrations are generally more usable than the actual abundances. It is therefore common to directly report the measured difference between the isotopic composition a sample (s) and an accepted standard (std) in terms of the delta ( $\delta$ ) notation (McKinney et al., 1950; Craig, 1961):

$$\delta_s = 1000 \frac{R_s - R_{std}}{R_{std}} \quad (1.1.1)$$

Where  $R_s$  and  $R_{std}$  are the isotope ratios (e.g. [D]/[H] or [ $^{18}\text{O}$ ]/[ $^{16}\text{O}$ ]) of the measured species and the standard respectively. The factor of 1000 converts the  $\delta$ -values to per mil (‰). This formulates the  $\delta\text{D}$  and  $\delta^{18}\text{O}$  values for a sample. Thus a positive  $\delta$  value implies that the ratio of the heavy isotope to the light isotope is higher in the sample than in the reference and vice versa for a negative  $\delta$  value. The measurements are made against a working or laboratory reference that has been calibrated against international reference material such as VSMOW (Vienna Standard Mean Ocean Water) (Gonfiantini, 1978; Craig, 1961). The conversion to an international reference scale allows for comparisons with measurements from other instruments.

## 1.2 Isotope fractionation

### 1.2.1 Equilibrium fractionation

The fractionation of different isotopes under equilibrium conditions (i.e. with no net fluxes) is essentially the product of underlying thermodynamic effects as the light isotopes have higher vibrational energies due to a different reduced mass of the system. The higher the vibration frequencies the more readily they can break the bonds and e.g. move from liquid into the vapor phase. These differences result in differences in vapor pressure between the different isotopes of water. Since the lighter isotopes therefore are more volatile this means that for e.g. liquid water in equilibrium with vapor in a closed system, the vapor will be depleted in the heavy isotopes compared to the composition of the liquid.

The equilibrium fractionation factor is defined to represent the partitioning of isotopes between two separate phases and in the case of the fractionation factor for the ice-vapor exchange in equilibrium conditions, it is defined as:

$$\alpha = \frac{R_{ice}}{R_{vapor}} \quad (1.2.1)$$

where,  $R_{ice}$  and  $R_{vapor}$  are the isotope ratios of the species investigated in each phase (e.g.  $[D]/[H]$  or  $[^{18}O]/[^{16}O]$ ). In equilibrium conditions the fractionation factor will be the ratio between the vapor pressures of the light component and the heavy component. In  $\delta$  notation the above becomes:

$$\alpha = \frac{\delta_{ice} + 1}{\delta_{vapor} + 1} \quad (1.2.2)$$

In this work we will refer to the ice-vapor equilibrium fractionation factor as  $\alpha$ . Other fractionation factors will always be denoted, e.g.  $\alpha_{lv}$  as liquid vapor fractionation factor.

Thus, since it controls the magnitude of the isotope fractionation during phase change the ice-vapor equilibrium fractionation factor is a core component in isotope models e.g. used to interpret ice core data or atmospheric processes in the hydrological cycle. Here, better knowledge of equilibrium fractionation will e.g. improve the condensation temperature estimation of precipitation on an ice sheet, which in turn will improve the knowledge about past climates.

### 1.2.2 Temperature dependence of equilibrium fractionation factors

One of the most important characteristics of isotope fractionation is that it is only dependent of temperature and not pressure. This is principally because the atomic nuclei hosting the neutrons only constitute a very small part of the total volume of the atoms (Criss, 1999). Detailed evaluation of the temperature dependence of equilibrium fractionation was made by e.g. Bigeleisen and Mayer (1947), Urey (1947), Bigeleisen (1961) and Boato et al. (1962) and is summed up by e.g. Criss (1999). Hence the following will be based largely on the formulation in Criss (1999) and Chacko et al. (2001) and the reader is referred to the above mentioned papers for more details.

It can be shown that the equilibrium fractionation factor  $\alpha$  between two substances 1 and 2 is directly related to the ratios of the partition functions for these. The ratio of the partition functions ( $Q_1$  and  $Q_2$ ) is a product of rotational, zero-point energy and vibrational energy spacings. Following the argumentation in Criss (1999) the ratio of partition functions of a diatomic gas in logarithmic form is given by

$$\ln \left[ \frac{Q_2}{Q_1} \right] = \ln \left[ \frac{\sigma_1 v_2}{\sigma_2 v_1} \right] + \left[ \frac{U_1 - U_2}{2} \right] + \ln \left[ \frac{1 - e^{-U_1}}{1 - e^{-U_2}} \right] \quad (1.2.3)$$

Here  $U_i$  represent the quantities  $h\nu_i/kT$  where  $h$  is Planck's constant,  $\nu$  is the frequency and  $k$  is the spring constant originating from the simple harmonic oscillator approximation.  $\sigma_i$  are the symmetry numbers (Criss, 1999).  $U$  is temperature dependent and since the last term approximates unity at low temperature, equation (1.2.3) reduces to

$$\ln \left[ \frac{Q_2}{Q_1} \right] \cong \ln \left[ \frac{\sigma_1 v_2}{\sigma_2 v_1} \right] + \left[ \frac{U_1 - U_2}{2} \right] \quad (1.2.4)$$

Since  $U$  is dependent of  $T^{-1}$  this equation will be of the form  $y = \text{constant} + \text{slope} * (T^{-1})$  indicating that the reduced partition function and in turn the fractionation factor  $\ln \alpha$  vary linearly with  $T^{-1}$  at low temperatures. At high temperatures the last term in equation (1.2.3) is significantly larger than zero and cannot be neglected. Criss (1999) expands this into a Taylor series and after canceling terms the following equation for diatomic molecules are obtained:

$$\ln \left[ \frac{Q_2}{Q_1} \right] = \ln \left[ \frac{\sigma_1}{\sigma_2} \right] + \left[ \frac{U_1^2 - U_2^2}{24} \right] - \left[ \frac{U_1^4 - U_2^4}{2880} \right] + \left[ \frac{U_1^6 - U_2^6}{181440} \right] - \left[ \frac{U_1^8 - U_2^8}{9676800} \right] + \dots \quad (1.2.5)$$

This was also deduced by Urey (1947) and since the higher order terms become small at high temperature this results in:

$$\ln \left[ \frac{Q_2}{Q_1} \right] \cong \ln \left[ \frac{\sigma_1}{\sigma_2} \right] + \left[ \frac{U_1^2 - U_2^2}{24} \right] \quad (1.2.6)$$

and

$$\ln \left[ \frac{Q_2}{Q_1} \right] \cong \ln \left[ \frac{\sigma_1}{\sigma_2} \right] + \sum_{i=1}^{3n-6} \frac{U_{1i}^2 - U_{2i}^2}{24} \quad (1.2.7)$$

for non-linear polyatomic molecules with more vibrational modes (Criss, 1999). From the same arguments as above we can see that these two equations will vary linearly with  $T^{-2}$  at high temperatures. Thus, these equations predicts a strict dependency of  $\ln \alpha$  of either  $T^{-1}$  or  $T^{-2}$  with the exact temperatures at which these limits occur depends on the substance under consideration.

However, due to the complexities of equilibrium fractionation in natural systems, approximations to these are commonly used to describe laboratory determinations of fractionation factors that over a certain temperature range do not appear to strictly follow either the  $T^{-1}$  or the  $T^{-2}$  limiting dependencies (Chacko et al., 2001; Criss, 1999; O'Neil, 1986). With  $C$  values as constants, the above  $T^{-1}$  dependency becomes  $\ln \alpha = C_1 + C_2/T$  which is used for many systems at low temperatures. The  $T^{-2}$  dependency becomes  $\ln \alpha = C_1 + C_3/T^2$  which is typically used for equilibria among solids with low vibra-

tional frequencies such that the high temperature condition as discussed above is obtained. Here,  $C_1$  has proved to be different than zero for equilibria with hydrous phases (Bottinga and Javoy, 1973). The combination of high- and low temperature approximations is captured in the following equation Bigeleisen (1961):  $\ln \alpha = C_1 + C_2/T + C_3/T^2$ , which have been useful for describing equilibria over limited temperature ranges. As argued by Criss (1999) no combination of terms can describe the partition function for a single phase except for the case where the system consist of multiple frequencies so different that some are in the large temperature case and some in the low temperature case. However the isotopic fractionation factor makes a comparison of two different phases which may have very different frequencies such as a gas and a liquid or solid (Jancso and Van Hook, 1974; Szydowski, 1994). This has also been investigated by the works of e.g. Van Hook (1968) and by Boato et al. (1962) who in an investigation of solid-vapor equilibria concluded that  $\ln \alpha = C_1 + C_2/T + C_3/T^2$  describes these systems best. It can be seen that the above types of empirical expressions only approach  $\alpha=1$  as temperature approaches infinity if  $C_1=0$ . However, as argued in Jancso and Van Hook (1974) the constant  $C_1$  could come from the contribution of anharmonicity effects.

### 1.2.3 Kinetic fractionation

Fractionation of the water isotopes also occur under nonequilibrium conditions where dynamics or under- or over saturation introduce diffusional processes affecting fractionation. But  $\alpha$  is still a crucial part of the formulation of the effective fractionation factor for these kinetic processes.

#### Evaporation

In the case of vapor flux from an evaporating water reservoir at steady state, the resulting evaporation fractionation factor  $\alpha_{evap}$  can be expressed following Criss (1999), Cappa et al. (2003) and Luz et al. (2009). Assuming that the boundary layer between the liquid surface and the air above it is at evaporative steady state then the effective evaporation fractionation factor  $\alpha_{evap}$  between an evaporating flux ( $e$ ) and liquid water ( $w$ ) can be expressed as:

$$\alpha_{evap} = R_w/R_e = \frac{\alpha_{diff}\alpha_{lv}(1-h)}{1-\alpha_{lv}h(R_v/R_w)} \quad (1.2.8)$$

Where  $\alpha_{lv}$  is the temperature dependent liquid-vapor equilibrium fractionation factor,  $h$  is the relative humidity,  $R_v$  is the isotopic ratio of the vapor,  $R_w$  is the isotope ratio of the liquid and  $\alpha_{diff}$  is the diffusion fractionation factor that accounts for the differences in the molecular transport properties of the water isotopes. Following Cappa et al. (2003) and Luz et al. (2009),  $\alpha_{diff}$  can be expressed as  $(D_{H_2^{16}O}/D_{H_2^{18}O})^n$  and  $(D_{H_2^{16}O}/D_{HD^{16}O})^n$ , where  $D_{H_2^{16}O}$ ,  $D_{H_2^{18}O}$  and  $D_{HD^{16}O}$  are the molecular diffusivities of  $H_2^{16}O$ ,  $H_2^{18}O$  and  $HD^{16}O$

respectively. The exponent  $n$  here depends on the ratio of turbulent to molecular diffusion and equals one for no turbulence. The diffusion fractionation factors have been measured by Merlivat (1978), Cappa et al. (2003), for oxygen only by Barkan and Luz (2007) and more lately for both  $\delta\text{D}$  and  $\delta^{18}\text{O}$  by Luz et al. (2009). Luz et al. (2009) obtains roughly the same values as Merlivat (1978) while Cappa et al. (2003) is off, maybe due to the estimates of evaporation cooling corrections, as discussed by Luz et al. (2009). In the experiments presented in this work, the only source of water vapor to the air above the water level is the flux of evaporating water vapor. Hence,  $R_w = R_e$  and  $\alpha_{evap} = R_w/R_v$ . Therefore, 1.2.8 can be rewritten to:

$$\alpha_{evap} = R_w/R_v = (\alpha_{diff}(1-h) + h)\alpha_{lv} \quad (1.2.9)$$

Established models describing the isotopic fractionation during evaporation have been around for many years (e.g. (Craig and Gordon, 1965) or Merlivat and Jouzel (1979)).

### Condensation

Contrary to the formation of an ice layer under equilibrium conditions with no net flux, when ice crystals are formed e.g. in a cloud the vapor deposition is not in equilibrium since the environment over the ice is often supersaturated Jouzel and Merlivat (1984). This also introduces kinetic processes influencing the fractionation since due to their lower molecular diffusivity, the HDO and  $\text{H}_2^{18}\text{O}$  molecules will tend to condense more slowly than  $\text{H}_2^{16}\text{O}$ . As a result of this, the vapor becomes more enriched in the heavy isotopes compared to equilibrium conditions. Investigations of these kinetic effects were pioneered by (Jouzel and Merlivat, 1984) who formulated the fractionation such that the effective fractionation is:

$$R_s = \frac{\alpha}{\alpha_{kin}} R_v \quad (1.2.10)$$

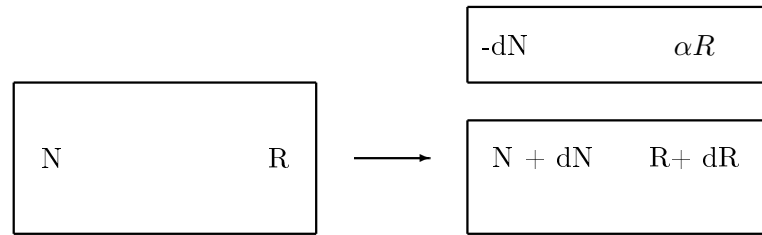
where  $R$  is the isotope ratio and subscripts  $s$  and  $v$  stands for solid and vapor respectively. The kinetic fractionation factor,  $\alpha_{kin}$ , is given by:

$$\alpha_{kin} = \frac{\alpha\alpha_{diff}(S-1) + 1}{S} \quad (1.2.11)$$

where  $S$  is the super saturation function and is usually assumed to be linearly related to the temperature (Petit et al., 1991; Landais et al., 2008) such that  $S = p - qT$  where  $T$  is temperature in  $^{\circ}\text{C}$ . Knowledge about the parameters of the super saturation function is sparse and the parameters  $p$  and  $q$  are usually obtained from best fitting of snow or ice isotopic composition. Examples of these parameters are  $S = 1 - 0.017T$ , as used by Landais et al. (2008).

### 1.2.4 Rayleigh Fractionation

Rayleigh fractionation is an important open system process in isotope defined by a progressive removal of a fractional increment of the system, such as removing vapor from system with vapor in equilibrium with liquid water. At the formation of the vapor the isotopic equilibrium between the vapor and water is maintained but once formed, the vapor is removed from the system. Since a larger fraction of the light isotopes is continuously removed from the system, the  $\delta$  value of the remaining water becomes progressively enriched with increasingly degree of evaporation. Following this, the  $\delta$  value of the newly formed vapor also becomes correspondingly enriched, depending on the fractionation factor at the temperature of evaporation. Following the same arguments as in Mook (2000), the Rayleigh fractionation can be described as below, assuming equilibrium in a reservoir with one sink shown by this simple box model:



Here,  $N$  is the total number of molecules,  $\alpha$  is the equilibrium fractionation factor and  $R$  is the isotope ratio (rare to abundant isotopes) such that  $N/(1 + R)$  is the number of abundant isotopic molecules and  $RN/(1 + R)$  is the number of rare isotopic molecules. For the removal of  $dN$  molecules with the fractionation factor  $\alpha$ , the mass balance for the rare isotope yields:

$$\frac{R}{1 + R}N = \frac{R + dR}{1 + R + dR}(N + dN) - \frac{\alpha R}{1 + \alpha R}dN \quad (1.2.12)$$

To a good approximation, the total number of molecules equals the number of the abundant isotope and all denominators can be set to  $1 + R$ . Now, the mass balance for the rare isotope becomes

$$RN = (R + dR)(N + dN) - (\alpha R dN) \quad (1.2.13)$$

And when neglecting the product of the differentials and rearranging:

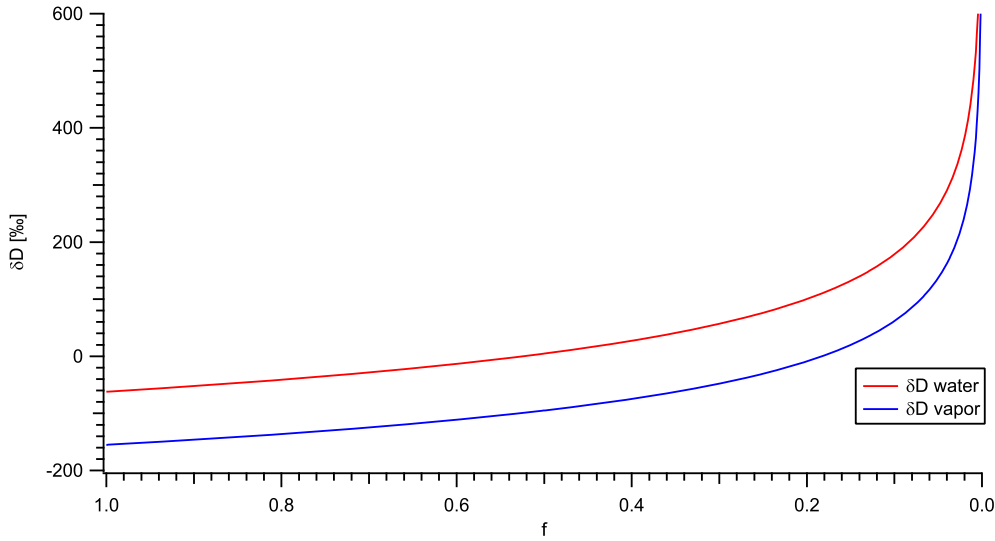


Figure 1.1: Rayleigh distillation in the vapor source (see next Chapter) with  $T=1.41^{\circ}\text{C}$  and initial composition of  $\delta\text{D} = -62.08\text{‰}$ .  $f$  is the fraction of the remaining water. Liquid-vapor equilibrium fractionation factors from Majoube (1971b).

$$\frac{dR}{R} = (\alpha - 1) \frac{dN}{N} \quad (1.2.14)$$

Assuming that the fractionation factor is constant, this can be integrated with the boundary conditions  $R = R_i$  at  $N = N_i$  (when nothing has evaporated yet) and we get:

$$\frac{R}{R_i} = f^{\alpha-1} \quad (1.2.15)$$

Here,  $f = \frac{N}{N_i}$  is the fraction of the original reservoir size remaining in the system at any time. With the continuous removal of molecules,  $f$  decreases from a value of unity towards zero. This well known result was originally given by Rayleigh (1902). Converting 1.2.15 to the delta notation gives the following expression:

$$\frac{1000 + \delta}{1000 + \delta_i} = f^{\alpha-1} \quad (1.2.16)$$

Figure 1.1 shows an example of such Rayleigh fractionation during continuous evaporation of the vapor source (see next Chapter). In this case it is used that  $R_v = \frac{R_w}{\alpha_{lv}}$  with the liquid-vapor equilibrium fractionation factors from Majoube (1971b) at a constant temperature  $T=1.41^{\circ}\text{C}$ . The red line shows the  $\delta\text{D}$  as a function of the remaining water  $f$ , starting with an initial  $\delta\text{D} = -62.1\text{‰}$ . The blue line shows the vapor in isotopic equilibrium with the water, starting with an isotopic value of  $\delta\text{D} = -155.1\text{‰}$ . With less and less water remaining, the isotopic ratio between the heavy and the light isotopes follows the

exponential function and the water becomes more and more enriched in heavy isotopes.

In the above a constant fractionation factor was assumed during the process but this is not always the case. For example, the progressive condensation of an air mass is usually the result of a continuous cooling of a given air parcel. The cooling results in a changed fractionation factor for the vapor to water (or vapor to ice) transition during the evolution of the precipitating system. Here, differential form of the Rayleigh equation still applies, but the integration has to be carried out with  $\alpha$  changing throughout the process. This was demonstrated by Dansgaard (1964).

### 1.3 Measuring the equilibrium fractionation factor

The main focus of this work is to investigate the temperature dependency of the ice-vapor equilibrium fractionation factor. In the next Chapter we will introduce the different parts of the experimental setup, but first we need to elaborate on the theory behind these experiments.

The equilibrium ice-vapor fractionation factor can be found by letting vapor with a known isotopic composition condense out under controlled conditions with the ice and the vapor in equilibrium. Measuring the isotopic composition of the vapor in equilibrium with ice can then lead to a calculation of the fractionation factor  $\alpha$ . The experiments presented in this work are based on this. The figure below depicts the above situation. Here the isotopic composition of the initial vapor is  $R_{v0}$  or  $\delta_{v0}$  and the mass of the initial vapor by  $m_{v0}$ . This vapor comes from a vapor source. The vapor is then introduced to an equilibrium chamber where a part of the vapor  $m_s$  then condense out as ice (solid) with the isotopic composition  $R_s$  or  $\delta_s$  and the remaining vapor in equilibrium with the ice has the mass  $m_{vi}$  and the isotopic composition  $R_{vi}$  or  $\delta_{vi}$ :

$$\begin{array}{ccc}
 \boxed{\begin{array}{c} m_{v0} \\ \delta_{v0} + 1 \\ R_{v0} \end{array}} & = & \boxed{\begin{array}{c} m_s \\ \delta_s + 1 \\ R_s \end{array}} + \boxed{\begin{array}{c} m_{vi} \\ \delta_{vi} + 1 \\ R_{vi} \end{array}} \\
 \text{Vapor} & & \text{Ice} \qquad \qquad \text{Vapor in equilibrium with ice}
 \end{array}$$

If the initial vapor is in equilibrium with the liquid water in the vapor source it will have the following isotopic composition according to the liquid-vapor fractionation factor  $\alpha_{lv}$ :

$$R_{v0} = \frac{R_l}{\alpha_{lv}} \quad (1.3.1)$$

and in  $\delta$  notation:

$$\delta_{v0} = \frac{\delta_l + 1}{\alpha_{lv}} - 1 \quad (1.3.2)$$

Where  $R_l$  and  $\delta_l$  are the isotopic composition of the liquid water in different notations. From mass conservation in the equilibrium chamber we know that:

$$m_{v0}(\delta_{v0} + 1) = m_s(\delta_s + 1) + m_{vi}(\delta_{vi} + 1) \quad (1.3.3)$$

and since we know that

$$m_{v0} = m_s + m_i$$

we can obtain this:

$$m_{v0}\delta_{v0} = m_s\delta_s + m_{vi}\delta_{vi} \quad (1.3.4)$$

By substituting  $m_s = m_{v0} - m_{vi}$  and since we know that  $\delta_s = \alpha(\delta_{vi} + 1) - 1$  we get this expression:

$$m_{v0}\delta_{v0} = (m_{v0} - m_{vi}) [\alpha(\delta_{vi} + 1) - 1] + m_{vi}\delta_{vi} \quad (1.3.5)$$

Since we know the pressure  $p_i$  and  $T_i$  in the equilibrium chamber and of the initial vapor  $p_{v0}$  and  $T_{v0}$  we can now define

$$g = \frac{m_{vi}}{m_{v0}} = \frac{p_i T_{v0}}{p_{v0} T_i} \quad (1.3.6)$$

By inserting  $g$  and rearranging 1.3.5, we obtain the following expression for the vapor in equilibrium with ice  $\delta_{vi}$ :

$$\delta_{vi} = \frac{\delta_{v0} - (\alpha - 1)(1 - g)}{(1 - g)\alpha + g} \quad (1.3.7)$$

With this expression we can explore the sensitivity of the experimental setup, assuming that the water and the vapor in the vapor source as well as the vapor and the ice in the equilibrium chamber are in equilibrium.

From 1.3.7 we can then finally obtain an expression for the equilibrium fractionation factor  $\alpha$ :

$$\alpha = \frac{\delta_{v0} - \delta_{vi}}{(\delta_{vi} + 1)(1 - g)} + 1 \quad (1.3.8)$$

Thus, with this expression, we can simply find  $\alpha$  as a function of temperature in the equilibrium chamber by measuring the initial vapor and the vapor in equilibrium with ice

when knowing the temperature and vapor pressure in the vapor source and equilibrium chamber.

The saturation vapor pressure can be found from the temperature. Throughout the years several expressions of the saturation vapor pressure as a function of temperature have been presented with the Goff Gratch equations (Goff, 1957, 1965) always being a reference among these. Lately the Clapeyron equation was integrated for a high detail by Murphy and Koop (2005) and we will use the formulation from their work. In general, the differences in between the Goff Gratch equations and the fit from Murphy and Koop (2005) are very small. The vapor pressure formulation of Murphy and Koop (2005) are as follows with the vapor pressure over water being:

$$p_{wv} = \exp\left(54.842763 - \frac{6763.22}{T} - 4.210 \ln(T) + 0.000367T\right) + \tanh(0.0415(T - 218.8))\left(53.878 - \frac{1331.22}{T} - 9.44523 \ln(T) + 0.014025T\right) \quad (1.3.9)$$

which is valid for  $123 < T < 332$ K. The vapor pressure over ice is:

$$p_{iv} = \exp\left(9.550426 - \frac{5723.265}{T} + 3.53068 \ln(T) - 0.00728332T\right) \quad (1.3.10)$$

which is valid for  $T > 110$ K.

## 1.4 Previous results

In general, two different experimental techniques can be used to measure the equilibrium fractionation factor: Vapor pressure ratio and isotopic fractionation techniques. The vapor pressure technique consists of measuring or modeling the ratio of the vapor pressures of pure samples of the two isotopes as a function of temperature using the relationship:

$$\ln \alpha = \ln(p^*/p)(1 + p(B_0 - (V/RT))) \quad (1.4.1)$$

where  $p$  and  $p^*$  are the vapor pressures of pure samples of the two isotopes,  $V$  is the molar volume of the condensed phase and  $B_0$  is the second virial coefficient of the vapor Bigeleisen et al. (1973). By assuming the validity of Raoult's law this simplifies to  $\alpha = (p^*/p)$  (Majoube, 1970), i.e for  $\delta^{18}\text{O}$  this will be:  $\alpha = p_{H_{16}O}/p_{H_{218}O}$  for pure samples. The isotope fractionation technique allows an isotope mixture to come to equilibrium at a certain temperature (as mentioned above) and the isotope ratios are measured with a mass spectrometer.

Classical thermodynamics investigates the relationships between measurable macroscopic properties of a system and the governing system variables. Hence the state of a system can be characterized through a set of functions and variables such as temperature

and pressure. As an example, it is possible to investigate the ice-vapor equilibrium fractionation factor with the Clausius-Clapeyron equation through the differences in vapor pressure of pure H<sub>2</sub>O and pure HDO by knowing the heat of vaporization of the process. Fundamentally, this approach is fine but in many cases, the properties of the different isotopomers are so similar that measurements (e.g. calorimetric measurements) are not sufficiently precise to make accurate predictions of their behavior. Statistical thermodynamics uses the microscopic properties of a system as well as statistical theory to calculate the macroscopic properties. In principle, all that is needed to calculate a thermodynamical property is contained in the spectroscopic properties of a substance, since the observed frequencies are related to energy states with discrete quantized levels. Here, it is necessary to determine the partition function  $Q$  for each of the various participating species in the isotope exchange (e.g. as in section 1.2.2).

The investigations of the ice-vapor equilibrium fractionation factor have mostly been done with vapor pressure ratio techniques and predictions based on statistical thermodynamics. Only two actual measurements of the isotopic fractionation have been performed and these have since then been the common references on this subject (Horita et al., 2008). These are the works of Merlivat and Nief (1967) and Majoube (1970) who measured the ice-vapor equilibrium fractionation factors for  $\delta\text{D}$  and  $\delta^{18}\text{O}$  respectively. These works were performed on a similar experimental setup in which vapor was allowed to condense out to ice under conditions between 0°C and -33°C. The vapor in equilibrium with this ice was then measured with a mass spectrometer.

In their experiments, they introduce vapor with a known isotopic composition into a 70 cm long tube with a temperature controlled dewar at the end. The vapor then diffuses towards a dewar where some part of the vapor condense out and the remaining vapor will be in equilibrium with the ice. Due to the diffusion there will be an isotopic gradient in the tube between the isotopic composition of the initial vapor and the vapor in equilibrium with the ice. This gradient is dependent of the vapor flow speed and the temperature. Thus, when measuring the isotopic composition of the initial vapor the vapor speed has to be high enough to avoid backdiffusion effects.

Merlivat and Nief (1967) found a temperature dependency of  $T^{-2}$  as a best fit for  $\delta\text{D}$  :

$$\ln \alpha = -9.45 \cdot 10^{-2} + \frac{16289}{T^2} \quad (1.4.2)$$

and Majoube (1970) found a best fit with the  $T^{-1}$  for  $\delta^{18}\text{O}$  :

$$\ln \alpha = -28.224 \cdot 10^{-3} + \frac{11.839}{T} \quad (1.4.3)$$

In both cases  $C_1 \neq 0$  (see above). Additionally, Majoube (1970) performed investigations of the ice-vapor equilibrium fractionation factor with statistical thermodynamics

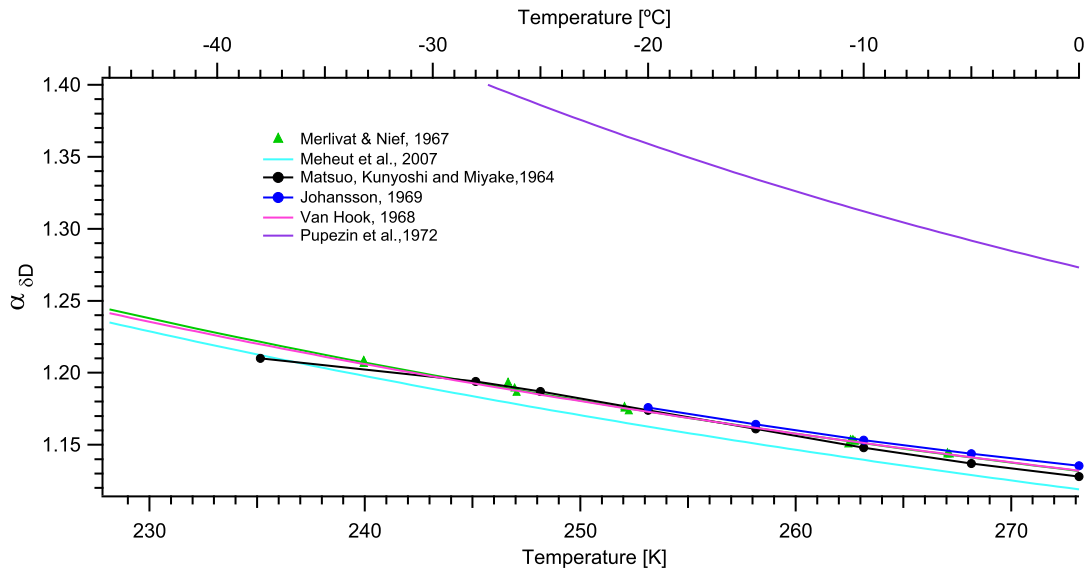


Figure 1.2: Previous work on the ice-vapor equilibrium fractionation factor for  $\delta D$

using spectroscopic data and found that the results from these agreed with the experiments. Besides from the above work, some other authors have investigated the ice-vapor equilibrium fractionation by either measuring the vapor pressure isotope effect or modeling. We will now introduce some of these. Some of the first to perform work on this field was Matsuo et al. (1964) who investigated  $\alpha$  for  $\delta D$  by measuring the vapor pressure of  $H_2O$  and  $D_2O$  ice between  $0^\circ C$  and  $-38^\circ C$  and found values close to the values measured by Merlivat and Nief (1967) as seen on Figure 1.2. Later Matsuo and Matsubaya (1969) investigated  $\alpha$  for  $\delta^{18}O$  by measuring the vapor pressure of  $H_2^{18}O$  ice in the temperature range of  $-5^\circ C$  to  $-20^\circ C$ . They obtained values smaller than Majoube (1970) as seen on Figure 1.3. Van Hook (1968) modelled the vapor pressure isotope effect based on the results of Bigeleisen (1961) and found  $\delta D$  and  $\delta^{18}O$ . His result agree fairly with Majoube (1970) but is not in line with Merlivat and Nief (1967). Another example is Johansson and Holmberg (1969) who made a simple calculation of  $\alpha$  for  $\delta D$  from vapor pressures and thermodynamical data and obtained results in the area of other works. Pupezin et al. (1972) (and earlier reports Jancso et al. (1970a), Jancso et al. (1970b)) presented vapor pressure measurements of the vapor pressure isotope effect of the  $H_2^{16}O$ - $H_2^{18}O$  system as well as for  $H_2^{18}O$  and  $D_2O$  for ice-vapor in the range of  $0^\circ C$  to  $-17^\circ C$ . The data are very scattered and the fit not too good. Their slope is not as high as compared to Majoube (1970), which they conclude are more realistic and agrees with theoretical slopes. Pupezin et al. (1972) also presented  $\alpha$  for  $\delta D$  between  $0^\circ C$  and  $-64^\circ C$  and these can be seen to be quite larger than other works (partially shown on Figure 1.2. Jakli and Staschewski (1977) also measured  $\alpha$  from vapor pressure isotope effect measurements of samples of  $H_2^{16}O$  and  $H_2^{18}O$  for the range of  $-50^\circ C$  to  $0^\circ C$ . As can be seen these values are also considerable smaller than the work of Majoube (1970). More

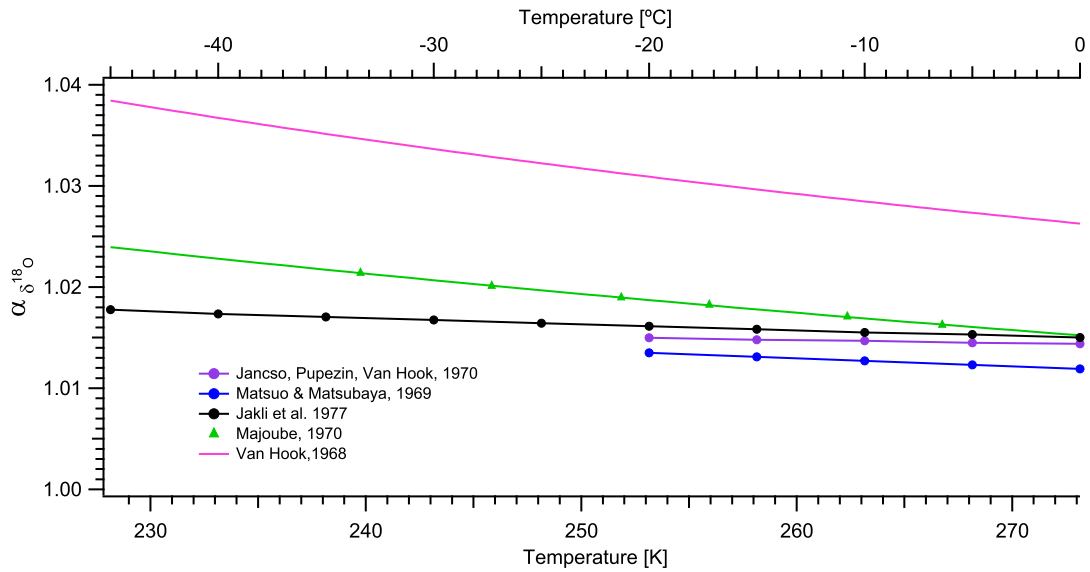


Figure 1.3: Previous work on the ice-vapor equilibrium fractionation factor for  $\delta^{18}\text{O}$

recently Méheut et al. (2007) used a theoretical, statistical thermodynamics approach to find the ice-vapor equilibrium fractionation factor. As showed on Figure 1.2, they obtain values slightly smaller than Merlivat and Nief (1967) for  $\delta\text{D}$  but with the same slope. For  $\delta^{18}\text{O}$  they obtain a difference of roughly  $+3.3\text{‰}$  at 273K but with roughly the same slope.  $\delta^{18}\text{O}$  is not reproduced on Figure 1.3 due to a possible typo in their article. In the above shown examples of previous works on the ice-vapor equilibrium fractionation factor it is worth noticing that all of the different expressions for the temperature dependency of  $\ln \alpha$  as mentioned above are used for both  $\delta\text{D}$  and  $\delta^{18}\text{O}$  and that  $C_1 \neq 0$ . For  $\delta^{18}\text{O}$  it can be seen that there are some scatter on the results from the different works presented. For  $\delta\text{D}$  the different works seem to agree better on the temperature dependency of  $\alpha$  but the  $\delta\text{D}$  plot is affected by the results of Pupezin et al. (1972) which are off compared to the other results.

The above also show that previous investigations on the fractionation factors are sparse, especially for temperatures below  $-20^\circ\text{C}$ . With the background in mind we will in the following chapter introduce the experimental setup used to improve the knowledge about the ice-vapor equilibrium fractionation factor.

## Chapter 2

# Experimental setup and instrumentation

In this chapter the different parts of the experimental setup are introduced and discussed. Sensitivity studies and investigation of the uncertainties associated with the different parts of the system are made in the following chapters.

To increase the knowledge about a process it is important to investigate it through different experimental setups with different approaches to eliminate the possibility of systematic errors. The design of this experimental setup use the principles from Section 1.3 and is inspired by the setup used by Merlivat and Nief (1967) and Majoube (1970), as described in section 1.4 (and later in 5.5). However, where the setup of Merlivat and Nief (1967) and Majoube (1970) use vapor diffusion as transport mechanism between the vapor reservoir and the condensation area, we use continuous flow with a carrier gas to take full advantage of the instrumentation available. This limits the possibility of back diffusion effects and the problem of disturbing equilibrium when sampling, but we still have to properly characterize the performance of the setup, e.g. to avoid kinetic fractionation effects. One of the advantages of using continuous flow is that we will be able to observe the important transients occurring as the system approaches equilibrium.

### 2.1 General setup design

Figure 2.1 shows a quick overview of the principles of the experimental setup. Just as Merlivat and Nief (1967) and Majoube (1970) , we force vapor from a vapor source with a known isotopic composition through a temperature controlled chamber which in the following will be denoted the equilibrium chamber. Depending on the saturation vapor pressure in the equilibrium chamber, a part of the vapor will condense out as ice and with proper exchange between the two phases the remaining vapor will stay in thermodynamic

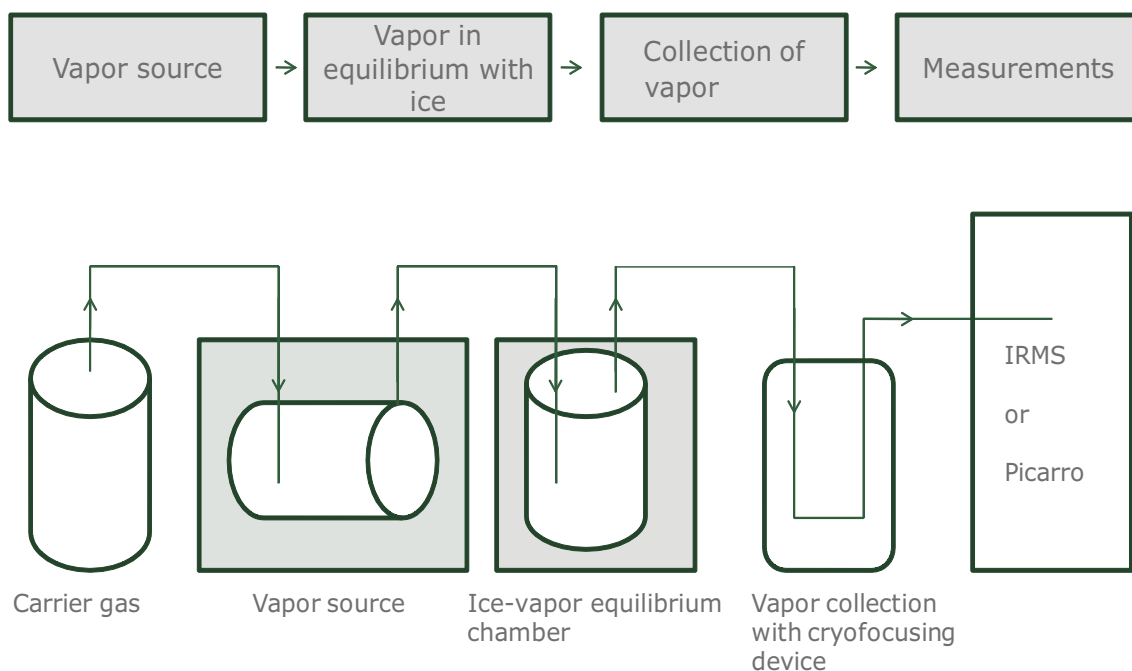


Figure 2.1: Sketch illustrating the principles of the experiments.

and isotopic equilibrium with the ice. Depending on the measurement technique, we then either measure directly on this vapor with the Picarro Isotopic Water Analyzer or collect it in the cryofocus cold trap for measurements with the TC/EA - IRMS system. As shown, the principles behind the experiments are relatively simple. However, to ensure that e.g. the vapor is in equilibrium with the ice (and not affected by kinetic effects) in the condensation chamber is difficult. Due to this the experimental setup has been through several iterations to improve its performance. That said, as every experimental setup, the setup has advantages and limitations and in the following sections and chapters we will discuss these.

Figure 2.2 shows a more detailed chart of the experimental setup and a picture of the setup can be seen on Figure 2.3. As mentioned before, we use either IRMS or laser spectroscopy to measure the isotopic composition of the vapor from the equilibrium chamber. To facilitate the connection between the experimental setup with continuous flow and the IRMS system we use two flow lines; one for collecting vapor and one for purging a collected sample into the TC/EA. We use either dry air ("Teknisk luft" from Air Liquide) or Helium as carrier gas from a pressure bottle. The flow is divided into the two flow lines (sample and purge), each with a Porter VCD 1000 Flow Controller attached. The sample flow line uses a typical flow rate of  $\sim 100$  mL/min (varied) and the purge flow use a fixed flow rate of  $\sim 60$  mL/min (see Section 2.3). Using two flow lines ensures that we can decouple the experimental setup from the instrumentation without affecting the ongoing measurements by e.g. pressure changes occurring downstream. The heart of the setup is a VICI 8 port

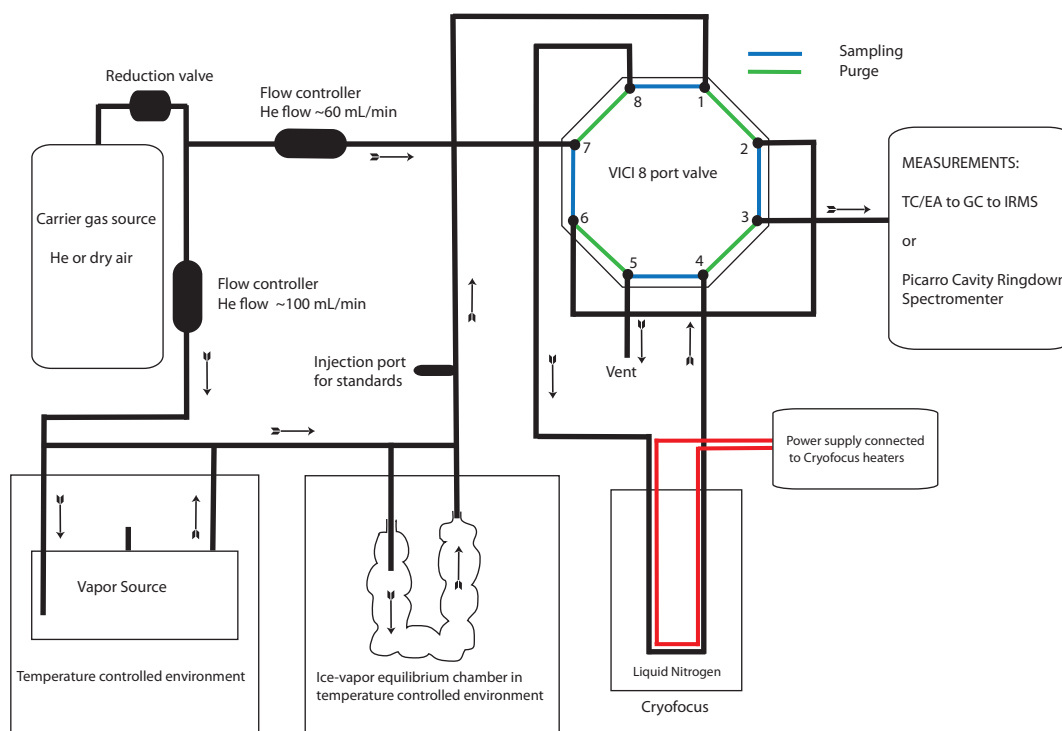


Figure 2.2: A chart of the flow lines in the experimental setup. A VICI 8-port valve is used to change the flow line (sample/purge) through the cryofocus. All tubing is heated with rope heaters.

valve that connects the two flow lines to the various parts of the setup as shown in 2.2. The valve has two positions that enables it to connect the cryofocus from the sample flow line to the purge flow line when injecting a sample into the IRMS system. The valve positions are changed manually. The VICI valve has a Nitronic 60 stainless steel valve body with a Valcon E rotor which makes it withstand temperatures up to 225°C. The valve can be seen on Figure 2.4. Unless otherwise noted, the setup consists of  $\frac{1}{8}$ " stainless steel tubing heated with rope heaters. Most parts of the setup (including the valve and the purge line) are heated to well above 100°C to limit adsorption and condensation in the tubing. The only parts of the setup that are not heated are the sample lines before the carrier gas enters the vapor source and the purge line before it enters the VICI valve (i.e. before the sample is introduced). The heaters are always on, even when the experimental setup is idle.

When in sampling mode, the purge line enters the valve and goes directly into the TC/EA to ensure a constant flow there. The sampling line carries the vapor from the vapor source to the equilibrium chamber where some part of the vapor condense out. The vapor in equilibrium with the condensate is then carried through the valve into the cryofocus. In sampling mode, the cryofocus is submerged into liquid nitrogen and all vapor

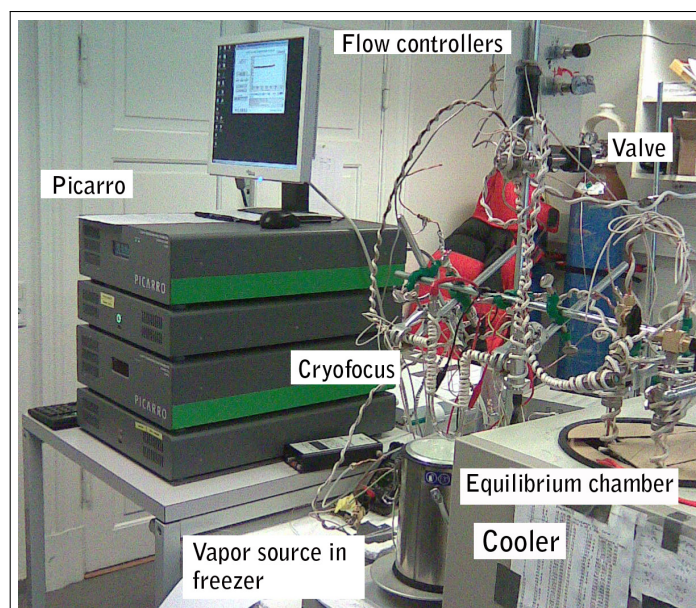


Figure 2.3: A picture of the experimental setup with indications of the different units.

in the Helium sample flow is collected. The sampling line ends in the vent where a long tube prevents back diffusion of vapor into the setup. When in purge mode the sampling line is directed to the vent and the purge flow through the cryofocus on the way to the TC/EA. Once the system is ready for measurement, the cryofocus is strongly heated both on the out- and on the inside and the collected sample is injected into the TC/EA. The setup uses two power supplies, one dedicated for heating the cryofocus and one dedicated for the rope heaters around the tubing. An injection port is added to the setup and allows for manual injections of standard water for VSMOW calibration.

All Swagelok connections are leak checked with an Agilent G3388A hand held leak detector. This device uses a thermistor actuated thermal conductivity cell to measure the conductivity and has a lower leak detection limit of 0.01 mL/minute. The cryofocus is also used to check for leaks since it will collect any water in the carrier gas. Here, blank tests show that no significant leaks are present in the setup. Furthermore, tests with the Picarro shows that we are able to obtain close to zero humidity (below 10 ppm, uncalibrated) when running dry air through the setup. This check is performed before every Picarro measurement. Another way to test for leaks or sample loss is by checking the peak volume on the IRMS samples. When injecting 0.2  $\mu\text{L}$  water through the setup through the standard injection port, we obtain the same peak area as when we inject 0.2  $\mu\text{L}$  water directly into the TC/EA. This is of course dependent on the integration algorithm used by Isodat and assumes identical peak shapes.

In the following sections we will introduce the instrumentation, namely the Picarro H<sub>2</sub>O laser spectrometer and the Delta V Advantage TC/EA-IRMS system.

## 2.2 Picarro Wavelength Scanned Cavity Ringdown Spectrometer

To analyze the variations of the water isotopes in natural waters with conventional IRMS, usually a chemical conversion of a discrete sample of water into light gas suitable for mass spectrometry (in our case with the TC/EA, H<sub>2</sub> and CO) is necessary. The Cavity Ring-Down Spectroscopy (CRDS) technique (O’Keefe and Deacon, 1988; Wahl et al., 2006; Berden et al., 2000) make use of photo absorption of water molecules and has managed to reach the required precision level for water isotope analysis (Gupta et al., 2009; Lis et al., 2008). The light from a laser is guided into a cavity with very high reflectance mirrors. These mirrors keep the laser beam inside the cavity for a high number of reflections, thus achieving a mean absorption path of kilometers. The light intensity inside the cavity increases over time and is monitored through a photo detector. The ring-down measurement is made by rapidly turning on and off the laser and measuring the intensity in the cavity as it decays due to the light absorption of the gaseous sample. The decay is exponential and is usually parameterized using a decay time constant (Crosson, 2008). By scanning the wavelength of the laser over the H<sub>2</sub>O spectral features and measuring the ring-down time, a detailed optical spectrum is made. By selecting spectral absorption features that are specific for single isotopologues, the concentration of the different isotopologues can be found from integration of the spectral features. Since the instrument works with absolute concentrations and since the different absorption peaks of the water isotopologues have different temperature sensitivities, the temperature and pressure of the ring-down cavity are monitored and actively stabilized with the temperature being around 80°C±20mK and pressure being around 35torr±0.1 torr (Gupta et al., 2009).

A Picarro L-1102i Isotopic Water Analyzer was used. This model uses a tunable diode laser (1392 nm) and a 35 mL cavity and this unit is similar to the units described in (Gupta et al., 2009) and (Brand et al., 2009).

The Picarro needs a constant flow rate of 30 mL/min through the cavity with dry air as carrier gas and has a pump to regulate the mass flow of the incoming sample gas. Due to this, we use an open split system at the Picarro sample intake. This consists of a three-way fitting with the Picarro connected to one end, the experimental setup to the second end and a 15 cm tube connected to the third end. The tube prevents back diffusion of atmospheric vapor into the sample flow. The open split enables us to have flow rates larger than 30 mL/min through the experimental setup with the excess going through the open split into the laboratory. To avoid using two types of carrier gas in the experimental setup we performed tests with Helium as carrier gas. But the pump had difficulties controlling the inlet pressure (which then was really dependent on the humidity). Furthermore, using Helium as carrier gas raises other issues as e.g. interference with the absorption lines which

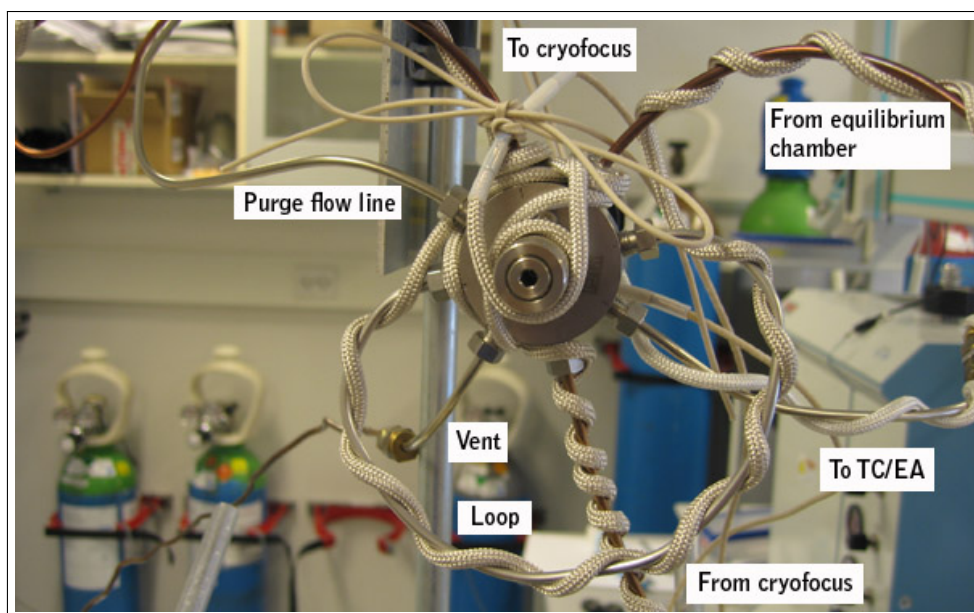


Figure 2.4: A picture of the VICI valve connecting the different parts of the experimental setup. The valve is heated with rope heaters and the location of the different connections are indicated.

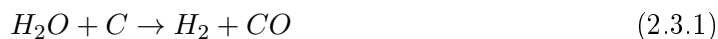
would require some calibrations. Therefore we only used dry air as carrier gas with the Picarro. Due to the low diffusion rate of  $\text{H}_2\text{O}$  in dry air compared to  $\text{H}_2\text{O}$  in Helium (see e.g. section 2.7.2), the exchange between e.g. ice and vapor would be larger with Helium as a carrier gas and this is therefore not a problem.

Since the Picarro allows for continuous measurements of the stable water isotopes, it is very well suited for characterizing the experimental setup since we can observe the transient changes in the isotopic values as they occur. This has not been possible before and gives the Picarro a big advantage compared to conventional IRMS since there is no need to collect vapor and inject it as a discrete sample. The main limitation of the  $\text{H}_2\text{O}$  Picarro is the humidity dependency since the measurement uncertainty increases with decreasing amount of water in the carrier gas (with fewer molecules it is harder to determine the spectral absorption features). In practice this means that we are not able to perform measurements at absolute humidities much lower than what corresponds to the saturation vapor pressure at  $-20^\circ\text{C}$ . As described in Brand et al. (2009) the humidity dependency has a non-linear behavior for absolute humidities below 10000 ppmv, and this will be discussed in the next chapter.

## 2.3 TC/EA GC-IRMS

For measurements of the samples collected with the cryofocus we use a TC/EA (High Temperature Conversion/Elemental Analyzer) high temperature furnace connected to a

Delta V Advantage IRMS system through a ConFlo III device (referred to as the IRMS system). This system allows us to measure both isotopes on a sample of a size less than  $0.3\mu\text{L}$ . The system allows for fast switches between gas species (with a magnet jump) and with the  $\text{H}_2$  and  $\text{CO}$  peaks being separated by a GC column, both  $\delta\text{D}$  and  $\delta^{18}\text{O}$  can be measured on the same sample. Before the  $\delta\text{D}$  and the  $\delta^{18}\text{O}$  ratios can be measured by the mass spectrometer, the  $\text{H}_2\text{O}$  is converted into  $\text{H}_2$  and  $\text{CO}$  by high temperature pyrolysis in the TC/EA:



The TC/EA comprises a two-tube design inside a reactor of  $1384^\circ\text{C}$  with a glassy carbon tube fitted inside a ceramic insulator tube of aluminum oxide ( $\text{Al}_2\text{O}_3$ ). The space between the two tubes is continuously flushed with Helium to prevent unintentional oxidation. The glassy carbon column is filled with glassy carbon chips from the bottom to about 10 cm above the hot zone where the most efficient pyrolysis occurs. The carrier gas flow enters the TC/EA at the septum head and divides into two streams; one through the core of the reactor and the other between the space of the glassy carbon and the ceramic tube. The typical Helium flow of 90 cc/min carries the  $\text{H}_2$  and  $\text{CO}$  to a GC where the gaseous products of the pyrolysis are separated by a molecular sieve. An illustration of the system can be seen on Figure 2.5. The size of the gas pulse entering the ion source of the mass spectrometer is controlled by a ConFlo III device. This is designed such that the pressure difference between the open split and the capillary line to the mass spectrometer causes the sample to be drawn into the capillary where it flows to the ion source and becomes ionized. Furthermore, the size difference between the open split and the capillary also causes loss of sample gas. The gaseous sample to be analyzed is fed into the ion source via the inlet system. In the ion source, ions are generated in a high vacuum by the impact of electrons. These ions are then accelerated to energies up to several keV and focused by electrostatic lenses into a beam. The ion beam then exits the ion source into the magnetic field. The magnetic field is generated by an electromagnet and the mass setting is achieved by varying the magnetic field strength and/or the accelerating voltage. The relation between the mass number  $m/z$  of the ions reaching the ion collector and the magnetic field strength  $H$  is given by  $\frac{m}{z} = k_M \times H^2$ . Hydrogen (for  $\delta\text{D}$ ) determination requires a system with Faraday collectors for the masses  $m/z = 2$  and  $m/z = 3$ , with  $m/z = 28$ ,  $m/z = 29$  and  $m/z = 30$  used to determine  $\text{CO}$  (for  $\delta^{18}\text{O}$ ). Here  $z$  as the number of charges on the ion and  $k_M = \frac{r^2}{2U}$  where  $r$  is the nominal radius of the ion path and  $U$  is the accelerating voltage. Thus,  $U$  and  $H$  can be varied to allow different species to be analyzed. Every measurement consists of a  $\text{H}_2$  reference peak followed by the  $\text{H}_2$  sample peak, both consisting of the  $m/z = 2$  and  $m/z = 3$  signals. Then the magnet jump changes configuration of the system to be able to measure the  $\text{CO}$  peaks consisting of the  $m/z = 28$ ,  $m/z = 29$  and  $m/z = 30$  signals. Again, we have a reference gas peak for  $\text{CO}$  followed by the  $\text{CO}$  sample peak. A full measurement run takes around 9 minutes. The reference peaks are measurements of

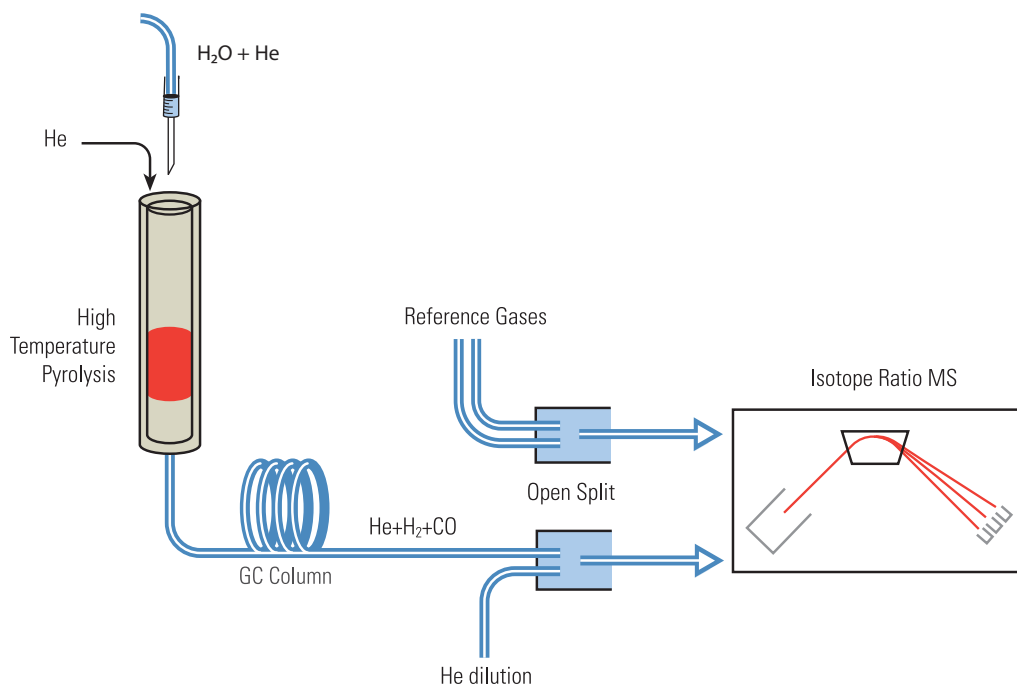


Figure 2.5: Sketch of the connection between the experimental setup, the TC/EA and the IRMS. (Modified figure from ThermoScientific TC/EA brochure)

gas that does not pass through the TC/EA but enters directly through the ConFlo III device. The separation of the  $\text{H}_2$  and  $\text{CO}$  species in the GC column is crucial for correct timing between the peaks. The isotope ratio of the sample is then obtained by peak area integration performed by the Isodat software. The isotope ratio of each sample is then found relative to the ratio of the respective reference peak. From the results of identical measurements of well known local standards the isotope ratios of the sample can then be calibrated towards the IAEA VSMOW standard (Gonfiantini, 1978; Craig, 1961). In addition to the peak area integration some corrections are done by Isodat to account for e.g. the  $\text{H}_3^+$  ions produced. We will now describe the most important calibrations and corrections.

### 2.3.1 $\text{H}_3^+$ factor corrections

One of the ionic fragments produced in the ion source of the mass spectrometer is  $\text{H}_3^+$  which has the same mass as  $\text{HD}^+$  (Friedman, 1953) and influences the  $m/z = 3$  signal. These ions therefore result in an apparent  $3/2$  ratio which is higher than desired and the isotopic analysis of hydrogen has to be corrected for this. The contribution of  $\text{H}_3^+$  can be minimized by adding a repeller electrode to the source using a high alternating voltage at the low gas pressure but the contribution still has to be characterized. The production of  $\text{H}_3^+$  is proportional to the pressure of the hydrogen gas in the source since the ion is

produced by the reaction  $H_2 + H_2^+ \rightarrow H_3^+ + H$ . To correct for the  $H_3^+$  production, the contribution is evaluated by measuring the  $m/z = 3/m/z = 2$  ion current ratio as a function of pressure. This is done with a standard reference gas on-off test containing reference gas pulses of different amplitudes (the pressure of the reference gas is varied between 0.6 bar and 1.5 bar on the ConFlo III). Due to the low ion source pressures, the reaction above is the main source for  $H_3^+$  (Friedman, 1953) and the production of  $H_3^+$  is given by (Sessions et al., 2000):

$$[H_3^+] \propto [H_2^+] [H_2] = K [H_2]^2 \quad (2.3.2)$$

The proportionality constant in this equation  $K$  is also known as the  $H_3^+$  factor. Thus, by knowing the relationship between pressure and the contribution of  $H_3^+$ , a correction algorithm in ISODAT finds the correction factor and automatically removes the  $m/z = 3$  contribution from the  $H_3^+$  ion.

### 2.3.2 $^{17}\text{O}$ Corrections

The  $^{18}\text{O}/^{16}\text{O}$  ratio of the samples correspond to the ratio of the peak areas of the molecular  $\text{CO}^+$  at masses 30 and 28 corrected for the small contribution of  $^{13}\text{C}^{17}\text{O}$  on  $m/z = 30$  by the Isodat software. Calculations show that Isodat uses the method by Santrock et al. (1985) that assumes that the three stable oxygen isotopes are linked by a mass dependent relationship with  $\lambda = 0.516$  as proportionality constant, obtained by experimental measurements. Other works on this, e.g. Craig (1957) obtain  $\lambda = 0.5$ . The relationship between the ratios  $^{17}\text{R}$  and  $^{18}\text{R}$  in meteoric water is now more documented (e.g. Barkan and Luz (2005)) and newer estimates of  $\lambda = 0.528$  have been made (Assonov and Brenninkmeijer, 2003a,b; Brand et al., 2010). This estimate would be better to use since we measure meteoric waters. However if making the corrections using the results from Craig (1957) or Assonov and Brenninkmeijer (2003a), the differences in the resulting  $\delta^{18}\text{O}$  are negligible compared to the mass spectrometer measurement uncertainty<sup>1</sup>. Due to this we simply use the  $\delta^{18}\text{O}$  calculated by Isodat. These corrections mean of course that it is not possible to determine  $\delta^{17}\text{O}$  in the samples.

### 2.3.3 Peak area dependencies

Due to the magnet jump cutting off a part of the peak tail and the settings of the integration routine used by Isodat, the measured isotope ratios have a dependency on the peak area (i.e. injection volume). An example of this dependency is seen on Figure 2.6 that shows  $\delta\text{D}$  for injections of 2 different standards as a function of injection volume. Before the shown injections, 15 injections are made to ensure that no memory effects are seen in the results. We have not accounted for background changes during these tests. Furthermore,

<sup>1</sup>Calculations performed by Myriam Guillevic

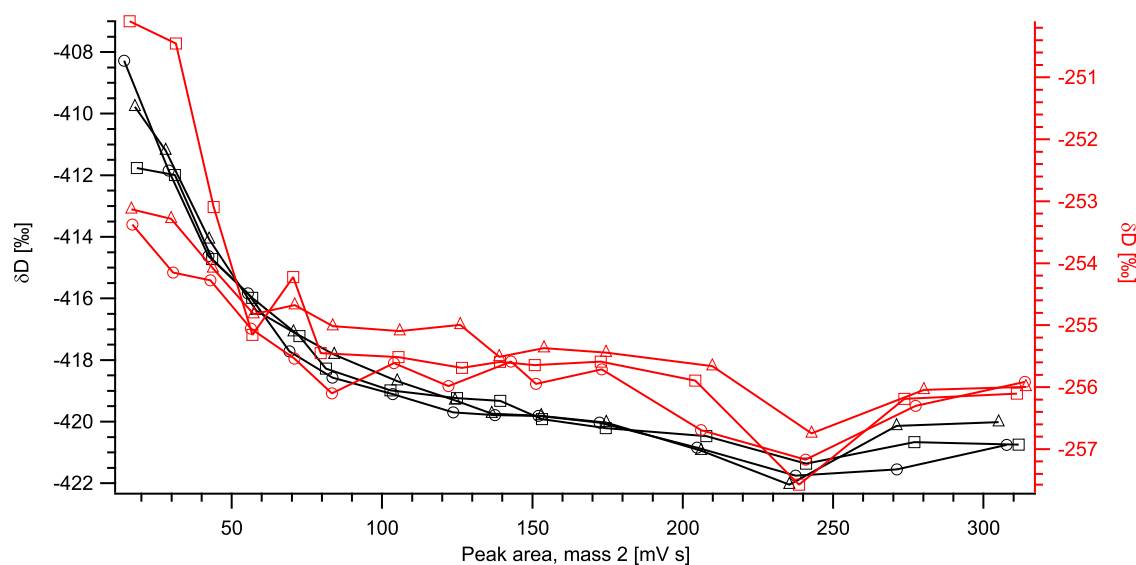


Figure 2.6:  $\delta D$  as a function of peak area for injections of two different standards. Some peak area dependencies on the resulting  $\delta D$  can be seen.

it has to be noted that the shown data points represent one injection only. A significant dependency between peak area and isotope ratio is seen with the slope being strongest for small injection volumes and tails off around 100 mVs. Here, the difference between e.g. 100 mVs and 150 mVs is around 1 ‰. Of course, this could be further investigated with many injections per injection volume. Due to this we maintain the same injection volume/peak area for all measurements and standard injections during a measurement run. This is typically 120 mVs or 130 mVs depending on the condition of the TC/EA. This corresponds to injection volumes of around  $0.2\mu\text{L}$  and the slope is relatively small in that range on Figure 2.6. The injection volume is controlled by keeping the cryofocus sampling time accurate within seconds. By doing this we obtain typical peak area fluctuations of roughly 10-15 mVs during a measurement run which make the possible impact of peak area fluctuations negligible.

### 2.3.4 Memory effects

The constant heating and continuous flow in the parts of the experimental setup limits the memory effects there and the main memory effect is found in the TC/EA in the IRMS system. The memory effect here varies with the condition of the glassy carbon tube in the TC/EA. It is generally larger for  $\delta^{18}\text{O}$  than  $\delta D$  and depending on the injection volume and the difference between the isotope ratios of two different samples, up to 10 injections are needed to completely remove the memory effect. Figure 2.7 shows an example of the memory effect both for  $\delta D$  and  $\delta^{18}\text{O}$  for injections of three standards. Here the impacts of the memory effect is clearly seen as the isotope values drift towards a stable level. The

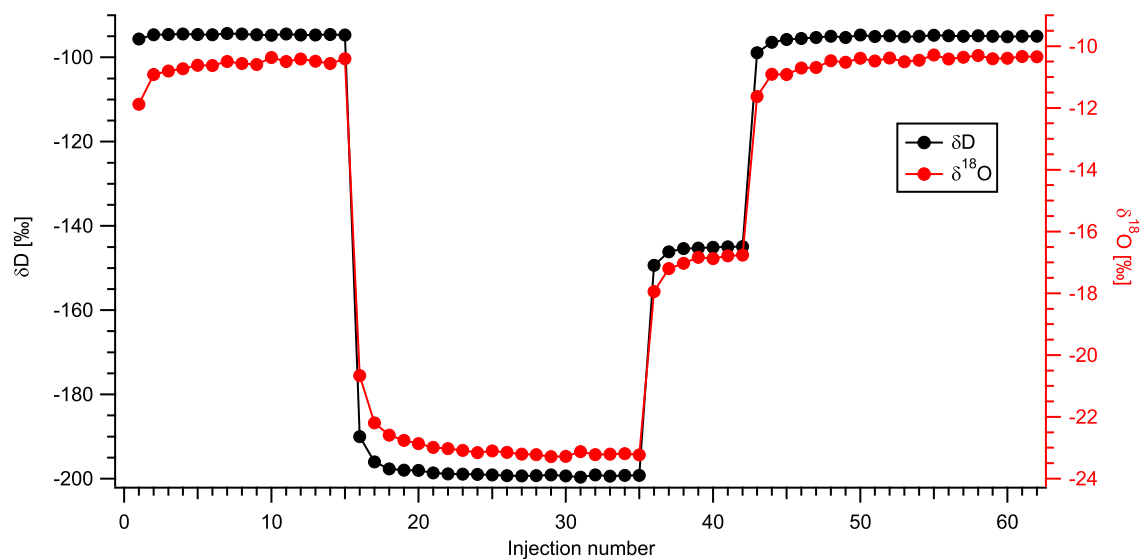


Figure 2.7:  $\delta\text{D}$  and  $\delta^{18}\text{O}$  as a function of injection number for three different standards. The memory effect of the system is stronger for  $\delta^{18}\text{O}$  than for  $\delta\text{D}$ .

memory effect can be quantified by fitting a function to the slopes as shown in Figure 2.7 and this can be used to correct the measured values. This is time consuming since several injections of two different standards are needed and essentially this has to be performed before each measurement since the memory effect can change with time. Furthermore, the uncertainty of this correction propagate into the uncertainty of the final result. To account for the memory effects in the system we therefore choose another approach with the use of conditioning and multiple measurements. Before each measurement run we condition the TC/EA with 15-20 manual injections of a standard with an isotopic composition close to the expected for the performed measurement. During the actual sample measurements there will be some slight sloping between the isotopic values of the conditioning standard and the sample. We continue to perform sample measurements until we obtain at least five or six measurements with stable values, i.e. where the slope is close to zero and where the standard deviation of the measurements approach the measurement uncertainty for the instrument. Thus, each measurement result consists of around ten sample measurements and roughly the same amount for the VSMOW calibration. As mentioned above, each measurement run takes around 9 minutes. Since this process is hard to automate fully (e.g. injecting standards through the injection port) and due to the sampling time the measurements are therefore very time consuming. If the system has been idle for a long time it "forgets" the previous sample. This is an issue for the long time sampling, e.g. for the  $-50^\circ\text{C}$  measurements, where the sampling time is more than one hour. Here it can take many measurements before stable isotope values are obtained.

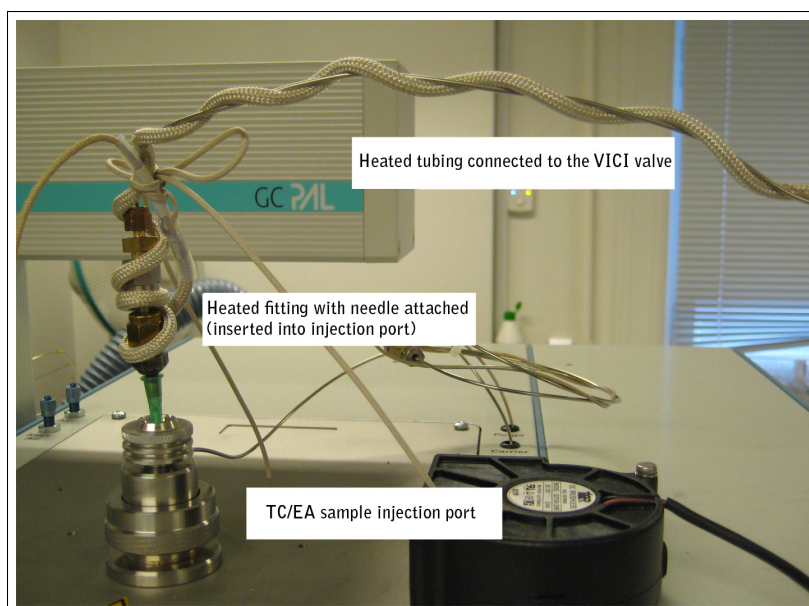


Figure 2.8: The experimental setup is connected to the TC/EA injection port through a fitting with a conical head attached to a needle. Rope heaters keep a high temperature to limit adsorption/condensation, Vacuum grease on and around the fitting head ensures leak tightness.

## 2.4 Connecting the experimental setup to the TC/EA

The TC/EA injection port is designed for autosampler droplet injections and consists of a septum enclosed in a metal housing with a hole for the autosampler syringe. To use this injection port with continuous flow from the experimental setup we use a custom solution with a needle connected to a conical fitting with a  $\frac{1}{8}$ " Swagelok fitting. This is indicated on Figure 2.5 and can be seen on Figure 2.8. The needle-fitting connection is leak tight with vacuum grease and this is checked before each measurement. Due to the continuous flow in the experimental setup ( $\sim 60$  mL/min), the normal pressure inside the TC/EA ( $\sim 1.2$  bar and  $\sim 90$  mL/min) is reduced such that the total pressure inside the TC/EA is maintained when the experimental setup is connected. This ensures optimal pyrolysis inside the TC/EA and since the conditions are the same as during normal operations with droplet injections the same amount of sample reaches the IRMS through the open split further downstream. This means that only a slightly modified version of the acquisition method in the Isodat software can be used. The Swagelok fitting with the needle attached is constantly heated to prevent condensation. The needle is inserted as deep into the TC/EA as possible which is a little deeper than normal autosampler injections. Due to the dead space in this end of the TC/EA and since we inject vapor directly, different insertion angles of the needle into the septum can cause changes in the peak shapes, peak size and in the size of the memory effect. This happens if a part of the sample does not enter the center of

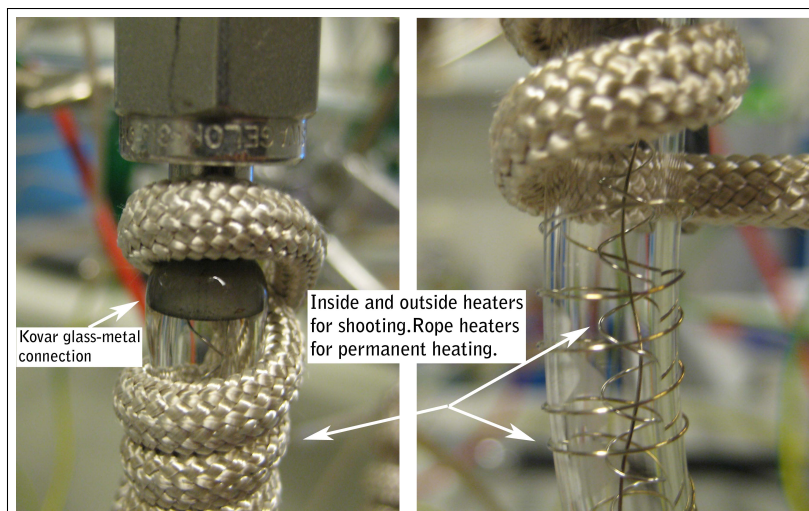


Figure 2.9: Left: Kovar glass-metal connection connected to a Swagelok fitting. Right: the NiCr heating wire inside and outside the cryofocus ensure quick heating of the collected sample during sample injection. Rope heaters are always on to limit adsorption and condensation in the tubing.

the glassy carbon column and is combusted incompletely. Due to this, the insertion depth and angle is carefully checked and changed if needed.

## 2.5 Cryofocus

The cryofocus (and the purge flow line) is only used when performing measurements on the IRMS system since the Picarro system can measure directly on the vapor flow from the equilibrium chamber. The cryofocus has two main purposes. It has to collect the water molecules in the gas stream (while letting the Helium pass through) and with enough sample collected, quick heating of the cryofocus will create a narrow vapor pulse to be injected into the TC/EA - IRMS system. This pulse has to be short and with large enough intensity such that it can be properly integrated by the Isodat software. Due to this, the design of the cryofocus is a trade off between low flow speed and large inner surface area to collect all vapor versus quick heating and high flow speed to reduce the peak width of the IRMS measurements. To accommodate these needs (as well as being durable), the cryofocus consists of a custom made U-shaped  $\frac{1}{4}$ " glass tube with three connections. All three connections are equipped with Kovar fittings for vacuum tight and heatable connections between the glass and the connected Swagelok fittings. The Kovar fittings are made of a Nickel-Cobalt ferrous alloy compatible with the thermal expansion characteristics of borosilicate glass and this glass-metal connection can therefore be strongly heated without breaking of the glass. The Kovar fittings can be seen on the left side of Figure 2.9 that also show the heaters on the cryofocus on the right side. The U-shape of the cryofocus makes

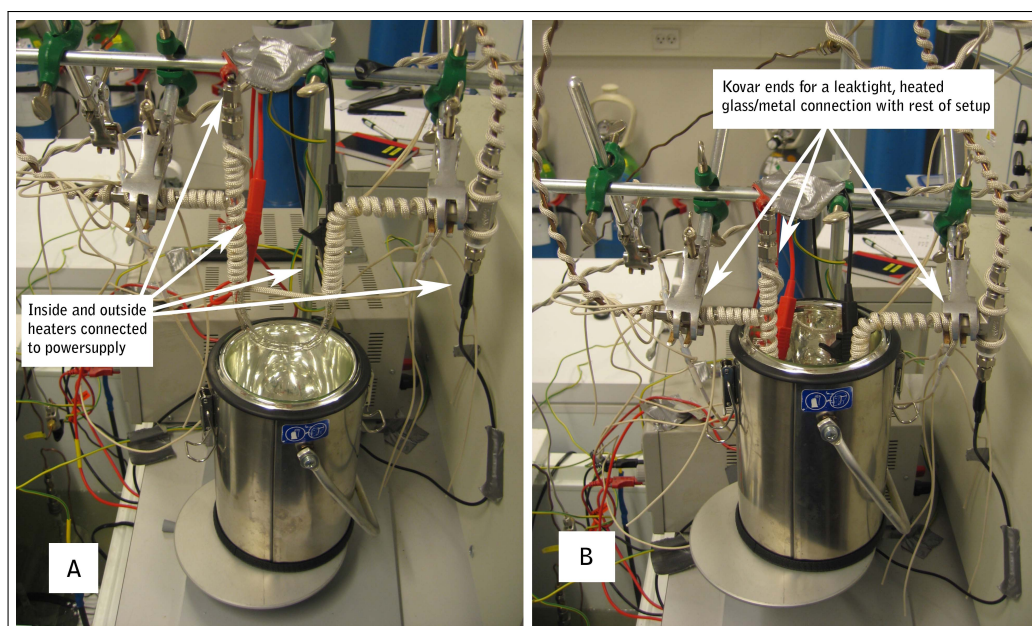


Figure 2.10: The cryofocus in purge mode (A) and sampling mode (B). The rope heaters can be seen heat a part of the cryofocus and the tubing permanently, while the NiCr heating wire is only on during sample injection.

the bottom part of the glass section able to be submerged into liquid nitrogen when sample collecting. This is seen on Figure 2.10 that shows the cryofocus with the heaters connected in purge mode (A) and sampling mode (B). This part of the cryofocus is not permanently heated as opposed to the upper parts of the glass section and the connected tubing and fittings that are strongly heated with rope heaters connected to the main power supply. Instead, resistance heating wires (80% Nickel and 20% Chromium) are pulled on the outside of the glass section as shown on Figure 2.9. Furthermore, resistance heating wire is pulled on the inside of the glass part between the connected fittings. The heating wires are not electrically insulated and are connected to a dedicated power supply through the Swagelok fittings at both ends with SGE graphite/vespel ferrules. These ferrules are reusable and make a leak tight connection. The experimental setup is grounded to avoid electrical current in the tubing. Both outside and inside heating wires are connected to the dedicated power supply and when "shooting" a collected sample this power supply is turned on. The power supply delivers 100W (25V / 4A) to the resistance heating wire such that it heats up the cryofocus from the temperature of the liquid nitrogen and evaporates the collected sample within a short moment of time. The peak shape of the vapor pulse is dependent on the heating and inertness of the cryofocus. Due to this Restek Siltek/Sulfinert coated stainless steel tubing  $\frac{1}{8}$ " is used for the connections between the cryofocus and the Valco 8 port valve. Restek Siltek is a highly inert coating and combined with strong permanent heating this limits the memory effects caused by the tubing. The cryofocus is leakchecked with the handheld leak detector, with dry air with the Picarro as well as with blank tests

and the connections have proved to be leak tight.

As will be shown in the next chapter, the cryofocus performs as expected. The peaks produced by the cryofocus have roughly same characteristics as typical autosampler droplet injections into the TC/EA and the peaks are suitable for integration in Isodat. However, some peak broadening can be seen, presumably due to memory effects in the tubing, dead space in the TC/EA and the heating time of the heating elements inside the cryofocus.

The above description the TC/EA IRMS system show that many custom solutions have to be used since we are not using the system as intended by the different manufacturers. First, developing these solutions and second making them work properly involves several iterations of the hardware. Furthermore tuning the setup and the IRMS system to find the right combination of e.g. sample size, cryofocus performance, TC/EA flow rate, purge flow rate, needle insertion solution, GC temperature as well as the different variables in the Isodat measurement routine proved to be a timely process with the IRMS system also being used for other purposes. Luckily the end configuration proved to work satisfactory.

## 2.6 The vapor source

The purpose of the vapor source is to deliver vapor with a stable humidity and a well known and stable isotopic composition. The vapor source has to be large enough such that isotopic enrichment of the water during ongoing evaporation is negligible on short time scales. Stable humidity implies proper temperature control as well as sufficient exchange between the incoming carrier gas and the water. Here, a low temperature as possible is preferred to keep the vapor pressure down and to limit the relative changes in vapor pressure due to temperature fluctuations. Commercial units can be found to deliver vapor with a constant isotope ratio to a high accuracy. An example of this is the Los Gatos Research (LGR) Water Vapor Isotope Standard Source (WVISS). However, we have chosen to design and make the vapor source in house due to the price and since a custom solution has the advantage that it can be directly connected to the rest of the setup with the carrier gas and run constantly for days without having the water changed. Figure 2.11 shows the vapor source. It consists of a  $\sim 2300$  mL inner volume glass cylinder with three in/outlet tubes, all  $\frac{1}{2}$ " diameter. The cylinder is filled with roughly  $\sim 1900$  mL of water such that there is enough head space above the water level for water/vapor exchange. The water in the vapor source is Milli-Q tap water from Copenhagen (CPH) to avoid impurities and calcium in the setup. The water has an isotopic composition of roughly  $\delta^{18}\text{O} = -9\text{‰}$  and  $\delta\text{D} = -61\text{‰}$  relative to VSMOW. The advantage of using CPH tap water is that it is readily available and that it is enriched in heavy isotopes compared to the various working standards in the laboratory. Due to this, the results from the experiment (with depletion

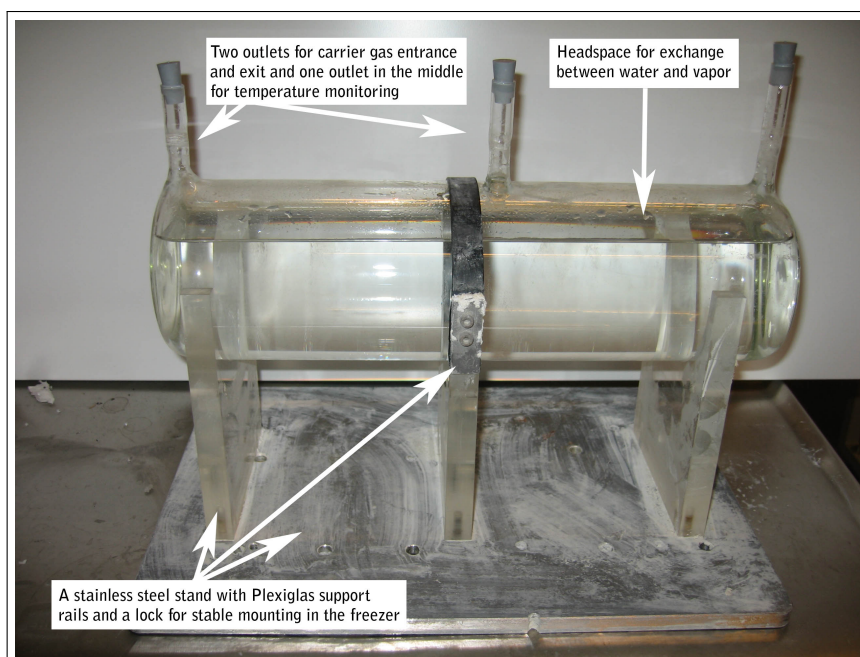


Figure 2.11: The vapor source water cylinder with three connections, mounted on a stainless steel stand.

of the vapor) can still be calibrated towards VSMOW with available local standards. The glass cylinder is connected to the rest of the experimental setup through two Swagelok UltraTorr  $\frac{1}{2}$ " stainless steel fittings that form a leak tight connection between the  $\frac{1}{8}$ " tubing and the  $\frac{1}{2}$ " glass connectors on the vapor source. The Swagelok connections are connected to two three-port valves such that the vapor source can be bypassed from the rest of the setup if needed. The connector in the middle of the glass cylinder is used for temperature monitoring of the water. For this, a bored through plastic cork is used to form a leak tight closure (with silicone sealant) around the thermistor being submerged into the water. The thermistor resistance is converted into temperature with the following Steinhart-Hart calculation (Steinhart and Hart, 1968):

$$T = -273.15 + \frac{1}{A + B * \ln(R) + C * \ln(R)^3} \quad (2.6.1)$$

where  $R$  is the resistance,  $T$  is temperature in  $^{\circ}\text{C}$  and the constants are:  $A=1.4659320\text{E-}03$ ,  $B=2.3861336\text{E-}04$  and  $C=1.0021682\text{E-}07$ . With this, the 10K thermistor has a precision of 50mK. We use a Fluke 289 Digital Multimeter to log the temperature as a function of time. When only monitoring the temperature in the vapor source, a normal multimeter is used.

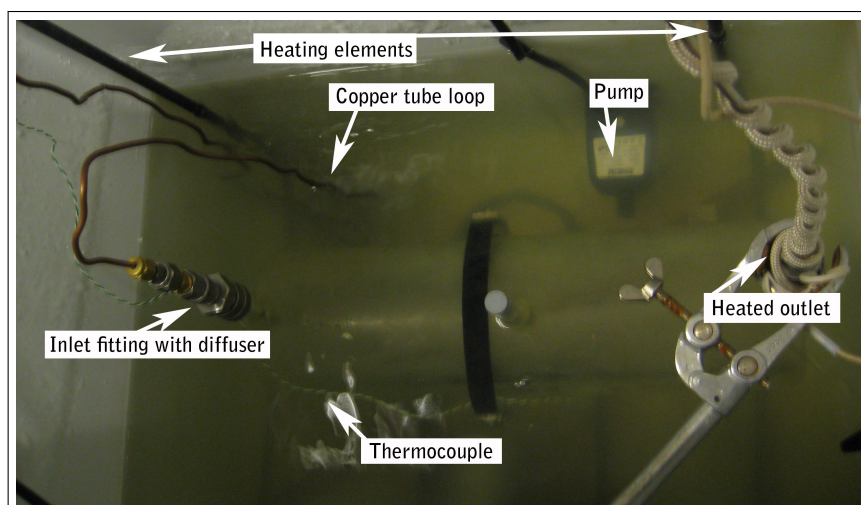


Figure 2.12: Freezer with the vapor source submerged and attached to the rest of the setup.

### 2.6.1 Temperature controlling of the vapor source

Proper temperature control of the vapor source is important since both humidity and isotopic composition of the vapor is strongly temperature dependent. As shown on Figure 2.11 the glass cylinder is mounted to a stainless steel stand with Plexiglas rails. This is submerged into a freezer partially filled with water. This can be seen on Figure 2.12. Silicone sealant is added to the corners of the freezer for water tightness. The freezer is always set to maximum cooling and the temperature of the water in the freezer and hence the vapor source is controlled with a temperature control unit (see below) attached to a heating element submerged into the freezer. The water in the freezer is well mixed due to 3 pumps with a total pumping capacity of 3000 L/hour and this enables the temperature control unit to maintain a stable temperature.

The carrier gas enters the freezer through a copper tube with several submerged loops. These loops ensure that the carrier gas has the same temperature as the water in the vapor source. To limit the vapor output, the temperature in the vapor source is kept around 1.5°C. Since this is below 4°C which is the maximum density temperature for water, buoyancy driven convection could be limited during evaporation and surface cooling can be an issue. To create mixing in the water of the vapor source the carrier gas enters the glass cylinder below the water surface through one of the fittings attached to the glass outlets. This inlet fitting is bored through such that a  $\frac{1}{4}$ " stainless steel tube can slide through the fitting and form a leak tight connection between the rest of the setup and the tube. The  $\frac{1}{4}$ " tube has a length such that it ends close to the bottom part of the glass cylinder, thus forcing the carrier gas to exit the tube beneath the water level in the cylinder. Here, a diffuser splits the carrier gas flow into small bubbles. This increases the exchange between the carrier gas and the water for the production of saturated water

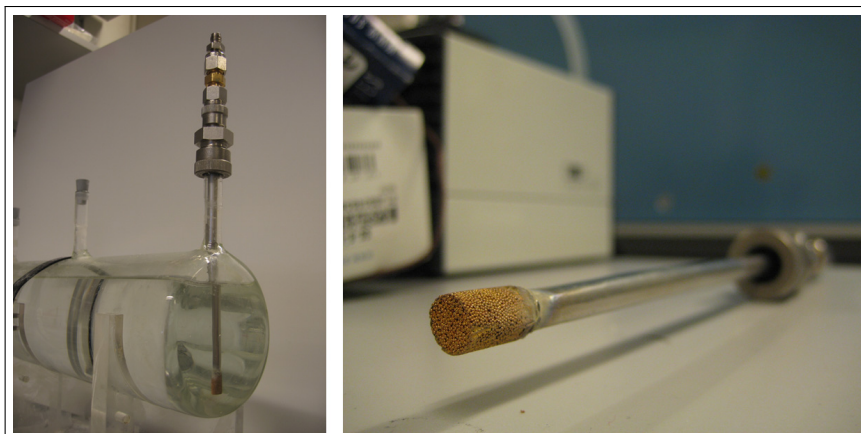


Figure 2.13: Left: Inlet fitting with diffuser mounted on the vapor source cylinder. Right: Diffuser mounted on the inlet fitting.

vapor. Furthermore the bubbles created by the diffuser create stirring of the water in the vapor source, thus keeping it mixed to avoid isotopic differences and surface cooling. Figure 2.13 shows the fitting with the diffuser mounted on the vapor source cylinder as well as the diffuser itself. The unit controlling the temperature of the vapor source is built for the purpose. Figure 2.14 shows the contents of the temperature control unit as well as an image of the temperature control unit box. The unit is built around an Omega Engineering CN7500 Series Proportional-Integral-Derivative (PID) controller connected to a 440VAC/25A solid state relay in a plastic housing. Controlled by the PID, the solid state relay connects the heating element to the 220VAC wall power. The heating element is 1500 W and consists of a 2440 mm Incoloy Nickel-Iron-chromium alloy tube, 7.9 mm in diameter, designed for immersion heating. The heating element is bent in such way that it fits in the freezer. This can be seen on Figure 2.12. The PID controller is connected to a thermocouple located next to the glass cylinder vapor source. The reason for not having the thermocouple inside the glass cylinder is that the response time of the system would be longer with resulting larger temperature fluctuations. To find the optimal control parameters for the PID controller we use the built-in autotune function. As will be shown in the next chapters this setup manages to keep a stable temperature inside the vapor source cylinder with fluctuations less than  $0.2^{\circ}\text{C}$ . The average temperature for all measurements performed is  $1.41^{\circ}\text{C} \pm 0.02^{\circ}\text{C}$  as will be discussed later.

## 2.7 Ice-vapor equilibrium chamber

The purpose of the ice-vapor equilibrium is to maintain an environment in which the incoming vapor can condense out as ice under equilibrium conditions. Since there is continuous flow in the system the chamber needs a certain volume (i.e. vapor containment time) for

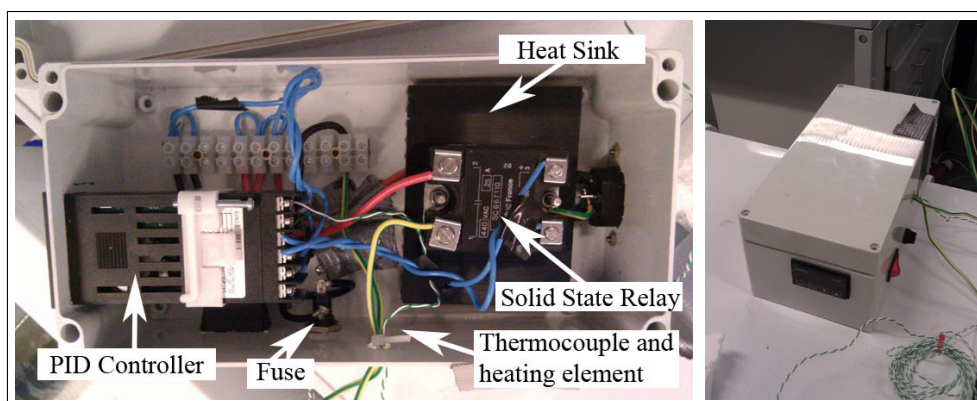


Figure 2.14: Temperature control unit. Right: PVC housing. Left: The different components inside the unit.

the exchange between the vapor and the ice to be large enough for this.

### 2.7.1 Temperature controlling of the equilibrium chamber

Accurate temperature control of the equilibrium chamber is needed for the range of  $0^{\circ}\text{C}$  to less than  $-60^{\circ}\text{C}$  to cover the range of the experiments. For this we use a FGR Multi Cool Low Temperature Bath from SP Industries. This can be seen on Figure 2.3. This low temperature bath is mechanically refrigerated and has a lower limit of  $-80^{\circ}\text{C}$ . The magnetic stirrer and vortex breaker design help ensure isothermal conditions in the bath throughout the temperature range. By using a liquid medium the Multi Cool handles heat loads better than using liquid nitrogen and it does not utilize expendable refrigerant. As liquid medium we use 96% ethanol. The cooler uses a digital controller providing  $\pm 0.1^{\circ}\text{C}$  stability according to the manufacturer. Since the temperature on the PID controller inside the cooler is not properly calibrated we log the temperature in the ethanol next to the submerged equilibrium chamber with a thermistor as described in the above section.

### 2.7.2 Design of the equilibrium chamber

The ice-vapor equilibrium chamber consists of a U-shaped glass container  $\sim 600$  mL in inner volume made by several merged glass spheres of diameter around 5 cm. This can be seen on Figure 2.15 to the left. The size is made to fit the bath of the cooler as mentioned above. Both ends consists of  $\frac{1}{2}$ " glass tubing, able to form a leak tight connection with the rest of the setup through two Swagelok Ultra-Torr fittings with o-rings. As with one of the connections to the glass cylinder in the vapor source, one of these Ultra-Torr fittings is bored through such that a  $\frac{1}{8}$ " copper tube can slide through the fitting into the glass container, which is can be seen in the middle picture on Figure 2.15. This copper tube is attached to the fitting with a Teflon ferrule. The copper tube ends below the liquid



Figure 2.15: The equilibrium chamber is custom made (right) of several spheres to increase the ice-vapor exchange (left). When mounted in the cooling bath the parts above the liquid level are heated and the addition of an outlet tube results in the vapor condensing out below the liquid level (middle).

level of the cooler and is heated with the rest of the setup and ensures that the vapor does not condense out on the glass sides above the liquid level (at a higher temperature than intended). Furthermore it lets the vapor out at a place where the glass sides are vertical such that ice crystals cannot grow easily into the vapor flow (this was a later modification to the first iteration of the equilibrium chamber). As with the vapor source, the top Swagelok connections are connected to two three-port valves such that the equilibrium chamber can be bypassed from the rest of the setup if needed. The components of the equilibrium chamber are heated all the way down to the ethanol level to avoid unintended condensation. In between each measurements the equilibrium chamber is dismounted from the setup and heated to well above  $100^{\circ}\text{C}$  with a heat gun. This evacuates the accumulated ice from the previous run. After this it is dried out with carrier gas before each run.

### Diffusion lengths of $\text{H}_2\text{O}$

Since we need a certain containment time of the incoming vapor we will now investigate the diffusion length of  $\text{H}_2\text{O}$  in Helium and Nitrogen. We can find the diffusion coefficient in a binary mixture of rigid elastic spherical molecules to first order in the density of the diffusing species (Chapman and Cowling, 1970):

$$D_{12} = \frac{3}{8n_0\sigma_{12}^2} \sqrt{\frac{kT}{2\pi} \left( \frac{1}{m_1} + \frac{1}{m_2} \right)} \quad (2.7.1)$$

The number density  $n_0$  is obtained from the ideal gas law,  $n_0 = p_0/kT$ ,  $\pi\sigma_{12}^2$  is the scattering cross section,  $k$  is the Boltzmann constant and  $m_1$  and  $m_2$  are the molecular masses.  $\sigma_{12}$  is found by averaging the molecular radii of each species,  $\sigma_{12} = (\sigma_1 + \sigma_2)/2$ .

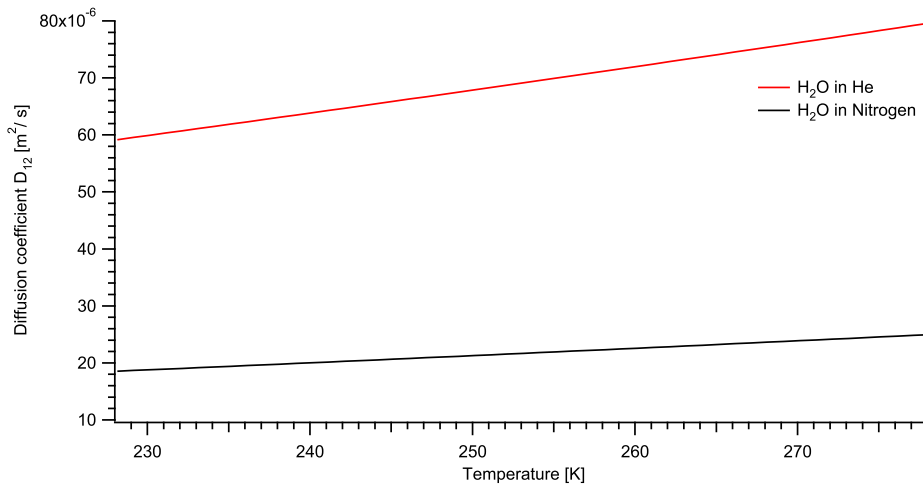


Figure 2.16: Diffusion coefficient of H<sub>2</sub>O in Helium and Nitrogen as a function of temperature at 1 atm

Using the values for listed in Table 2.1 along with the molecular mass of the species the diffusion coefficient of H<sub>2</sub>O in Helium and H<sub>2</sub>O in Nitrogen is found. The results can be seen in Figure 2.7.2 that shows the diffusion coefficient at 1 atm. The numbers seen for H<sub>2</sub>O in Helium agree with Paganelli and Kurata (1977) that obtained  $8.36\text{e-}5 \text{ m}^2/\text{s}$ . The diffusion coefficient of H<sub>2</sub>O in N<sub>2</sub> roughly three times lower than for H<sub>2</sub>O in Helium and also agree with the measured values of  $2.44\text{e-}5 \text{ m}^2/\text{s}$  at 21°C (Merlivat, 1978) and  $2.53\text{e-}5 \text{ m}^2/\text{s}$  (Paganelli and Kurata, 1977) and  $2.56\text{e-}5 \text{ m}^2/\text{s}$  Schwertz and Brow (1951)). From this number we can find the typical diffusion length  $L_D = \sqrt{4D_{12}t}$  for the vapor in the equilibrium chamber. A low estimate for the time in the equilibrium chamber would be 10 minutes with a volume of 600 mL and a 60 mL/min flow rate (assuming a complete turnover). For -40°C this gives a diffusion length of  $L_D \approx 40 \text{ cm}$  (and  $L_D \approx 22 \text{ cm}$  for nitrogen). Due to this the diameter of the equilibrium chamber is kept between 3 and 5 cm, roughly one order of magnitude lower than the above to ensure proper exchange between the vapor and the ice on the walls. The equilibrium chamber is designed with a changing diameter to increase mixing and disturb the flow of the carrier gas which would increase the exchange. Additionally, as shown later the actual time to empty the equilibrium chamber is longer due to the mixing (depending on the flow rate). Due to the above, if we observe equilibrium with dry air the conditions are most likely the same for Helium.

Parameter	Value	Reference
$\sigma_{H_2O}$	2.700 Å	Schwertz and Brow (1951)
$\sigma_{N_2}$	3.784 Å	Chapman and Cowling (1970)
$\sigma_{Helium}$	2.193 Å	Chapman and Cowling (1970)

Table 2.1: Molecular radii of different species assuming hard elastic spheres.

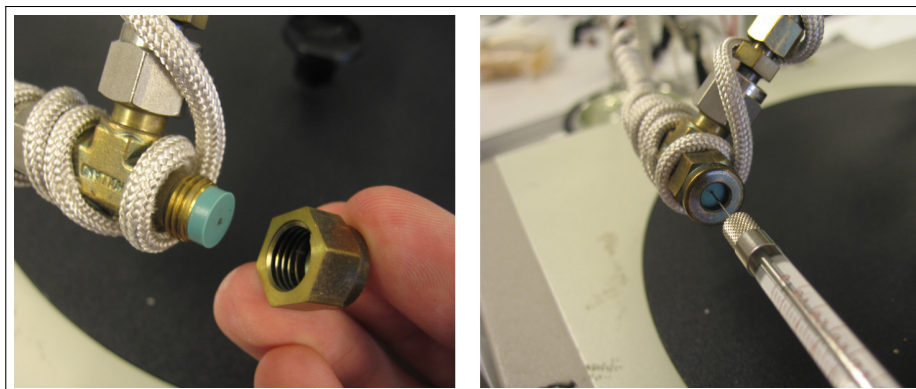


Figure 2.17: Left: Dismantled standard injection port which shows the septum and the modified nut. Right: Manual injections of  $0.2\mu\text{L}$  standard water is done with a SGE syringe.

As will be discussed in the next chapters, the above design and considerations resulted in an expected performance of the ice-vapor equilibrium chamber within a certain temperature range. The vapor condensed out properly below the liquid level as seen on Figure 2.15 and the resulting vapor has stable isotope values.

## 2.8 Standard injection port

To facilitate the injection of standard water for VSMOW calibrations, a standard injection port is connected to the setup. This consists of a  $\frac{1}{4}$ " brass tee connected to the sample line downstream from the ice-vapor equilibrium chamber (see Figure fig:labsketch). The leg of the tee that is not attached to the setup has a part of the thread removed such that a 9.5mm diameter injection septum can be placed on the flat part and form a leak tight connection when the nut is fastened to the tee. By injecting standard water with a syringe at this point we make sure that the standard follows the same path through the setup as the vapor from the equilibrium chamber. The brass tee is strongly heated with rope heaters to a temperature well above  $100^{\circ}\text{C}$  and points downwards while the connected tubing to the VICI valve is vertical. The injected droplet will therefore land on a strongly heated surface and only vapor will reach the VICI valve. For the standard water injections we use a Thermo Scientific GC Autosampler Syringe produced by SGE. This is the same syringe that is being used by the autosampler normally connected to the IRMS setup. Compared to Hamilton syringes, we found that this syringe has higher durability at high temperatures. Figure 2.17 shows the dismantled standard injection port as well as when injecting standard water into the setup. The septum can be seen fit very nicely on the flat surface of the modified thread and the septum is changed when worn out and leak checked before every use.

## 2.9 Conclusion of this chapter

In the above the different parts of the experimental setup and instrumentation were described. Most of these parts have been made for the purpose and besides from the instrumentation only a few commercial units are used. As mentioned, one of the main advantages of using self-designed units is that they can be designed for the exact purpose intended. Of course, this requires some evolutionary cycles before the final design is found which can be time consuming. Additionally, Murphys law was confirmed several times during the building and testing of the setup. Some fine tuning and changes to the setup were needed in order to make the different units work well with the instrumentation. This was achieved and the experimental setup proved to work as intended. This will be discussed in the next chapters, as we will discuss the datasets obtained and the calibrations needed.

## Chapter 3

# Dataset and calibrations

In the previous chapter the different parts of the experimental setup were introduced and described. In short, the vapor source and equilibrium chamber performed as expected and measurements on the resulting vapor from the equilibrium chamber were made. In the next chapter we will discuss the equilibrium conditions in the vapor source and equilibrium chamber but before we can do that we need fully calibrated datasets. In this chapter, we will therefore introduce the datasets obtained, and discuss the calibrations needed.

In general the measurement routine is as follows after a previous measurement run has finished:

- Close off vapor source and equilibrium chamber; only carrier gas through setup
- Change setpoint of multi-cooler if needed
- Unmount equilibrium chamber and heaters
- Empty equilibrium chamber with heat gun
- When multi-cooler has reached the setpoint, mount equilibrium chamber and heaters
- Dry out equilibrium chamber with carrier gas
- When dry, close off equilibrium chamber and open vapor source to humidify tubing
- With stable humidity, open equilibrium chamber
- Wait for equilibrium and perform measurements
- When stable values for  $\delta\text{D}$  and  $\delta^{18}\text{O}$  are obtained, close off vapor source and equilibrium chamber; only carrier gas through setup
- Injections of standard water for VSMOW calibration

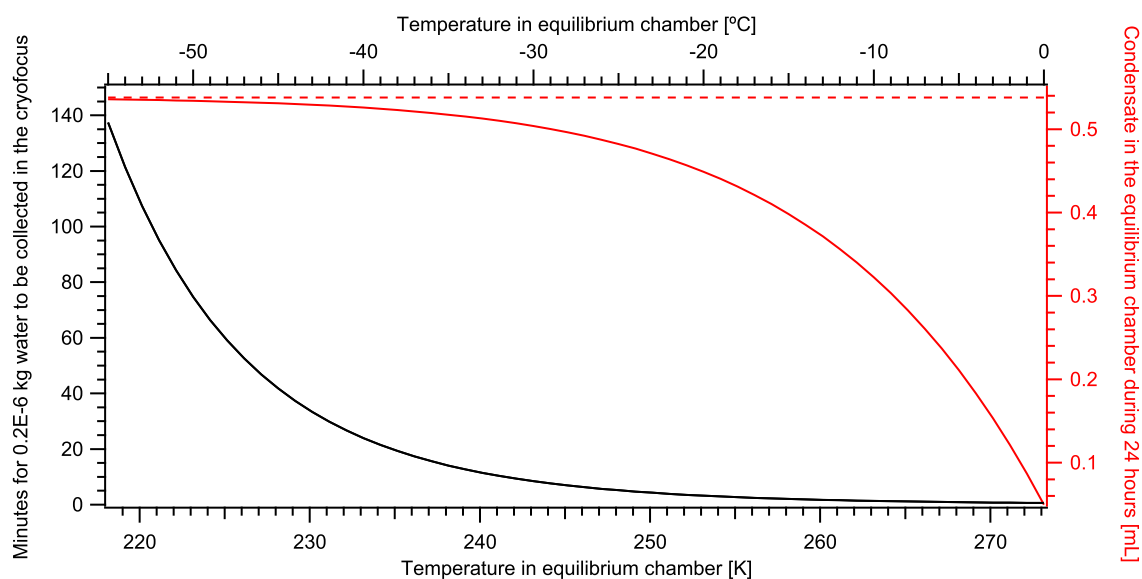


Figure 3.1: Collection time for  $0.2\text{E-}6$  kg water as a function of temperature in the equilibrium chamber. The calculations are based on vapor pressure differences. The mass of condensate can be seen approaching the total mass of the vapor entering the equilibrium chamber (dashed) as the temperature decreases.

The time required to perform the above routine depends mainly of the sampling time which again depends on the vapor pressure in the equilibrium chamber. In general, one measurement run with a following VSMOW calibration can be made per day. Figure 3.1 shows the estimated time for collection of  $0.2\mu\text{L}$  water in the cryofocus with a flow rate of  $70\text{ mL/min}$ . The calculation is based on the differences in saturation vapor pressure between the vapor entering the equilibrium chamber and the vapor exiting assuming equilibrium. It can be seen that it will take approximately 1.5 minutes to collect at  $-10^\circ\text{C}$ , 3 minutes to collect at  $-20^\circ\text{C}$ , 8.5 minutes for  $-30^\circ\text{C}$  and roughly 24 minutes to collect at  $-40^\circ\text{C}$ . During the measurements this sampling time was observed. The figure also shows the amount of ice condensed out in the equilibrium chamber during 24 hours as a function of temperature. The dashed line indicate the amount of vapor removed from the vapor source during the 24 hours and it can be seen that the amount of condensate approach this value as the temperature becomes lower. This increases the sampling time exponentially and therefore limits the possible daily sample amount as the temperature decreases.

In the following sections we will describe and discuss the dataset obtained with the Picarro and the IRMS system.

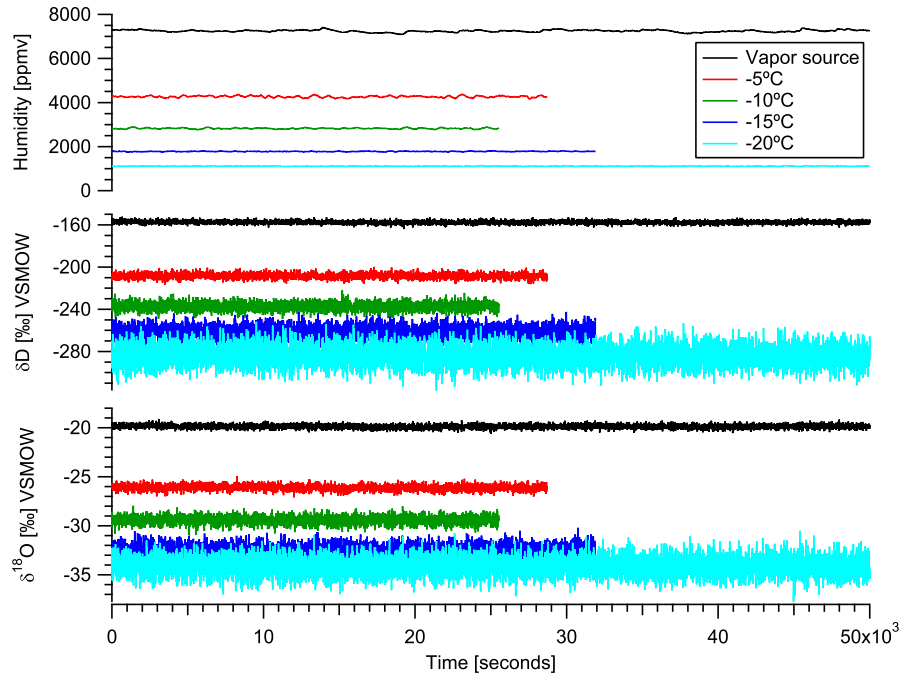


Figure 3.2: Typical examples of the Picarro dataset (absolute humidity,  $\delta D$  and  $\delta^{18}O$  as a function of time) for the vapor source and vapor from the equilibrium chamber. Note that the sensitivity decreases with decreasing temperature. The temperature of the samples are within  $0.2^\circ C$  of the temperature in the legend.

### 3.1 Picarro datasets

As mentioned in the previous chapter the Picarro was connected directly to the equilibrium chamber or the vapor source and besides from testing and validating the setup some measurement runs were made. Due to limited time allocation with the instrument and due to limitations of the instrument itself, the Picarro dataset is not as complete as the IRMS dataset and it will therefore mainly be used as a secondary dataset. However, as will be shown, the Picarro is an invaluable tool to characterize the performance of the experimental setup.

In total 36 measurements of the vapor source and the equilibrium chamber were made, the majority of these were carried out in February 2010.

#### 3.1.1 Typical measurements

Figure 3.2 shows typical data from the Picarro measurements of the vapor source directly as well as vapor from the EC at four different temperatures. The average temperature of the measurements are within  $0.2^\circ C$  of the temperature shown in the figure legend. The selected intervals are all obtained after the isotopic composition of the vapor exiting the equilibrium chamber has reached a stable value. The details of this will be discussed later.

The selected intervals serve as typical measurements for the different temperatures. The sampling time varies between 6 and 8 seconds for the Picarro measurements. The top part of the figure shows the absolute humidity as a function of time in seconds, as measured by the Picarro. The absolute humidity of the measurements is of course dependent of the temperature in the equilibrium chamber (or of the vapor source for direct measurements of this). In general the humidity is stable within 200 ppmv with the largest fluctuations occurring in the humidity of the vapor source. This is due to the exponential temperature dependence of the pressure (the absolute changes are larger for higher temperatures) and due to differences in the two systems (PID controllers etc.). This will also be discussed in more detail below. The middle graph shows  $\delta D$  and the bottom graph shows  $\delta^{18}O$ , also as a function of time in seconds. The isotope values are stable for these intervals and in principle these graphs illustrate the fractionation occurring between the vapor from the vapor source and the vapor in equilibrium with ice in the equilibrium chamber. Figure 3.2 also illustrates the previously mentioned limitations of the Picarro with the standard deviation of the signal increasing with decreasing temperature. It can be seen that we obtain a very high amount of data on the isotopic composition of the vapor with a stable signal for e.g. 2 hours. We will now investigate how to properly assess this large dataset to obtain a representative value with uncertainty for each measurement run.

Assuming that the data points  $x_1, \dots, x_N$  are normally distributed then the mean  $\bar{x}$  is:

$$\bar{x} = \frac{1}{N} \sum_{i=1}^N x_i \quad (3.1.1)$$

And the standard deviation  $\sigma_x$  will be:

$$\sigma_x = \sqrt{\frac{1}{N-1} \sum_{i=1}^N (x_i - \bar{x})^2} \quad (3.1.2)$$

For the sample size  $N$ , the standard deviation of the mean (SDOM)  $\sigma_{\bar{x}}$  will then be:

$$\sigma_{\bar{x}} = \frac{\sigma_x}{\sqrt{N}} \quad (3.1.3)$$

From (3.1.3), it can be seen that in the case of a system without drifts, the SDOM decreases with increasing sample size (or integration time). However, instrumental drifts are difficult to avoid and these will limit the benefits of using long integration times. To analyze the stability of our system, we use a similar approach as Czerwinski et al. (2009); Werle et al. (1993); Gkinis et al. (2010) by calculating the Allan variance (variance of the mean) as a function of integration time. A perfectly stable system could be averaged infinitely but unfortunately real systems are only stable for a limited amount of time. Allan

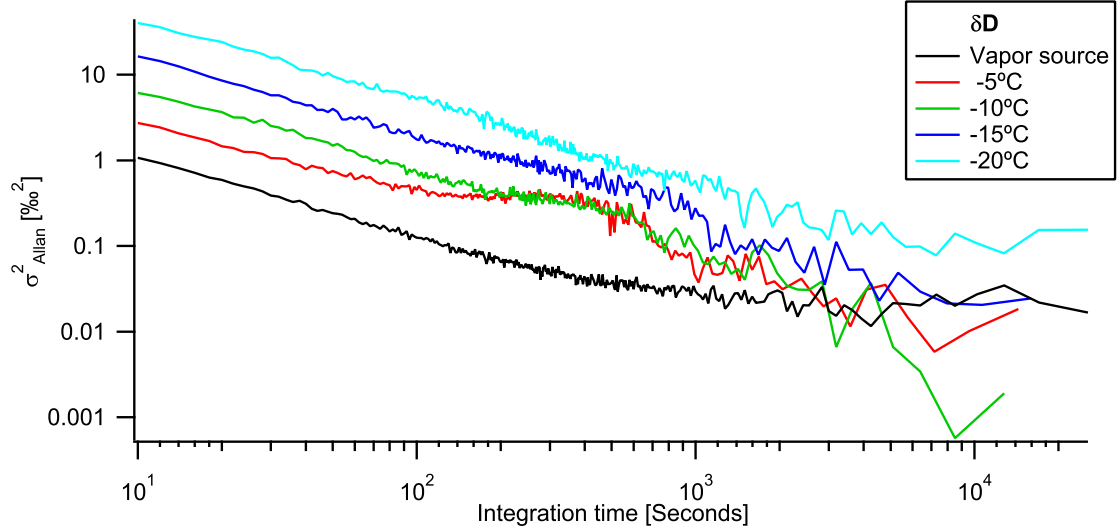


Figure 3.3: Allan variance as a function of integration time for  $\delta D$  for measurements of the vapor source directly as well as for vapor from the equilibrium chamber at different temperatures.

variance was developed to reveal low frequency drift phenomena and can be used to find the optimal integration time for a system (Allan, 1966). We can divide a time series with sample size  $N$  into  $m$  subgroups, each with a sample size  $k = \frac{N}{m}$ . With the acquisition time being  $t_i$ , the integration time for each subset will be  $\tau_m = kt_i$  the Allan variance will be defined as:

$$\sigma_{Allan}^2(\tau_m) = \frac{1}{2m} \sum_{s=1}^m (\bar{x}_{s+1} - \bar{x}_s)^2 \quad (3.1.4)$$

When plotted as a function of  $\tau_m$ , the minimum in the Allan variance indicates the optimal integration time  $\tau_{opt}$  as a characteristic property for the given system (i.e. dependent on the instrument and the stability of the experimental setup). Figures 3.3 and 3.4 show the Allan variance for the intervals of  $\delta D$  and  $\delta^{18}O$  in Figure 3.2 as a function of integration time. The datasets have been interpolated to account for the varying sampling time in the original dataset and use a fixed time step of 2 seconds which resolves the original dataset very accurately. The Allan variance is shown for integration times above 10 seconds (note that the measurement frequency for the Picarro is around 7 seconds). For  $\delta D$ , the Allan variance on all graphs decreases linearly suggesting a white noise behavior until  $\tau_{opt}$  (in general considered as the local minimum on the curve) which lies around 2000 seconds for the vapor source and even higher for  $-15^\circ C$  and  $-20^\circ C$ . The same patterns can be seen for  $\delta^{18}O$  where  $\tau_{opt}$  is around 1000 seconds for the vapor source with a higher value for  $-15^\circ C$  and  $-20^\circ C$ . For  $-5^\circ C$  and  $-10^\circ C$  (both on  $\delta D$  and  $\delta^{18}O$ ), the curve flattens out around 100 seconds followed by a constant variance as a function of integration time

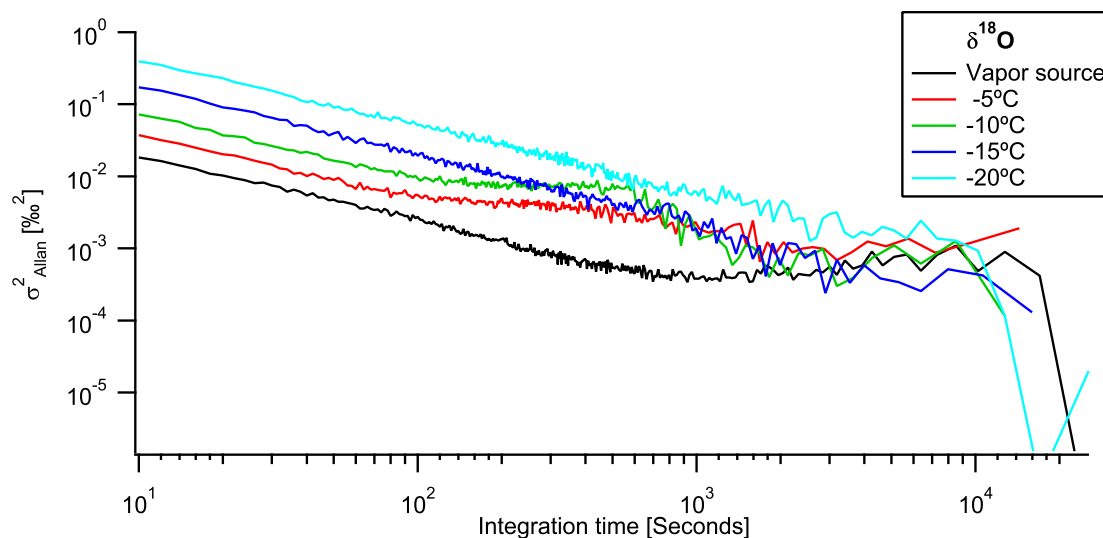


Figure 3.4: Allan variance as a function of integration time for  $\delta^{18}\text{O}$  for measurements of the vapor source directly as well as for vapor from the equilibrium chamber at different temperatures.

until the Allan variance decreases again around 700 seconds. After this the  $-5^\circ\text{C}$  and  $-10^\circ\text{C}$  graphs follows the above pattern with a global  $\tau_{opt}$  around 4000 seconds which is similar to the integration time obtained with a vaporizer (Gkinis et al., 2010). This underscores the system stability on longer timescales. The Allan plot indicates how to avoid drifts when choosing an integration time. However since the temperature does vary in our system we do have periodicity in the isotopes and we want to average over these variations to obtain an average value of the isotopes at the average temperature. The flattening of the curves (note that the Allan variance does not increase) for  $-5^\circ\text{C}$  and  $-10^\circ\text{C}$  is definitely caused by the temperature variations mainly driven by the equilibrium chamber PID controller. The reason for why these periodicities do not show up in the Allan variance for  $-15^\circ\text{C}$  and  $-20^\circ\text{C}$  is most likely due to the decreased measurement uncertainty for those temperatures. Since we do want to capture the temperature variations in the system we choose integration times larger than 1000 seconds (and up to 1000 seconds for the  $\delta^{18}\text{O}$  measurements of the vapor source). Tests using smaller integration times (around 100 seconds) with a following weighted averaging of these intervals do not yield any significant difference in the results.

## 3.2 Picarro calibrations

Even though the Picarro is generally a "plug and play" instrument compared to the IRMS system, the results still need proper humidity calibration and calibration towards the VS-MOW standard before comparisons can be made with other results. In the following we will introduce and discuss the calibrations performed on the Picarro data.

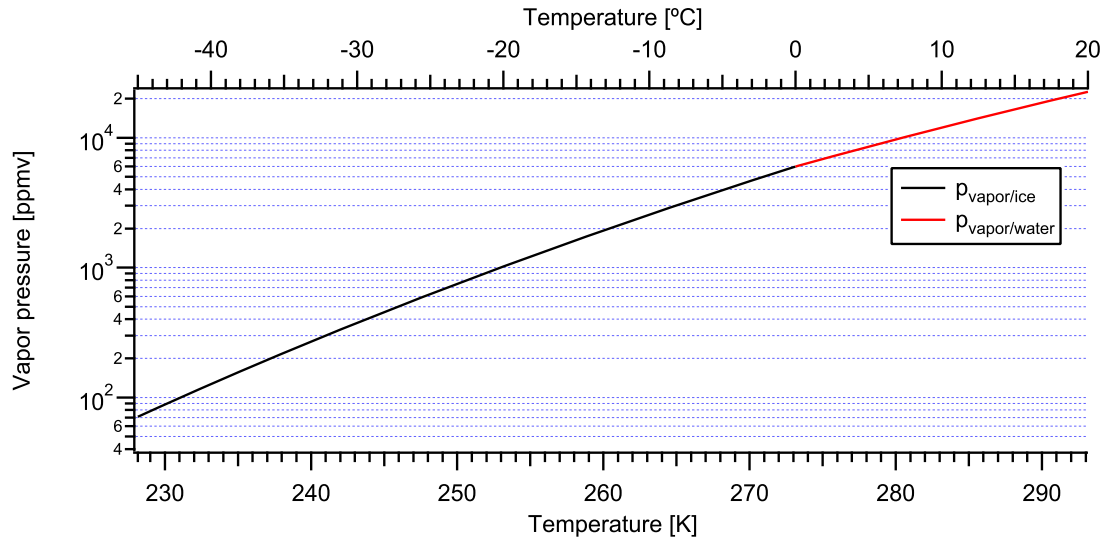


Figure 3.5: The vapor pressure or absolute humidity in ppmv as a function of temperature based on 1 atm (101325 Pa) in the system.

### 3.2.1 Picarro humidity calibration

As mentioned in e.g. Gupta et al. (2009) and Brand et al. (2009), the isotope values measured with the H<sub>2</sub>O Picarro have a humidity dependency and this has to be corrected for. Figure 3.5 shows the saturation vapor pressure over ice and over liquid water as a function of temperature, based on equation (4.1.2) (see below). The figure shows that the absolute humidity will be around 1000 ppmv at -20°C and roughly 7000 ppmv at the vapor source temperature of 1.4°C which means that our humidity calibration should be well defined over this range.

The humidity calibration is found by varying the humidity of a flow with constant isotopic values. For this, a Los Gatos Research (LGR) Water Vapor Isotope Standard Source (WVISS) is used. This device provides a controllable flow of humid air with a stable isotopic composition over a continuous range of absolute humidities between 500 ppmv and 30000 ppmv. By alternating the output humidity between a reference value and a range of humidity levels, the humidity dependence of the measured water isotopes can be characterized. By using a reference value, slopes due to possible instrument drifts can be subtracted. An example of this can be seen on Figure 3.6 that shows a section of the used humidity calibration. This section has a reference level around 18000 ppmv with the humidity being varied from around 13000 ppmv to 4000 ppmv. For each of the humidity levels the isotope values and uncertainties for  $\delta D$  and  $\delta^{18}O$  can be found. The humidity calibration is made from two runs with two different reference values (18150 ppmv and 5100 ppmv), in total covering humidity levels from a range of 682 ppmv to 12861 ppmv. The isotope values and corresponding uncertainties are found. The isotope values relative

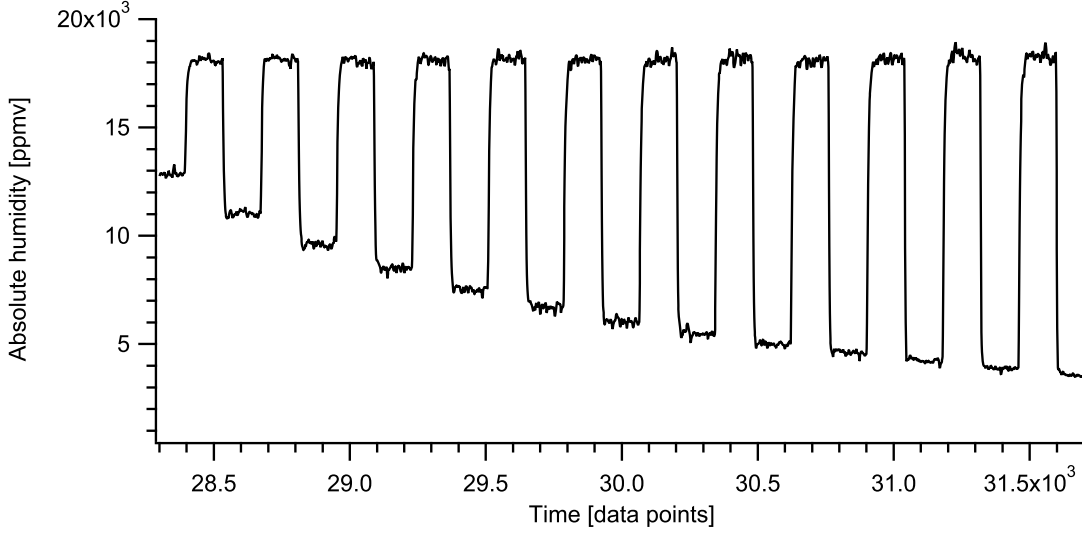


Figure 3.6: A section of the H<sub>2</sub>O Picarro humidity calibration measurements. There are between 6 and 8 seconds between each data point. The reference humidity is 18150 ppmv and the humidity is being varied from  $\sim 12800$  ppmv to  $\sim 4000$  ppmv in this section.

to a reference level of 6021 ppmv are found and the correction values are fitted to a function which is then used for calibrating the measured isotope values. The reference level of 6021 ppmv is chosen since the VSMOW calibration is performed at this humidity level (see below). Figures 3.8 and 3.7 shows the humidity calibrations for  $\delta D$  and  $\delta^{18}O$  relative to the 6021 ppmv value as a function of absolute humidity. Both humidity calibrations show non-linear behavior (especially the calibration for  $\delta^{18}O$ ) which make them hard to fit. But since the highest humidity experienced during the measurements is the vapor directly from the vapor source (with  $\sim 7400$  ppmv), the fits should mainly cover values lower than this. The humidity calibration for  $\delta^{18}O$  is fitted with a seven degree polynomial:

$$\delta^{18}O_{correction} = K_0 + K_1x + K_2x^2 \dots K_7x^7 \quad (3.2.1)$$

with the coefficients being  $\pm$  one standard deviation  $K_0=4.901\pm 0.451$ ,  $K_1=-6.459\pm 0.001$ ,  $K_2=3.616E-6\pm 8.22E-7$ ,  $K_3=-1.075E-9\pm 3.15E-10$ ,  $K_4=1.806E-13\pm 6.40E-14$ ,  $K_5=-1.712E-17\pm 7.02E-18$ ,  $K_6=8.51E-22\pm 3.93E-22$  and  $K_7=-1.724E-26\pm 8.78E-27$ . This fit covers the data points well even for low humidities and captures the minimum around 5000 ppmv. Besides from the point around 6800 ppmv, the fit is within the uncertainties of the data points. The fit does not perform that good for humidities well above 8000 ppmv due to the nature of the polynomial but this is acceptable since we do not have measurements at this humidity. The  $\delta D$  humidity calibration is fitted with a double exponential function:

$$\delta D_{correction} = y_0 + A_1 \exp\left(\frac{-(x-x_0)}{\tau_1}\right) + A_2 \exp\left(\frac{-(x-x_0)}{\tau_2}\right) \quad (3.2.2)$$

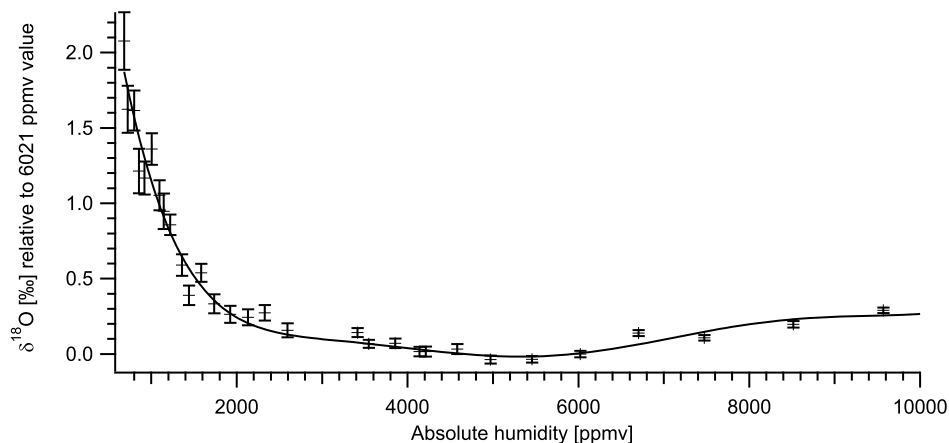


Figure 3.7: H<sub>2</sub>O Picarro humidity calibration fit for  $\delta^{18}\text{O}$ . The graph shows the difference in isotope value caused by a change in humidity. A seven degree polynomial is used for fitting and this performs well for the range needed.

with the coefficients being  $\pm$  one standard deviation being  $y_0=2.423\pm 0.849$ ,  $A_1=-16.31\pm 2.84$ ,  $\tau_1=443.58\pm 100.00$ ,  $A_2=-16.10\pm 2.52$ ,  $\tau_2=2917\pm 773$  and  $X_0=682.42$ . The fit is within the uncertainties for all data points (we note the point around 6800 ppmv being a little off here as well) and captures the trend very well from low to high humidity values.

From the above it is clear that the instrument is not well calibrated for such low humidities and that a proper humidity calibration is crucial for correct measurements. The correction is up to 30‰ for  $\delta\text{D}$  and 2‰ for  $\delta^{18}\text{O}$  for the very low humidities and compared to typical isotopic ratios the corrections are a considerable fraction of these. The lowest typical humidity encountered during our measurements is around 1100 ppmv (corresponding to the vapor pressure over ice at  $-20^\circ\text{C}$ ) which is in the area where the non-linearity is strong. Nevertheless, the observed humidity dependencies of the measured isotopes on the Picarro were reproduced with different methods of varying the humidity and are similar to other results with similar or same instruments (Brand et al., 2009; Gkinis et al., 2010). This supports the validity of the humidity calibrations.

### 3.2.2 Picarro VSMOW calibration

The Picarro VSMOW calibration is made by measuring well known local standards at a stable and well know humidity level (at or close to 6100 ppmv) such that the humidity calibrated isotope values are easily calibrated towards VSMOW. The VSMOW values of the local standards used can be seen on Table 3.1 and the range of these cover the range of isotope values of the measurements. They do not cover the vapor measurements from the vapor source but the -22 standard has values close to these measurements. The reason for this is that the VSMOW calibration was performed while the instrument was used for

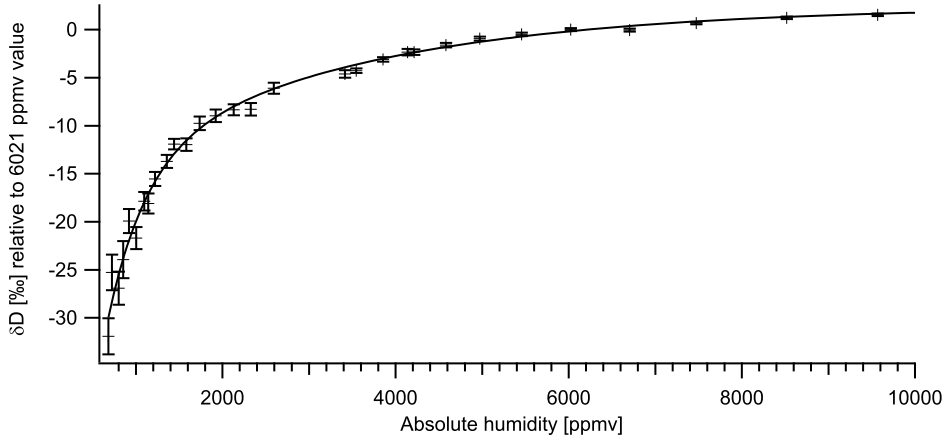


Figure 3.8: Picarro humidity calibration fit for  $\delta D$ . The graph shows the difference in isotope value caused by a change in humidity. A double exponential function is used for fitting and this performs very well for the range needed.

other purposes. The liquid standard is vaporized with a vaporizer using the same method as Gkinis et al. (2010) and the vapor is injected into the Picarro using dry air as carrier gas. The vaporizer maintains a stable humidity with a complete vaporization of the injected standard thus avoiding fractionation.

Figures 3.9 and 3.10 show the measurements with the VSMOW values on the x-axis and the measured values on the y-axis. A clear linear relationship for both isotopic values is seen and the fits perform generally quite well through the one  $\sigma$  uncertainty of the measured data points. The data points on the graph can also be seen on table 3.1. The four data points on the graph are made with two calibration runs, each with two standards. Usage of the instrument over a period of weeks show that drifting in the VSMOW calibration is generally not an issue (Steen-Larsen, 2010). With a linear relationship, the VSMOW calibration line fit will be:

$$X_{meas} = aX_{VSMOW} + b \quad (3.2.3)$$

Where  $X_{meas}$  is the measured (humidity calibrated) value of the isotopic species  $\delta^{18}O$  or  $\delta D$  and  $X_{VSMOW}$  is the VSMOW calibrated value for the standard.  $a$  is the slope of the calibration line and  $b$  is the zero intersect and can be seen in Table 3.2. From this calibration line the humidity and VSMOW calibrated result of a measurement can be found:

$$X_{VSMOW} = \frac{X_{meas} - b}{a} \quad (3.2.4)$$

On the table we can see that the fit uncertainty for the intersect of  $\delta D$  is relatively large compared to the  $\delta^{18}O$  fit. This will create a relatively larger uncertainty for the final  $\delta D$  Picarro results since the uncertainties for the calibration propagates through.

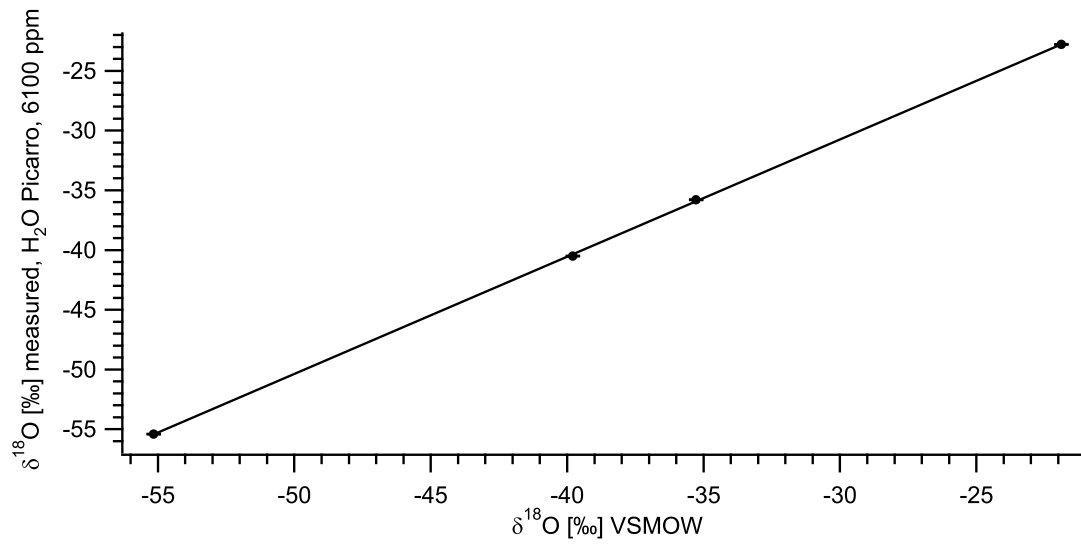


Figure 3.9: H<sub>2</sub>O Picarro VSMOW calibration for  $\delta^{18}\text{O}$  performed around 6100 ppm humidity. A clear linear relationship is seen.

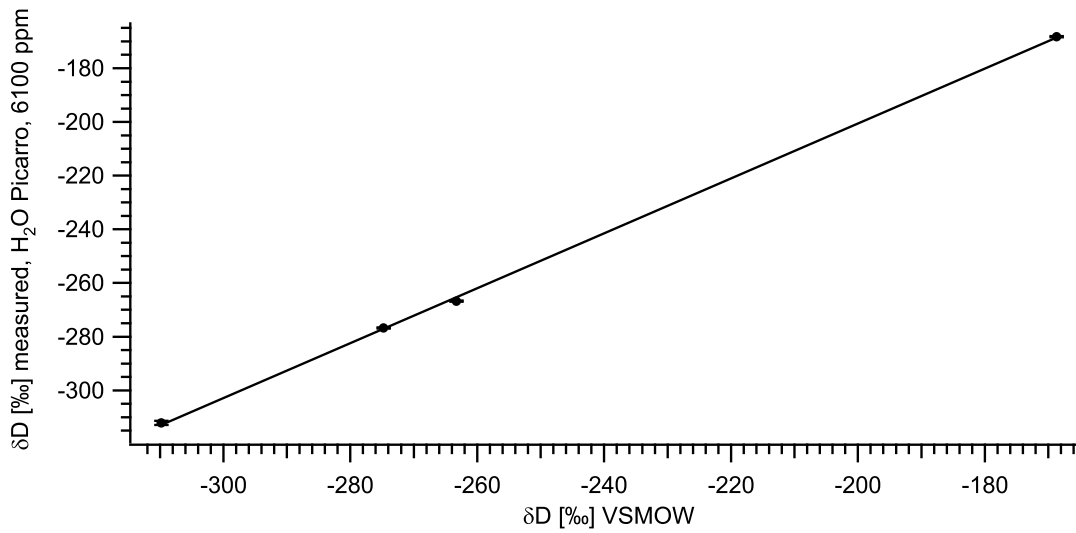


Figure 3.10: H<sub>2</sub>O Picarro VSMOW calibration for  $\delta\text{D}$  performed around 6100 ppm humidity. A clear linear relationship is seen.

Standard	$\delta\text{D}$ VSMOW	$\delta\text{D}$	SDOM $\delta\text{D}$	$\delta^{18}\text{O}$ VSMOW	$\delta^{18}\text{O}$	SDOM $\delta^{18}\text{O}$
Iswasser	-274.76	-276.78	0.26	-35.28	-35.78	0.02
B-SLAP	-263.29	-266.81	0.18	-55.16	-55.40	0.02
-22	-168.7	-168.22	0.27	-21.89	-22.79	0.03
-40	-309.8	-312.17	0.81	-39.79	-40.50	0.03

Table 3.1: Working standards in ‰ for VSMOW calibrations as well as measured values for  $\sim 6100$  ppm in ‰. SDOM is the standard deviation of the mean of the intervals used (typically 60 data points)

### 3.2.3 Uncertainty for the Picarro data

For characterizing the error propagation we use the following relationship for sum and difference of independent random errors. If  $q$  is the sum or difference  $q = x + \dots + z - (u + \dots + w)$  then:

$$\delta q = \sqrt{(\delta x)^2 + \dots + (\delta z)^2 + (\delta u)^2 + \dots + (\delta w)^2} \quad (3.2.5)$$

From the theory of error propagation (Taylor, 1997), if  $q = q(x, \dots, z)$  is a function of  $x, \dots, z$  then the general formula for error propagation is defined as

$$\Delta q = \sqrt{\left(\frac{\partial q}{\partial x} \Delta x\right)^2 + \dots + \left(\frac{\partial q}{\partial z} \Delta z\right)^2} \quad (3.2.6)$$

The uncertainty for the final humidity and VSMOW calibrated result of a measurement is found as described above. First, the uncertainty of the humidity calibrated results are found with the partial derivatives of equations (3.2.1) and (3.2.2) and the uncertainties of the fits as input in equation (3.2.6). These results are then used as input in the uncertainty calculation for the VSMOW calibrated results along with the partial derivatives of (3.2.4). For the humidity we use the standard deviation for each interval used since the Allan variance show that it is not possible to integrate over the same interval as the isotopes due to small fluctuations in the humidity. The total uncertainty of the partial derivatives mentioned above are lengthy and will not be included here.

As an example of the error propagation we will show the results from a  $-10^\circ\text{C}$  run with the measured values  $\delta D_{meas} = -245.77 \pm 0.16\text{‰}$  and  $\delta^{18}\text{O}_{meas} = -30.36 \pm 0.02\text{‰}$ . Performing the humidity calibration the values then become  $\delta D_{hum} = -240.19 \pm 2.13\text{‰}$  and  $\delta^{18}\text{O}_{hum} = -30.48 \pm 0.02\text{‰}$ . After the VSMOW calibration the values are now  $\delta D_{VSMOW}$

	$\delta\text{D}$	$\delta^{18}\text{O}$
a	$1.023 \pm 0.012$	$0.981 \pm 0.006$
b	$3.896 \pm 3.000$	$-1.296 \pm 0.025$

Table 3.2:  $\text{H}_2\text{O}$  Picarro VSMOW calibration line fits with  $y = ax + b$

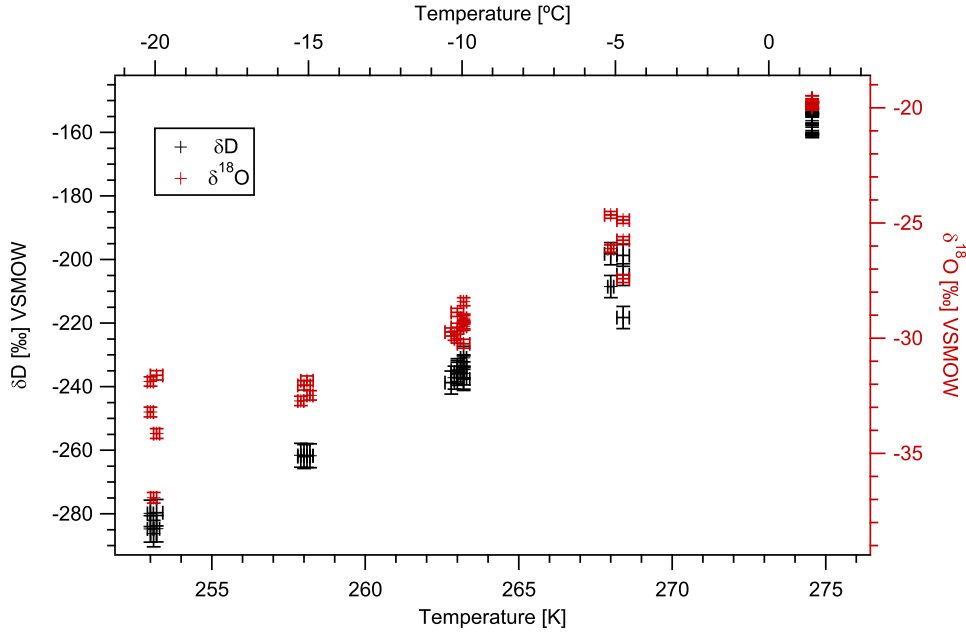


Figure 3.11: Picarro results for  $\delta D$  and  $\delta^{18}O$  as a function of temperature. All measurements are shown including tests and non-stable measurements which create some deviation in the distributions. The data points can be seen in Table 3.3

$= -238.69 \pm 3.60\%$  and  $\delta^{18}O_{VSMOW} = -29.73 \pm 0.18\%$ . This shows that the uncertainty for the humidity calibration is a major contributor to the uncertainty for the final result with around 2‰ for  $\delta D$ .  $\delta^{18}O$  is not affected as much by the propagation of the VSMOW calibration as  $\delta D$  which ends up with a final uncertainty of  $\pm 3.60\%$ . This will have some effect on the determination of the fractionation factor. Due to this and the fact that the Picarro dataset is not as large, we therefore mainly consider the Picarro data as a secondary data set for the fractionation factor experiments.

### 3.2.4 The final Picarro dataset

For each measurement run we choose an interval with the proper integration time once the isotope values have stabilized. The above calibrations are performed on these intervals and the uncertainties are found. These data have not been corrected for possible drifts in the vapor source as will be discussed in the next chapter. We present isotope values both from the vapor source directly and from the vapor from the equilibrium chamber. The vapor from the vapor source was sampled right before opening the equilibrium chamber to check the state of the vapor source but not all of these measurements were long enough for proper integration and are therefore not included. A few of the vapor source measurements are performed by sampling overnight to study the stability of the vapor source. Since only some measurements of the vapor source have direct temperature measurements, these are not shown. As mentioned, the average temperature for all measurements per-

formed is  $1.41^{\circ}\text{C}\pm 0.02^{\circ}\text{C}$ . With the Picarro, measurements between  $-5^{\circ}\text{C}$  and  $-20^{\circ}\text{C}$  were performed. For low temperatures we are limited by a large standard deviation on the signal as well as the uncertainties of the humidity calibration. For high temperatures we are limited by possible super cooled water in the equilibrium chamber (will be discussed below). Table 3.3 shows all measurements including tests and non-stable measurements which creates some deviation in the distributions and this can also be seen on Figure 3.11. The temperature for the vapor source is set to the average value of  $1.41^{\circ}\text{C}$ . We can see a clear temperature dependency on the isotope values which is promising for the fractionation factor calculations. As mentioned above the error on the  $\delta\text{D}$  value can be seen to be relatively large.

### 3.3 TC/EA-IRMS data

We will now introduce the data from the IRMS measurements. Compared to the Picarro dataset, the IRMS dataset is larger since this system is not directly limited to a certain temperature range and this is the primary dataset of this work. As described in the previous chapter the IRMS measurements were performed by collecting sample vapor from the equilibrium chamber with the cryofocus and injecting it into the TC/EA for measurements. In total more than 80 direct measurements of the vapor from the equilibrium chamber were made with even more measurements and injections made for testing purposes. The temperature range used with the IRMS measurements is between  $-10^{\circ}\text{C}$  and  $-50^{\circ}\text{C}$  as these turned out to be the limits for the setup. We did perform a few measurements at  $-5^{\circ}\text{C}$ , especially before properly testing the setup with the Picarro, but to avoid possible supercooled water in the equilibrium chamber and since experience showed that equilibrium was hard to obtain here, we focused on  $-10^{\circ}\text{C}$  as the lower limit instead.

#### 3.3.1 Typical measurements

Figure 3.12 shows a typical measurement run with the TC/EA-IRMS system. We measure both  $\delta\text{D}$  and  $\delta^{18}\text{O}$  in one run using a magnet jump between the peaks. Peak 1 is the  $\text{H}_2$  reference peak, 2 is the  $\text{H}_2$  sample peak, 3 is the  $\text{CO}$  reference peak and 4 is the  $\text{CO}$  sample peak. The magnet jump that allows jumping from  $m/z = 2$  and  $3$  to  $m/z = 28, 29$  and  $30$  can be seen right before peak 3. The peaks are separated by varying the GC temperature and due to the long peak tails of both  $\text{H}_2$  and  $\text{CO}$  peaks we use a GC temperature between  $40^{\circ}\text{C}$  or  $45^{\circ}\text{C}$  depending on the performance of the TC/EA. The vapor is injected into the TC/EA with use of the heaters on the cryofocus such that there is roughly 20 seconds between the reference peaks and the sample peaks.

As mentioned in Section 2.3 Isodat performs the peak integration to obtain the isotope ratios relative to the reference gas and in this process several corrections are applied. Each

T [K]	$\sigma T$	$hum_{av}$	$\sigma hum$	SDOM hum	$\delta^{18}O$ [‰]	$\delta^{18}O$ error[‰]	$\sigma \delta^{18}O$	SDOM $\delta^{18}O$	$\delta D$ [‰]	$\delta D$ error[‰]	$\sigma \delta D$	SDOM $\delta D$
		7356	25	1.5	-19.60	0.12	0.20	0.01	-156.24	3.21	1.38	0.08
		7250	27	1.2	-19.89	0.12	0.20	0.01	-157.19	3.22	1.43	0.06
		7285	54	3.1	-19.85	0.12	0.19	0.01	-157.54	3.22	1.44	0.08
		7457	29	1.7	-19.59	0.12	0.22	0.01	-156.95	3.21	1.37	0.08
		7276	31	2.5	-19.94	0.13	0.22	0.02	-158.40	3.22	1.40	0.12
		7250	20	1.1	-19.93	0.13	0.23	0.01	-156.72	3.22	1.40	0.08
		7331	11	0.9	-19.76	0.12	0.17	0.01	-157.69	3.22	1.39	0.11
		7216	6	0.4	-19.86	0.12	0.20	0.01	-158.24	3.22	1.41	0.09
		7478	28	1.8	-19.97	0.13	0.20	0.01	-157.38	3.21	1.28	0.08
		7341	16	0.9	-19.85	0.12	0.20	0.01	-157.25	3.21	1.35	0.08
		7251	21	1.0	-19.92	0.13	0.22	0.01	-157.81	3.22	1.51	0.07
268.4	0.2	4502	40	1.8	-27.42	0.17	0.26	0.01	-218.21	3.46	2.20	0.10
268.4	0.2	4583	43	1.8	-24.87	0.15	0.25	0.01	-198.68	3.45	2.05	0.09
268.4	0.2	4587	55	2.3	-25.75	0.16	0.26	0.01	-204.73	3.45	2.21	0.09
268.0	0.1	4269	38	1.7	-26.11	0.16	0.28	0.01	-208.51	3.48	2.40	0.11
268.0	0.2	4474	58	2.6	-24.65	0.15	0.27	0.01	-198.20	3.46	2.24	0.10
263.2	0.1	2823	28	1.3	-29.42	0.18	0.40	0.02	-237.16	3.60	3.61	0.16
263.2	0.1	2826	23	1.0	-29.13	0.18	0.38	0.02	-235.85	3.60	3.46	0.14
263.2	0.1	2910	35	1.6	-29.48	0.18	0.36	0.02	-230.90	3.60	3.22	0.14
263.2	0.1	2838	16	0.7	-29.19	0.18	0.39	0.02	-233.93	3.60	3.88	0.16
263.2	0.1	2825	28	1.2	-28.42	0.18	0.37	0.02	-233.64	3.60	3.53	0.15
263.2	0.2	2785	26	1.1	-30.24	0.19	0.38	0.02	-237.60	3.60	3.43	0.14
263.0	0.2	2819	21	1.0	-28.88	0.18	0.38	0.02	-235.97	3.60	3.45	0.15
263.0	0.2	2858	31	1.4	-29.53	0.18	0.38	0.02	-234.83	3.60	3.37	0.15
263.0	0.1	2861	22	1.0	-30.02	0.19	0.38	0.02	-235.45	3.60	3.47	0.16
262.9	0.1	2807	25	1.1	-29.90	0.19	0.38	0.02	-237.14	3.60	3.46	0.15
262.8	0.2	2773	21	0.9	-29.73	0.18	0.38	0.02	-238.69	3.60	3.49	0.16
258.2	0.1	1785	9	0.5	-32.48	0.20	0.57	0.03	-261.77	3.75	5.46	0.28
258.1	0.2	1755	15	0.6	-31.84	0.20	0.56	0.02	-261.68	3.76	5.48	0.23
258.0	0.2	1784	9	0.4	-32.05	0.20	0.56	0.02	-261.99	3.75	5.67	0.25
257.9	0.1	1761	14	0.6	-32.72	0.20	0.57	0.02	-261.63	3.76	5.75	0.24
253.2	0.1	1110	7	0.3	-34.14	0.21	0.92	0.04	-284.70	4.15	9.04	0.41
253.2	0.2	1110	7	0.3	-31.61	0.20	0.86	0.04	-279.66	4.15	8.32	0.35
253.1	0.1	1104	7	0.3	-36.93	0.23	0.88	0.04	-286.22	4.15	8.71	0.36
253.0	0.1	1104	7	0.3	-33.20	0.21	0.84	0.03	-284.75	4.15	8.57	0.35
253.0	0.1	1114	9	0.4	-31.88	0.20	0.84	0.04	-279.89	4.15	9.04	0.40

Table 3.3: Picarro results for  $\delta D$  and  $\delta^{18}O$ . All values are humidity and VSMOW calibrated. SDOM is the standard deviation of the mean of the integration interval and  $\sigma$  indicates the deviation of the integration interval.  $T$  is the temperature,  $\sigma T$  is the deviation on  $T$ ,  $hum_{av}$  is the average absolute humidity and  $\delta^{18}O$  and  $\delta D$  error are the propagated errors.

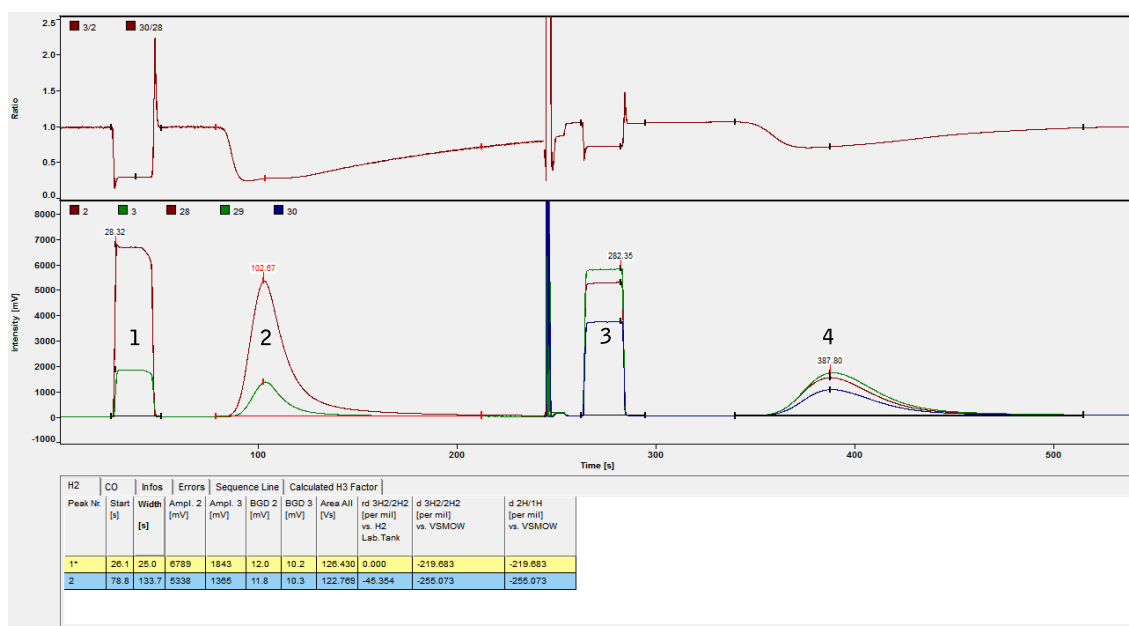


Figure 3.12: Typical IRMS mass chromatogram of  $m/z = 2$  and  $3$  and  $m/z = 28, 29$  and  $30$ . Top: The isotope ratios of the different species. Middle: Peaks with intensity in mV. Bottom: Results from Isodat routine. The different peaks denoted by numbers are: 1:  $H_2$  reference gas peak, 2:  $H_2$  sample peak, 3: CO reference peak, 4: CO sample peak.

measurement run consists of multiple measurements to avoid memory effects and to obtain good statistics for the result. We make sure that the peak shape and peak area are identical for these. Furthermore, we make sure to condition the system with standard water close to the expected isotopic values for the sample measurement. After each measurement run, we inject appropriate standard water through the injection port on the setup for the VSMOW calibration.

An example of such a measurement run can be seen on Figure 3.13. This run consists of vapor measurements from the EC at  $-30^\circ\text{C}$ . The run is performed after conditioning the TC/EA. The solid line indicate the mean value of the stable measurements and the dashed lines indicate  $\pm$  standard deviation of the mean based on the (in this case) 6 last measurements for  $\delta D$  ( $-329.9 \pm 0.3\text{‰}$ ) and the 8 last measurements for  $\delta^{18}\text{O}$  ( $-38.40 \pm 0.04\text{‰}$ ). The memory effect of the system can be seen in the first measurements. As discussed in the previous chapter, the "burn in" measurement amount varies with the condition of the TC/EA-IRMS system, the frequency of the samples and how close the isotopic composition of standard used for conditioning is to the composition of the actual measurements. This makes the measurement amount vary in between the different measurement runs. In this case ( $-30^\circ\text{C}$ ) the sampling time for the cryofocus is 7:25 minutes and with roughly 10 minutes for the IRMS measurements this gives a total time of almost 20 minutes per measurement.

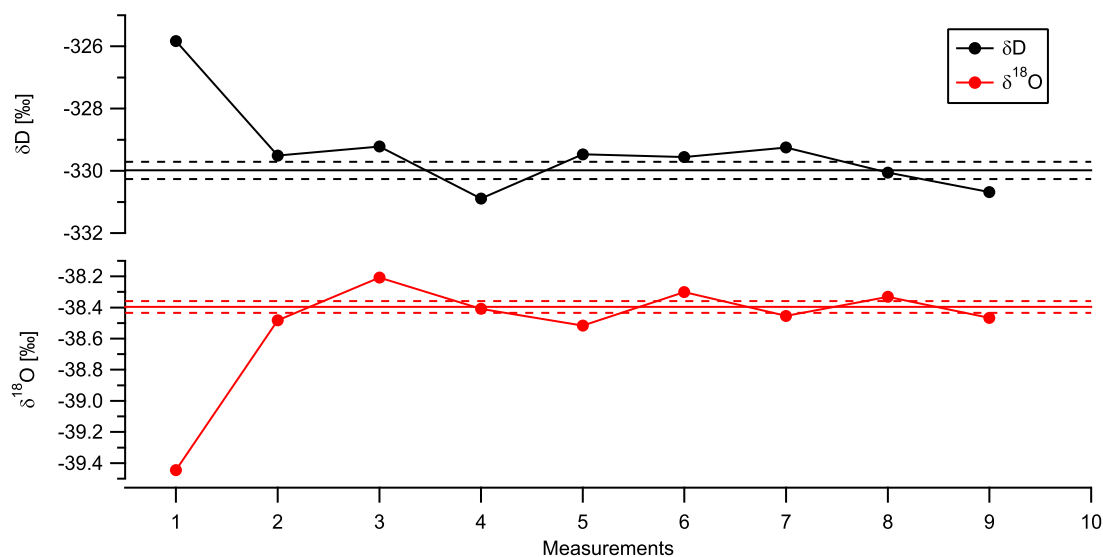


Figure 3.13: A typical IRMS sample run consisting of 9 measurements. The first measurements are affected by the memory effect of the system and are discarded when calculating the mean values. The ‰ values are uncalibrated.

### 3.3.2 IRMS VSMOW calibrations

It is important to calibrate the sample measurements with local standards with an isotopic composition close to the measured samples. Due to the relatively high memory effect in the TC/EA this saves time due to a lower sample amount and decreases the measurement uncertainty originating from calibration line uncertainties. Therefore, in addition to the normal Center for Ice and Climate working standards, we produce a new set of working standards to better cover the range of the vapor isotope values during the measurements. These standards have isotopic compositions close to the expected  $\delta D$  of vapor from Milli-Q Copenhagen tap water entering the equilibrium chamber and equilibrating at  $-10^{\circ}C$ ,  $-30^{\circ}C$  and  $-50^{\circ}C$ . The expected values are found with the isotope model in Section 1.3 with use of the fractionation factors from (Merlivat and Nief, 1967) and (Majoube, 1970). These working standards are referred to as MQ-10C, MQ-30C and MQ-50C. The VSMOW values of all local standards used can be seen in Table 3.4. The custom made standards were measured with the normal PAL auto sampler measurement routine on the TC/EA-IRMS system with active corrections for drifts and memory effects and calibrated towards VSMOW with three local standards. The uncertainties of the local standards are  $\pm 0.1$  for  $\delta D$  and  $\pm 0.05$  for  $\delta^{18}O$  unless otherwise noted.

A VSMOW calibration is performed after each measurement run and the VSMOW calibration lines are found by plotting the values obtained by measuring standard water injected through the setup versus the accepted VSMOW values as described in section 3.2.2. The ideal calibration would consist of measurements of two or more different standards for

each measurement run. But due to the measurement time (due to memory effects etc.), this is not possible and the VSMOW calibration is performed with one standard with a value near the measured sample. The VSMOW calibration line fit is therefore based on calibration measurements performed after each sample measurements during several days and short time scale drifting of the IRMS system can influence the location of the points on the above mentioned fit. Assuming that the slope of the main calibration line  $a$  is constant and that the intersect  $b$  is allowed to change over time, the offset from the main calibration line can be taken into account and the final calibration will be:

$$X_{VSMOW} = \frac{X_{meas} - b}{a} + \left( Y_{VSMOW} - \frac{Y_{meas} - b}{a} \right) \quad (3.3.1)$$

Here,  $Y_{VSMOW}$  is the VSMOW calibrated value for the injected standard for either  $\delta^{18}\text{O}$  or  $\delta\text{D}$  and  $Y_{meas}$  is the measured value of the injected standard.  $X_{VSMOW}$  and  $X_{meas}$  are in this case the VSMOW calibrated and measured values of the sample measurements and  $a$  and  $b$  are the slope and zero intersection of the fit. We are not able to correct for drifts occurring over shorter time scales (hourly) since we do not inject standard values during the measurement runs. However, other measurements on the same system show that the possible drifts on these shorter time scales are lower than the measurement uncertainty and these are therefore neglected. The measurements of local standards after each run form the VSMOW calibration set for the IRMS data and the results can be seen on Figures 3.14 and 3.15. The values of the standard runs are presented in Table 3.5. As can be seen, the VSMOW calibration lines are divided into six parts, each consisting of different standard injections. This is done since the VSMOW calibration lines are subject to small changes due to changes in the TC/EA-IRMS system. Examples of this could be maintenance issues such as change of filament, change of magnet control board, change of reference gas bottle, and long term drifts of the IRMS system. Additionally, changes in the experimental setup affecting the peak shape also cause changes in the VSMOW calibration. Examples of this could be changes in the purge flow speed, output effect of the heaters in the cryofocus and the needle insertion in the TC/EA. The calibration lines are divided after run numbers: A = 278-304, B = 305-317, C = 318-335, D = 336-359, E = 360-385 and F = 386-400 (as seen on Table 3.5). Each calibration line consists of several standard measurements over the full range of the isotopic values of the vapor measurements.

The graphs show that the VSMOW calibration can be based on a clear linear rela-

	-9	-22	MQ-10C	Crete	MQ-30C	-40	MQ-50C	DC-02
$\delta\text{D}$	-58.3	-168.7	-222.9±0.2	-262.1	-284.1±0.1	-309.8	-321.1±0.1	-427.60
$\delta^{18}\text{O}$	-8.31	-21.89	-28.59±0.09	-33.38	-36.60±0.05	-39.79	-41.23±0.03	-54.01

Table 3.4: Working standard values vs. VSMOW in ‰ used for IRMS VSMOW calibrations. Uncertainties are ± 0.1‰ for  $\delta\text{D}$  ‰ and 0.05 for  $\delta^{18}\text{O}$  unless otherwise noted.

Name	Run no.	$\delta D_m$ [‰]	$\delta^{18}O_m$ [‰]	$\delta D_t$ [‰]	$\delta^{18}O_t$ [‰]	$\delta D$ n	$\delta^{18}O$ n	$\delta D \sigma_{\bar{x}}$	$\delta^{18}O \sigma_{\bar{x}}$
A	276	-412.51	-49.27	-427.60	-54.01	6	6	0.40	0.11
	277	-169.16	-20.46	-168.70	-21.89	6	4	0.12	0.09
	278	-257.35	-30.83	-262.10	-33.38	5	5	0.19	0.06
	279	-302.08	-37.18	-309.80	-39.79	3	4	0.11	0.08
	281	-220.37		-222.95	-28.59	5		0.23	
	282	-282.42		-284.06	-36.60	4		0.10	
	285	-258.09	-32.28	-262.10	-33.38	5	5	0.14	0.14
	287	-302.99	-38.16	-309.80	-39.79	6	4	0.22	0.07
	288	-278.63	-35.39	-284.06	-36.60	5	5	0.09	0.08
	290	-279.21	-33.61	-284.06	-36.60	5	2	0.76	0.07
	293	-304.09	-35.99	-309.80	-39.79	4	4	0.24	0.08
	296	-219.38	-27.00	-222.95	-28.59	7	4	0.16	0.05
	297	-278.70	-33.73	-284.06	-36.60	7	8	0.27	0.14
	299	-219.07	-27.23	-222.95	-28.59	4	4	0.12	0.11
303	-253.91	-30.75	-262.10	-33.38	3	3	0.22	0.01	
	304	-57.11	-8.83	-58.30	-8.31	4	5	0.15	0.07
B	306	-294.66	-38.13	-309.80	-39.79	8	7	0.31	0.07
	308	-294.85	-38.80	-309.80	-39.79	5	8	0.13	0.07
	309	-413.93	-51.25	-427.60	-54.01	5	5	0.14	0.09
	311	-205.85	-28.77	-222.95	-28.59	12	7	0.32	0.11
	313	-245.85	-33.20	-262.10	-33.38	6	5	0.22	0.08
	315	-266.90	-35.72	-284.06	-36.60	11	11	0.28	0.06
	317	-267.90	-35.70	-284.06	-36.60	7	9	0.13	0.06
C	319	-240.90	-31.48	-262.10	-33.38	8	7	0.26	0.11
	320	-287.92	-37.49	-309.80	-39.79	7	6	0.18	0.10
	322	-203.18	-27.90	-222.95	-28.59	5	6	0.22	0.07
	326	-147.18	-21.70	-168.70	-21.89	8	9	0.16	0.09
	327	-410.51	-50.54	-427.60	-54.01	5	8	0.27	0.05
	329	-265.15	-35.48	-284.06	-36.60	8	8	0.18	0.07
	331	-302.71	-38.62	-321.12	-41.23	6	8	0.29	0.05
	333	-263.33	-34.55	-284.06	-36.60	7	7	0.23	0.08
	335	-263.42	-34.88	-284.06	-36.60	5	9	0.16	0.05
	D	337	-258.94	-33.96	-284.06	-36.60	6	6	0.13
339		-234.26	-32.13	-262.10	-33.38	10	10	0.22	0.07
341		-235.02	-32.37	-262.10	-33.38	8	15	0.30	0.05
343		-194.13	-28.05	-222.95	-28.59	7	7	0.27	0.03
345		-193.59	-28.13	-222.95	-28.59	5	5	0.40	0.07
347		-132.39	-22.05	-168.70	-21.89	4	3	0.34	0.06
349		-278.30	-37.70	-309.80	-39.79	4	7	0.10	0.11
351		-189.27	-27.68	-222.95	-28.59	7	7	0.22	0.07
352		-133.74	-22.03	-168.70	-21.89	7	7	0.33	0.15
354		-190.17	-27.58	-222.95	-28.59	6	8	0.25	0.05
357		-278.90	-37.50	-309.80	-39.79	6	7	0.22	0.05
359		-279.60	-38.17	-309.80	-39.79	5	5	0.07	0.06
363		-201.66	-21.36	-168.70	-21.89	8	4	0.09	0.16
E		364	-332.91	-37.39	-309.80	-39.79	5	6	0.29
	365	-255.02	-28.36	-222.95	-28.59	13	8	0.06	0.06
	367	-291.75	-32.53	-262.10	-33.38	10	7	0.07	0.16
	369	-335.05	-38.16	-309.80	-39.79	9	10	0.17	0.06
	371	-311.72	-35.67	-284.06	-36.60	7	7	0.09	0.14
	373	-253.71	-28.08	-222.95	-28.59	7	7	0.13	0.08
	375	-252.79	-27.57	-222.95	-28.59	8	6	0.17	0.03
	377	-288.61	-31.48	-262.10	-33.38	11	6	0.13	0.20
	379	-309.06	-34.84	-284.06	-36.60	6	5	0.15	0.03
	381	-347.54	-39.62	-321.12	-41.23	6	4	0.14	0.13
	383	-348.37	-39.59	-321.12	-41.23	8	7	0.13	0.14
F	385	-332.67	-37.82	-309.80	-39.79	6	4	0.18	0.05
	387	-299.58	-35.75	-284.06	-36.60	6	5	0.19	0.21
	389	-278.16	-31.50	-262.10	-33.38	6	7	0.06	0.13
	391	-324.15	-37.53	-309.80	-39.79	6	6	0.14	0.17
	393	-241.59	-27.84	-222.95	-28.59	8	7	0.14	0.11
	395	-324.40	-38.16	-309.80	-39.79	10	12	0.13	0.10
	397	-275.87	-31.31	-262.10	-33.38	6	5	0.10	0.05
400	-185.37	-20.03	-168.70	-21.89	10	6	0.14	0.18	

Table 3.5: VSMOW calibration injection results for the IRMS measurements. The calibration runs are divided into several sections to account for long term changes. Subscripts  $m$  and  $t$  indicates measured and true (VSMOW) values respectively.  $n$  is the amount of values and  $\sigma_{\bar{x}}$  indicates standard deviation of the mean.

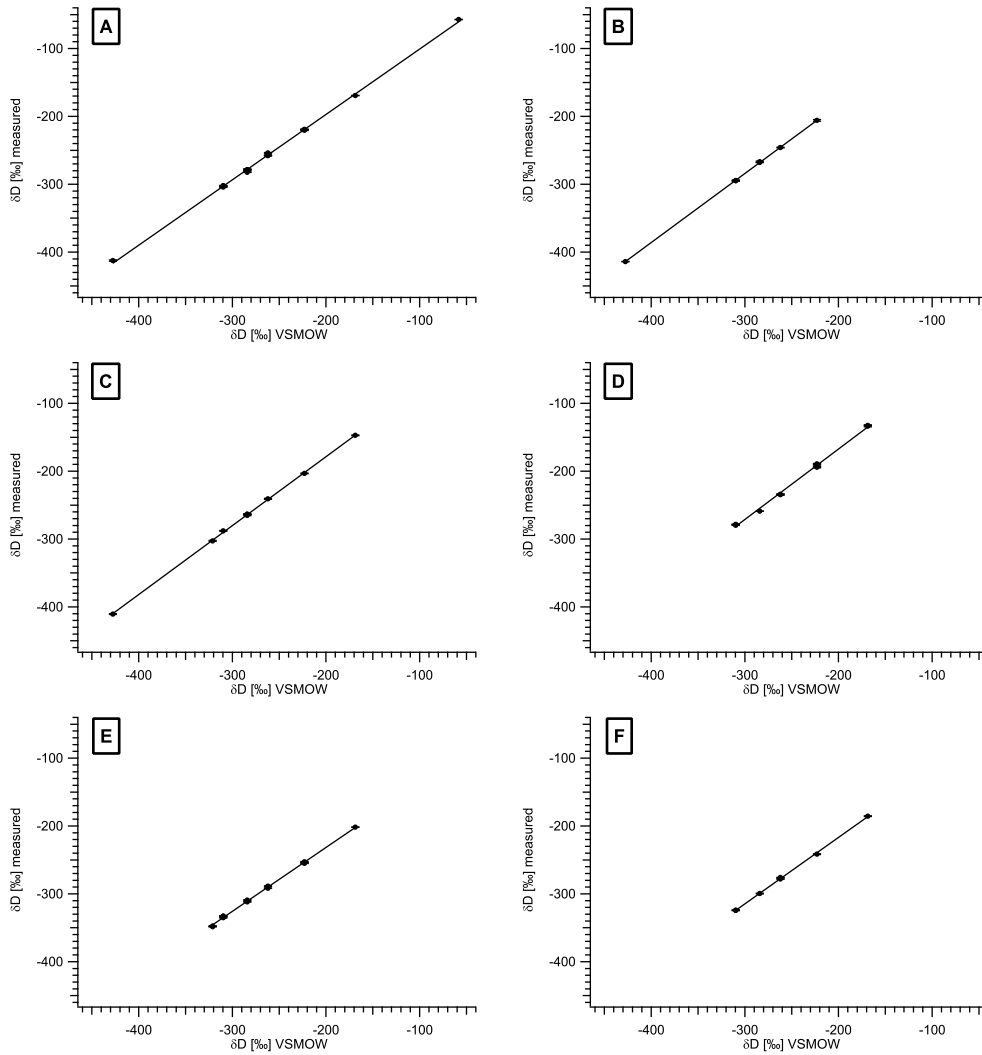


Figure 3.14:  $\delta D$  VSMOW calibration lines based on run numbers from Table 3.5: A = 278-304, B = 305-317, C = 318-335, D = 336-359, E = 360-385, F = 386-400.

relationship and the slope  $a$  and intercept  $b$  of the different calibration lines can be seen on Table 3.6. Some variations are seen between the different calibration lines but the slope uncertainty is relatively low, which is a good sign. A low uncertainty of the VSMOW calibration is important since the uncertainty of the final VSMOW calibrated result will depend on this.

### 3.3.3 Uncertainty of the IRMS data

The uncertainty of  $X_{VSMOW}$  depends on the uncertainty of the measured value  $X_{meas}$  and the uncertainty of the calibration line  $a$  and  $b$  as well as the local calibration point  $Y_{meas}$  and  $Y_{VSMOW}$ . Assuming that the errors are random and independent, we can express the error

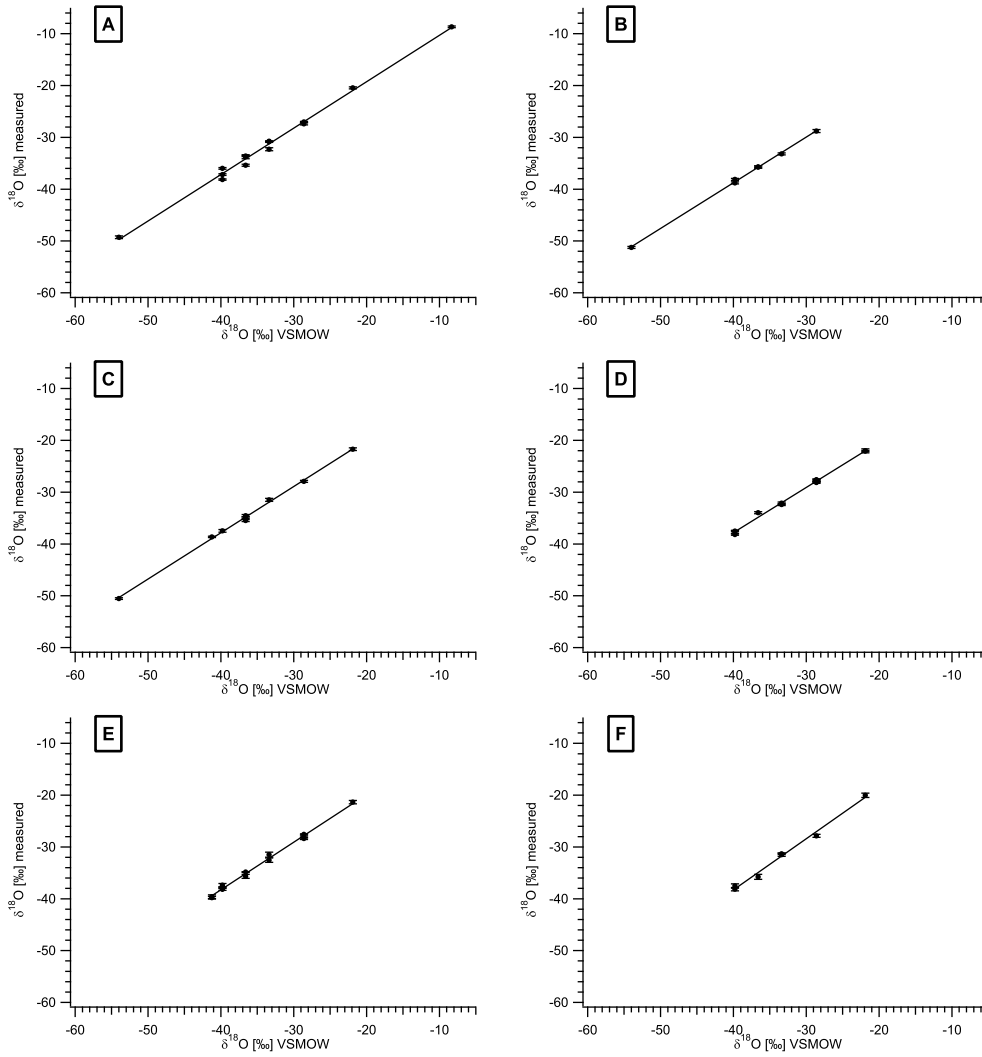


Figure 3.15:  $\delta^{18}\text{O}$  VSMOW calibration lines based on run numbers from Table 3.5: A = 278-304, B = 305-317, C = 318-335, D = 336-359, E = 360-385, F = 386-400.

with equation (3.2.6) and the uncertainty of the VSMOW calibrated value  $\Delta X_{VSMOW}$  will be:

$$\begin{aligned} \Delta X_{VSMOW} = & \left( \left( \frac{\partial X_{VSMOW}}{\partial X_{meas}} \Delta X_{meas} \right)^2 + \left( \frac{\partial X_{VSMOW}}{\partial Y_{meas}} \Delta Y_{meas} \right)^2 \right. \\ & \left. + \left( \frac{\partial X_{VSMOW}}{\partial Y_{VSMOW}} \Delta Y_{VSMOW} \right)^2 + \left( \frac{\partial X_{VSMOW}}{\partial b} \Delta b \right)^2 + \left( \frac{X_{VSMOW}}{\partial a} \Delta a \right)^2 \right)^{\frac{1}{2}} \end{aligned} \quad (3.3.2)$$

with the partial derivatives of the variables as defined above. The impact of the uncertainty on the VSMOW calibration can be illustrated with an example. With the measured values  $\delta D_{meas} = -279.77 \pm 0.24\text{‰}$  and  $\delta^{18}\text{O}_{meas} = -36.74 \pm 0.08\text{‰}$  (Run 336,  $-30^\circ\text{C}$ ), the measured standard values (MQ-30C) give  $\delta D_{st} = -258.94 \pm 0.27\text{‰}$  and  $\delta^{18}\text{O}_{st} = 33.96 \pm 0.11\text{‰}$  and they have the calibrated values  $\delta D_{st,VSMOW} = -284.06 \pm 0.12\text{‰}$  and  $\delta^{18}\text{O}_{st,VSMOW} = -$

$\delta D$	A	B	C	D	E	F
a	$0.96 \pm 0.01$	$1.018 \pm 0.004$	$1.02 \pm 0.01$	$1.04 \pm 0.02$	$0.94 \pm 0.01$	$0.98 \pm 0.01$
b	$-4.57 \pm 1.96$	$21.08 \pm 1.22$	$24.38 \pm 1.83$	$40.25 \pm 4.22$	$-43.27 \pm 2.87$	$-21.23 \pm 2.95$
$\delta^{18}O$	A	B	C	D	E	F
a	$0.89 \pm 0.02$	$0.88 \pm 0.01$	$0.89 \pm 0.02$	$0.87 \pm 0.02$	$0.92 \pm 0.02$	$0.99 \pm 0.04$
b	$-1.43 \pm 0.69$	$-3.53 \pm 0.54$	$-2.11 \pm 0.55$	$-2.95 \pm 0.58$	$-1.62 \pm 0.73$	$1.19 \pm 1.38$

Table 3.6: IRMS VSMOW calibration line fits  $y = ax + b$  with uncertainties ( $\pm 1\sigma$ ) for the different calibration lines A-F.

$36.60 \pm 0.05\%$ . This gives VSMOW calibrated values of  $\delta D_{VSMOW} = -304.11 \pm 0.53\%$  and  $\delta^{18}O_{VSMOW} = -39.80 \pm 0.18\%$ . In this case, the uncertainty for  $\delta D$  increases by roughly  $0.2\%$  and for  $\delta^{18}O$  it increases roughly  $0.1\%$ . This case shows upper values for the typical uncertainty of the VSMOW calibration since the local standard used (MQ-30C) has a relatively high uncertainty compared to the rest.

### 3.3.4 Final IRMS dataset

With the above calibrations made, we can now present the full IRMS dataset which can be seen on Figure 3.16 and Table 3.7. Again, these data have not been corrected for possible drifts in the vapor source as will be discussed in the next chapter. The dataset presented shows the 51 measurements obtained after testing and characterization of the setup was made. As seen in the run number many other measurements have been discarded, either since they were for testing purposes, because they were made before proper characterization was made with the Picarro or since they were made before an improvement was made to the experimental setup (e.g. the outlet tube in the equilibrium chamber).

Figure 3.16 shows that both  $\delta^{18}O$  and  $\delta D$  follow a clear temperature dependence which is promising for the fractionation factor calculations. The limitations of equilibrium chamber seems to be reached below  $-40^\circ C$ . For these temperatures a large deviation in the data points is seen with some measurements having very enriched values considering the overall distribution. At this point ice crystals began to grow towards the vapor flow in the equilibrium chamber. With this, diffusion effects become an issue and this results in a smaller effective fractionation factor which is also seen in the distribution of data points for both  $\delta^{18}O$  and  $\delta D$ . Due to this we will discard measurements with clear indications of growing ice crystals when calculating the equilibrium fractionation factor and this will be discussed later. Besides from the limitations at low temperatures,

## 3.4 Conclusion of this chapter

In this chapter the fully calibrated datasets of isotope values from both IRMS and Picarro measurement runs were presented. The humidity calibrations introduced for the Picarro

Run no.	T [K]	T $\sigma$	$\delta^{18}\text{O}$ [‰]	$\delta^{18}\text{O}$ SDOM	$\delta^{18}\text{O}$ $n$	$\delta\text{D}$ [‰]	$\delta\text{D}$ SDOM	$\delta\text{D}$ $n$
398	223.1	0.1	-37.23	0.91	5	-285.98	1.47	3
380	223.2	0.1	-39.54	0.28	3	-297.56	0.78	5
330	226.3	0.1	-45.57	0.37	8	-326.39	0.55	7
382	228.1	0.1	-41.49	0.33	5	-303.66	0.36	5
307	232.9	0.2	-42.34	0.14	6	-328.98	0.25	5
305	232.9	0.1	-40.42	0.10	5	-316.44	0.40	4
356	233.0	0.1	-43.59	0.28	5	-337.70	0.53	5
368	233.2	0.1	-42.02	0.16	9	-329.99	0.43	6
358	233.2	0.1	-45.61	0.23	6	-348.70	0.70	7
384	233.2	0.1	-39.94	0.13	4	-309.98	0.24	3
348	233.3	0.1	-43.02	0.22	5	-335.25	0.48	4
390	233.4	0.2	-39.44	0.24	7	-313.21	0.23	5
394	237.8	0.1	-41.91	0.24	9	-321.31	0.24	6
316	243.0	0.1	-40.74	0.13	7	-309.00	0.25	5
328	243.1	0.1	-40.08	0.12	5	-306.28	0.34	5
370	243.2	0.1	-39.58	0.18	8	-303.45	0.39	6
386	243.2	0.1	-40.29	0.35	5	-304.20	0.40	5
336	243.2	0.1	-39.80	0.15	6	-304.11	0.43	8
332	243.2	0.1	-39.63	0.14	7	-303.04	0.43	7
378	243.2	0.1	-40.11	0.10	6	-304.55	0.32	7
334	243.3	0.1	-40.33	0.11	7	-305.68	0.28	14
314	243.3	0.1	-38.81	0.11	10	-297.83	0.30	5
396	248.2	0.1	-36.78	0.18	5	-286.86	0.33	9
388	253.0	0.1	-35.01	0.17	6	-271.50	0.27	6
312	253.0	0.1	-34.75	0.13	11	-271.00	0.26	5
340	253.2	0.1	-34.99	0.10	7	-270.13	0.36	10
376	253.2	0.1	-35.21	0.27	6	-271.55	0.25	8
338	253.2	0.1	-34.87	0.11	9	-267.03	0.33	10
366	253.2	0.1	-35.72	0.23	8	-272.62	0.27	6
318	253.4	0.1	-34.46	0.15	10	-269.31	0.32	7
342	258.2	0.1	-32.21	0.13	7	-250.57	0.58	15
382	258.2	0.1	-32.15	0.17	5	-251.33	0.44	10
382	258.3	0.1	-32.69	0.27	7	-251.41	0.45	6
321	258.4	0.1	-31.70	0.16	9	-250.78	0.43	6
344	258.5	0.3	-32.83	0.16	10	-252.38	0.68	8
310	263.0	0.1	-29.60	0.17	12	-230.90	0.44	10
374	263.1	0.1	-29.44	0.11	6	-229.92	0.32	6
350	263.2	0.1	-30.08	0.20	9	-230.03	0.37	5
353	263.2	0.1	-29.20	0.22	6	-227.49	0.36	7

Table 3.7: IRMS measurement results for  $\delta\text{D}$  and  $\delta^{18}\text{O}$ . All values are VSMOW calibrated. SDOM is the standard deviation of the mean based on  $n$  measurements.

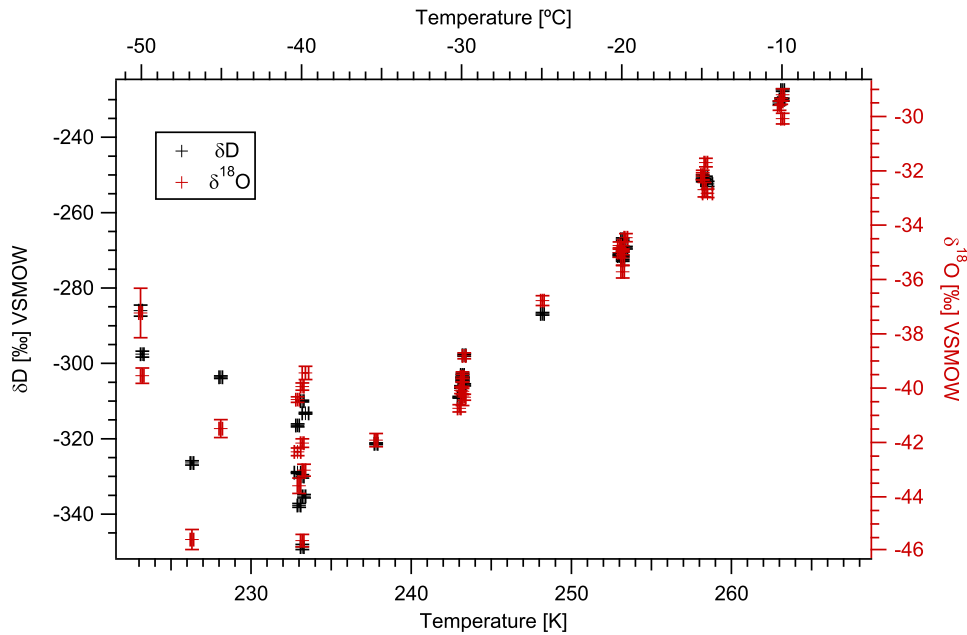


Figure 3.16: IRMS results for  $\delta\text{D}$  and  $\delta^{18}\text{O}$  as a function of temperature. All measurements are shown including tests and non-stable measurements. The deviation in the distributions can be seen to grow as a function of lower temperature. The limits of the setup can be seen below  $-40^\circ\text{C}$ . The data points can be seen in Table 3.7

data were non-linear but reproduced earlier work which supports their validity. The VSMOW calibrations introduced for both Picarro and IRMS datasets show linear relationships with low time variability. Both datasets have strong temperature dependencies and it is clear that the experimental setup and the measurement routines perform satisfactory although data acquisition is very time consuming (one data point per day). The dataset proves that the method and experimental setup have good reproducibility. The limitations for the equilibrium chamber are reached for temperatures lower than  $-40^\circ\text{C}$ . The uncertainties for the IRMS VSMOW calibrated measurements are on the order of  $0.4\text{‰}$  for  $\delta\text{D}$  and  $0.2\text{‰}$  for  $\delta^{18}\text{O}$  which is satisfying considering the custom methods used with the IRMS system. For the Picarro measurements, the uncertainty for  $\delta^{18}\text{O}$  is roughly the same but for  $\delta\text{D}$  it is roughly  $3\text{‰}$  due to the uncertainties of the VSMOW and humidity calibrations. The IRMS dataset is therefore most extensive, covering a temperature range of  $-10^\circ\text{C}$  to  $-40^\circ\text{C}$  while the Picarro dataset is more sparse with a temperature range between  $-5^\circ\text{C}$  and  $-20^\circ\text{C}$  due to limited time allocation and humidity limitations. We now have good datasets of the vapor from the equilibrium chamber as a function of temperature. But before we can properly assess the equilibrium fractionation factor for each measurements we need to discuss the equilibrium conditions of the vapor source and the equilibrium chamber.

## Chapter 4

# Characterization of the experimental setup

With the calibrated measurements of the isotopic composition of the vapor we are now able to investigate the performance of the vapor source and the equilibrium chamber. This is necessary for the calculation of the fractionation factor. First, the equilibrium conditions of the vapor source are discussed. Then we will focus on the equilibrium conditions for the ice-vapor equilibrium chamber. The equilibrium conditions are crucial for the results of this work and proper characterization is needed.

### 4.1 Characterization of the vapor source

The performance of the vapor source is important to know in detail since the fractionation factor depends directly on the incoming vapor as seen in equation (1.3.8). From this equation it can also be seen that strictly speaking we do not need the vapor source to be in equilibrium as long as we know the isotopic composition, temperature and pressure of the vapor in detail and these are all stable with time. Nevertheless the vapor source was designed to deliver vapor in equilibrium with the water in the vapor source e.g. to avoid kinetic effects when varying the carrier gas flow rate and since this reduces the amount of variable parameters in equation (1.3.8). In the following we will now characterize the vapor source with different examples and tests using the Picarro. Due its ability to perform continuous measurements the Picarro is optimal for such investigations as we can observe the important transients in the isotope values while occurring. We will show that although some surface cooling might be possible in the vapor source, we can conclude that the vapor source produces water with isotope ratios in accordance with equilibrium conditions.

### 4.1.1 Temperature and humidity stability

Figure 4.1 shows the output from the vapor source during 12 hours of sampling time. The temperature is shown as measured by the thermistor inside the vapor source cylinder. The absolute humidity,  $\delta\text{D}$  and  $\delta^{18}\text{O}$  are measured by the Picarro. In addition, smoothed versions of  $\delta\text{D}$  and  $\delta^{18}\text{O}$  are shown (blue) as well as expected isotopic compositions assuming equilibrium (black). The expected isotopic composition is found using the liquid-vapor equilibrium fractionation factor results from Majoube (1971b) along with the relationship:

$$R_v = \frac{R_l}{\alpha_{lv}} \quad (4.1.1)$$

where  $\alpha_{lv}$  is the liquid vapor fractionation factor and  $R_v$  is the isotope ratio of the vapor in equilibrium with liquid water with the isotope ratio  $R_l$ . In this model input values of  $\delta\text{D} = -62.08\text{‰}$  and  $\delta^{18}\text{O} = -8.82\text{‰}$  are used. These are measured values from samples of the vapor source (as discussed below). For the system to be in equilibrium, the relative humidity must be 100%. One way to investigate the performance of the vapor source is to compare the measured humidity and isotopes with the expected humidity and equilibrium isotope values, as described in section 1.3. A first order expression for the absolute humidity can be found by assuming a pressure of 1 atm (101325 Pa) in the setup and calculate the ratio of the partial pressure:

$$p_{ppm} = \frac{p_w}{101325 + p_w} * 10^6 \quad (4.1.2)$$

Here  $p_w$  is the partial pressure of water vapor at temperature  $T$  as described by Murphy and Koop (2005). This model gives an upper value for the partial pressure since there is slightly more than 1 atm in the setup and this will lower the absolute humidity. Furthermore the partial pressure of vapor in equilibrium with water  $p_w$  at  $1.41^\circ\text{C}$  is small compared to the total pressure of 101325 Pa so neglecting this in the denominator does not increase the absolute humidity much.

Figure 4.1 shows that the typical temperature variations in the vapor source are of the order of  $\pm 0.1^\circ\text{C}$  (some  $0.2^\circ\text{C}$  peaks are seen) occurring over a time scale of a few hours. During the depicted 12 hours, the average temperature is  $1.45^\circ\text{C}$ . The overall average of the temperature measurements of the vapor source is  $1.41^\circ\text{C} \pm 0.02^\circ\text{C}$  (based on all temperature measurements). With the liquid having the above isotopic composition and the average temperature of  $1.41^\circ\text{C}$ , the expected equilibrium values for  $\delta\text{D}$  and  $\delta^{18}\text{O}$  are  $-155.12\text{‰}$  and  $-20.155\text{‰}$  respectively and for  $1.45^\circ\text{C}$ , the expected values for  $\delta\text{D}$  and  $\delta^{18}\text{O}$  are  $-155.07\text{‰}$  and  $-20.152\text{‰}$  respectively. This illustrates that these variations in the mean temperature of the vapor source will not impact the isotope measurements much since the difference is usually below the measurement uncertainty. The impact of these variations on the final fractionation factor will be discussed in Chapter 5.

Besides from an offset of roughly 500 ppmv, the humidity of the vapor source behaves

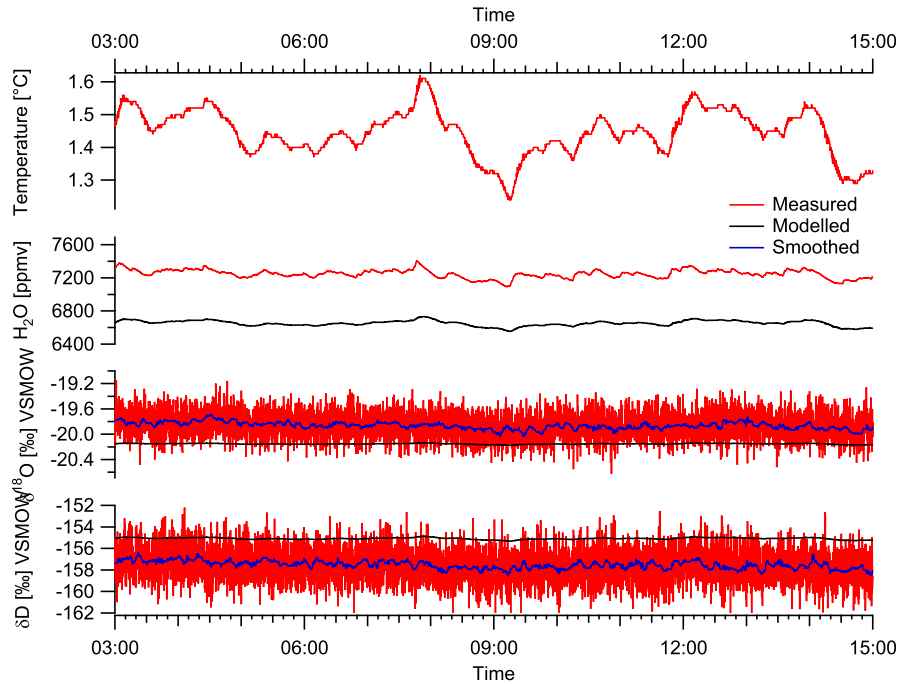


Figure 4.1: Vapor source measurements over 12 hours showing temperature measured in vapor source water, absolute humidity,  $\delta D$  and  $\delta^{18}O$  as measured by the Picarro. Smoothed versions of  $\delta D$  and  $\delta^{18}O$  are shown, as is expected humidity and isotopic composition assuming equilibrium.

as expected and we are able to predict even small changes in humidity from the changes in temperature with the simple model described in 4.1.2. The isotope values of the vapor are relatively close to the expected values assuming equilibrium fractionation during evaporation.  $\delta D$  is roughly 2 ‰ higher and  $\delta^{18}O$  is roughly 0.4‰ lower.

The reason for these offsets from expected values will now be discussed. As mentioned before the Picarro calibrate the absolute humidity in the cavity to an external relative humidity sensor and the output for the absolute humidity is therefore not calibrated to a high accuracy. Furthermore, tests show an offset of roughly 400 ppm around 7000 ppmv between the Picarro and an other better calibrated instrument (Steen-Larsen, 2010). Based on the measurement results obtained with the Picarro we can make a calibration for the absolute humidity assuming that the vapor that has been through the equilibrium chamber is in equilibrium (see argumentation in Section 4.2). Thus if vapor from the equilibrium chamber has the correct humidity we can then make a calibration line by using the data from the different measurements by plotting humidity as a function of temperature.

Figure 4.1.1 shows the measured absolute humidity for all Picarro measurements of vapor in equilibrium with ice (with  $\pm\sigma$  as uncertainty) versus the modelled value based on the temperature measurements. By assuming that the environment in the equilibrium chamber is in equilibrium (with 100% relative humidity) and by assuming that equation

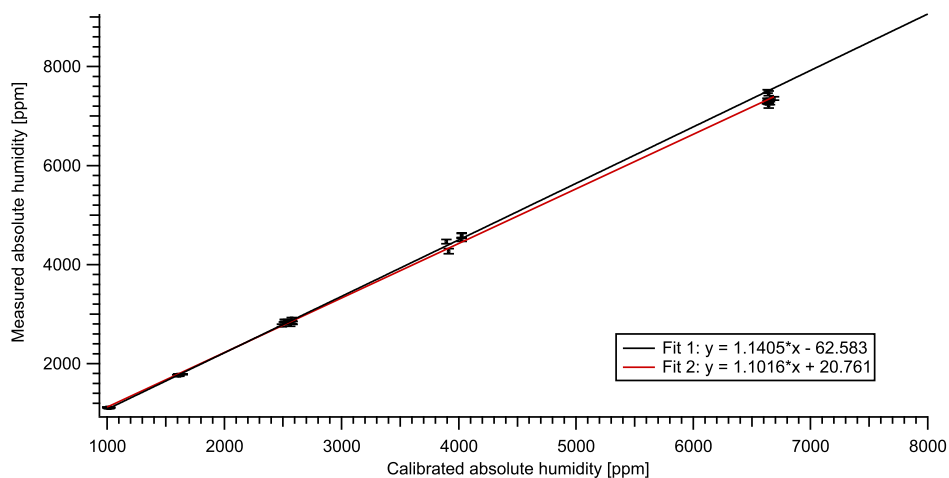


Figure 4.2: Measured humidity versus modelled (calibrated) humidity based on temperature measurements. Fit 1 is based on measured data below 5000 ppmv and Fit 2 is based on all datapoints

4.1.2 is true, then the measured values should equal the modelled values and based on this we can obtain a calibration line through these points. Fit 1 on Figure 4.1.1 is based only on data from the equilibrium chamber (data points with a modelled humidity of 1000-4000 ppmv, saturation vapor pressure over ice) and shows a linear relationship between the measured and calibrated (modelled) values. The data points from the vapor source (around 6800 ppm in modelled values, saturation vapor pressure over water) are slightly off this line and by using fit 1 as a calibration line, the values of the humidity measurements from the vapor source with the average humidity of 7316 ppmv are calibrated into an average of 6359 ppmv, roughly 250 ppmv lower than the modelled vapor pressure of around 6600 ppmv, in this case indicating a relative humidity of around 96%. Fit 2 on Figure 4.1.1 is based on all data points, thus including the data points from the vapor source, and shows that a linear fit is possible within the uncertainties of the humidity measurements suggesting that the relative humidity in the vapor source is very close to 100%.

From the above argumentation, we can conclude that the absolute humidity in the vapor source seems to be very close to 100%. This is also supported by the fact that the magnitude of the changes due to temperature variations are predicted by the model assuming equilibrium.

We will now investigate the isotope ratios of the vapor from the vapor source. We can see that  $\delta D$  is slightly below (as in more negative) and  $\delta^{18}O$  is slightly above the expected value for liquid vapor equilibrium fractionation. Here, we have to keep in mind that even though the shown Picarro data has been humidity and VSMOW calibrated, the uncertainties for these calibrations are not shown. As discussed above, typical uncertainties for  $\delta D$  is around  $\pm 3\text{‰}$  and  $\pm 0.2\text{‰}$  for  $\delta^{18}O$  and this makes the observed values correspond

fairly with the equilibrium values within the uncertainties. Hence, the isotope values also indicate equilibrium fractionation in the vapor source. However, we will still investigate the vapor source for non-equilibrium processes for a full characterization.

#### 4.1.2 Isotopic composition of the vapor

Kinetic fractionation during evaporation occurs when the relative humidity is lower than 100% and diffusion effects leaves a higher amount of the light isotopes in the vapor (Merlivat, 1978). This process has been investigated in detail by Merlivat (1978), Cappa et al. (2003) and recently by Luz et al. (2009) who observed a possible temperature dependency of the kinetic fractionation factor. In a similar experiment by Dansgaard (1961) a kinetic effect was seen for  $\delta^{18}\text{O}$  for flow rates higher than  $\sim 60$  cc/min with nitrogen passing over a water surface. As described in section 2.6 the vapor source is designed to avoid these effects by using a submerged tube with a diffuser to force the carrier gas under the liquid surface as small bubbles. Since kinetic effects in the vapor source result in more depleted vapor, these effects will in turn make the observed equilibrium fractionation factor smaller than with vapor from an equilibrium process (if equilibrium vapor was assumed in the calculations for the fractionation factor). The vapor source was investigated for possible kinetic fractionation effects directly. This was done by adjusting the carrier gas flow and observe the possible changes in the isotope ratios for  $\delta\text{D}$  and  $\delta^{18}\text{O}$ . Figure 4.3 shows  $\delta\text{D}$  and  $\delta^{18}\text{O}$  as a function of carrier gas flow measured with the Picarro. Dry air is used as carrier gas. The minimum flow rate in the system is 30 mL/min due to the inlet pump in the Picarro. The flow rate is varied between 40 mL/min and 325 mL/min. The absolute humidity can be seen decreasing with time, and could be indicating a decrease in relative humidity. However, this change is most likely due to the temperature fluctuations in the vapor source as we do not see the change in isotope ratios as seen in Dansgaard (1961) and since the decrease in humidity is negligible between 200 mL/min and 325 mL/min. The total change in relative humidity is around 300 ppmv over the course of 2 hours which are normal fluctuations in the vapor source at this temperature. It has to be noted that the temperature in the vapor source for these tests is around  $10^\circ\text{C}$  and is therefore higher than the average of  $1.4^\circ\text{C}$  normally used during the measurements (similar tests here show the same pattern). We do not see a clear decrease in the isotope ratios with increasing flow rates.  $\delta\text{D}$  is constant within the uncertainties and the slight increase in isotope ratio for  $\delta^{18}\text{O}$  is most likely due to the humidity calibration for that humidity range. Thus, from the above results we can conclude that kinetic effects are negligible in the vapor source during these conditions. Since the diffusivity of  $\text{H}_2\text{O}$  in He is higher than for  $\text{H}_2\text{O}$  in dry air (or  $\text{N}_2$ ), this conclusion should be the same when using He as carrier gas. Nevertheless, we avoid performing measurements with flow rates higher than 100 mL/min for both IRMS and Picarro measurements.

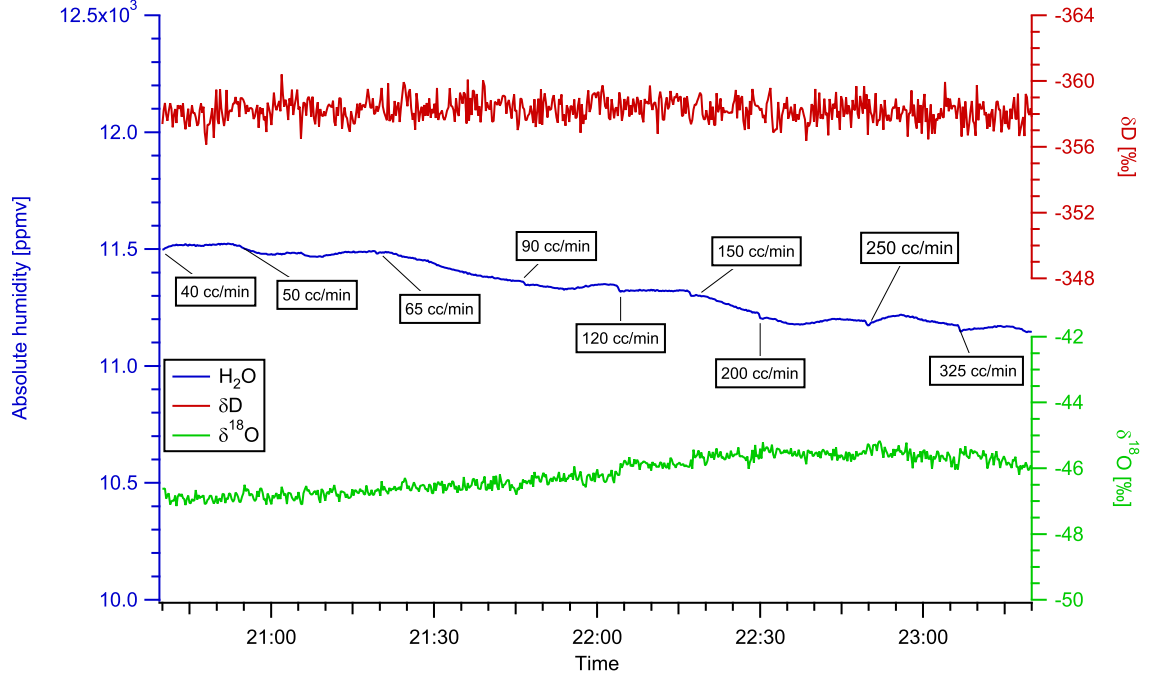


Figure 4.3: Test for kinetic fractionation in the vapor source. The carrier gas flow rate was varied to check for changes in  $\delta D$  and  $\delta^{18}O$  as a function of this. No significant changes can be seen.

If we for a short moment neglect the uncertainties on the observed isotope ratios in Figure 4.1 and assume that the difference between observed values and expected values were due to kinetic effects we can try to quantify this. Since the resulting vapor would be lighter than if it was only an equilibrium process, we cannot deduce much from  $\delta^{18}O$  since it is more enriched as expected. Using 1.2.9, we can investigate the isotope values for  $\delta D$  with a relative humidity of 96% and an average temperature of 1.41°C, as obtained above. For this temperature the equilibrium fractionation factor is 1.1101 for  $\delta D$  (Majoube, 1971b). The diffusive fractionation factor  $\alpha_{diff}=1.026$ , manually read from Luz et al. (2009). This is roughly the same as in Merlivat (1978) who obtained  $\alpha_{diff}$  1.028 for  $\delta D$ . Equation 1.2.9 gives us:

$$\frac{R_w}{R_v} = (\alpha_{diff}(1-h) + h)\alpha_{lv} \quad (4.1.3)$$

and to find the isotopic composition of the vapor:

$$R_v = \frac{R_w}{(\alpha_{diff}(1-h) + h)\alpha_{lv}} \quad (4.1.4)$$

Inserting the above mentioned numbers, we get  $\delta D = -155.8‰$  and  $\delta^{18}O = -20.97‰$  for the vapor, which could explain some of the difference between the observed and the measured values for  $\delta D$  on Figure 4.1. It takes a relative humidity of 90% to obtain  $\delta D = -157.46‰$  for the vapor, which is close to the measured values. In this case,  $\delta^{18}O$  would be  $-22.89‰$ ,

which is definitely outside the uncertainties of the measurement.

To summarize the above, we can conclude that the vapor source is in -or very close to being in- equilibrium and that the offset seen between measured values and expected values can be explained by calibration and measurement uncertainties of the Picarro data and in a smaller degree uncertainties on the liquid sample that served as input in the model. Some more investigations of the performance and stability of the vapor source will be performed in the next section. Here we will look at the long term changes based on measurement of liquid samples from the vapor source.

### 4.1.3 Changes in the isotopic composition of the vapor

Even though we only remove a small fraction of the water in the vapor source when performing measurements, the progressive removal of vapor from the vapor source will change the isotopic composition of the water following a Rayleigh distillation as discussed in Section 1.2.4. This will enrich the vapor entering the equilibrium chamber and in turn make the observed equilibrium fractionation factor larger than it should be (if equilibrium vapor was assumed in the calculations for the fractionation factor). To quantify this effect, liquid samples are collected at different times during the measurement period for measurements of  $\delta\text{D}$  and  $\delta^{18}\text{O}$  of the water in the vapor source. The results of these measurements are introduced in this section.

The samples were measured on the TC/EA-IRMS system using the PAL autosampler. Most samples were measured as a part of the normal measurement routine of 98 samples in which the dataset is actively corrected for memory effects and drifts and calibrated the result towards VSMOW with three local standards. A minor part were measured separately without these active corrections. These measurements were performed with many injections ( $> 20$ ) to account for the memory effect in the system. The stable values were then corrected for drifts and calibrated towards VSMOW by the use of two or three local standards. Bad measurements (with  $\sigma > 1\%$  for  $\delta\text{D}$  and  $\sigma > 0.6\%$  for  $\delta^{18}\text{O}$ ) were removed and the weighted mean was found.

The results of these measurements are shown in Table 4.1. The results are written as  $\bar{x} \pm \sigma_{\bar{x}}$  (see 3.1.2) and are shown with sample date,  $\delta\text{D}$ ,  $\delta^{18}\text{O}$ , the standard deviation of the mean of these as well as the amount of samples for that calculation. Furthermore, the estimated amount of sampling days are shown. This number is estimated assuming that the total amount of vapor removed from the vapor source during a full measurement run is constant. Generally one measurement was performed per day and the estimate includes testing of the setup. During the course of the measurements the vapor source water was changed (on 160410) to avoid too much fractionation and change in head space in the vapor source. Due to this, the measurement results are divided into two parts. In the following we will refer to these as MQ1 and MQ2, referring to the Copenhagen tap Milli-Q

	Date	Sampling days	$\delta\text{D}$	$\delta^{18}\text{O}$	SDOM $\delta\text{D}$	SDOM $\delta^{18}\text{O}$	$n$
MQ1	190110	0	-60.73	-8.37	0.15	0.09	7
	250210	40	-60.50	-8.99	0.66	0.18	4
	260310	61	-59.84	-8.52	0.15	0.03	47
	160410	74	-59.41	-8.46	0.15	0.05	53
MQ2	160410	0	-62.08	-8.82	0.14	0.03	52
	120510	20	-61.48	-8.73	0.15	0.03	46
	250510	23	-61.13	-8.62	0.15	0.03	44

Table 4.1: Measurements of vapor source water isotopic composition. Sampling days are estimated assuming the amount of vapor removed for each measurement run. SDOM is the standard deviation of the mean based on  $n$  samples.

water in the vapor source. These can also be seen on Figures 4.4 and 4.5. Some changes in the isotopic composition of the water in the vapor source is seen. Even though MQ1 and MQ2 comes from the same source, they have different initial values and in both cases the isotopic composition of the water in the vapor source becomes more enriched with the amount of samples which is expected. For MQ1,  $\delta\text{D}$  changes for each measurement with a total change around 1.3‰.  $\delta^{18}\text{O}$  does not have the same observable change and in fact it becomes more depleted in the heavy isotopes. The measurements performed on 250210 do not consist of that many samples which might influence the result. Furthermore it has to be noted that the memory effects in the system in general are larger for  $\delta^{18}\text{O}$  than for  $\delta\text{D}$  and it is possible that the corrections applied do not fully correct for this. Neglecting this measurement makes the total change close to the typical measurement uncertainty for the TC/EA-IRMS system. For MQ2 the values for  $\delta\text{D}$  shows an enrichment in the heavy isotopes of around 1‰ and here the values for  $\delta^{18}\text{O}$  also show enrichment of 0.2‰, close to the measurement uncertainty. To summarize, we do see indications of an enrichment of the vapor source both for  $\delta\text{D}$  and  $\delta^{18}\text{O}$ . The trend is clear for  $\delta\text{D}$ , whereas the changes are close to the measurement uncertainty for  $\delta^{18}\text{O}$ . It is clear that more measurements before, during and after the measurement runs would have improved this knowledge. The question is now what impact this enrichment has on the vapor entering the equilibrium chamber. To compare the isotope measurements with expected values, we can set up a simple Rayleigh model for the vapor source.

#### 4.1.4 Rayleigh model for the vapor source

From the above arguments we can assume thermodynamic and isotopic equilibrium in the vapor source and based on Section 1.2.4 we can set up a Rayleigh model for this with the equilibrium liquid-vapor fractionation factors from Majoube (1971b). We will assume constant temperature (the average vapor source temperature  $1.41^\circ\text{C}\pm 0.02^\circ\text{C}$ ) since the vapor source temperature is constant on longer time scales. By inserting the measured values for  $\delta\text{D}$  of the water in the vapor source we can find the total removed mass of MQ1

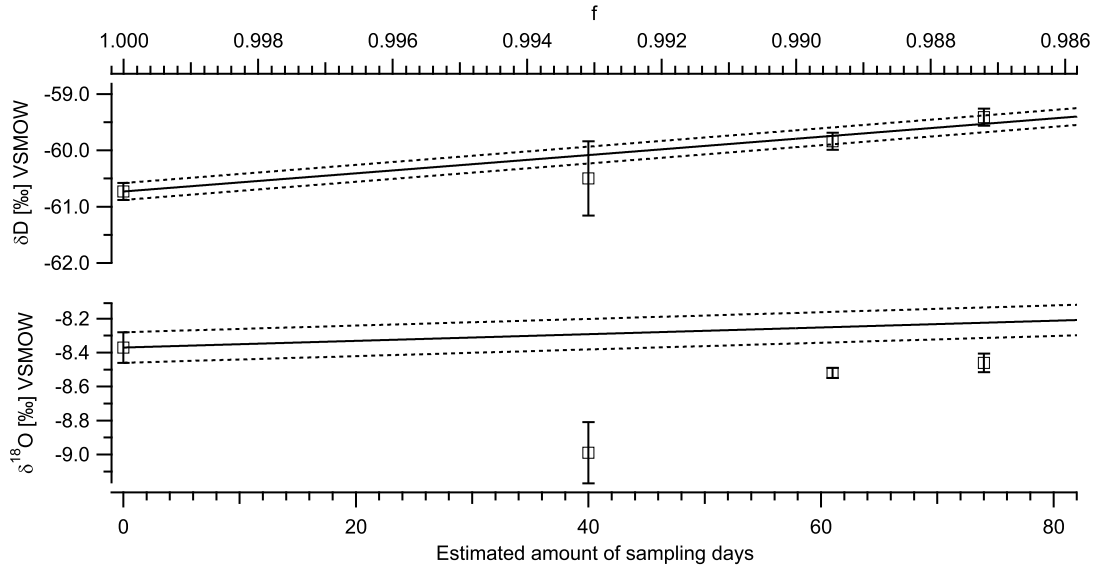


Figure 4.4: The Rayleigh model (full) for MQ1 based on  $\delta D = -60.73 \pm 0.15\text{‰}$  with the propagated uncertainties (dashed) along with the values from Table 4.1.  $f$  is the fraction of the initial water left in the vapor source.

and MQ2 (we only do this for  $\delta D$  since  $\delta^{18}O$  did not show any significant change). An example of this model can be seen on Figure 1.1 which shows  $\delta D$  of the water and the vapor in the vapor source as a function of the remaining fraction  $f$  with initial conditions of  $\delta D = -62.08\text{‰}$ , corresponding to the initial conditions for MQ2.

Figure 4.4 shows the Rayleigh model for MQ1 along with the MQ1 values from 4.1. By aligning the model values such that it makes a best fit to the MQ1  $\delta D$  values from 4.1 as a function of  $f$ , we can see that it fits the enrichment of the  $\delta D$  in the vapor source very well. The  $\delta^{18}O$  values are expectedly off due to the reasons discussed above. Figure 4.5 shows the Rayleigh model for MQ2 with the MQ2 values from 4.1. By performing the same alignment for the model to the  $\delta D$  values, we also see a good fit here and in this case the  $\delta^{18}O$  values are also covered by the model.

Since we know the approximate flow rate of the carrier gas and vapor pressure of the vapor in isotopic equilibrium with the water from (1.3.9), we can find an estimate of the water removed as a function of time by using the ideal gas law:

$$m = \frac{p_w V_{flow} m_{H_2O}}{RT_w} \quad (4.1.5)$$

where  $R=8.314$  is the universal gas constant,  $T_w$  is the temperature of the water in the cylinder in Kelvin,  $m_{H_2O}=18E-3$  kg/mol is the molar mass of water,  $V_{flow}$  is the flow rate of the carrier gas and  $p_w$  is the partial pressure of the water from Murphy and Koop (2005).

The Rayleigh model for MQ1 indicates that there is a fraction of 0.9872 left at sampling

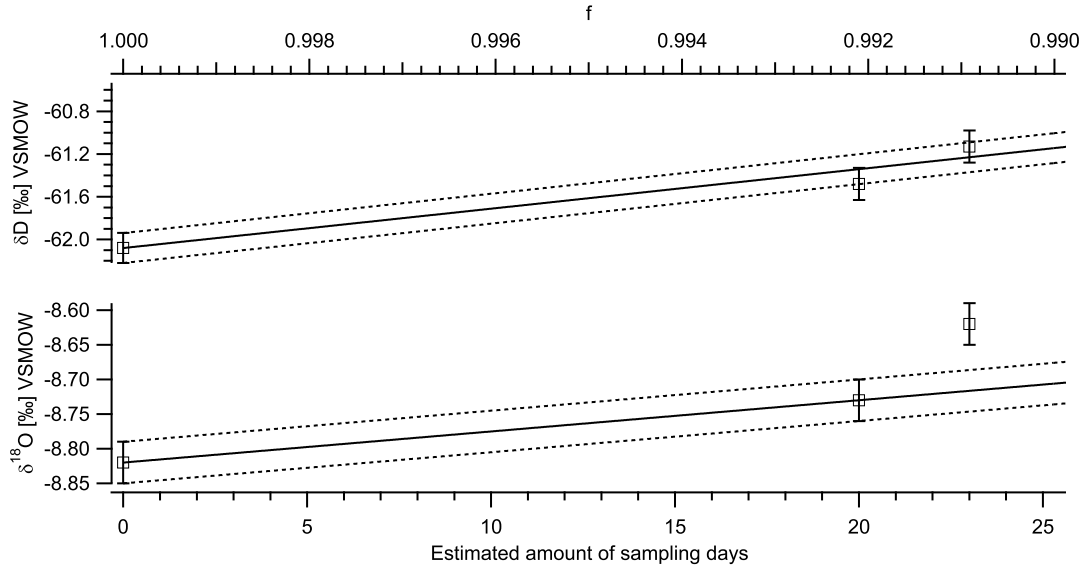


Figure 4.5: The Rayleigh model (full) for MQ2 based on  $\delta D = -62.08 \pm 0.14\text{‰}$  with the propagated uncertainties (dashed) along with the values from Table 4.1.  $f$  is the fraction of the initial water left in the vapor source.

day 74 for  $\delta D$  and since the Rayleigh model is fairly linear in this area, this gives a removed fraction of  $1.73\text{E-}4/\text{sampling day}$ . With a total volume of 1900 mL, this gives a lost volume of 0.33 mL/sampling day. For some of these runs the flow speed was varied depending on the sampling temperature from 50 mL/min to around 100 mL/min. With equation 4.1.5, a temperature of  $1.41^\circ\text{C}$  and with an average flow speed of 70 mL/min we would then get 0.54 mL/day (see also Figure 3.1 for this scenario) which fits the result from the Rayleigh fit very well considering the assumptions of these calculations. The Rayleigh model for MQ2 indicates a fraction of 0.9909 left at sampling day 23 for  $\delta D$  which gives a removed fraction of  $0.40\text{E-}4/\text{sampling day}$ . With a total volume of 1900 mL, this is a daily loss of 0.75 mL/sampling day. During these runs, we typically used 100 mL/min as flow speed and with this flow speed, we obtain 0.77 mL/day which fits really good with the value from the Rayleigh fit.

Knowing the isotopic composition of the vapor source water as a function of sample days, we can now investigate the impact of the enrichment on the vapor with the same assumptions as above with the model based on equation 1.2.16. Figures 4.6 and 4.7 shows fully calibrated vapor source measurements with Picarro and IRMS systems with uncertainties versus estimated sample days as well the expected isotopic composition of the vapor from the Rayleigh model with the same assumptions as above. The uncertainties on the curves are based on the propagated uncertainties for the liquid sample measurements and the temperature measurements. The remaining fraction of water in the vapor source  $f$  is connected to the estimated sampling days from the fits in Figures 4.4 and 4.5.

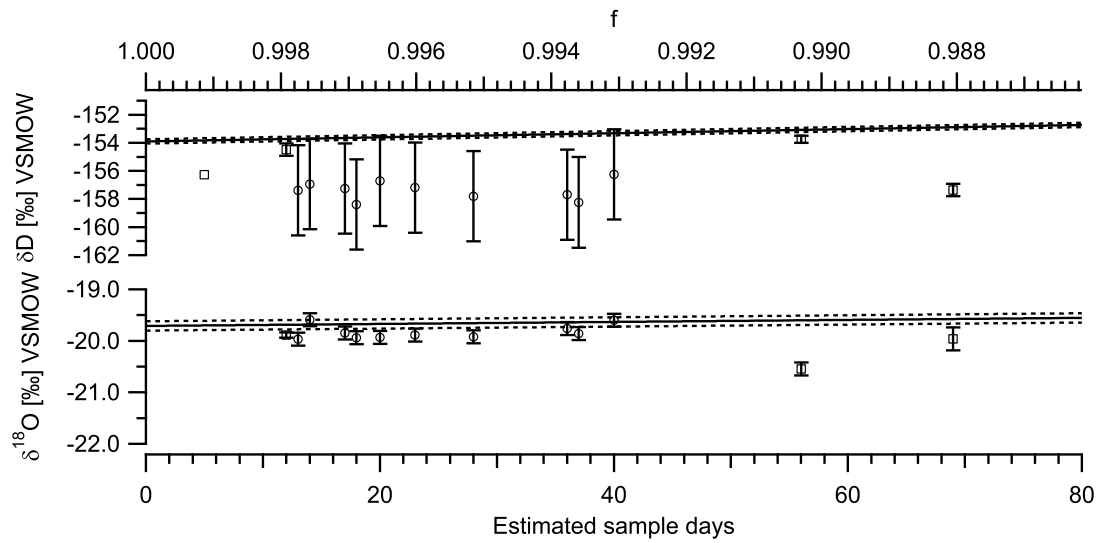


Figure 4.6: Rayleigh model (full) with uncertainties (dashed) and vapor source measurements as a function of time for MQ1.

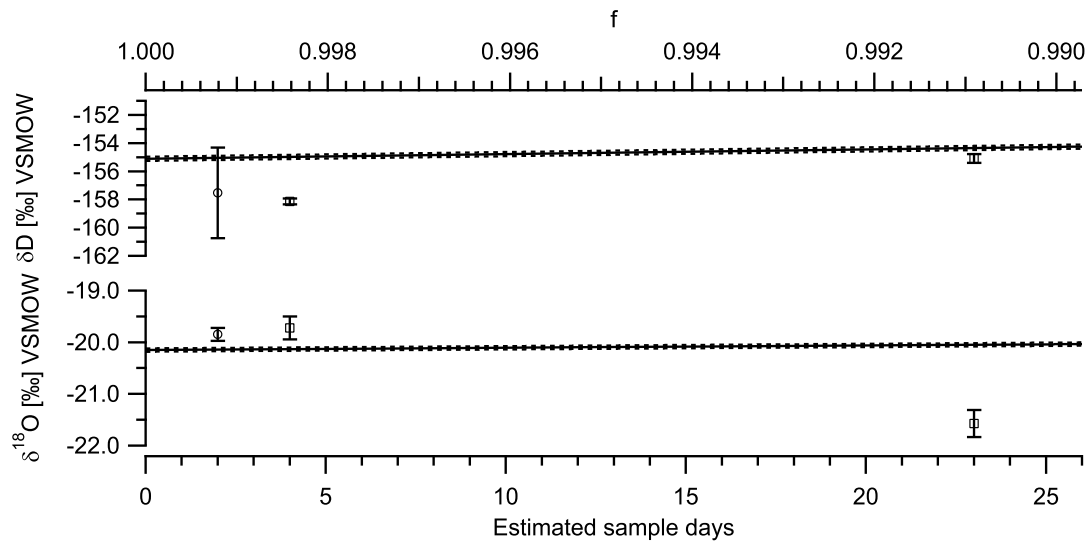


Figure 4.7: Rayleigh model (full) with uncertainties (dashed) and vapor source measurements as a function of time for MQ2.

In general the simple Rayleigh model has shown to perform quite well for both  $\delta D$  and  $\delta^{18}O$ , especially for MQ1 but also for MQ2 even though there are some bad data points in both. In the following we will focus the interpretation on the results from MQ1 due to the lack of measurements for MQ2. For  $\delta D$  the Rayleigh model is close to be within the measurement uncertainties for both the IRMS and Picarro vapor measurements and is roughly 2-3‰ off the average value for the Picarro and IRMS vapor measurements that is  $\delta D = -154.6‰ \pm 0.2‰$  and  $\delta^{18}O = -19.99‰ \pm 0.05‰$ . For  $\delta^{18}O$  the Rayleigh model fits both the Picarro and the IRMS measurements very well. Considering the assumptions and the simplicity of the Rayleigh model we must conclude that it performs very well and that our vapor source responds as if in equilibrium. The slope of the Rayleigh curve is non-significant for  $\delta^{18}O$  where it shows an effective enrichment of the vapor source smaller than the measurement uncertainty for single measurements during 80 sample days. The same can be argued for  $\delta D$  where the effective enrichment is roughly 1‰ during 80 sample days. This is more significant but still effectively close to the measurement uncertainty. The possible impact of the enrichment of the vapor source water on the measured equilibrium fractionation factor will be discussed in Chapter 5.

#### 4.1.5 Surface cooling investigations

If heat is not supplied rapidly to the surface of the evaporating liquid in the vapor source the endothermic nature of the process will cause the liquid surface to cool below the value of the rest of the bulk water. Furthermore, since the temperature of the vapor source is below the maximum density temperature of water of 3.98°C (Lide, 1990), buoyancy driven convection is limited, possibly enhancing the effect of surface cooling in the case of no active mixing. This process is limited by forcing the carrier gas under the water level with the diffuser thus creating mixing in the water in the vapor source and starting the liquid-vapor interactions below the surface level. Since the temperature used in the  $\alpha$  calculations is based on direct thermistor measurements, it is important to investigate these effects in detail. We will investigate this with different approaches: humidity, direct temperature measurements, and from the isotope values with or without kinetic effects.

The above arguments indicate that we do have close to 100% relative humidity in the vapor from the vapor source and that the vapor is in isotopic equilibrium with the water. The measured (but uncalibrated) humidity is larger than expected and after performing the calibration (assuming equilibrium in the equilibrium chamber along with a linear relationship), indications of a relative humidity of 96-97% at the average measured temperature is seen. The calibrated average humidity of 6359 ppmv mentioned above corresponds to a relative humidity of 100% at 0.82°C (from equations (4.1.2) with the vapor pressure of Murphy and Koop (2005), thus indicating surface cooling of roughly 0.6°C. This assumes that the vapor is in equilibrium with a liquid surface at this temperature. In the vapor

source the dry air exits the diffuser as bubbles under the liquid level and the vapor creation occurs where the bubbles reach the liquid level and when the vapor interacts with the rest of the liquid surface. Considering the assumptions (and the fits) in Figure 4.1.1  $0.6^{\circ}\text{C}$  is therefore probably a high estimate for the effect of surface cooling.

Direct measurements by (Paulson and Parker, 1972) of the surface cooling at water temperatures around  $25^{\circ}\text{C}$  (without stirring) show that the surface cooling should not be greater than  $2^{\circ}\text{C}$ . Other experiments have been made by e.g. Ward and Stanga (2001) on evaporation from distilled water at surface temperatures below  $4^{\circ}\text{C}$ . Here, the temperature increased strongly with depth due to a lack of buoyancy driven convection combined with a high evaporation rate and lack of active mixing. Tests were performed with the vapor source to investigate the surface cooling effect. The temperature in the vapor source was measured with 5 second intervals with the thermistor placed right in the liquid level (partially above, partially below) or submerged roughly 3 cm into the water in the vapor source. Tests were performed with no Helium flow and with a Helium flow speed of 75 mL/min (a typical flow speed for the measurements). The different configurations ran for roughly 24 hours each to investigate the possible differences in the temperature. These tests show no significant changes in temperature with or without flow and also no changes when the thermistor is submerged in the water. Furthermore, measurements right above the liquid level did also not show any significant changes in temperature. It has to be noticed that the actual evaporation happens in the liquid level close to the diffuser where the bubbles reach the surface. The thermistor was placed in the middle of the vapor source roughly 10 centimeters from this. These measurements do therefore not exclude the possibility that surface cooling is occurring in the vapor source. However since the vapor is created in one end of the vapor source it will interact with the liquid surface and vapor on its way towards the exit and this will probably limit the surface cooling effect if happening.

When looking at the values for  $\delta^{18}\text{O}$  and  $\delta\text{D}$  in the vapor measurements on Figures 4.7 and 4.6 we can see that the average values for the vapor measurements generally lie under (up to  $2\text{‰}$ ) the expected value for  $\delta\text{D}$  and very close to the expected values for  $\delta^{18}\text{O}$ . As discussed above these calculations assume equilibrium in the vapor source and are based on the liquid measurements. Assuming 100% relative humidity and using a temperature of  $0.82^{\circ}\text{C}$  in the vapor source (as discussed above), the expected values in Figure 4.6 become  $-154.6\text{‰}$  for  $\delta\text{D}$  and  $-19.77\text{‰}$  for  $\delta^{18}\text{O}$  compared to the  $-153.9\text{‰}$  for  $\delta\text{D}$  and  $-19.71\text{‰}$  for  $\delta^{18}\text{O}$  for the measured average of  $1.41^{\circ}\text{C}$  as shown on the Figure. For the values in Figure 4.7 the values are  $-155.82\text{‰}$  for  $\delta\text{D}$  and  $-20.22\text{‰}$  for  $\delta^{18}\text{O}$  for  $0.82^{\circ}\text{C}$  compared to the  $-155.1$  and  $-20.15$  with  $1.41^{\circ}\text{C}$  as shown.

As mentioned above the average value for the IRMS measurements (weighted average) is  $\delta\text{D} = -154.6\text{‰} \pm 0.2\text{‰}$  and  $\delta^{18}\text{O} = -19.99\text{‰} \pm 0.05\text{‰}$  (MQ1) and  $\delta\text{D} = -157.2\text{‰} \pm 0.2\text{‰}$  and  $\delta^{18}\text{O} = -20.49\text{‰} \pm 0.17\text{‰}$  (MQ2). Hence, a surface cooling of around  $0.6^{\circ}\text{C}$  will change

the isotopic composition of the vapor from the vapor source towards the shown average values. Especially for MQ1, this fits well the vapor measurements. Furthermore, it can be seen that the change in temperature affects  $\delta D$  to a larger extent than  $\delta^{18}O$  due to the stronger temperature dependence of  $\delta D$ .

In the above, we assumed equilibrium fractionation only. We will now investigate conditions with a relative humidity below 100%. This has been discussed earlier in this Section with equation (4.1.4) but in that case we did not allow the temperature in the vapor source to change. In the following we will use the same assumptions as before with liquid-vapor equilibrium fractionation factors from Majoube (1971b) the diffusion fractionation factors from Luz et al. (2009).

Since we know the isotopic composition of the liquid as well as the vapor, we can solve (4.1.4) as two equations with two unknowns and find the corresponding temperature  $T_w$  and relative humidity  $h$ . Using the liquid measurements of  $\delta D = -60.73\text{‰} \pm 0.15\text{‰}$  and  $\delta^{18}O = -8.37\text{‰} \pm 0.09\text{‰}$  along with the average values for the IRMS measurements of  $\delta D = -154.6\text{‰} \pm 0.2\text{‰}$  and  $\delta^{18}O = -19.99\text{‰} \pm 0.05\text{‰}$ , we obtain a relative humidity of  $h = 0.992 \pm 0.004$  and a temperature of  $T_w = 1.00^\circ\text{C} \pm 0.19$ . This indicates a surface cooling effect of roughly  $0.4^\circ\text{C}$ . Using the liquid measurements of  $\delta D = -62.08\text{‰} \pm 0.14\text{‰}$  and  $\delta^{18}O = -8.82\text{‰} \pm 0.03\text{‰}$  along with the less well defined average values for the IRMS measurements of  $\delta D = -157.2\text{‰} \pm 0.2\text{‰}$  and  $\delta^{18}O = -20.49\text{‰} \pm 0.17\text{‰}$ , leads to a relative humidity of  $h = 0.994 \pm 0.007$  and  $T_w = -0.221^\circ\text{C} \pm 0.137$ . A negative temperature for the MQ2 measurements as well as a relative humidity above 1 within the uncertainties, indicates that the average is here influenced by the low number of measurements. This is also underlined by the fact that it is possible to obtain  $T_w = 0.9^\circ\text{C}$  and  $h = 0.99$  with the average of  $\delta^{18}O$  and  $\delta D = -156.0\text{‰}$  which is within the uncertainties of the Picarro MQ2  $\delta D$  measurements.

Based on the above we can conclude that it is possible within the uncertainties of the Picarro measurements that there is a surface cooling effect in the vapor source. If there, this effect is most likely around  $0.4^\circ\text{C}$  giving an average surface temperature of  $T_w = 1.00^\circ\text{C} \pm 0.19$  and a relative humidity of  $h = 0.9915 \pm 0.0043$  (based on the isotope measurements). However, we still keep in mind that the vapor source did not show any significant changes in humidity and isotopic values (Figure 4.3) when increasing the carrier gas flow and that the IRMS measurements are very close to the expected values for equilibrium fractionation.

To summarize, this characterization of the vapor source showed that it performs to deliver vapor with a stable isotopic composition at stable temperature and humidities suitable for our needs. Some discrepancies between expected and observed values for the absolute humidity and isotopes were seen. These can be explained by the uncertainties of the Picarro measurements as well as a weak humidity calibration from the manufacturer. Tests and investigations show that significant kinetic effects are not present during evap-

oration. Indications of long term enrichment of the vapor source are seen and the trend in isotope values can be well fitted to a Rayleigh model, confirming our assumptions. The resulting changes in  $\delta D$  and  $\delta^{18}O$  of the vapor due to this are close to the measurement uncertainties of the instrumentation. The vapor source was investigated for surface cooling during evaporation and we can conclude that a cooling effect of  $0.4^{\circ}C$  is possible within the uncertainties of the measurements. However, direct investigations do not indicate a surface cooling effect. Additionally, it has to be noted that since the Picarro and IRMS vapor measurements are performed with two different carrier gases, it is assuring that the vapor measurements are in agreement with each other.

## 4.2 Ice-vapor equilibrium chamber

The equilibrium chamber was designed to let the incoming vapor condense out at a certain temperature with the ice and vapor phases in equilibrium. Obtaining equilibrium in the ice-vapor equilibrium chamber is a core part of the experiments and this will now be investigated. As in the above section we will base this on Picarro measurements. Since we are able to observe the changes occurring in  $\delta D$  and  $\delta^{18}O$  with changing conditions in the setup, these will now be analyzed for a typical measurement run.

### 4.2.1 Transients in the isotope values before equilibrium

Figure 4.8 shows the different parts of a Picarro measurement run starting out with measurements on the vapor source directly. Focusing on the humidity, at 19:00 the vapor source is closed off and only dry air flows through the setup. If we were using the IRMS system, the carrier gas would be Helium. In the meantime the Multi-Cooler (see Section 2.7) has reached a stable temperature and the equilibrium chamber has been heated and mounted to the setup only containing room air. The equilibrium chamber is now dried out by flushing carrier gas through until the humidity reaches a value close to zero (keeping in mind that the Picarro humidity calibration will be a little off), typically around 50 ppmv. During this process we can see that the humidity reaches the saturation vapor pressure for the equilibrium chamber until it begins to dry out. This part also serves as a leak check of the system and depending on the flow rate this takes around 30-40 minutes. The flow speed on the measurement run on Figure 4.8 is  $\sim 80$  mL/min of dry air (with  $\sim 30$  mL/min entering the cavity of the Picarro). When the absolute humidity approaches zero ppmv, the equilibrium chamber is bypassed from the flow and the tubing is humidified/conditioned by letting vapor from the vapor source through the setup. This is done to prevent fractionated vapor from adsorbed water on the tubing walls to enter the equilibrium chamber and to check the isotopic composition of the vapor source. When the humidity has reached a stable level for some time, the equilibrium chamber is opened and vapor is allowed to

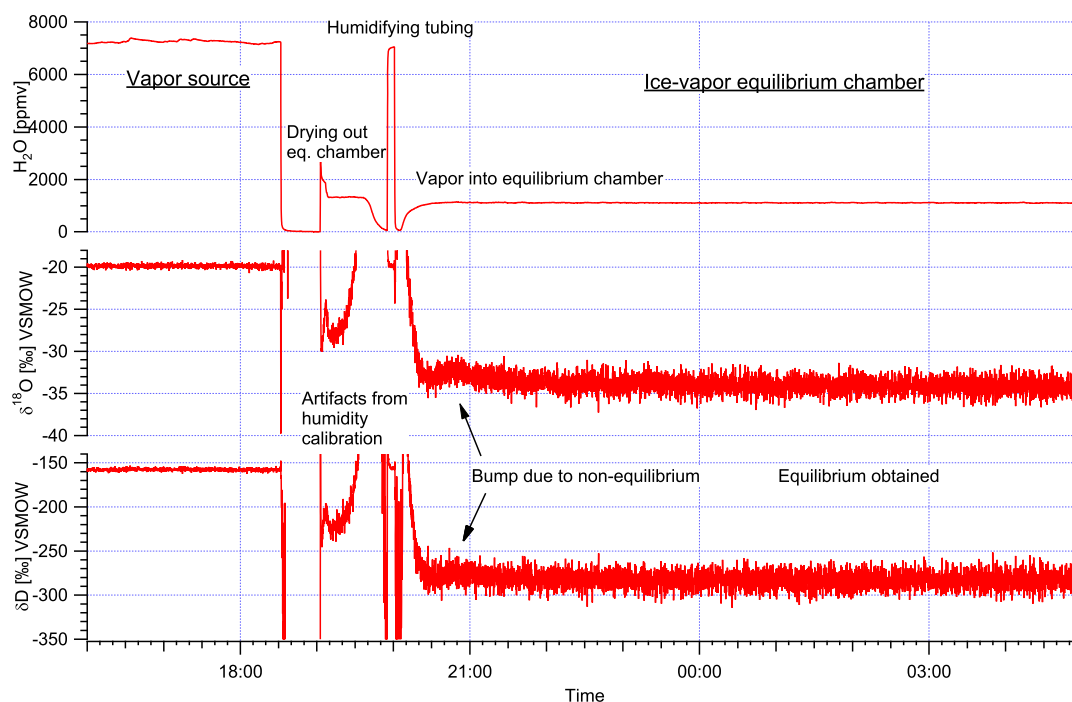


Figure 4.8: A typical Picarro run starting out with measurements of the vapor source. After this the equilibrium chamber is dried out and the tubing is humidified. Then vapor is allowed to enter the equilibrium chamber and the experiment starts. After being in non-equilibrium the system reaches an equilibrium state.

enter. Now the experiment has started and after some of time the system becomes in equilibrium. The ice forming on the sides of the equilibrium chamber is typically evenly distributed from a point below to the ethanol line and downwards. Usually the layer of ice is thin and spread out across the glass surface (see Figure 2.15). As mentioned in the previous Chapter ice crystals begin to grow out and away from the glass surface towards the vapor flow from the copper tube for temperatures below  $-40^{\circ}\text{C}$ .

We will now investigate the above described processes in more detail since Figure 4.8 and 4.9 also shows the humidity- and VSMOW calibrated values of  $\delta\text{D}$  and  $\delta^{18}\text{O}$  of the equilibrium chamber. When drying out the equilibrium chamber, it starts out containing atmospheric air which is then being more and more diluted with carrier gas. As this happens, the isotope values indicate a Rayleigh distillation. At a certain point (in this case around 19:45) the humidity reaches a point where the humidity calibration begins to perform poorly (below 800 ppmv) and the isotope values are a subject of this. The humidity reaches a point close to zero and the equilibrium chamber is now filled with dry air. It is then closed off and the vapor source is opened for  $\sim 10$  minutes to humidify the tubing. The isotope values reacts as expected and stabilizes at the vapor source level.

Now the experiment is ready to be started and the valves on the equilibrium chamber

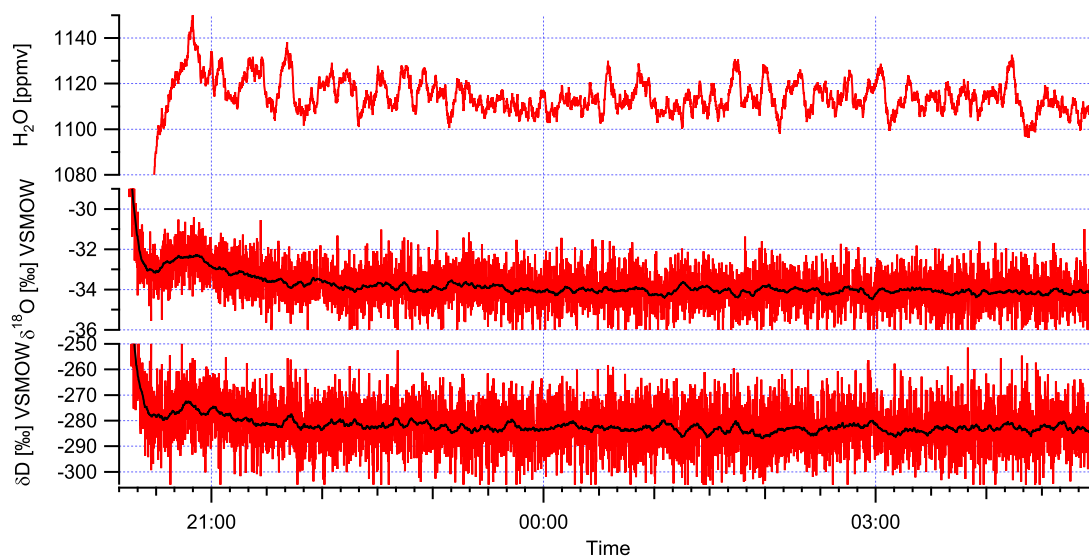


Figure 4.9: The part of Figure 4.8 containing the experiment start, the non-equilibrium and the equilibrium parts.

are opened such that vapor from the vapor source enters the chamber. This part of the process is in focus in Figure 4.9. In the beginning the humidity is still close to zero but starts to climb towards the saturation vapor pressure at the temperature in the equilibrium chamber. Before the humidity reach the limit of the humidity calibration the isotope values are affected by the bad calibration and can be ignored. When the humidity is above this point, we can see that the isotopes move from high (more positive) values towards more negative values, essentially moving away from the isotopic composition of the incoming vapor.

This transient can be explained by the incoming vapor mixing with the dry air until it reaches the saturation vapor pressure. This transition is most likely influenced by a complex mixture of diffusivity effects and possible condensation of some of the vapor taking place right after the vapor exits the tube, before proper mixing and exchange occur.

When the humidity approaches the saturation vapor pressure the isotope values flatten out towards the equilibrium level as there will be more exchange. The humidity can be seen peaking at a slightly higher level than the later obtained equilibrium level. For this run ( $-20^{\circ}\text{C}$ ) the saturation vapor pressure is around 1110 ppmv (the stable value around 00:00). As the humidity inside the equilibrium chamber increases, it becomes slightly over saturated at some point before the system finds an equilibrium state with the condensation of the incoming vapor. This slight over saturation along with increased exchange with the early condensates causes the isotope values of the vapor to drift towards slightly more positive values (see e.g. Chapter 1). Then, as the humidity drifts towards the saturation vapor pressure with full exchange between the ice and the vapor as more vapor condense

out, the isotopes drift towards the equilibrium values. It is noted that the "bump" takes roughly the same time as a complete exchange of the gas in the chamber when emptying it (see above).

To sum up the above, the observed changes in the isotope values from vapor source vapor to vapor in equilibrium with ice are based on different non-equilibrium processes before the system reaches an equilibrium state with non-drifting isotope values. As the ice-vapor exchange increases and as more vapor condense out the impacts of the initial non-equilibrium processes become smaller as the system reaches an equilibrium state. The patterns observed in the humidity and the isotope values as described above are typical for the Picarro measurements and once the equilibrium state is obtained it is constant until we stop the measurement.

#### 4.2.2 Stability in the equilibrium state

With the system in an equilibrium state we will now investigate the small scale changes occurring here. Figure 4.10 shows the temperature measured in the ethanol in the Multi-Cooler along with the humidity and  $\delta D$  and  $\delta^{18}O$  readings from the Picarro during a period of 9 hours. The temperature in the Multi-Cooler has an average of around  $-10.2^{\circ}C \pm 0.2^{\circ}C$  due to the PID cycles. The absolute humidity is stable at a measured value of 2800 ppmv with 50 ppmv fluctuations. A modelled value is also shown. This is based on the measured temperature and the simple approach of equation (4.1.2). The level of the modelled absolute humidity is below the measured due to the incomplete humidity calibration of the instrument (see 4.1). If we look at the relative changes the modelled humidity captures the small scale changes due to the temperature fluctuations with high accuracy, both regarding timing and magnitude. It has to be noted that there might be differences between the clocks of the Fluke multimeter measuring the temperature and the Picarro as well as a delay due to the sample transport time from the equilibrium chamber to the Picarro. Furthermore there are mixing in the cavity of the Picarro. These effects will misalign the peaks slightly and perform smoothing on the measured data. The observed response is a good indication that the vapor pressure in the equilibrium chamber is very close to the saturation vapor pressure over ice. Figure 4.10 also shows the measured and modelled values for  $\delta D$  and  $\delta^{18}O$  as well as smoothed versions of both isotopes. The modelled values are based on equilibrium conditions as described in Section 1.3 and we use (1.3.7) to find the output  $\delta$  values. The fractionation factors for Merlivat and Nief (1967) and Majoube (1970) are used. As input in the model we use the measured temperature as a function of time as well as  $\delta D_{vapor} = -157.38\text{‰}$  and  $\delta^{18}O_{vapor} = -19.82\text{‰}$  from the vapor source with the average vapor source temperature of  $1.41^{\circ}C$ . Comparing the modelled curve with the smoothed (50 data points) curve for  $\delta D$  and  $\delta^{18}O$ , the simple model captures the relative changes in the isotopes very well. The modelled and the smoothed curves

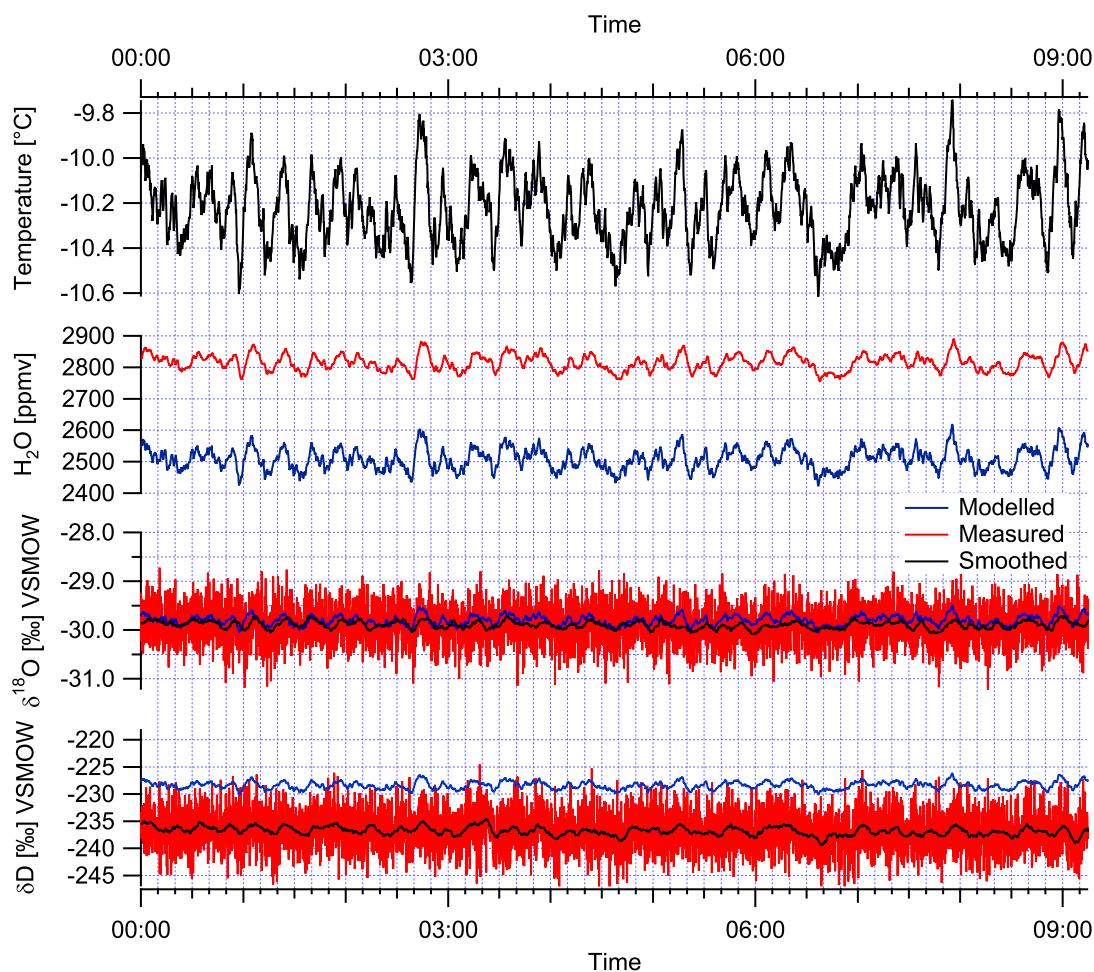


Figure 4.10: Picarro absolute humidity,  $\delta D$  and  $\delta^{18}O$  for  $-10^{\circ}C$  vapor measurements from the equilibrium chamber along with the temperature in the Multi-Cooler, measured separately.

for  $\delta^{18}O$  are almost identical, both in level and to a large extent it captures the small scale changes. For  $\delta D$  there is an offset between the levels but the small scale changes are also the same to a large extent which also confirms the model but indicates a higher fractionation factor here. The important conclusion from this plot is that the small scale changes in temperature in the equilibrium chamber are reproduced to a high detail in both the vapor pressure and for  $\delta D$  and  $\delta^{18}O$ . This indicates equilibrium conditions and that equilibrium fractionation is the governing process for the observed isotope values of the vapor from the equilibrium chamber for these temperatures.

### 4.2.3 General performance and limitations of the equilibrium chamber

In addition to the above investigations, we also performed tests with different flow rates to characterize the response of the equilibrium chamber. Results of this can be seen on Figure

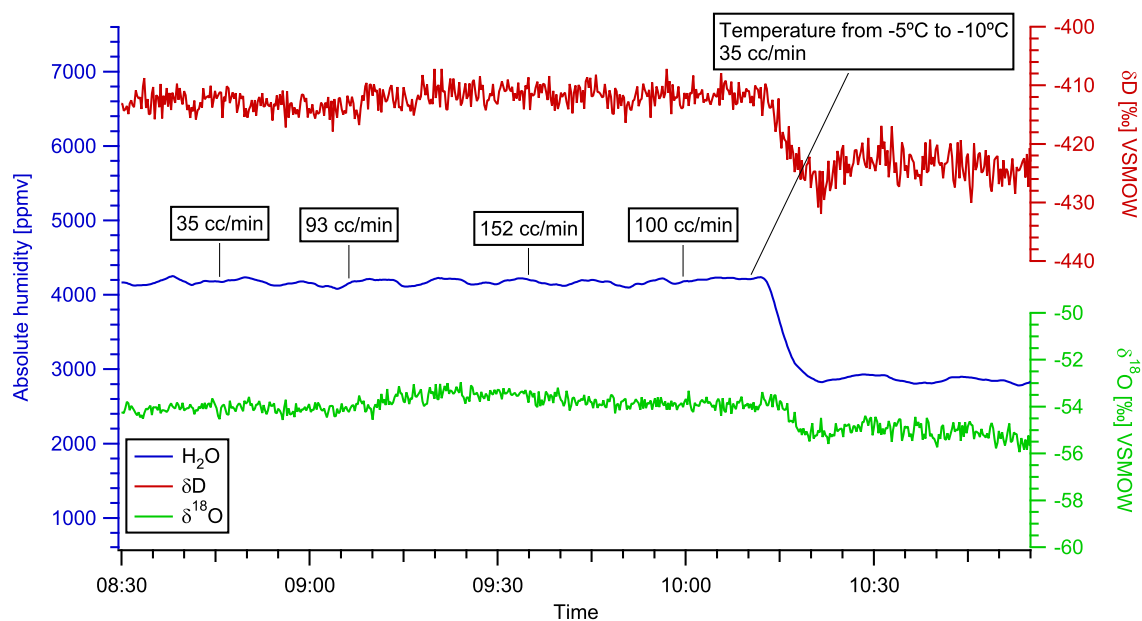


Figure 4.11: Response of the equilibrium chamber as a function of flow rate. No significant changes are seen in neither absolute humidity or in the isotope values.

4.11. The flow rate is varied from 35 mL/min (which is a minimum due to the inlet pump of the Picarro) to 152 mL/min and back to 100 mL/min before the temperature is changed from  $-5^{\circ}\text{C}$  to  $-10^{\circ}\text{C}$ . Some changes in absolute humidity is seen due to the PID controller in the Multi-Cooler and the response time for the temperature change is around 5 minutes. Looking at the isotope values, both  $\delta\text{D}$  and  $\delta^{18}\text{O}$  are overall stable. Some small scale changes are seen when changing the flow rate which is an indication that the equilibrium chamber has some adjustment time to a different flow rate. Due to this we performed all experiments with a fixed flow rate, usually not larger than 100 mL/min. The isotope values follow the temperature change almost instantaneously which is a good sign of proper exchange in the equilibrium chamber. Detailed investigations of the isotope ratios for  $\delta\text{D}$  and  $\delta^{18}\text{O}$  (and hence the fractionation factors) from these data are not optimal since the incoming vapor is exchanging with ice condensed out under different conditions.

Changes in flow speeds once equilibrium was obtained in the equilibrium chamber were seen to have an effect on the exiting vapor (which became more enriched in heavy isotopes indicating kinetic effects). During this the vapor source proved to maintain a stable humidity so the observed changes occurred in the equilibrium chamber. However, starting experiments with different, fixed flow rates did not change the isotope values in equilibrium state. Therefore, the experiment was only run with fixed flow rates. The observed flow-induced changes are therefore most likely due to sudden changes in the humidity.

To ensure that the vapor exits below the ethanol level in the equilibrium chamber, an

outlet tube was added to the inlet fitting. Before characterizing the setup with the Picarro some initial IRMS measurements were performed. Some of these do not have proper temperature recordings from the equilibrium chamber and some were performed without an outlet tube in the equilibrium chamber. Due to the lack of temperature monitoring, these measurements are not suitable for the end result fitting and they are therefore disregarded for those purposes. However since these measurements were performed at the same set point on the equilibrium chamber cooling system as later measurements, the average temperature will to some extent be identical (the deviation of the average temperature is around  $0.1^{\circ}\text{C}$ ). They can therefore be compared with later measurements to investigate the impacts of adding the outlet tube to the experimental setup. For this comparison we will use the fractionation factor  $\alpha$  based on fixed initial conditions with the uncertainty of the temperature measurements being estimated to be  $0.2^{\circ}\text{C}$  which serves as an upper value for the average temperature compared to real measurements. The details of this can be seen in the next chapter. Figure 4.12 shows values for  $-10^{\circ}\text{C}$ ,  $-20^{\circ}\text{C}$ ,  $-30^{\circ}\text{C}$  and  $-40^{\circ}\text{C}$  before and after the installation of the outlet tube in the equilibrium chamber. In general the  $\alpha$  values are higher with the outlet tube. This is seen on all values but the value for  $\delta\text{D}$  at  $-30^{\circ}\text{C}$ . The difference between the values with and without outlet tube becomes larger with more negative temperatures, confirming the theory that we avoid condensation at higher temperatures than intended. The figure also shows the issue with kinetic isotope effects due to growth of ice crystals in the equilibrium chamber. This can be seen on the values for  $-30^{\circ}\text{C}$  and  $-40^{\circ}\text{C}$  that are almost identical and in the case for  $\delta^{18}\text{O}$ ,  $\alpha$  for  $-30^{\circ}\text{C}$  is higher than for  $-40^{\circ}\text{C}$ . These investigations are based on only a few measurements under possible different conditions so final conclusions cannot be drawn from this. However, there are indications that the addition of the outlet tube is justified.

As seen in the data presented in the previous chapter, limitations of the equilibrium chamber were seen for temperatures below  $-40^{\circ}\text{C}$  or  $-45^{\circ}\text{C}$  with an increased variation in the data points with lower temperatures. Furthermore, we did see some limitations at  $-5^{\circ}\text{C}$  where equilibrium conditions were some times hard to obtain. In between these temperatures the equilibrium chamber seems to perform as expected. The limitations at high temperatures are most likely due to formation of super cooled water but also the lower amount of condensate in the equilibrium could play a role here. Supercooled water is metastable with respect to ice since it has a larger vapor pressure than ice. This means that the super cooled water cannot be stable if there is also ice in the equilibrium chamber. There will be a net flux towards the ice. During the testing we did see indications of super cooled water at temperatures around  $-5^{\circ}\text{C}$ . Here the isotope values were drifting before a sudden change towards more depleted values which agree with larger fractionation for the ice-vapor exchange than ice-liquid exchange. Of course there could be other reasons for this and the observed humidity did not change as significantly as the isotopes. Proper exchange between the ice and vapor in the equilibrium chamber is dependent on the diffusion

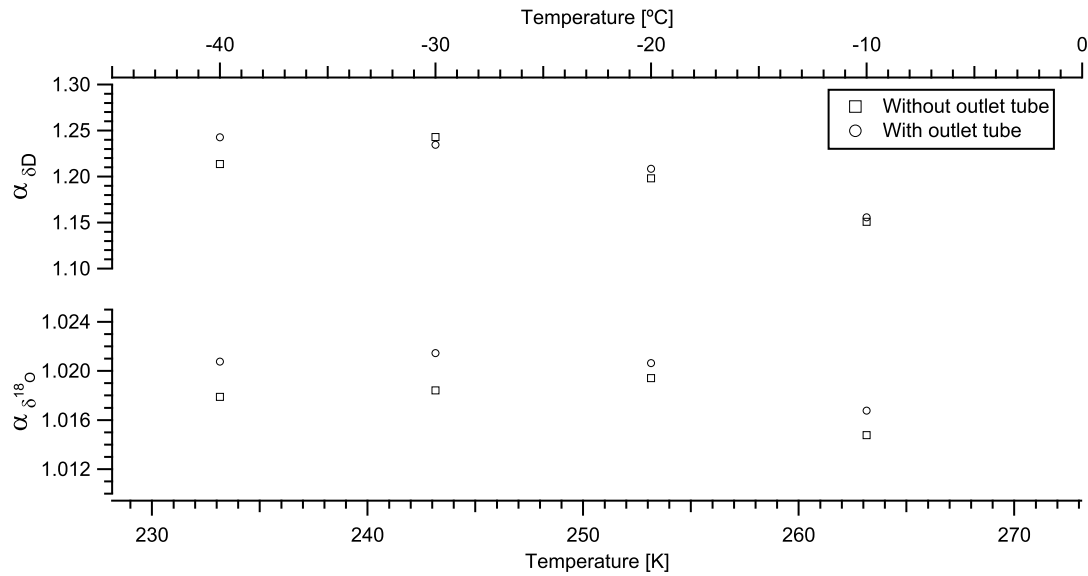


Figure 4.12:  $\alpha$  for  $\delta D$  and  $\delta^{18}O$  as a function of temperature with and without outlet tube in the equilibrium chamber. In general, a stronger fractionation is seen with the outlet tube, confirming the theory that the outlet tube will limit diffusion effects in the equilibrium chamber.

length of  $H_2O$  in Helium or Nitrogen as described in Section 2.7.2. To investigate whether the exchange between ice and vapor in the equilibrium chamber could be optimized (e.g. at  $-5^\circ C$ ) we increased the surface area drastically by filling it partially with glass beads (diameter 2 mm). The result did not show any significant changes in the isotope values and in fact the fractionation turned out being a little less for some runs, maybe due to kinetic effects due to limited exchange with the ice once the vapor reached the glass beads. Therefore, all measurements were performed without glass beads. As mentioned before the limitations at low temperatures are clearly due to the combination of ice crystal growth towards the vapor flow and the long sampling time (and subsequent memory effects etc.). The ice crystals will have an impact on the isotope values of the vapor in equilibrium with the ice since they grow by diffusion under super saturated conditions. Ideally, we would like to have a thin layer of ice created by condensation distributed over a large area such that we are sure that there is enough exchange between the ice and the vapor in the equilibrium chamber. As discussed in 1.2.3 the formation of ice crystals adds a kinetic fractionation factor to the equations (Jouzel and Merlivat, 1984) which will result in the measured isotope values drifting towards more positive values since a larger part of the light isotopes condense out which is also observed. Some part of the observed effects could also be due to the ice condensing out under higher temperatures than intended but since the vapor pressure will be higher here this ice will not be stable.

To summarize this section, the analysis of the observed changes in the isotope values during a measurement run strongly indicates that the system obtains equilibrium condi-

tions with stable isotope values after an explained initial period of a non-equilibrium state. This is supported by investigations of the system once equilibrium conditions were reached. Here, the small scale changes in the temperatures are captured to high details with models for the humidity and the isotope values. Kinetic effects do not seem to be present and the response of the equilibrium chamber indicate proper exchange between the vapor and ice phases. The addition of an outlet tube and the limitations for high and low temperatures and during changing flow rates were discussed.

### 4.3 Conclusion

In this chapter we investigated the equilibrium conditions for the vapor source and the equilibrium chamber mainly with the Picarro. This instrument proved to be very valuable for this since we were able to observe and analyze the changes occurring in the system. Overall, the vapor source and the equilibrium chamber performs as expected and as needed for these investigations. The vapor source performs to deliver vapor with a stable isotopic composition at stable temperature and humidities suitable for our needs. Some differences between observed and expected isotope values were seen but these were explained by uncertainties and weak humidity calibration from the manufacturer of the instrument. Kinetic effects are not present during evaporation but some long term enrichment of the vapor source was seen. The magnitude of this was expected and the resulting changes in  $\delta D$  and  $\delta^{18}O$  of the vapor are close to the measurement uncertainties of the instrumentation. Surface cooling is most likely not an issue in the vapor source but a cooling effect of  $0.4^{\circ}C$  is possible within the uncertainties of the measurements. Since the Picarro and IRMS vapor measurements are performed with two different carrier gases, it confirms the assumptions behind the setup that the vapor measurements are in agreement with each other. The main limitation of the vapor source characterization was the low amount of water and vapor samples. Higher sampling frequency here could have improved the investigation of the enrichment of the vapor source.

Investigations of the changes in the isotope ratios during a typical measurement run strongly indicated that equilibrium conditions are obtained in the equilibrium chamber. Furthermore, the small scale changes in isotope ratios and humidity due to temperature fluctuations in the equilibrium chamber could be predicted to a high detail by models assuming equilibrium. Kinetic effects do not seem to be present and the response of the equilibrium chamber indicate proper exchange between the vapor and ice phases for temperatures above  $-40^{\circ}C$ . For temperatures below this, kinetic effects begin interrupting the equilibrium conditions as mentioned in the previous chapter.

# Chapter 5

## Results and discussion

In the previous chapters we introduced the Picarro and IRMS datasets and the calibrations used and we discussed the performance of the vapor source and the equilibrium chamber. These were both found to perform as needed for these investigations. In this chapter we will find the ice-vapor equilibrium fractionation factor  $\alpha$  from the datasets presented, we will discuss the uncertainties of this and compare with previous results. Finally we will discuss the results and the limitations and possible improvements of the experimental setup. Before finding  $\alpha$  based on the presented measurements we will first discuss the error on  $\alpha$  and the different variables used to find  $\alpha$ .

### 5.1 Uncertainties on the measured fractionation factor

If we consider the equation for  $\alpha$ , (1.3.8):

$$\alpha_i = \frac{\delta_{v0} - \delta_{vi}}{(\delta_{vi} + 1)(1 - g)} + 1 \quad (5.1.1)$$

it is clear from equation (3.2.6) that the error on the fractionation factor  $\Delta\alpha$  will be:

$$\Delta\alpha = \sqrt{\left(\frac{\partial\alpha}{\partial\delta_{v0}}\Delta\delta_{v0}\right)^2 + \left(\frac{\partial\alpha}{\partial\delta_{vi}}\Delta\delta_{vi}\right)^2 + \left(\frac{\partial\alpha}{\partial g}\Delta g\right)^2} \quad (5.1.2)$$

$\Delta\delta_{v0}$  and  $\Delta\delta_{vi}$  are determined directly from the measurements while  $\Delta g$  depends on the pressure and the temperature (see equation (1.3.6)):

$$\Delta g = \sqrt{\left(\frac{\partial g}{\partial p_i}\Delta p_i\right)^2 + \left(\frac{\partial g}{\partial T_w}\Delta T_w\right)^2 + \left(\frac{\partial g}{\partial T_i}\Delta T_i\right)^2 + \left(\frac{\partial g}{\partial p_w}\Delta p_w\right)^2} \quad (5.1.3)$$

This can be written as:

$$\Delta g = \sqrt{\left(\frac{T_w}{T_i p_w} \Delta p_i\right)^2 + \left(\frac{p_i}{T_i} \frac{\partial}{\partial T_w} \left(\frac{T_w}{p_w}\right) \Delta T_w\right)^2 + \left(\frac{T_w}{p_w} \frac{\partial}{\partial T_i} \left(\frac{p_i}{T_i}\right) \Delta T_i\right)^2 + \left(\frac{T_w p_i}{-p_w^2 T_i} \Delta p_w\right)^2} \quad (5.1.4)$$

Here,  $\Delta T_w$  and  $\Delta T_i$  are determined from the direct measurements while  $\Delta p_i$  and  $\Delta p_w$  are temperature dependent (see equation (1.3.9)):

$$\Delta p_i = \frac{\partial p_i}{\partial T_i} \Delta T_i \quad (5.1.5)$$

$$\Delta p_w = \frac{\partial p_w}{\partial T_w} \Delta T_w \quad (5.1.6)$$

These are found from the derivatives of the pressure functions (1.3.9) and (1.3.10). As  $T_w$  the average of the vapor source is  $1.41 \pm 0.02$  and based on those values  $\Delta p_w = 0.97$  Pa. Since  $T_i$  is varying between  $-5^\circ\text{C}$  and  $-50^\circ\text{C}$  in our measurements, we will now investigate  $\Delta p_i$  as a function of temperature. The average standard deviation of the temperature measurements in the equilibrium chamber is  $0.12^\circ\text{C}$ . With this uncertainty,  $\Delta p_{i,-5\text{C}} = (401.76 \text{ Pa}) \pm 4.12$  Pa giving a relative uncertainty of 1.03% and  $\Delta p_{i,-50\text{C}} = (3.94 \text{ Pa}) \pm 0.06$  Pa giving a relative uncertainty of 1.52%.

We will now investigate  $g$  and equation (5.1.4) as a function of  $T_i$  since  $T_w$  has the average temperature of  $1.41^\circ\text{C}$ . In the interval of  $-50^\circ\text{C} < T_i < -5^\circ\text{C}$  and with  $\Delta T_i = 0.12^\circ\text{C}$  and  $\Delta T_w = 0.02^\circ\text{C}$ ,  $\Delta g$  varies between 1.4% (at  $-5^\circ\text{C}$ ) to 2.1% (at  $-50^\circ\text{C}$ ) in relative uncertainty. More importantly, we can from equation (5.1.4) investigate the contributions from each variables in  $g$ . From this, we can see that it is the first and the last part of (5.1.4) that are the main contributors to the total uncertainty of  $g$  with several orders of magnitude. These two parts are the error in  $g$  due to  $\Delta p_i$  and  $\Delta p_w$  alone and is expected due to the exponential relationship between pressure and temperature. Knowing  $\Delta g$ , we can investigate  $\Delta \alpha$ . The partial derivatives in equation (5.1.2) are:

$$\frac{\partial \alpha}{\partial \delta_{v0}} = \frac{1}{(\delta_{vi} + 1)(1 - g)} \quad (5.1.7)$$

$$\frac{\partial \alpha}{\partial \delta_{vi}} = \frac{\delta_{v0} + 1}{(\delta_{vi} + 1)^2 (g - 1)} \quad (5.1.8)$$

$$\frac{\partial \alpha}{\partial g} = \frac{\delta_{v0} - \delta_{vi}}{(\delta_{vi} + 1)(1 - g)^2} \quad (5.1.9)$$

Since the isotope values also depends indirectly on the temperature, we will use typical scenarios with  $\delta_{v0}$  and  $\delta_{vi}$  for different  $T_i$  with  $T_w = 1.41^\circ\text{C}$  with the above uncertainties. This is shown on Tables 5.1 and 5.2 for  $\delta\text{D}$  and  $\delta^{18}\text{O}$  respectively. For typical values for  $\delta\text{D}$

Temperature	$\delta_{v0}$	$\delta_{vi}$	$\alpha$	$\Delta\alpha$	$(\frac{\partial\alpha}{\partial\delta_{v0}}\Delta\delta_{v0})^2$	$(\frac{\partial\alpha}{\partial\delta_{vi}}\Delta\delta_{vi})^2$	$(\frac{\partial\alpha}{\partial g}\Delta g)^2$
-5	-156‰	-212‰	1.1811	0.0046	2.62e-6	3.00e-6	1.60e-5
-20	-156‰	-274‰	1.1948	0.0014	6.81e-7	9.20e-7	3.83e-7
-40	-156‰	-330‰	1.2656	0.0013	5.83e-7	9.25e-7	1.32e-8

Table 5.1:  $\Delta\alpha$  investigations for  $\alpha_{\delta D}$ . Typical values of  $\delta D \pm 0.5\text{‰}$  for each temperature are used.

Temperature	$\delta_{v0}$	$\delta_{vi}$	$\alpha$	$\Delta\alpha$	$(\frac{\partial\alpha}{\partial\delta_{v0}}\Delta\delta_{v0})^2$	$(\frac{\partial\alpha}{\partial\delta_{vi}}\Delta\delta_{vi})^2$	$(\frac{\partial\alpha}{\partial g}\Delta g)^2$
-5	-20‰	-27‰	1.0183	8.2e-4	2.74e-7	2.78e-7	1.64e-7
-20	-20‰	-36‰	1.0199	4.1e-4	6.18e-8	6.38e-8	3.99e-9
-40	-20‰	-42‰	1.0235	3.1e-4	4.56e-8	4.77e-8	1.03e-10

Table 5.2:  $\Delta\alpha$  investigations for  $\alpha_{\delta^{18}O}$ . Typical values of  $\delta^{18}O \pm 0.2\text{‰}$  for each temperature are used.

and  $\delta^{18}O$  for the three different temperatures ( $-5^\circ\text{C}$ ,  $-20^\circ\text{C}$  and  $-40^\circ\text{C}$ ) we can see that  $\Delta\alpha$  decreases with lower temperatures since the difference between  $\delta_{v0}$  and  $\delta_{vi}$  becomes larger and since the relative change of vapor pressure is not as big here. This can also be seen by the contribution from the different partial derivatives where the relative contribution of  $g$  becomes smaller with lower temperatures. The uncertainty  $\Delta\alpha$  can be seen vary between 0.0046 and 0.0013 for  $\alpha_{\delta D}$  and 8.15e-4 and 3.07e-4 for  $\alpha_{\delta^{18}O}$ . This uncertainty for single measurements of  $\alpha$  on the fourth significant digit for  $\delta D$  and on the fifth significant digit for  $\delta^{18}O$  allows us to measure  $\alpha$  with high enough precision to properly characterize the temperature dependency. In the dataset presented in Table 3.7 for the IRMS measurements (and to some extent Table 3.3 for the Picarro measurements) the typical measurement uncertainty is lower on  $\delta_{vi}$  and  $\delta_{v0}$  which brings the uncertainty down. The presented examples were made with typical isotope ratios with the well estimated values for the errors on  $T_i$  and  $T_w$  as mentioned in the previous chapter. For comparison, a "worst case" scenario can be made with  $-5^\circ\text{C}$  in the equilibrium chamber with an uncertainty on  $\delta D$  of  $\pm 0.5\text{‰}$  and larger uncertainties for the temperatures, being  $\pm 0.2^\circ\text{C}$  for  $\Delta T_i$  and  $\pm 0.2^\circ\text{C}$  for  $\Delta T_w$ . This gives an uncertainty of  $\pm 0.009$  which of course is larger than before but effectively this is still an uncertainty on the fourth significant digit for  $\alpha$  for  $\delta D$ . For  $\delta^{18}O$  the result is similar with the uncertainty being  $\pm 0.0011$ . These numbers will also decrease with lower temperatures. Since the above uncertainties are for single measurements of  $\alpha$  it is clear that multiple measurements on each temperature will bring down the uncertainty on the final result of  $\alpha$ .

Before we can produce the final dataset we need to discuss the initial conditions  $\delta_{v0}$ . In the previous chapter we discussed that the vapor source is in equilibrium but as was shown, enrichment due to Rayleigh distillation and surface cooling can have some effects on  $\alpha$  and in the following this will be discussed.

## 5.2 Initial conditions for the $\alpha$ calculations

When calculating the final dataset for the ice-vapor equilibrium fractionation factor  $\alpha$ , the result will change due to different assumptions for the main variables  $\delta_{v0}, \delta_{vi}$  and  $g$ .  $\delta_{vi}$  is well known from the isotopic measurements and the uncertainty is well defined through the different calibrations. Furthermore, the temperature and vapor pressure in the equilibrium chamber (going into  $g$ ) are well defined. The impact on  $\alpha$  with different approaches for  $\delta_{v0}$  will now be discussed.

In the first approach,  $\delta_{v0}$  can be based directly on the liquid measurements of the vapor source and the following Rayleigh model for the vapor as discussed in Section 4.1.4. In this case  $\delta_{v0}$  are indirectly based on the liquid-vapor results of Majoube (1971b) assuming a relative humidity of 100 percent in the vapor source as well as the estimated sample days.

The second approach includes fewer assumptions. Here,  $\alpha$  is based directly on the vapor measurements of the vapor in the vapor source as well as the assumption of equilibrium there. Since the enrichment due to the Rayleigh distillation occurring during the constant removal of vapor from the vapor source is comparable to the measurement uncertainties of the vapor measurements, an average isotopic value of the measurements can be used as  $\delta_{v0}$  in the calculations of  $\alpha$ . Furthermore, from the argumentation that the small discrepancy between the Picarro data and the IRMS data is caused by the Picarro calibration, we will perform a simple correction on the Picarro data such that the average value of the vapor measurements from the two measurement methods are identical and equal to the average IRMS value. Of course this simple calibration will only have a limited effect since it does not account for offsets for more negative isotope values. In these two approaches we use the measured temperature of  $T_w = 1.41^\circ\text{C} \pm 0.02^\circ\text{C}$  and saturation vapor pressure as input in  $g$  assuming equilibrium in the vapor source based on the argumentation in the previous chapter. It is clear that the first approach is based on more assumptions than the second one and we will now investigate the significance of the changed  $\delta_{v0}$  on the calculations of  $\alpha$ . The calculations are based on the data presented in Tables 3.7 and 3.3 and equation (5.1.1).

### 5.2.1 The impact of different $\delta_{v0}$ approaches on $\alpha$

Figure 5.1 shows the residual between  $\alpha$  based on  $\delta_{v0}$  from the Rayleigh curves shown in Figures 4.6 and 4.7 and  $\alpha$  based on average values of  $\delta_{v0}$  of the vapor measurements ( $\delta\text{D} = -154.6\text{‰} \pm 0.2\text{‰}$  and  $\delta^{18}\text{O} = -19.99\text{‰} \pm 0.05\text{‰}$  for MQ1 and  $\delta\text{D} = -157.2\text{‰} \pm 0.2\text{‰}$  and  $\delta^{18}\text{O} = -20.49\text{‰} \pm 0.05\text{‰}$  for MQ2). For comparison the uncertainties of the  $\alpha$  based on average values of  $\delta_{v0}$  of the vapor measurements is shown. Since the  $\delta_{v0}$  is larger (less negative) in the Rayleigh approach the difference between  $\delta_{v0}$  and  $\delta_{vi}$  in equation (1.3.8) becomes larger which results in a slightly larger  $\alpha$ . The difference between the two scenarios is between

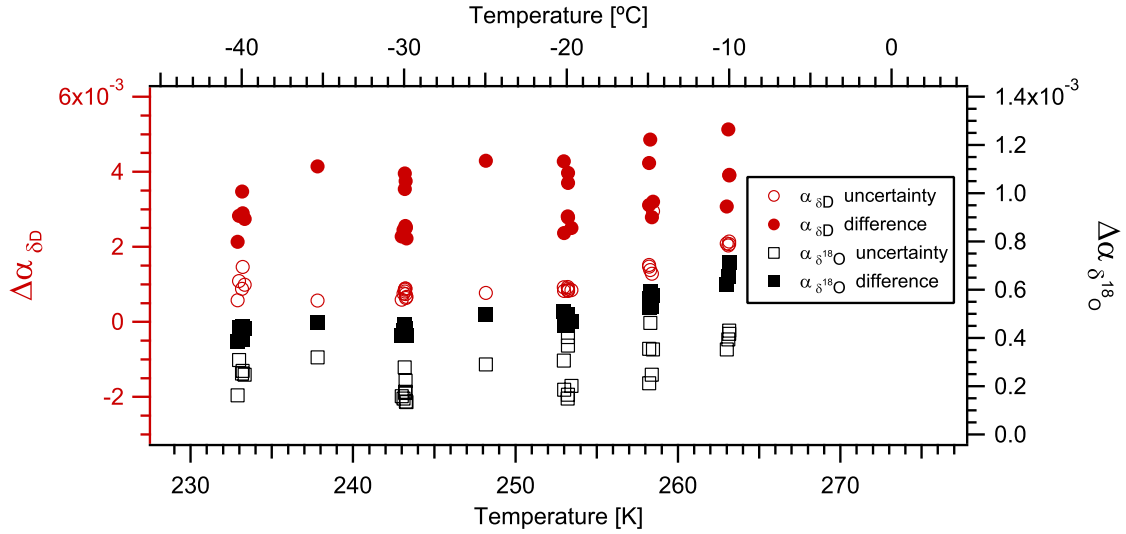


Figure 5.1: The difference ( $\Delta\alpha$ ) for  $\delta\text{D}$  and  $\delta^{18}\text{O}$  between  $\alpha$  with  $\delta_{v0}$  based on the average vapor measurements and  $\alpha$  with  $\delta_{v0}$  based on the Rayleigh model.

0.002 and 0.004 for  $\delta\text{D}$  and between 0.0004 and 0.0007 for  $\delta^{18}\text{O}$ . The larger variation in data points for  $\delta\text{D}$  is because of the higher slope of the Rayleigh curve as seen on e.g. Figure 4.6. The difference is also seen to become smaller for lower equilibrium chamber temperatures. Compared to the uncertainties of  $\alpha$  with  $\delta_{v0}$  based on average values of the vapor measurements the difference between the two scenarios is slightly larger but of the same magnitude as the uncertainties of the measurements. In section 4.1.4 it was shown that the Rayleigh curves fitted the observed vapor data very well considering the assumptions. Nevertheless, to limit the assumptions (and the uncertainties of these) behind our final  $\alpha$  results we will therefore base  $\delta_{v0}$  in the calculations of  $\alpha$  on the average values of the vapor measurements being  $\delta\text{D} = -154.6\text{‰} \pm 0.2\text{‰}$  and  $\delta^{18}\text{O} = -19.99\text{‰} \pm 0.05\text{‰}$  for MQ1 and  $\delta\text{D} = -157.2\text{‰} \pm 0.2\text{‰}$  and  $\delta^{18}\text{O} = -20.49\text{‰} \pm 0.05\text{‰}$  for MQ2. With this we will neglect the enrichment of the vapor source with time since this is close to the measurement uncertainty.

### 5.2.2 The impact of surface cooling on $\alpha$

We will now investigate the impact of a changed temperature and humidity in the calculations of  $\alpha$ . The temperature and partial pressure of the  $\text{H}_2\text{O}$  in the vapor source enters the calculation for  $\alpha$  as a part of  $g$  which also depends on the pressure and temperature and  $\text{H}_2\text{O}$  partial pressure of the equilibrium chamber. As stated above uncertainties in  $g$  are important for the calculations of the fractionation factor.

Figure 5.2 shows the residual ( $\Delta$ ) in  $\alpha$  between  $T_w = 1.41^\circ\text{C} \pm 0.02^\circ\text{C}$  and  $h=100\%$  and  $T_w = 1.0^\circ\text{C} \pm 0.2^\circ\text{C}$  and  $h=99.15\%$  as a function of the equilibrium chamber temperature. In these calculations,  $\alpha$  has  $\delta_{v0}$  based on the vapor measurements (as discussed above). The

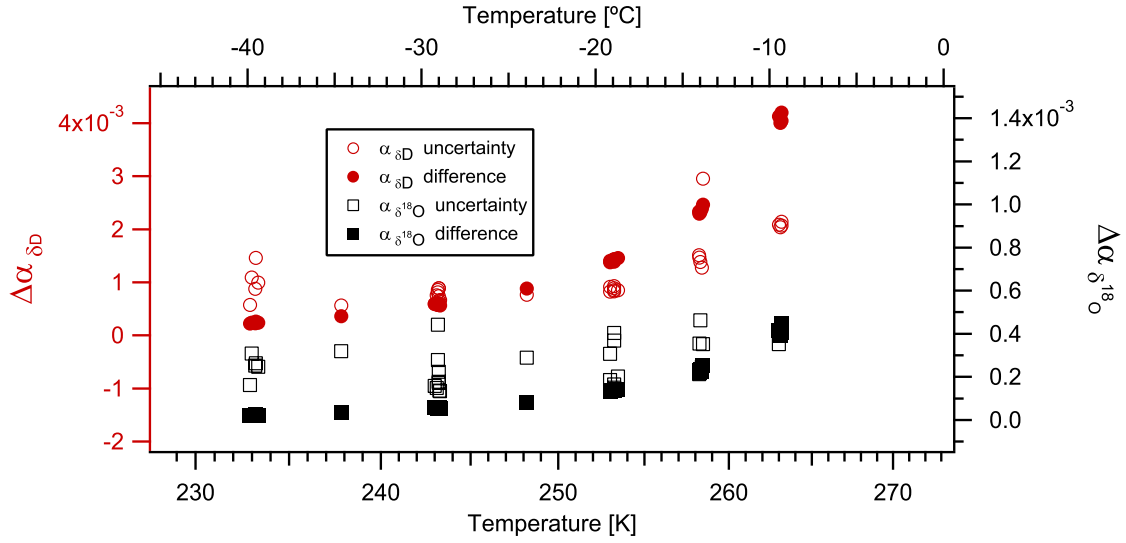


Figure 5.2: The difference ( $\Delta\alpha$ ) for  $\delta D$  and  $\delta^{18}O$  between  $\alpha$  with  $\delta_{v0}$  based on the average vapor measurements and  $\alpha$  with  $\delta_{v0}$  based on conditions with a surface cooling effect of  $0.41^\circ C$ .

difference due to changed temperature and humidity is then compared with the uncertainty for  $\alpha$  with  $T_w = 1.41^\circ C \pm 0.02^\circ C$  and  $h=100\%$ . The difference in temperature and pressure for these two cases gives a difference in  $g$  of 3.75%. The figure shows that the values with surface cooling as expected generally produce a smaller  $\alpha$ . The difference between these two scenarios are of the order of 0.004 for  $\delta D$  at  $-10^\circ C$  in the equilibrium chamber. The difference decreases with decreasing equilibrium chamber temperatures and is below 0.001 for  $\delta D$  at  $-25^\circ C$ . For  $\delta^{18}O$  the difference is around 0.0004 at  $-10^\circ C$  and quickly decreases here as well. Compared with the uncertainty of  $\alpha$  it can be seen that the difference between the two scenarios are only larger for equilibrium temperatures higher than  $-10^\circ C$ . This pattern is mostly pronounced for  $\delta D$  since the uncertainty for  $\delta^{18}O$   $\alpha$  is usually higher than the difference between  $\alpha$  of the two scenarios. Investigations of  $g$  where only the humidity is changed with a temperature of  $1.41^\circ C$  in the vapor source shows that the changes here are slightly smaller and that the above conclusion is the same.

Since the surface cooling, if present, will only change the measured  $\alpha$  significantly for temperatures above  $-10^\circ C$  we will neglect this in the calculations of the fractionation factor. To summarize, our dataset will therefore have  $\alpha$  based directly on the vapor measurements of the vapor in the vapor source at an average temperature of  $1.41^\circ C$  with the assumption of equilibrium there. However, we will still compare the results of  $\alpha$  from this with the dataset obtained with the possible surface cooling effect.

$\alpha_{\delta^{18}O}$	$\alpha_{\delta^{18}O}error$	$\alpha_{\delta D}$	$\alpha_{\delta D}error$	T [K]	T $\sigma$
1.0165	0.0003	1.212	0.008	253.0	0.1
1.0213	0.0003	1.215	0.008	253.1	0.1
1.0178	0.0003	1.213	0.008	253.2	0.1
1.0179	0.0003	1.189	0.008	257.9	0.1
1.0170	0.0003	1.190	0.008	258.0	0.2
1.0167	0.0003	1.190	0.008	258.1	0.2
1.0177	0.0004	1.191	0.008	258.2	0.1
1.0167	0.0004	1.175	0.009	262.8	0.2
1.0173	0.0004	1.168	0.009	263.0	0.1
1.0165	0.0004	1.167	0.009	263.0	0.2
1.0154	0.0004	1.169	0.009	263.0	0.2
1.0179	0.0004	1.175	0.009	263.2	0.2
1.0148	0.0004	1.166	0.009	263.2	0.1
1.0167	0.0004	1.160	0.009	263.2	0.1
1.0161	0.0004	1.167	0.009	263.2	0.1
1.0161	0.0004	1.172	0.009	263.2	0.1
1.0166	0.0005	1.175	0.009	263.2	0.1
1.0162	0.0006	1.162	0.012	268.0	0.1
1.0159	0.0007	1.156	0.013	268.4	0.2
1.0149	0.0003	1.202	0.008	253.0	0.1
1.0146	0.0003	1.203	0.008	253.2	0.2
1.0171	0.0004	1.172	0.009	262.9	0.1
1.0123	0.0005	1.127	0.012	268.0	0.2
1.0205	0.0008	1.203	0.014	268.4	0.2
1.0136	0.0006	1.135	0.013	268.4	0.2

Table 5.3: Equilibrium fractionation factor  $\alpha$  results from the Picarro measurements. Data points flagged as bad are shown below the line.

### 5.3 Presentation of the final dataset

From the discussion above, the data in Tables 3.7 and 3.3 and equation (5.1.1) we now have final datasets with  $\alpha$  as a function of temperature. These datasets need to be sorted since some fraction of the measurements can be flagged as bad and should not be considered in the final evaluation. The bad data points are either measurements that use a different configuration (such as different flow, no outlet tube etc.) or measurements where the isotopic values were not stable due to memory effects or due to ice crystals growing rapidly on the sides of the equilibrium chamber. For the Picarro measurements, most of the bad data points are measurement runs with trending water isotope values due to tests with e.g. tube heaters or due to possible supersaturated water in the equilibrium chamber.

The Picarro data can be seen in Table 5.3 and the IRMS data in Table 5.4. The tables show the data points flagged as bad below the line. Figures 5.3 and 5.4 shows all data points for  $\delta D$  and  $\delta^{18}O$  respectively. Here the corrected Picarro data as well as the vapor

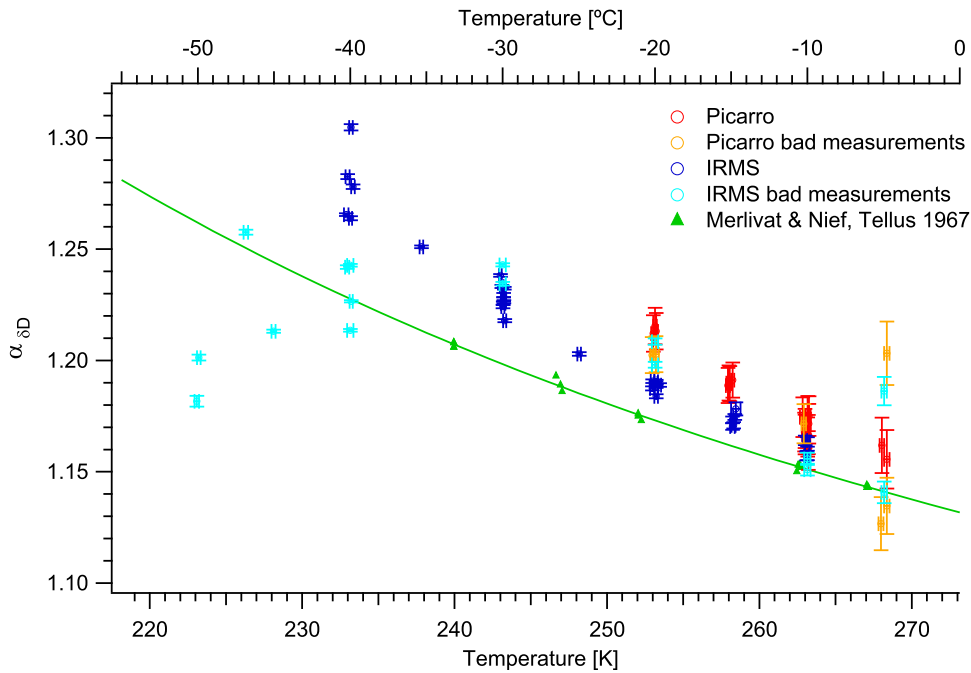


Figure 5.3: Equilibrium fractionation factor  $\alpha$  results for  $\delta D$ . All data for Picarro and IRMS measurements are shown.

IRMS data are used as discussed above. For comparison the data from Merlivat and Nief (1967) and Majoube (1970) are also shown. The data points for the bad measurements are also shown. For the Picarro data we can see that we have bad data points for all measured temperatures with several for the  $-5^{\circ}\text{C}$  runs, most likely due to supercooled water and the high vapor pressure at this temperature. For the IRMS data there are more bad data points simply due to the larger amount of measurements here. Especially at low temperatures we can see that most bad data points are clear outliers with lower values of  $\alpha$  supporting the fact that the observed ice crystals had an effect on the isotope values. The removal of the bad data points limits our measurements to the temperature range between  $-5^{\circ}\text{C}$  and  $-40^{\circ}\text{C}$  but leaves the dataset with more clear temperature dependency.

For  $\delta^{18}\text{O}$  we can see that both Picarro and IRMS data are a little lower but close to the shown data and fit from Majoube (1970) for temperatures between  $-5^{\circ}\text{C}$  and  $-20^{\circ}\text{C}$ . For temperatures of  $-30^{\circ}\text{C}$  and  $-40^{\circ}\text{C}$  a higher fractionation factor is indicated. The deviation of the data points seem to become larger with lower temperatures as discussed before. The two single data points for  $-25^{\circ}\text{C}$  and  $-35^{\circ}\text{C}$  can be seen to fit well with the overall trend of the data. The difference between the Picarro and the IRMS data points for  $\delta D$  was discussed earlier and it is also seen here. Both IRMS and Picarro datasets seem to follow the same clear trend which has a higher slope than the shown data from Merlivat and Nief (1967), with the Picarro data being slightly superposed compared to the IRMS data. This agrees very well with argument that the differences between the two dataset

T [K]	T $\sigma$	$\alpha_{\delta^{18}O}$	$\alpha_{\delta^{18}O}error$	$\delta^{18}O$ $n$	$\alpha_{\delta D}$	$\alpha_{\delta D}error$	$\delta D$ $n$
232.9	0.2	1.0239	0.0002	6	1.266	0.001	5
233.0	0.1	1.0252	0.0003	5	1.283	0.001	5
233.2	0.1	1.0230	0.0003	9	1.264	0.001	6
233.2	0.1	1.0275	0.0003	6	1.305	0.001	7
233.3	0.1	1.0246	0.0002	5	1.278	0.001	4
237.8	0.1	1.0232	0.0003	9	1.251	0.001	6
243.0	0.1	1.0231	0.0002	7	1.238	0.001	5
243.1	0.1	1.0223	0.0001	5	1.233	0.001	5
243.2	0.1	1.0212	0.0003	8	1.224	0.001	6
243.2	0.1	1.0220	0.0004	5	1.226	0.001	5
243.2	0.1	1.0220	0.0002	6	1.229	0.001	8
243.2	0.1	1.0219	0.0002	7	1.227	0.001	7
243.2	0.1	1.0218	0.0002	6	1.226	0.001	7
243.3	0.1	1.0226	0.0001	7	1.232	0.001	14
243.3	0.1	1.0209	0.0001	10	1.218	0.001	5
248.2	0.1	1.0189	0.0003	5	1.203	0.001	9
253.0	0.1	1.0180	0.0003	6	1.188	0.001	6
253.0	0.1	1.0183	0.0002	11	1.191	0.001	5
253.2	0.1	1.0187	0.0001	7	1.190	0.001	10
253.2	0.1	1.0183	0.0004	6	1.188	0.001	8
253.2	0.1	1.0185	0.0002	9	1.184	0.001	10
253.2	0.1	1.0190	0.0004	8	1.190	0.001	6
253.4	0.1	1.0181	0.0002	10	1.189	0.001	7
258.2	0.1	1.0171	0.0002	7	1.173	0.002	15
258.2	0.1	1.0163	0.0004	5	1.170	0.001	10
258.3	0.1	1.0171	0.0005	7	1.171	0.001	6
258.4	0.1	1.0165	0.0002	9	1.175	0.001	6
258.5	0.3	1.0181	0.0004	10	1.178	0.003	8
263.0	0.1	1.0164	0.0004	12	1.164	0.002	10
263.1	0.1	1.0153	0.0004	6	1.157	0.002	6
263.2	0.1	1.0174	0.0004	9	1.163	0.002	5
263.2	0.1	1.0158	0.0004	6	1.157	0.002	7
232.9	0.1	1.0218	0.0001	5	1.242	0.001	4
226.3	0.1	1.0271	0.0004	8	1.258	0.001	7
223.2	0.1	1.0200	0.0004	3	1.201	0.001	5
228.1	0.1	1.0222	0.0004	5	1.213	0.001	5
233.2	0.1	1.0207	0.0002	4	1.227	0.001	3
233.4	0.2	1.0202	0.0003	7	1.233	0.001	5
223.1	0.1	1.0175	0.0010	5	1.182	0.002	3

Table 5.4: Equilibrium fractionation factor  $\alpha$  results from the IRMS measurements. Data points flagged as bad are shown below the line.  $n$  is the amount of samples.

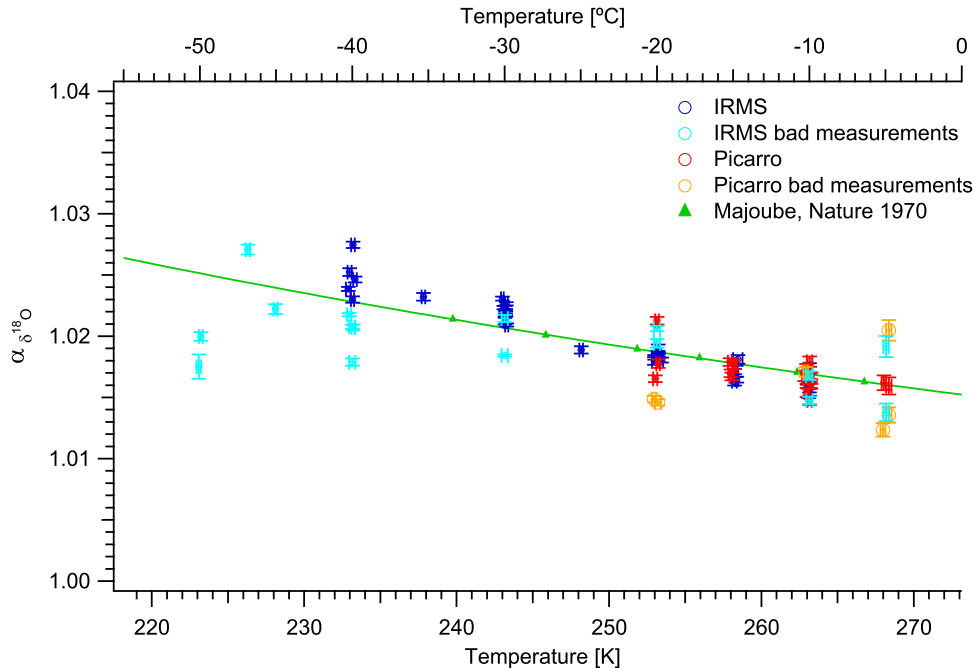


Figure 5.4: Equilibrium fractionation factor  $\alpha$  results for  $\delta^{18}\text{O}$ . All data for Picarro and IRMS measurements are shown.

are caused by the calibration for the  $\delta\text{D}$  Picarro data. It has to be noted that the small correction made on the Picarro data only corrected the data properly for values from the vapor source measurements. Therefore, the  $\delta\text{D}$  Picarro data are still off for equilibrium chamber measurements.

## 5.4 Fitting the data and comparison with theory

With the final dataset we will now investigate the observed temperature dependencies of the data. As described in section 1.2.2 theory predicts a dependency of  $\ln \alpha$  of  $T^{-2}$  or  $T^{-1}$  with  $\alpha$  approaching unity with infinite temperatures. However, as also described the introduction of a constant  $C_1$  as well as a combined function of  $T^{-1}$  and  $T^{-2}$  have been discussed. For the fitting we only use the IRMS data points due to the limitations of the Picarro data. We use all but the single data points for  $-25^\circ\text{C}$  and  $-35^\circ\text{C}$  and perform the fitting with errors in  $T$  and  $\alpha$ . For the following figures we present  $\ln \alpha$  for  $\delta\text{D}$  and  $\delta^{18}\text{O}$  as a function of  $T^{-1}$ ,  $T^{-2}$  or the combination of the two. All data points are shown (black for  $\delta\text{D}$  and red for  $\delta^{18}\text{O}$ ) along with the averages for each temperature (blue) as seen on Table 5.6. The average Picarro data are also shown (grey) along with the data of Majoube (1970) and Merlivat and Nief (1967) (green) for comparison for  $\delta^{18}\text{O}$  and  $\delta\text{D}$  respectively. The vertical dashed line indicate  $0^\circ\text{C}$ . Two different fits are shown; the full lines are based on the shown data and the dashed lines are based on data with the possible surface cooling

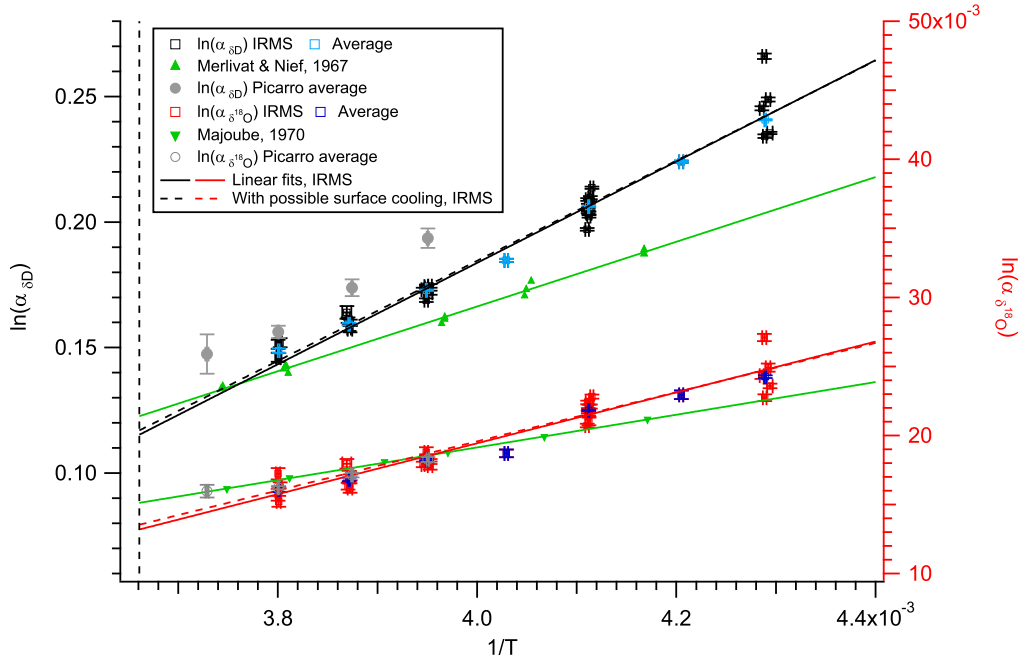


Figure 5.5:  $\ln \alpha$  for  $\delta D$  and  $\delta^{18}O$  as a function of  $T^{-1}$ , fitted with  $\ln \alpha = C_1 + C_2/T$ . The dashed line indicate  $0^\circ C$ . The fitting result can be seen in Table 5.5.

(with  $T_w=1.0^\circ C$  and  $h=0.99$  in the vapor source as discussed above).

Figure 5.5 shows  $\ln \alpha$  for  $\delta D$  and  $\delta^{18}O$  as a function of  $T^{-1}$ . In this case the data of Merlivat and Nief (1967) has been fitted with the linear regression routine and the data of Majoube (1970) is shown with the fit obtained in the article. The fit values for all fits can be seen in Table 5.5 and it can be seen that the data cannot be fitted with  $C_1=0$ . The intersection with  $0^\circ C$  is at  $\alpha = 1.1222$  for  $\delta D$  and  $\alpha = 1.0133$  for  $\delta^{18}O$ . Overall the  $T^{-1}$  dependency performs quite well for both  $\delta D$  and  $\delta^{18}O$ . The fit is very close to the observed average values in most cases. However, for temperatures of  $-10^\circ C$  there is some curvature in the data that is not captured that well by the fit, especially for  $\delta D$ . This curvature is also seen in the Picarro data which is superposed for  $\delta D$  (as discussed) and fit quite well for  $\delta^{18}O$ . The dashed lines show the fits based on the data with surface cooling values. Here we can see the possible impact on  $\alpha$  for temperatures higher than  $-10^\circ C$  as the fit has a slightly different slope and intersect. Compared to the data of Merlivat and Nief (1967),  $\ln \alpha$  for  $\delta D$  can be seen to have a significantly higher slope as discussed above and with this fit  $\ln \alpha$  has smaller values for temperatures between  $0^\circ C$  and around  $-7^\circ C$ . Comparing the  $\delta^{18}O$  fit to Majoube (1970), this fit type gives a different slope and the two fits cross around  $-20^\circ C$ . To summarize, the fit captures the temperature dependency of the data well to a first order but at higher temperatures there is some curvature that is not captured.

Figure 5.6 shows  $\ln \alpha$  for  $\delta D$  and  $\delta^{18}O$  as a function of  $T^{-2}$ . In this case the data of

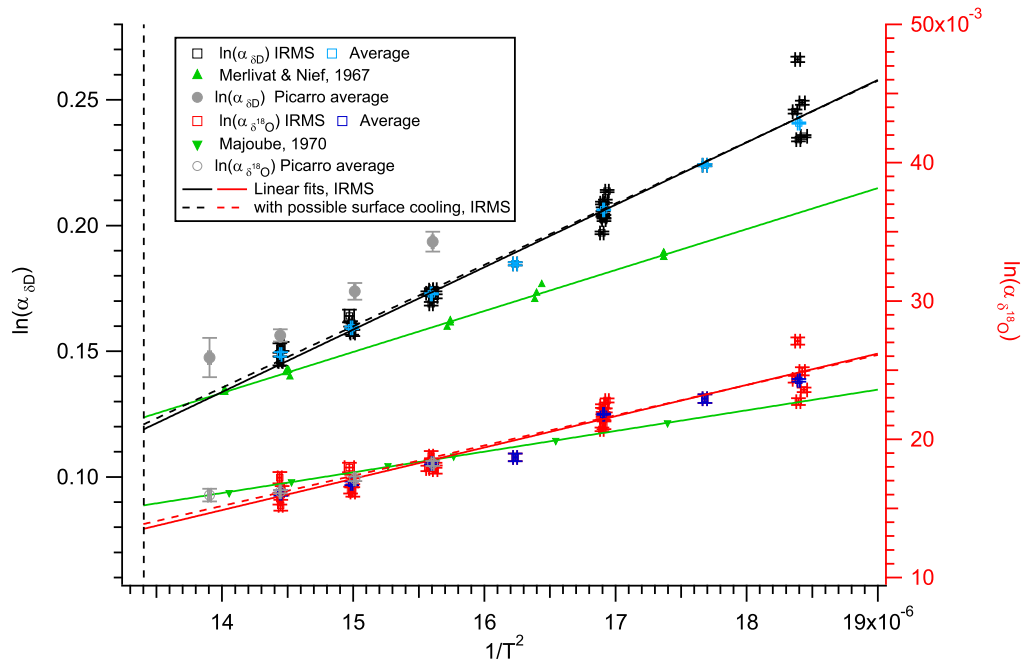


Figure 5.6:  $\ln \alpha$  for  $\delta D$  and  $\delta^{18}O$  as a function of  $T^{-2}$ , fitted with  $\ln \alpha = C_1 + C_3/T^2$ . The dashed line indicate  $0^\circ C$ . The fitting result can be seen in Table 5.5.

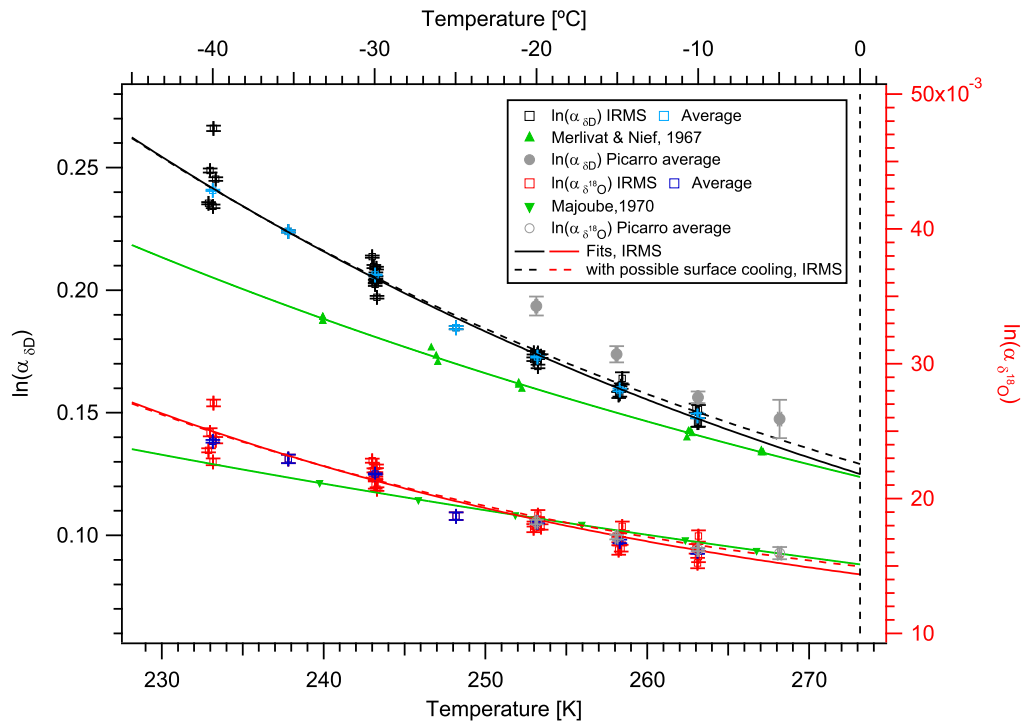


Figure 5.7:  $\ln \alpha$  for  $\delta D$  and  $\delta^{18}O$  as a function of  $T$ , fitted with  $\ln \alpha = C_1 + C_2/T + C_3/T^2$ . The dashed line indicate  $0^\circ C$ . The fitting result can be seen in Table 5.5.

	$\delta\text{D}$		
	$C_1$	$C_2$	$C_3$
$\ln(\alpha) = C_1 + \frac{C_2}{T}$	$-0.6238 \pm 0.0049$	$201.88 \pm 1.21$	
$\ln(\alpha) = C_1 + \frac{C_3}{T^2}$	$-0.2137 \pm 0.0025$		$24820 \pm 150$
$\ln(\alpha) = C_1 + \frac{C_2}{T} + \frac{C_3}{T^2}$	$0.2133 \pm 0.0116$	$-203.10 \pm 5.42$	$48888 \pm 668$
	$\delta^{18}\text{O}$		
	$C_1$	$C_2$	$C_3$
$\ln(\alpha) = C_1 + \frac{C_2}{T}$	$-0.0542 \pm 0.0012$	$18.414 \pm 0.294$	
$\ln(\alpha) = C_1 + \frac{C_3}{T^2}$	$-0.0168 \pm 0.0006$		$2263.4 \pm 36.2$
$\ln(\alpha) = C_1 + \frac{C_2}{T} + \frac{C_3}{T^2}$	$0.0831 \pm 0.0087$	$-49.192 \pm 4.280$	$8312.5 \pm 529.0$

Table 5.5: Fitting results for the three different temperature dependencies.

Majoube (1970) has been fitted with the linear regression routine and the data of Merlivat and Nief (1967) is shown with the fit obtained in the article. Here the  $T^{-2}$  dependency also performs quite well. The fit captures the curvature seen for higher temperatures in a slightly better way and still performs as the previous fit for lower temperatures. Since this type of fit captures the curvature better the fit intersects with  $0^\circ\text{C}$  for higher values of  $\alpha$ , being 1.1263 for  $\delta\text{D}$  and 1.0136 for  $\delta^{18}\text{O}$ . Comparing this fit to the surface cooling version and to the results of Majoube (1970) for  $\delta^{18}\text{O}$  and Merlivat and Nief (1967) for  $\delta\text{D}$  the results are similar to the above. Furthermore we see that it is not possible to fit these data with  $C_1=0$ .

Figure 5.7 shows  $\ln \alpha$  for  $\delta\text{D}$  and  $\delta^{18}\text{O}$  as a function of a combination of  $T^{-1}$  and  $T^{-2}$ , this time with  $T$  on the x axis for clarity. For  $\delta\text{D}$  the fit performs well for low temperatures as well as the high temperatures. It captures the curvature better as the fit is closer to the average value of the  $-10^\circ\text{C}$  data and due to this the intersection with  $0^\circ\text{C}$  is a little higher than on the  $T^{-1}$  and  $T^{-2}$  fits. The surface cooling version shows the same patterns as above and give a higher value of  $\ln \alpha$ . Overall, the same is seen for  $\delta^{18}\text{O}$ . The fit performs well and captures the curvature of the data at high temperatures while it keeps the same performance for low temperatures. The result of this work can be seen having a very similar slope as Majoube (1970) for temperatures between  $0^\circ\text{C}$  and  $-10^\circ\text{C}$ . Here, the intersection with  $0^\circ\text{C}$  is  $\alpha=1.1331$  for  $\delta\text{D}$  and  $\alpha=1.0145$  for  $\delta^{18}\text{O}$ . Compared to the above values, this is closer to the values obtained by Merlivat and Nief (1967) and Majoube (1970).

Figure 5.8 shows the residual between the average values for each temperature and the fit values. The figure emphasizes the conclusions from the different fits above. We can see that the fit including the combination of the  $T^{-1}$  and  $T^{-2}$  dependencies better captures the data for the high temperature values whereas the difference between the different fit methods becomes smaller with decreasing temperature. It can also be seen that generally the fits perform best for  $\delta\text{D}$  and have some over- and underestimation for  $\delta^{18}\text{O}$ , compared

T	T error	$\alpha_{\delta D}$	$\alpha_{\delta D error}$	$\alpha_{\delta^{18}O}$	$\alpha_{\delta^{18}O error}$	$\alpha_{\delta D fit}$	$\alpha_{\delta^{18}O fit}$
233.15	0.05	1.2720	0.0004	1.02455	0.00010	1.2732	1.02535
237.82	0.12	1.2511	0.0006	1.02321	0.00032	1.2507	1.02350
243.18	0.04	1.2290	0.0002	1.02205	0.00006	1.2273	1.02160
248.18	0.11	1.2029	0.0008	1.01887	0.00029	1.2076	1.02005
253.21	0.04	1.1886	0.0003	1.01841	0.00008	1.1897	1.01865
258.30	0.06	1.1727	0.0007	1.01696	0.00013	1.1732	1.01739
263.10	0.07	1.1604	0.0010	1.01623	0.00020	1.1591	1.01635

Table 5.6: Weighted average values of the IRMS measurements as well as the values from the  $\ln \alpha = C_1 + C_2/T + C_3/T^2$  fit.

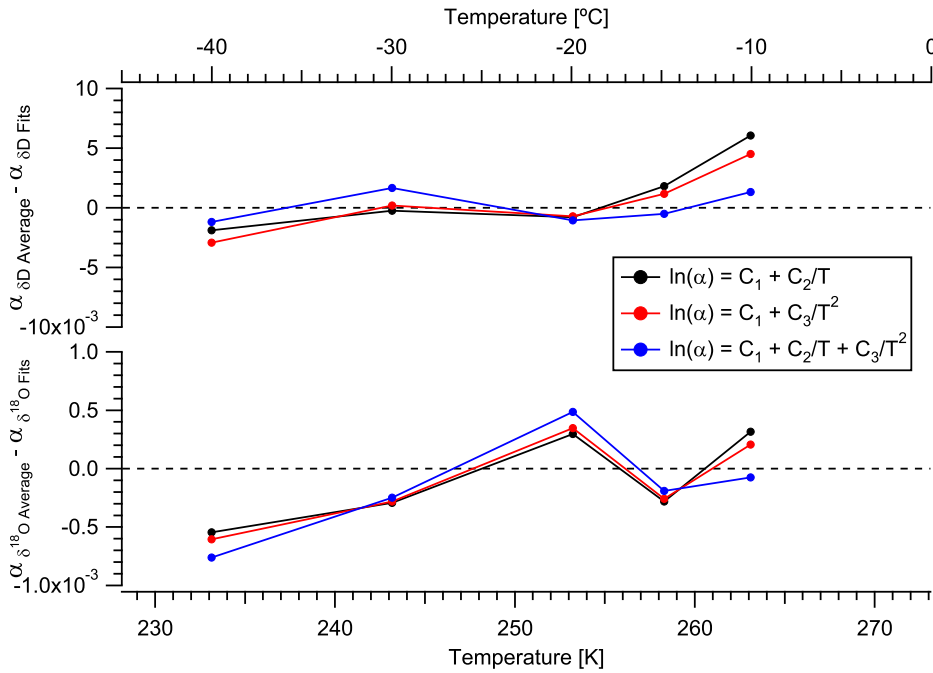


Figure 5.8: Residual between the average  $\alpha$  values and the different fit types, as seen in Table 5.6.

to the average values that this residual is based on. But as can be seen the magnitude of this is comparable to the uncertainty of the data points which is acceptable. The fits are generally driven by the points at  $-30^\circ\text{C}$ ,  $-20^\circ\text{C}$  and  $-10^\circ\text{C}$  where there are many points with relatively little scattering which is also indicated by the uncertainty on the average values on Table 5.6. It is clear that more data points especially for temperatures above  $-10^\circ\text{C}$  and below  $-30^\circ\text{C}$  would improve the fitting.

To summarize, the data in this work agree very well with the expected temperature dependency for equilibrium fractionation. All fit types ( $T^{-1}$ ,  $T^{-2}$  and the combination of  $T^{-1}$  and  $T^{-2}$ ) performs well within the uncertainties of the dataset. However, the curvature is best captured by the fit with  $\ln \alpha = C_1 + C_2/T + C_3/T^2$  which agree with the discussion for solid-vapor phase transition problems Van Hook (1968); Boato et al. (1962);

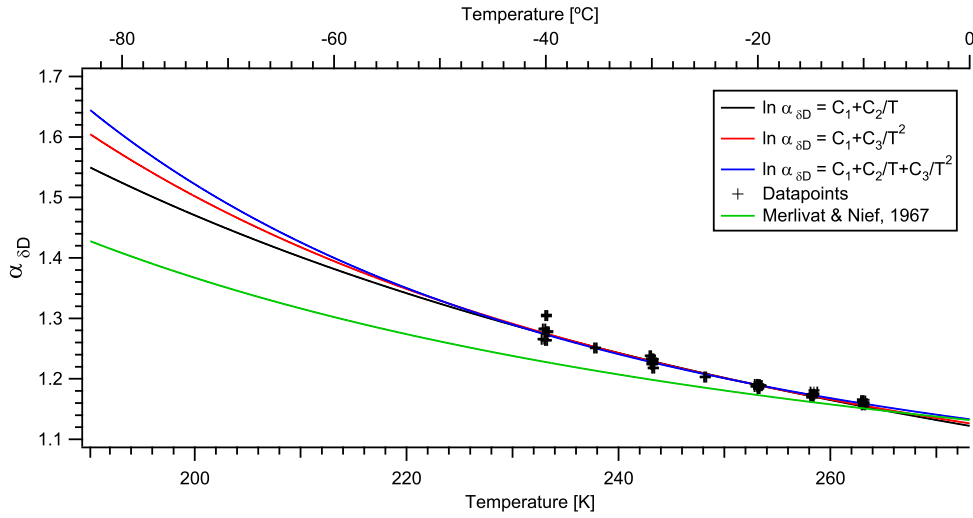


Figure 5.9: Comparison of the different fits and the previous published data for  $\delta D$  when extrapolating outside the measurement range.

Jancso and Van Hook (1974). In the following we will therefore use this fit to represent the results. The fit type and the magnitude of the constants in the  $\ln \alpha = C_1 + C_2/T + C_3/T^2$  approximation do give information about the system under consideration. This is outside the scope of this work and more discussion of this can be found in e.g. Szydlowski (1994) and Van Hook (1968).

It is important to emphasize that the fits are only valid within the temperature range of the measurements. This is illustrated on Figures 5.9 and 5.10 that shows the different fit types presented above along with extrapolated results from Merlivat and Nief (1967) for  $\delta D$  and Majoube (1970) for  $\delta^{18}O$ . For  $\delta D$  the different fit types begins to separate around  $-48^\circ C$  and at  $-80^\circ C$  there is a difference in  $\alpha$  of almost 0.1 between the  $T^{-1}$  fit and the fit based on the combination of  $T^{-1}$  and  $T^{-2}$ . For  $\delta^{18}O$  the fits separate even earlier and the difference in  $\alpha$  is around 0.01 at  $-80^\circ C$ . These differences are significant and would introduce a large uncertainty in the isotope values if used in a model.

## 5.5 Comparison with previous measurements and discussion

In Section 1.4 previous results were presented. Here, some discrepancies between the different results of  $\alpha$  for  $\delta D$  and  $\delta^{18}O$  was seen and most of the previous results have been based on vapor pressure isotope effect measurements or modeling. In this section we will compare our results to work shown in Figures 1.2 and 1.3 and discuss the differences.

Figures 5.11 and 5.12 shows the results of this work compared to the results presented in Section 1.4. As mentioned above, our results for  $\delta^{18}O$  are close to the points measured by Majoube (1970) for temperatures between  $-5^\circ C$  and  $-20^\circ C$ . For lower temperatures our

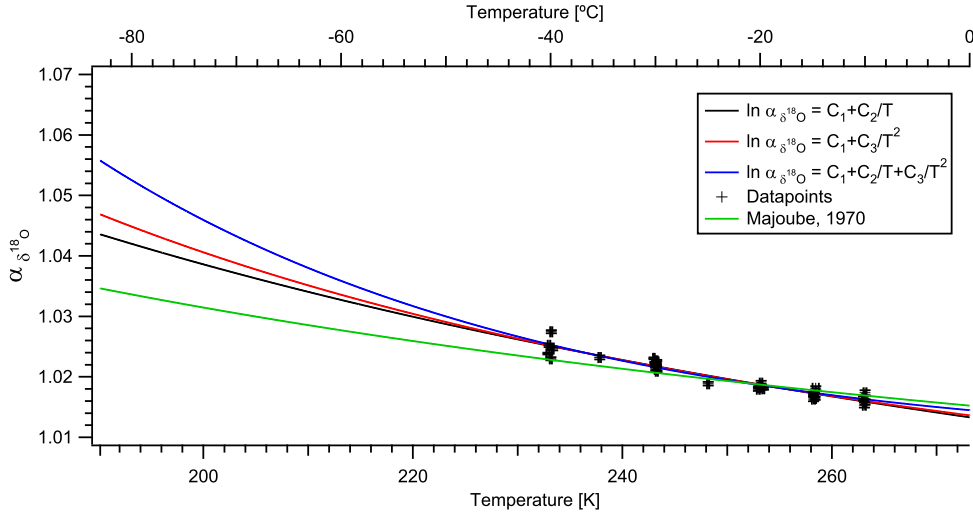


Figure 5.10: Comparison of the different fits and the previous published data for  $\delta^{18}\text{O}$  when extrapolating outside the measurement range.

results indicate a larger  $\alpha$  which causes the fit to have a higher slope here. For  $\delta\text{D}$  the same is seen to a certain degree. Here, our results agree somewhat with previous results for temperatures higher than  $-10^\circ\text{C}$  (neglecting the very large results by Pupezin et al. (1972)) but our result indicate a significantly larger  $\alpha$  for temperatures lower than  $-10^\circ\text{C}$ , again with a larger slope. At  $0^\circ\text{C}$  our results agree with previous results for both  $\delta\text{D}$  and  $\delta^{18}\text{O}$ . Still we have to keep in mind that we essentially extrapolate for temperatures higher than  $-10^\circ\text{C}$ , but e.g. the Picarro data for  $\delta^{18}\text{O}$  indicate that the fits are still valid here.

The differences between our work and the vapor pressure isotope effect work is expected since most of that work are based on different measurement techniques and modeling based on assumptions of the system under consideration. From this point of view our work should mainly be compared with the work of Majoube (1970) and Merlivat and Nief (1967) since these are the only other results obtained with a method similar to this. Here we can see that this work as well as the work of Majoube (1970) and Merlivat and Nief (1967) in general indicate larger fractionation factors for both  $\delta^{18}\text{O}$  and  $\delta\text{D}$  which could indicate that the vapor pressure isotope effect measurements and modeling works do not capture all details of the ice-vapor equilibrium system. On the other hand, it could also indicate that the the used method of obtaining isotopic equilibrium and measure the fractionation of the species with a mass spectrometer has limitations. Still, this seems unlikely since the vapor pressure measurements of pure samples require very high accuracy. Jakli and Staschewski (1977) argues that the difference between their results and the results by Majoube (1970) was due to the experimental technique. As in this work Majoube (1970) measures  $\alpha$  with an isotopically non-enriched sample using mass spectrometry whereas Jakli and Staschewski (1977) measures the vapor pressure of enriched samples directly and Jakli and Staschewski (1977) concludes that Majoube (1970) must have had experimental

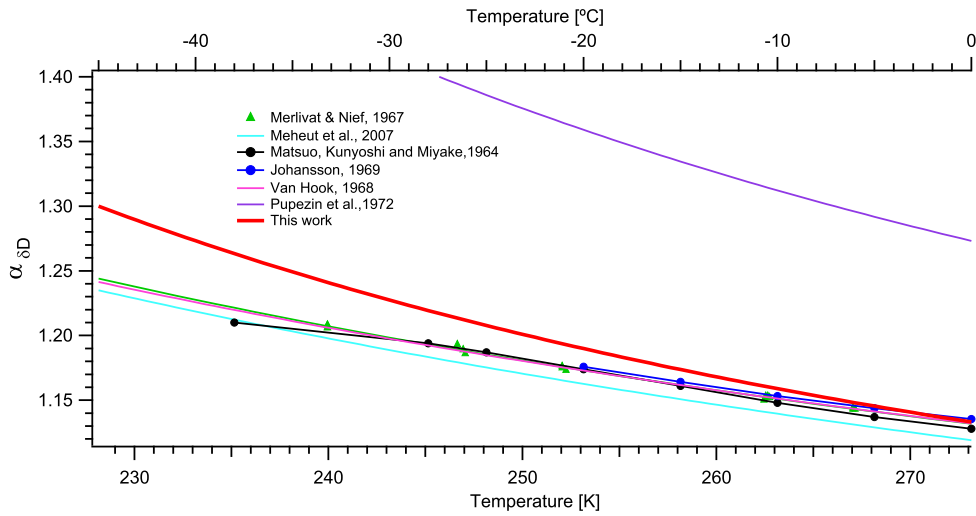


Figure 5.11:  $\alpha$  for  $\delta D$  for this work compared with previously published results.

difficulties in obtaining both physical and isotopic equilibrium at lower temperatures. This argument can also be made on the difference between the results of this work and previous results. As discussed in Chapter 3 we have strong evidence that the ice and the vapor in the equilibrium chamber is in equilibrium with stable isotope values and that the humidity was stable at the saturation level. In fact, we did observe the kinetic effects in the equilibrium chamber driven by supersaturation with a large amount of ice crystals. As discussed earlier this effect drives the isotopic values toward less depleted values since a larger fraction of the light isotopes condense out compared to the equilibrium condition and this effect would then lead to a smaller  $\alpha$  than intended. Thus, kinetic effects during condensation does not explain the larger  $\alpha$  obtained at lower temperatures in this work. In fact, if these kinetic effects were significant at higher temperatures as well this would indicate that our measured fractionation factors are too low.

One important thing to note is that even though our results are lower, we obtain values close to the values of Majoube (1970) for temperatures higher than  $-20^{\circ}\text{C}$  where the same measurements for  $\delta D$  show a significantly different slope and magnitude than Merlivat and Nief (1967). Thus, assuming that the measurements for  $\delta^{18}\text{O}$  are correct this could indicate some systematic errors for  $\delta D$ . As mentioned in Section 1.4 the works of Merlivat and Nief (1967) and Majoube (1970) were more or less based on the same experimental setup but they were still carried out with different measurement techniques with some years in between. Our results for  $\delta D$  and  $\delta^{18}\text{O}$  have been measured at the same time with the same instruments and this supports our results for  $\delta D$ .

In the following we will discuss possible errors in our system and the possible impacts they would have on the results. By characterizing the setup with the Picarro we can quickly rule out effects such as leaks, kinetic effects and adsorbed water in the tubing, a drifting

vapor source and non-stable isotope values in the equilibrium chamber. Furthermore, we know the temperature and pressure in both vapor source and equilibrium chamber with high detail. Those issues simply cannot be investigated properly without the Picarro and due to this we can make sure that we only perform measurements on a stable system.

In fact, the majority of the possible errors in the experimental setup would result in a smaller  $\alpha$ . Equation 1.3.8 is based on the fact that the temperature does not change during the condensation of ice in the equilibrium chamber. If the heat is not removed properly the relatively hot Helium and vapor that are injected into the equilibrium chamber will heat the glass walls and the ice there. This will lead to a smaller measured  $\alpha$  assuming equilibrium. This is also the case if diffusion effects are present in the exchange between the ice and the vapor as discussed above. Furthermore, as the ice crystal grows, the surface is also heated by the latent heat of sublimation. Super cooled water in the equilibrium chamber would also lower the observed  $\alpha$  since the equilibrium fractionation here is smaller (Merlivat and Nief, 1967; Majoube, 1971b). And leaks with vapor from ambient air mixing with the vapor from the equilibrium chamber would also show as less depleted values. As discussed in Chapter 3 the uncertainties of the calibrations are not large enough to cause the observed differences in  $\alpha$ . Condensation of a small amount of atmospheric vapor in the beginning of the process (after mounting the equilibrium chamber) described in Section 4.2 would also imply a lower  $\alpha$  since this condensate will be very enriched due to the very low relative humidity when flushing with carrier gas.

Only a few effects will cause a larger  $\alpha$  than intended in our system. As shown in the above figures, possible surface cooling can increase the observed  $\alpha$  due to wrong estimations of the temperature and pressure in the calculation for  $\alpha$ . We did investigate the performance of the vapor source with time and investigations of the surface cooling (see Section 4.1.5 and 5.2.2) did show that this is most likely not an issue and if this was present it would only have significance for temperatures larger than  $-10^{\circ}\text{C}$ .

Another effect that could cause more depleted ice/vapor in the equilibrium chamber could be Rayleigh distillation especially in the beginning of each experiment before much ice has condensed out. This would produce light condensates at the end of the distillation process in the case of limited exchange between the vapor and the condensate. There is essentially no homogenization of the isotopes in the condensate because of the low diffusivities of water molecules in ice. Then, if the following vapor also becomes depleted due to Rayleigh distillation or exchanges with the light ice this could lead to more depleted vapor exiting the equilibrium chamber, resulting in a larger  $\alpha$  than intended. This process could occur if the exchange is not large enough in the equilibrium chamber and the condensates are "removed" from the system. The design of the equilibrium chamber was made to account for this effect by heating all tubes, including the copper tube inside the equilibrium chamber. This only allows the vapor to condense out on the glass walls of the equilibrium

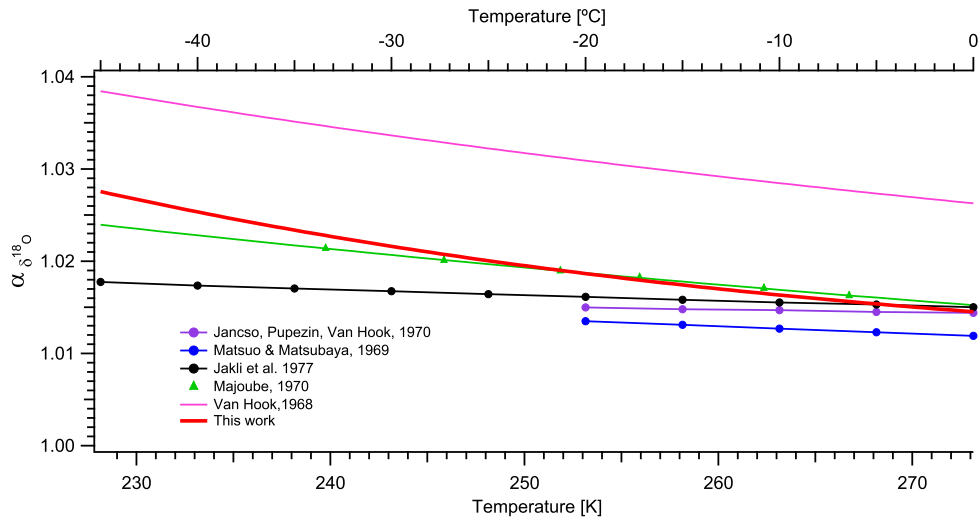


Figure 5.12:  $\alpha$  for  $\delta^{18}\text{O}$  for this work compared with previously published results.

chamber where the vapor due to the diffusion length is forced to exchange with the walls before it exits. The above effects would most likely be amplified for larger flow rates (due to less time to exchange) but the investigations of the equilibrium chamber in section 4.2 do not show any indications of this. Also, the transient occurring in the beginning of each experiment as well as the investigation of the system in equilibrium state behave as expected, and do not indicate exchange with depleted ice once the vapor pressure and isotope values have stabilized.

Finally, one could argue again that since the  $\delta^{18}\text{O}$  equilibrium fractionation factor from Majoube (1970) is close to our results at temperatures above  $-20^\circ\text{C}$ , this suggests that there are no major errors associated with the experiments. Of course this assumes that the results of Majoube (1970) are perfectly correct for these temperatures and that the differences at lower temperatures for  $\delta^{18}\text{O}$  and the differences for  $\delta\text{D}$  are due to limitations of the experimental setup used by Merlivat and Nief (1967) and Majoube (1970). As mentioned in Section 1.4, Merlivat and Nief (1967) and Majoube (1970) use vapor flow with diffusion as transport mechanism and therefore need to make some assumptions about their system in order to be able to find the fractionation factor  $\alpha$ . In the following we will investigate these to see if these can explain the observed differences.

### 5.5.1 The work of Merlivat and Nief (1967) and Majoube (1970)

Equation 4 in Merlivat and Nief (1967) is fundamental since it describes the isotopic composition (or gradient) in the diffusion tube as a function of distance between the temperature

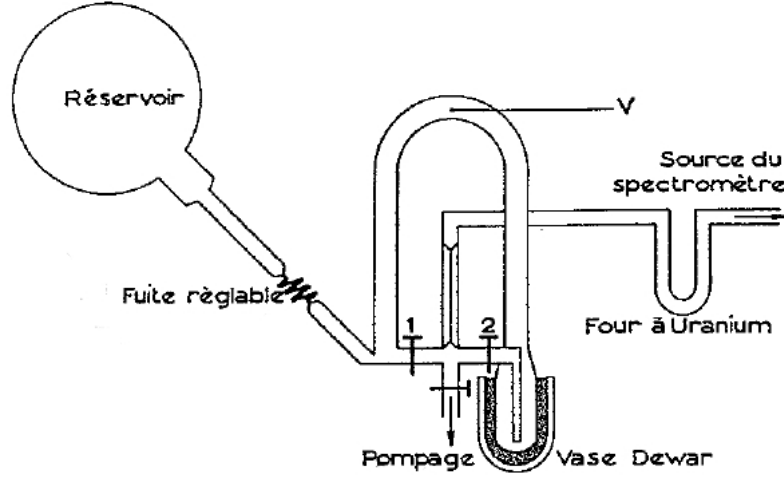


Figure 5.13: Figure 1 from Merlivat and Nief (1967) showing their experimental setup.

controlled dewar where the ice condensation takes place and their vapor source:

$$R_v - R_0 = R_0 \left( \frac{1}{\alpha} - 1 \right) \exp \left( \frac{-vx}{D} \right) \quad (5.5.1)$$

Here  $R_v$  is the isotope ratio of the vapor in equilibrium with the condensed ice,  $R_0$  is the isotope ratio of the initial vapor source,  $\alpha$  is the ice-vapor fractionation factor,  $v$  is the flow of the vapor,  $x$  is the distance between the vapor source and the condensation dewar and  $D$  is the diffusion coefficient of the vapor. To find equation (5.5.1) they have to assume that at the surface of the ice  $x = 0$  then  $R_v = R_0/\alpha$  (equilibrium) and at a large distance  $x \rightarrow \text{inf}$  then  $R_v = R_0$ . The different parts of their setup can be seen on Figure 5.13 that shows Figure 1 from Merlivat and Nief (1967). This is more or less identical to the setup of Majoube (1970) besides from the different measurement technique and the ability to measure with two capillaries here. Figure 5.13 shows that they measure the initial vapor  $R_0$  by opening valve number 1. If the distance  $x = l$  (the length of the diffusion tube) is large then  $R_v(x = l) \approx R_0$  and they can then find  $\alpha$ :

$$\alpha = R_v(x = l)/R_v(x = 0) \quad (5.5.2)$$

Thus if  $\epsilon$  is the measurement uncertainty, then for the expression to be correct, they will need:

$$\left( \frac{R_v(x = l) - R_0}{R_0} \right) \ll \epsilon \quad (5.5.3)$$

and hence

$$\left( \frac{1}{\alpha} - 1 \right) \exp \left( \frac{-vl}{D} \right) \ll \epsilon \quad (5.5.4)$$

Therefore,

$$\ln\left(\frac{1}{\alpha} - 1\right) - \frac{vl}{D} \ll \ln \epsilon \quad (5.5.5)$$

And this finally gives

$$\frac{-D}{l} \ln\left(\frac{\alpha\epsilon}{\alpha - 1}\right) \ll v \quad (5.5.6)$$

Equation (5.5.6) shows that if equation (5.5.2) to be true the vapor flow has to have a certain value depending on  $D$  and  $l$  and this approximation has weaknesses if the experiments are not carefully carried out. In the above equations  $D$  is assumed constant for the system at a certain temperature. But since  $D$  vary with temperature it will vary if the temperature of the system is not constant. Furthermore, in Merlivat and Nief (1967) it is not described how e.g. the diffusion tube is heated to prevent condensation before it reaches the dewar with the controlled temperature and in Majoube (1970) it is indicated that the setup is at room temperature (25°C). An uncontrolled backdiffusion effect would give a lower measured fractionation factor and the same would be seen with the vapor condensing out in equilibrium at higher temperatures. On the other hand, a Rayleigh distillation in the tube would have the opposite effect on the measured  $\alpha$  if there is no exchange between the first condensate and the remaining vapor but this is probably unlikely. The vapor flow from the vapor source is also assumed constant in the equations above and since it has direct influence on the backdiffusion effect, flow variations would alter the measured  $\alpha$ . According to Merlivat and Nief (1967) the flow is varied with an adjustable copper valve while Majoube (1970) describes it as a copper capillary. Merlivat and Nief (1967) states that the flow is of the order of a few centimeters per second while Majoube (1970) gives examples that show how the flow speed is increased for lower temperatures according to considerations along the line of equation (5.5.6). Additionally, Majoube (1970) measures the flow speed indirectly with the mass spectrometer by calculating the time it takes for the dewar to reach the saturation vapor pressure at a certain temperature while this is not mentioned in Merlivat and Nief (1967). Thus, the above could indicate differences in how the experiments were carried out. It is a good question how stable the flow is and the above methods suggest that some uncertainty in the flow rate could be found in their system. This could make some of the above assumptions invalid if the backdiffusion effect is large enough to impact the measurements of the initial vapor. An undiscussed element in both articles is the isotopic stability of the vapor source during the measurements. And although it is thoroughly discussed in both articles another issue could be the sample collection from their dewar since they essentially remove vapor from a system in equilibrium. Here Majoube (1970) does mention that the measurement uncertainty depends on the placement of the tube that leads to the mass spectrometer.

Backdiffusion and vapor flow issues are generally not present in our system since we use continuous flow with a carrier gas (which is accurately measured and characterized). We

are also able to measure the vapor from the vapor source directly without it being subject to backdiffusion effects from the equilibrium chamber. Furthermore we are able to see the transients in the isotope values as they occur while Majoube (1970) and Merlivat and Nief (1967) have to trust their calculations and assumptions about the system.

Still, one could argue that even though we have strong evidence that the system is in equilibrium there might be some ice physics effects e.g. related to the crystal size of the condensates or perhaps a thin liquid film on the ice grain boundary which might interfere with the "true" equilibrium. If significant, these effects would also influence the work of Majoube (1970) and Merlivat and Nief (1967) and essentially the results presented here would then be "effective equilibrium fractionation factors" since these effects would also be present in nature. Of course, this system is difficult to model which could be one reason for the use of constants in the theory for the temperature dependency and could explain the offset between this work and the work of Majoube (1970) and Merlivat and Nief (1967) when compared to other results.

### 5.5.2 Summary of this section

To summarize this section, we obtain fractionation factors with a temperature dependency in accordance with theory. There are some differences between this work and previous work. We obtain significantly larger fractionation factors for  $\delta D$  while for  $\delta^{18}O$  this is only seen for temperatures below  $-20^{\circ}C$ . For temperatures higher than this our results for  $\delta^{18}O$  are lower but close to the work of Majoube (1970). This supports the theory that the differences between this work and the work by Merlivat and Nief (1967) and Majoube (1970) could be due to backdiffusion effects in their system which might happen to be more pronounced for the results on  $\delta D$  of Merlivat and Nief (1967), maybe due to limited vapor flow control. Most errors in our experimental setup would reduce the fractionation factor and the errors increasing it do not seem likely to occur. Furthermore, we have evidence from the Picarro continuous measurements that the experimental setup obtains equilibrium between ice and vapor, and this supports our results. Besides from the memory effects and long sampling time, the main issue for our experimental setup is kinetic effects occurring for temperatures below  $-40^{\circ}C$ . These effects could be present for lower temperatures (but not as significant), also indicating higher fractionation factors than measured here.

## 5.6 Experimental setup performance and improvements

The experimental setup went through some iterations before the right performance was achieved. In the following we will discuss this performance and possible improvements of the experimental setup and the measurement routines.

### 5.6.1 Setup

The vapor source generally performed as needed but of course more accurate temperature stabilization and more active mixing could improve the output. Again, more accurate measurements of the mass balance of the vapor source and the isotope values of the water and the vapor would improve the knowledge of the vapor entering the equilibrium chamber. This could be done with more frequent measurements of the water as well as vapor collection before and after each measurement run for later measurements. Additionally, with more accurate temperature measurements inside the vapor source cylinder we could investigate possible surface cooling in a better way. Alternatively, a commercial unit could perform better under the right circumstances but of course, this also has limitations. Generally the cryofocus also proved to work as intended and the main peak tailing most likely originated from dead volume in the TC/EA. But the design was not optimal in some ways. Due to the instant heating and to avoid currents in the setup it was made of glass. This needed Kovar ends to be properly connected to the Swagelok fittings while heated. This design was fragile. An improvement here could be a U shaped glass form with no bending at the ends. Furthermore improving the way the heaters are connected could minimize the dead space in the cryofocus. Alternatively, using stainless steel tubing with another heating method could also have been an option.

The equilibrium chamber proved to have limitations below  $-40^{\circ}\text{C}$  but for temperatures up to  $-5^{\circ}\text{C}$  it performed quite well. Improvements to this could be e.g. addition of condensation nuclei on the sides for easier condensation. Increasing the exchange and thus limiting the kinetic effects could be done by lowering the flow rate and maybe increase the volume slightly although this increases the measurement time considerably. This could also allow for better measurements for temperatures higher than  $-10^{\circ}\text{C}$  that would help constrain the fits better. Besides from the presence of kinetic effects the vapor sampling time at low temperatures effectively made a limit for measurements here due to the memory effects. Another way to investigate the equilibrium in the equilibrium chamber and to support the vapor data would have been to measure the isotopic composition of the ice that forms in the equilibrium chamber. However, this was not done for two reasons. First, due to the design of the equilibrium chamber it was hard to get the ice out without heating it, thus creating phase transitions and thereby inducing fractionation effects. Second, since only a small fraction of the initial vapor entering the equilibrium chamber exits it, the ice formed inside the equilibrium chamber will have an isotopic composition very close to the one of the initial vapor. To measure this would require high accuracy and this will also be affected by the possible fractionation effects due to phase transitions.

The above raises the main issue with the experiments which might just be the total time of the measurement routine. Depending on the sampling temperature and the performance of the instruments it generally took one full day of actively performing measurements to

obtain enough stable values from the sample vapor with the following VSMOW calibrations. With this, the equilibrium chamber usually equilibrated during the night and the measurements started the morning after. Thus, including testing and modifying the experimental setup, each data point on the shown graphs represent several working days and these quickly add up. It is hard to optimize the direct sampling and measurement technique used with e.g. pneumatic or electrical actuators since the standard injections for example still need to be injected by hand. A more autonomous sampling technique could have been advantageous. An idea for this could be to collect the vapor in a vial with liquid nitrogen for later measurements with the autosampler on the TC/EA - IRMS system. This would also allow for transferring of the samples for measurements on other instruments, e.g. for  $^{17}\text{O}$  investigations. Still, the vapor pressure is the main factor dictating the collection time and a changed collection method does not change this. The method used by Merlivat and Nief (1967) and Majoube (1970) also faced difficulties at lower temperatures due to the low vapor pressure, so using a similar method to this does not necessarily improve much. As will be mentioned below the laser based techniques might solve these problems.

### 5.6.2 Instrumentation

By using both Picarro and IRMS instruments for the characterization and measurements we were able to use the advantages of both techniques. The Picarro proved very valuable in the characterization of the system due to the ability of continuous monitoring the isotopes, but this technique had limitations for the actual measurements at low vapor pressures. The IRMS system on the other hand was handicapped in the characterization of the system due to the discrete measurements but this was the advantage for the measurements since we could just increase the sampling time.

To avoid the introduced uncertainty of having two different carrier gases, it would have been an advantage with the use of Helium as a carrier gas with the Picarro. With this, we could have tested the cryofocusing of the samples with the same configuration for both IRMS and Picarro instruments. Unfortunately this was not possible. Since the diffusion length of  $\text{H}_2\text{O}$  in Helium is larger than in Nitrogen this should not be a problem and the Picarro and IRMS vapor source and equilibrium chamber measurements proved to be very similar, which strongly supports this.

We were able to obtain less than 10 ppmv absolute humidity with the dry air used as carrier gas with the Picarro. Of course, the instrument is not perfectly calibrated for these low humidities but this amount should not have any effect on our measurements. However, the VSMOW calibration is made with Drierite where we were able to obtain  $\sim 100$  ppmv. If this vapor is very depleted (fractionation could occur in the Drierite) it could have a slight influence on the calibration. We made sure to use the same background for the data points and most likely the error due to this is within the uncertainties of

the measurements. Besides from the above we faced no significant issues when working with the Picarro. It is clear that for measurements of this type the Picarro has several advantages. With improved instruments in the future with smaller cavity, better algorithms and better humidity calibration, it will be possible to cover the temperature range of 0°C to -50°C completely with these instruments. With the use of these laser based instruments we can avoid the sample collection issues as mentioned above. Furthermore, to be able to continuously monitor the important shifts in the isotope values will increase the knowledge about the system under consideration. Of course, the sensitivity of such instruments are demanding for the experimental setup since small scale changes and drifts are registered. The high temporal resolution of these instruments also demands some post-processing of the data in addition to the calibrations but this might just be a luxury problem.

The TC/EA-IRMS system made it possible to collect and measure at the very low vapor pressures that was crucial for these measurements. Still, some improvements can be made to this system as well. There is a great amount of sample loss in the TC/EA and ConFlo III devices and clearly not all the injected sample (only a few percent) are used by the IRMS. Since it takes a long time to collect 0.2  $\mu\text{L}$  at -50°C any improvements here would be significant. Furthermore, different packing the reactor of the TC/EA did to some point impact the performance of the system since broader peaks or peaks with large tailing due to weak pyrolysis are not integrated properly. This has also been investigated by e.g. LaPorte et al. (2009). Lowering the memory effects of the TC/EA would also be significant for this work. Here, the injection routine is the most crucial since once the vapor is on the other side of the hot zone of the reactor the memory effect is negligible due to the high temperature (1384°C). Since we do not use the reverse plumbing as mentioned by Gehre et al. (2004), most of the memory effect will come from mixing in the dead volume before the sample enters the hot zone and from sample vapor following the flow outside the carbon tube, limiting the pyrolysis. The latter has a big influence on the peak tailing. We performed tests with different insertion angles for the needle connecting the experimental setup to the TC/EA and saw some differences in peak shape depending on the insertion angle of the needle. Besides from the improvements by reversing the flow inside the TC/EA, these effects could be limited by using a longer needle to limit the mixing in the upper part of the TC/EA and to force a larger part of the sample inside the carbon tube. This is of course limited by the heating of the plastic parts of the needle.

## 5.7 Conclusion

In this chapter we presented the results of the experiments, compared them with previous work and discussed their validity. Our results show fractionation factors with a temperature dependency in accordance with theory for temperatures down to -40°C. The best fit was found with the expression of  $\ln \alpha = C_1 + C_2/T + C_3/T^2$  which gives the following expressions

for our results:

$$\ln(\alpha_{\delta D}) = 0.2133 - \frac{203.10}{T} + \frac{48888}{T^2} \quad (5.7.1)$$

$$\ln(\alpha_{\delta^{18}O}) = 0.0831 - \frac{49.192}{T} + \frac{8312.5}{T^2} \quad (5.7.2)$$

Compared to previous results, especially the works of Majoube (1970) and Merlivat and Nief (1967) we obtain a significantly larger fractionation factor for  $\delta D$  while for  $\delta^{18}O$  the fractionation factor is larger for temperatures below  $-20^\circ C$  and slightly lower for temperatures above this. The possible errors in the experimental setup were discussed and we conclude that most errors would reduce the fractionation factor while the errors increasing it were argued unlikely to occur, based on the observed behavior of the setup. In addition to this we argue that the observed differences between this work and the work of Merlivat and Nief (1967) and Majoube (1970) could be due to the differences in the experimental setups with their system possibly being influenced by backdiffusion.

Improvements for the experimental setup, instrumentation and measurement routine were also discussed. Here, it is clear that even though the experimental setup performed as needed for these investigations, several improvements could increase its performance. To extend the temperature range of the measurements would essentially imply longer sampling times, in which a different collection and measurement method would be needed. It is clear that in the future this will be possible with improved instrumentation performance.

As mentioned in Chapter 1 the ice-vapor equilibrium fractionation factor is a core component in isotope models since it controls the magnitude of the fractionation during phase changes. This work is therefore highly relevant for e.g. climate studies and the results of this work emphasizes the need for better characterization of many basic parameters in the hydrological cycle. Examples of these parameters could be the ice-liquid fractionation factors (Arnason, 1969; O'Neil, 1968), the liquid-water fractionation factors (Majoube, 1971b), the kinetic fractionation effects under condensation and the super saturation function (Jouzel and Merlivat, 1984), the possible temperature dependency of the diffusion fractionation factor (Luz et al., 2009) or  $\alpha$  for  $^{17}O$  (Landais et al., 2009).

In the next chapters we will give examples of the impacts due to the differences between the results of this work and the fractionation factors of Merlivat and Nief (1967) and Majoube (1970). Still, we will now give an example of the use of the obtained results, since by knowing the ice-vapor equilibrium fractionation factor as well as the liquid-vapor fractionation factor we can calculate the ice-liquid fractionation factor Arnason (1969):

$$\alpha_{ice-liquid} = \frac{\alpha_{ice-vapor}}{\alpha_{liquid-vapor}} \quad (5.7.3)$$

We can calculate  $\alpha_{ice-liquid}$  from the results of this work using the  $\alpha_{liquid-vapor}$  from Majoube (1971b) of 1.0117 for  $\delta^{18}\text{O}$  and 1.1123 for  $\delta\text{D}$ . As mentioned earlier the intersection with  $0^\circ\text{C}$  is  $\alpha_{ice-vapor}=1.1331$  for  $\delta\text{D}$  and  $\alpha_{ice-vapor}=1.0145$  for  $\delta^{18}\text{O}$  for the fit with  $\ln \alpha = C_1 + C_2/T + C_3/T^2$ . This gives  $\alpha_{ice-liquid} = 1.0187$  for  $\delta\text{D}$  and 1.00277 for  $\delta^{18}\text{O}$  based on this work. For comparison for the  $\delta\text{D}$  value, Arnason (1969) measured  $\alpha_{ice-liquid}=1.0208$ , the work of O'Neil (1968) gives 1.0195 and the data of Merlivat and Nief (1967) gives 1.0235. Thus, our value is in better agreement with the other measured values than Merlivat and Nief (1967). For  $\delta^{18}\text{O}$  Majoube (1971b) obtains 1.0034 for  $\delta^{18}\text{O}$  with his value for  $\alpha_{ice-vapor}$  (Majoube, 1971a) and O'Neil (1968) obtains 1.0030. Here, we also get a good agreement and our value is also closer to the measured than the value of Majoube (1971b). Some small differences are seen between the different fits. Using the intersections for the  $T^{-1}$  fit ( $\alpha_{ice-vapor}=1.1222$  for  $\delta\text{D}$  and  $\alpha_{ice-vapor}=1.0133$  for  $\delta^{18}\text{O}$ ) gives 1.0089 for  $\delta\text{D}$  and 1.0016 for  $\delta^{18}\text{O}$ . Comparing these results to the above give too low values for both isotopes. This also supports the observation that the fit for the  $T^{-1}$  dependency alone did not capture the measurements fully for temperatures above  $-10^\circ\text{C}$ . In summary, the ice-liquid equilibrium fractionation factor calculated from the results of this work agree very well with previous measurements.

## Chapter 6

# Implications for the martian water cycle

One of the main objectives of this work was to extend the temperature range of the ice-vapor equilibrium fractionation factor. The initial plan was to extend the measured temperature range ideally to 200K since this would be of much use for investigations of the ice-vapor exchange on Mars as well as low temperature exchange on Earth. As discussed, this proved to be very difficult and the temperature range was only extended with measurements down to 233K. Nevertheless we will now investigate the implications of the observed differences in fractionation factors between the work of Merlivat and Nief (1967) and this work when extrapolating to Mars temperatures. This is done with a case study using a simple model of ice-vapor exchange in the martian atmosphere.

### 6.1 The Martian water cycle

The exploration of Mars the last 40 years has shown a picture of a more dynamical climate than previously thought. The seasonal variations in the martian climate are, compared to the other planets in the solar system, much like the variations on Earth. The martian atmosphere consists mainly of CO<sub>2</sub> (95%) with a total atmospheric pressure of around 700 Pa depending on altitude, latitude and season. Because of the large temperature variations, the CO<sub>2</sub> condense out of the atmosphere in the respective hemispheric winters and forms a seasonal CO<sub>2</sub> layer in the polar regions (Leighton and Murray, 1966; Owen, 1992). Due to this phenomenon the atmospheric pressure varies up to 20% (Kieffer, 1992). Water is present in the martian atmosphere with a typical partial pressure of 0.1 Pa (or around 20 precipitable  $\mu\text{m}$  of water in the atmospheric column). The hydrological cycle on Mars is in some ways simpler to study than Earth's since there are no oceans and H<sub>2</sub>O is only stable near the surface in the vapor and solid phases due to the low temperature and

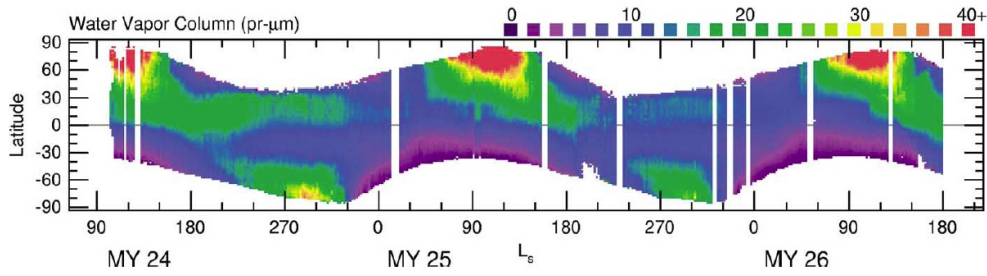


Figure 6.1: Column abundance of water vapor in the martian atmosphere as a function of  $L_s$  (time) and latitude as observed by MGS-TES (Smith, 2004). MY indicates Mars year.

pressure (Jakosky, 1983; Kieffer, 1992). In the current climate on Mars the polar regions are the largest cold traps. The polar layered deposits have a size of around 1000 km in diameter in the north and around 1500 km in south and consists of layers of  $H_2O$  and  $CO_2$  deposited through millions of years (Hvidberg, 2003; Fishbaugh and Hvidberg, 2006). The northern polar layered deposits or ice cap is the largest single source of water vapor in the martian hydrological cycle (Smith, 2002). In addition to this, massive ground ice deposits have been revealed within a few centimeters of the surface at latitudes polewards of 60, both from orbit by Mars Odyssey (Boynton, 2002) and from in-situ measurements by the Phoenix Mars Lander (Smith et al., 2009). Secondary water reservoirs are ancient glaciers scattered around the low latitudes and adsorbed water in the regolith (Kieffer, 1992). During the spring and summer these reservoirs become activated and releases vapor to the atmosphere (Smith, 2002). Figure 6.1 shows the column abundance of water vapor in the martian atmosphere as a function of  $L_s$  (solar longitude with  $L_s = 0$  as northern spring equinox) and latitude as observed by MGS-TES (Smith, 2004). Here the water abundance above the north polar layered deposits can be seen increase drastically during the northern summer where measurements of over 100 precipitable  $\mu m$  are seen. Precipitable  $\mu m$  is a common expression for the water concentration in the Martian atmosphere. The same pattern is seen to some extent over the south polar region. A "tongue" of water vapor can be seen extending from the north polar region towards equator during autumn and winter due to the adsorbed water and subsurface ice reservoirs (Smith, 2002).

Since the dominant gas  $CO_2$  rapidly equilibrates with  $H_2O$ , the  $\delta^{18}O$  values of the ice and vapor are affected by this (Clayton and Mayeda, 1988; Niles et al., 2010; Krasnopolsky et al., 2007) and  $\delta D$  is mainly used to investigate the hydrological cycle on Mars. Due to the very enriched values of  $\delta D$  on Mars, it is common to use the definition of D/H as being relative to VSMOW. Hence, a D/H value of 1 is equal to the VSMOW composition and  $D/H = 2$  corresponds to 1000 ‰ in the  $\delta$  notation. The presence of channels, valley networks and ancient lakes at the surface provides evidence for a hydrological cycle earlier in the Mars history when the planet had a warmer climate. Since then, the water has been stored in the above mentioned reservoirs, being lost to space or being stored in subsurface

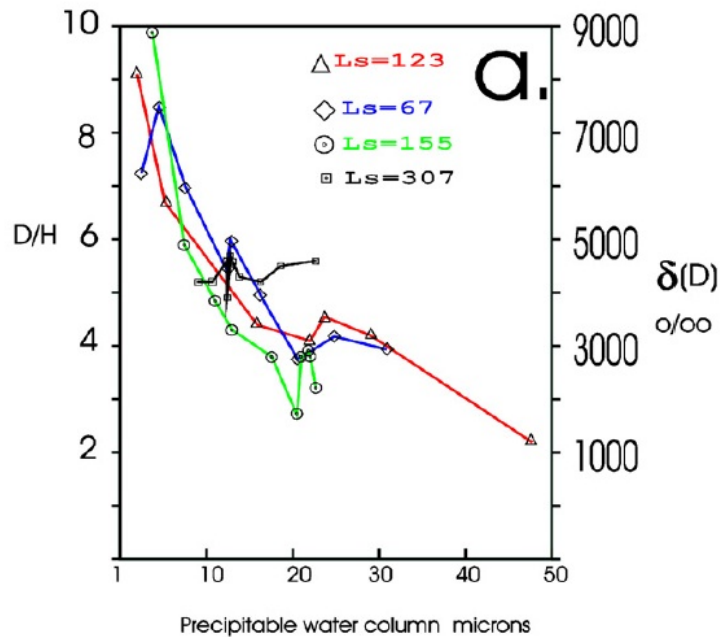


Figure 6.2:  $\delta D$  as a function of precipitable water content in the martian atmosphere. Figure from Fisher (2007), data reproduced from Mumma et al. (2003)

water reservoirs. One important clue to constrain the relative sizes of these reservoirs is the  $\delta D$  ratio in the current martian atmosphere (Yung et al., 1988; Jakosky, 1991; Montmessin et al., 2005; Owen et al., 1988; Krasnopolsky and Feldman, 2001). Until the work of Mumma et al. (2003) and Novak et al. (2005, 2007) it was assumed that the D/H of the atmospheric vapor had a single value of 5.5 (Krasnopolsky et al., 1997; Owen et al., 1988). Their work was based on spectral methods and indicated D/H ratios between 2.3 and 10 depending on the season and latitude. This large deuterium enrichment results from the preferential Jeans escape at the top of a planetary atmosphere which removes the lighter isotopes from the planet. Due to this, D/H can be interpreted as a measure of the ratio of the current active water reservoirs to the initial water reservoir. The processes responsible for these high values of D/H, the distribution of D/H in the martian atmosphere as well as the reservoir sizes have been discussed for a long time and still is (Yung et al., 1988; Jakosky, 1991; Montmessin et al., 2005; Yung and Kass, 1998; Krasnopolsky et al., 1998; Fisher, 2007).

Figure 6.2 shows the D/H ratio and  $\delta D$  of the vapor in the Martian atmosphere as a function of Pr (Precipitable microns, the height of the water column in  $\mu m$ ) (Mumma et al., 2003; Fisher, 2007). The different markers indicate different solar longitude  $L_s$ . The figure shows that D/H is large with low water concentrations and falls with higher concentrations of water in the atmosphere. In Fisher et al. (2008) a mixed cloud stable isotope model is

used to show that the seasonal progress of the D/H in the polar region of Mars cannot be used to explain this alone and that the seasonal cycle in D/H is most likely due to exchange between several water reservoirs, each with a D/H cycle. Spread around different latitudes, these reservoirs of different sizes with a unique average D/H would have different response times (Fisher, 2007) and the observed D/H (Mumma et al., 2003; Novak et al., 2005) must be a product of this. As discussed in Fisher (2007) the two main (known) water reservoirs on Mars are the ice cap and the ground ice and these are the main vapor sources and probably drive the D/H cycle in the summer and early fall. When the vapor from these two sources condensates out during fall, the D/H of the vapor in the atmosphere probably originates from smaller sources towards equator where it is still warm. This can be seen when plotting the observed D/H (Mumma et al., 2003; Novak et al., 2005) in the atmosphere as a function of time and atmospheric water concentration (Smith, 2002) in latitudinal bins as e.g. in Fisher et al. (2008). Here, the D/H over the polar region shows a minimum when the atmospheric vapor concentration is largest, whereas in the lower latitudes there are secondary minima indicating different reservoirs. As discussed in Fisher (2007) this indicates a long mixing time in the atmosphere and as a first approximation, the D/H of the vapor in the atmosphere can be interpreted as the D/H of the given reservoir. Due to the low diffusion rates within ice, the surface ice becomes enriched in the heavier isotope as the lighter isotope is preferentially removed by sublimation. The concentration of the heavier isotope in the sublimated gas then increases until it reaches the same concentration as that of the bulk sample.

Modeling the D/H in the martian atmosphere requires knowledge about the equilibrium fractionation factor for temperatures below 200K. When choosing the equilibrium fractionation factor some authors have been cautious in extrapolating  $\alpha$  from the known values. Since the temperature range covered by the measurements of Merlivat and Nief (1967) only span  $0^{\circ}\text{C}$  to  $-33^{\circ}\text{C}$  this is far outside the range of the polar temperature of Mars and some authors have used a constant of  $\alpha$  below the known temperature range. Fisher et al. (2008) used a constant of  $\alpha=1.35$ , (Yung et al., 1988) used  $\alpha = 1.30$  and Montmessin et al. (2005) and Fouchet and Lellouch (2000) used the extrapolated values or a constant of  $\alpha = 1.24$  beyond the measurement range. It has been argued that some of the seasonal exchange between the atmosphere and the ice cap is complete and therefore occurs practically without fractionation (Jakosky, 1991; Mcelroy and Yung, 1976) in which case  $\alpha = 1$ . The problem of extrapolating  $\alpha$  at lower temperatures was illustrated on Figures 5.9 and 5.10 that showed the different fit types presented in Section 5.4 along with extrapolated results from Merlivat and Nief (1967) and Majoube (1970). Here a difference in  $\alpha$  of up to 0.1 between the values for D/H can be seen at 200K which will have a significant impact for any process governed by this.

### 6.1.1 Phoenix Mars Lander

In addition to the Viking Lander in-situ measurements of the martian atmosphere (Owen et al., 1977) on low latitudes, the knowledge of D/H in the martian atmosphere comes from remote sensing (e.g. (Mumma et al., 2003; Novak et al., 2005)). To investigate the D/H in the atmosphere and subsurface ice, one of the instruments aboard the Phoenix Mars Lander (Smith et al., 2008, 2009) housed a mass spectrometer able to measure this. After a successful landing in the Martian arctic at 68.2N, 234E on 25 May 2008 the Phoenix lander operated actively through 151 sols (1 sol = 24 h 40 m) (Smith et al., 2009). This corresponds to  $L_s = 77.15$  with  $L_s = 0$  as northern spring equinox. The primary goals for Phoenix were to characterize the local geomorphology, the physical properties of the soil layers and investigate the near-surface ice at the landing site as well as the climate and habitability of the Martian arctic (Smith et al., 2008). The mission carried several instruments to characterize the environment of the Martian arctic including a meteorological station with a LIDAR (Whiteway et al., 2009; Taylor et al., 2010) and a mass spectrometer inside a unit called the thermal evolved gas analyzer (TEGA) (Hoffman et al., 2008; Boynton et al., 2009). This consisted of two components; a set of eight ovens that could heat samples of surface and subsurface ice-soil mixtures and a mass spectrometer that served as analysis tool for the gases evolved from the oven samples and also for measurements of the composition and isotopic ratios of the gases in the martian atmosphere. One of the goals for TEGA was to perform measurements of the D/H ratio in the subsurface ice and the atmosphere on Mars. However, due to problems with the ice sublimating too fast and since there was not enough water vapor in the atmosphere for determination of D/H these measurements were never performed. These data would have been highly relevant for this work. Nevertheless, TEGA proved as a success and did confirm the presence of water on Mars, confirmed the presence of calcium carbonates and measured the isotopic composition of the  $\text{CO}_2$  in the atmosphere (Smith et al., 2009; Boynton et al., 2009; Niles et al., 2010).

## 6.2 Investigations with the results of this work

Due to their possible age, the ice caps on Mars are valuable archives of the climatic history of Mars. Investigating e.g. the impact on observed D/H from a martian ice core would have been a very interesting case for this chapter. However, the D/H of the ice cap is likely more affected by the Jeans escape than seasonal changes which also have not been properly characterized so far (Fisher, 2007). Since the equilibrium fractionation factor has largest impact on the seasonal changes we will focus on a case study of this. Here the same model as presented in Fisher et al. (2008) is used. In this approach an open cloud model (Rayleigh distillation) is extended to include mixed removal processes since the

preferred condensation of the heavy isotopes cannot explain the enrichment of the D/H in the atmosphere with vapor condensing out. As argued in Fisher et al. (2008), the maximal fractionation of the vapor  $\delta D$  in the atmosphere can be approximated with a Rayleigh distillation (Dansgaard, 1964):

$$a_v(t) = a_v(0) \left( \frac{q_v(t)}{q_v(0)} \right)^{(\alpha-1)} \quad (6.2.1)$$

where  $a_v$  is D/H at a time  $t$  from the time of the maximum D/H with  $a_0$  is equal to the minimum D/H.  $q_v$  is the total H amount in the vertically integrated atmospheric vapor column and  $q_v(t)/q_v(0)$  can be given by  $\text{Pr} / \text{Pr maximum}$ . In their work, Fisher et al. (2008) divides the water abundance into three parts; vapor in the air, water ice in clouds and water ice deposited on the ground either by direct deposition ( $\alpha = 1$ ) or by precipitation ( $\alpha > 1$ ). Assuming that the column is well mixed and that the vapor in the atmosphere is in equilibrium with the deposited ice on the surface they prescribe the proportion of the removal mechanism for direct deposition and precipitation as  $w_s$  and  $w_p$  respectively. If the fraction of total water in the clouds is  $f$  and this is constant, then equation (6.2.1) becomes:

$$\frac{a_v(t)}{a_v(0)} = \frac{q_v(t)}{q_v(0)}^{\frac{w_s + w_p \alpha - 1 - f(\alpha - w_s - w_p \alpha)}{1 + f \alpha}} \quad (6.2.2)$$

Thus, with no clouds,  $f=0$  and if the phase change occurs by precipitation only  $w_s=0$  and  $w_p=1$  then (6.2.2) reduces to (6.2.1) as one end member.  $w_s=1$  and  $w_p=0$  and  $\alpha = 1$  is the other end member with direct deposition. By investigating different cases of removal of vapor from the atmosphere Fisher et al. (2008) compare the output with the pattern seen in Figure 6.2. Here, 0.1 for the cloud cover  $f$  is used and it is assumed that the vapor is in equilibrium with the ice in the clouds. Of course, this is a simple model and does not include e.g. the complex mass balance of the ice cap with the different albedo due to the predominant scarps as well as contribution from other reservoirs. The model runs consist of various cases of deposition and cloud cover. Case 1 consists of mixed open cloud and direct deposition ( $w_s = 0.75$  and  $w_p=0.25$  with  $f=0.1$ ). Case 2 is pure direct deposition with no clouds ( $w_s = 1$  and  $w_p=0$  with  $f=0$ ). Case 3 consists of direct deposition with clouds ( $w_s = 1$  and  $w_p=0$  with  $f=0.1$ ). Case 5 is pure open cloud precipitation ( $w_s = 0$  and  $w_p=1$  with  $f=0.1$ ) and in their work Case 6 are a mixture of both processes ( $w_s = 0.5$  and  $w_p=0.5$  with  $f=0.1$ ). For this,  $\alpha = 1.35$ , extrapolated from Merlivat and Nief (1967) at a temperature of 202K. The results of their work can be seen on Figure 6.3 as the dashed lines. The figure shows the D/H fraction as a function of remaining vapor in the atmosphere with D/H = 1 at the maximum vapor content,  $q_v/q_0=1$  and should be compared with Figure 6.2.

As concluded in Fisher et al. (2008), the only case that reproduces the increase in

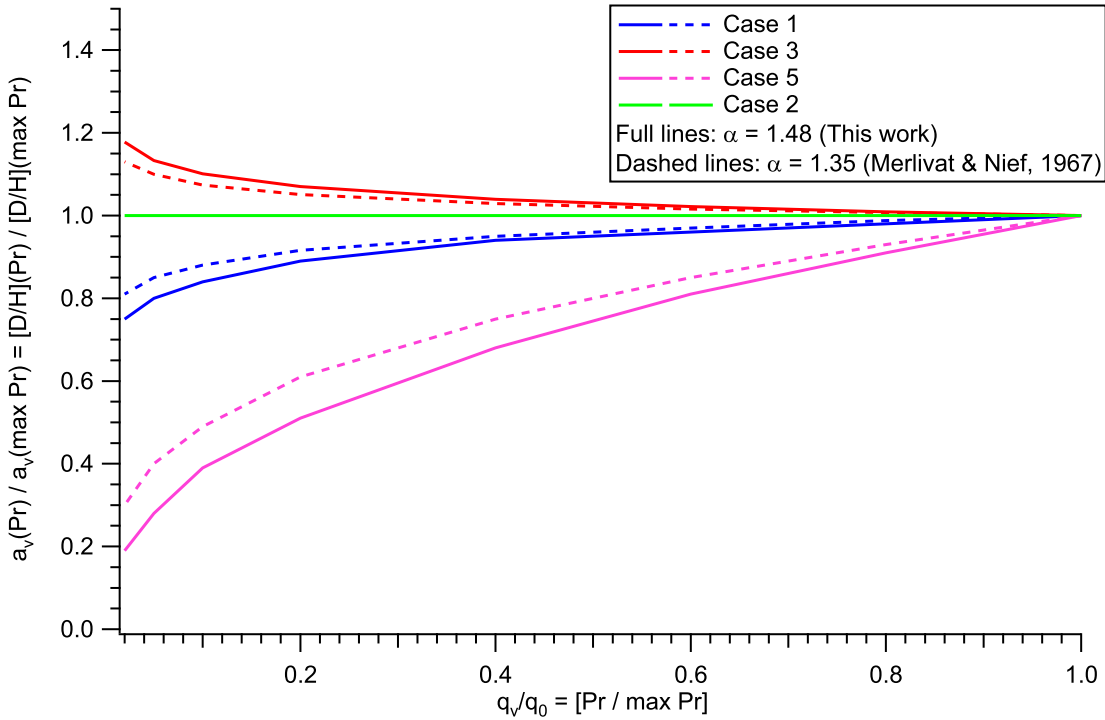


Figure 6.3: Fractionation of the atmospheric vapor as a function of precipitable water content with the different cloud models as described in Fisher et al. (2008).

D/H values with decreasing vapor amount in the atmosphere is case 3. Here, the clouds acts as a buffer or reservoir in the atmosphere and cause the continuous enrichment of the vapor in the atmosphere. The vapor in the atmosphere is in equilibrium with the water ice in the clouds which is enriched with heavy isotopes compared to the vapor in the rest of the atmosphere. When vapor is then removed from the atmosphere directly, the remaining part of the vapor in the atmosphere will become enriched due to the exchange with the enriched clouds. This continuous removal of light vapor from the atmosphere drives the enrichment as a function of smaller water column in the atmosphere. In the case of precipitation the depletion of the heavy isotopes in the atmosphere drives the D/H values towards more negative values as expected. The increase in D/H seen from case 3 is not significant compared to the observed changes seen on Figure 6.2 and it is concluded in the paper that the observed D/H must be due to the combination of several reservoirs.

The solid lines on Figure 6.3 show the same model runs with  $\alpha = 1.48$ , extrapolated from the results of this work at a temperature of 202K. Here we can see that the increased fractionation factor causes significant changes to the results discussed above. The runs with a higher  $\alpha$  do not change the conclusion that this Rayleigh type mixed cloud model is inadequate in explaining the observed D/H evolution alone. But the increased fractionation factor amplifies the patterns observed before and the differences are up to 0.1 in D/H

fraction (for case 5 with open precipitation). If the isotope ratio at the maximum vapor content is  $D/H = 2$ , this corresponds to a change in  $D/H$  of 0.2 or 200‰ which is a significant change for the model output. From this it is clear that the difference in  $\alpha$  originating from different fit types will also be able to change the model output considerably. That the fractionation factor is essentially unknown at these temperatures therefore introduces a large uncertainty for isotope modeling of the martian climate.

### 6.3 Conclusion

$D/H$  in the martian climate is an important indicator for the vapor fluxes between the different water reservoirs on a seasonal scale and the key to understand the evolution and size of previous and present water reservoirs on Mars. These are subjects where fundamental knowledge about the governing processes is still missing and where investigations with isotope models use the equilibrium fractionation factor at temperatures down to 200K. Extrapolating the fits for the equilibrium fractionation factor at low temperatures is dangerous since the fits are only valid within the measured temperature range. In the above, investigations on this were done with a simple model. The main conclusions from the modeling results do not change with the change in  $\alpha$  and further interpretation of these is out of the scope of this work. However, not surprisingly it was seen that the differences between extrapolated  $\alpha$  from Merlivat and Nief (1967) and from this work can cause significant changes in model output.

It is clear that more knowledge about the different water reservoirs and their vapor exchange is needed in order to properly understand the martian water cycle and its history. In the future, seasonal investigations of the  $D/H$  in the martian atmosphere as well as maybe a  $D/H$  record from an ice core from the north polar layered deposits or the subsurface ice will hopefully give much information about the vapor fluxes between the water reservoirs on Mars. To some extent, the results of this work can help constrain the isotope models used to interpret and understand these processes. But it is clear that more knowledge about the equilibrium fractionation factor at martian temperatures is needed for these purposes.

## Chapter 7

# Implications for isotope hydrology

In this chapter, we will investigate some of the implications that changes in the ice-vapor equilibrium fractionation factor have for isotope hydrology and the understanding of the water cycle on Earth. As mentioned in Chapter 1, the fractionation factors are crucial for the understanding of the isotopic signal in ice cores as well as understanding the importance of different sources and sinks in the hydrological cycle. One important tool in isotope hydrology is the deuterium excess,  $dxs$ , defined as:

$$dxs = \delta D - 8 * \delta^{18}O \quad (7.0.1)$$

This second order parameter is defined as the deviation from the global meteoric water line (Dansgaard, 1964). As mentioned in Chapter 1, differences in diffusivity of the water isotopologues cause kinetic fractionation under conditions with a relative humidity different than 1. Since  $\alpha_D$  varies more strongly with temperature than  $\alpha_{18O}$  the relationship between  $\delta D$  and  $\delta^{18}O$  changes as a function of temperature and relative humidity. Consequently the deuterium excess will also vary as a function of temperature and relative humidity. The deuterium excess therefore preserves information about the fractionation processes occurring during the transport of an air parcel from source to sink. Due to this, the deuterium excess can be used to identify the possible moisture sources for condensates, e.g. on the Greenland ice cap (Dansgaard, 1964; Jouzel and Merlivat, 1984; Merlivat and Jouzel, 1979).

As mentioned earlier, during the ice crystal formation in a cloud the condensation takes place under supersaturated conditions with respect to the vapor pressure over ice. During this condensation the super saturation function is an important parameter controlling the effective fractionation process (see Section 1.2.3):

$$R_s = \frac{\alpha_{sv}}{\alpha_{kin}} R_v \quad (7.0.2)$$

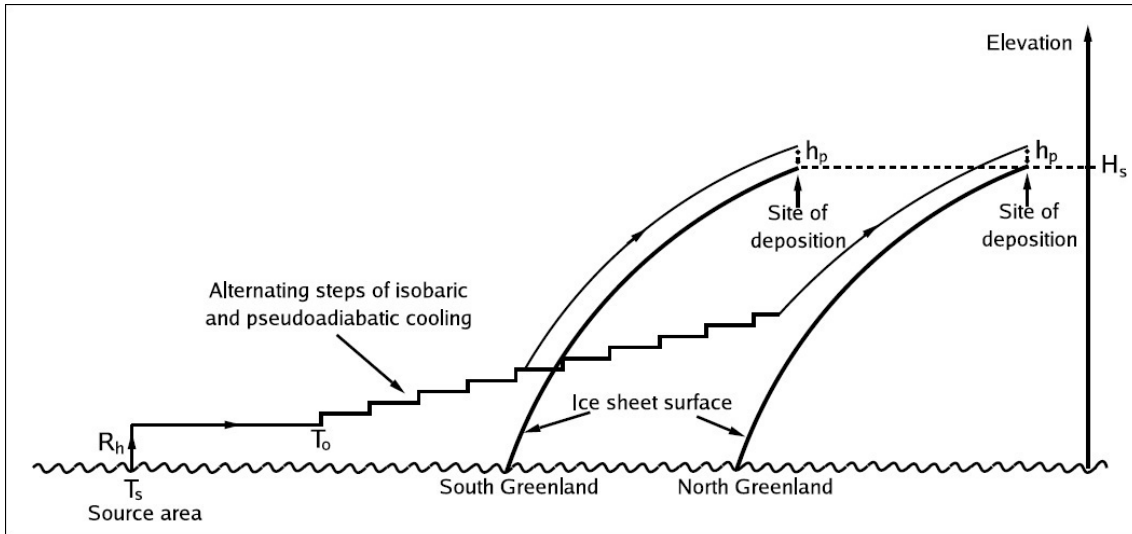


Figure 7.1: Illustration of the moisture transport from the evaporation site to the Greenland ice sheet. Here,  $R_h$  is the relative humidity,  $T_s$  is the surface temperature,  $h_p$  is elevation above the ice sheet and  $H_s$  is the site height. Figure from Sjolte (2005), adapted from Johnsen et al. (1989).

where  $R$  is either  $\text{H}_2^{18}\text{O}/\text{H}_2^{16}\text{O}$  or  $\text{HD}^{16}\text{O}/\text{H}_2^{16}\text{O}$  and subscripts  $s$  and  $v$  stands for solid and vapor respectively. The kinetic fractionation factor,  $\alpha_{kin}$ , is given by:

$$\alpha_{kin} = \frac{\alpha_{sv}\alpha_{diff}(S - 1) + 1}{S} \quad (7.0.3)$$

Because of the differences in diffusivity in air between the heavy and the light isotopologues of  $\text{H}_2\text{O}$  the heavy isotopologues will deposit slower than the light ones causing kinetic fractionation (as seen in the equilibrium chamber for temperatures lower than  $-45^\circ\text{C}$ ).

In the following, we will perform investigations of the impact of the observed differences in equilibrium fractionation factors between the values of this work and previous work. In the first approach we will investigate how the modelled isotopic composition of precipitation on the ice sheet will change, assuming same initial and vapor transport conditions. In the second approach we will investigate a scenario with fixed initial and final precipitation values and observe how the differences in ice-vapor equilibrium fraction factors will change the deuterium excess and the super saturation function needed for the precipitation values to match the initial conditions. For this, we use the Rayleigh distillation model developed by Johnsen et al. (1989). The model was designed to investigate the deuterium excess signal in Greenland ice cores. It includes the kinetic isotopic fractionation processes during the evaporation from the ocean surface (Merlivat and Jouzel, 1979), the transport of the air parcel from source area to the ice sheet as well as the isotopic fractionation occurring in the condensation process by using the super saturation function relating temperature

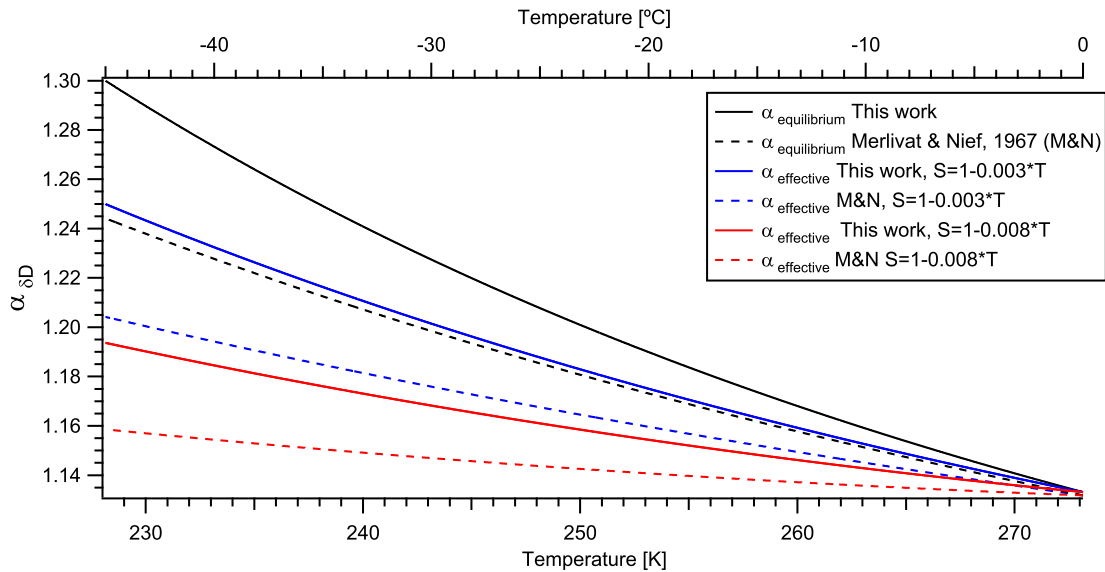


Figure 7.2: Effective fractionation of  $\delta D$  for two different super saturation functions compared to equilibrium fractionation. M&N indicates the work of Merlivat and Nief (1967).

and relative humidity over the surface of the formed snow crystals (Jouzel and Merlivat, 1984). The model has proved to correctly simulate the isotopic variability of precipitation samples. A full description of this model can be found in Johnsen et al. (1989) and Sjolte (2005). We use the same model setup as described in Steen-Larsen et al. (2010). The model simulates the transport of an air parcel from the source area of evaporation to the condensation site on the ice sheet. The model makes use of fixed locations of both sites. In between these locations, the trajectory is described in terms of elevation and temperature. The air parcel starts the trajectory at the source site with a prescribed relative humidity (RH) and sea surface temperature (SST) and is then cooled off as it is transported northwards. The air parcel gets lifted on its path to the ice sheet following a combination of isobaric and pseudoadiabatic cooling. As mentioned above the initial  $\delta$  values of the vapor depends on the temperature and relative humidity. When the parcel reaches the dew point the Rayleigh condensation is initiated. The water droplets are formed without supersaturation and the fractionation will be governed by simple Rayleigh condensation and the condensate is assumed removed from the cloud instantaneously. At a certain temperature ( $-5^{\circ}\text{C}$ ), the vapor from the air parcel will condense as snow and diffusion effects will affect the fractionation since the deposition of vapor occurs with the air being supersaturated with respect to ice. This is illustrated by figure 7.1.

The driving parameter in the model is the precipitation  $\delta^{18}\text{O}$ . We perform model runs with different super saturation functions and solid-vapor equilibrium fractionation factors for changing values of  $\delta^{18}\text{O}$ , SST and RH. From this dataset it is possible to extract the  $\delta D$  and  $T_{precip}$  corresponding to the right combination of SST, RH and  $\delta^{18}\text{O}$  for e.g. an

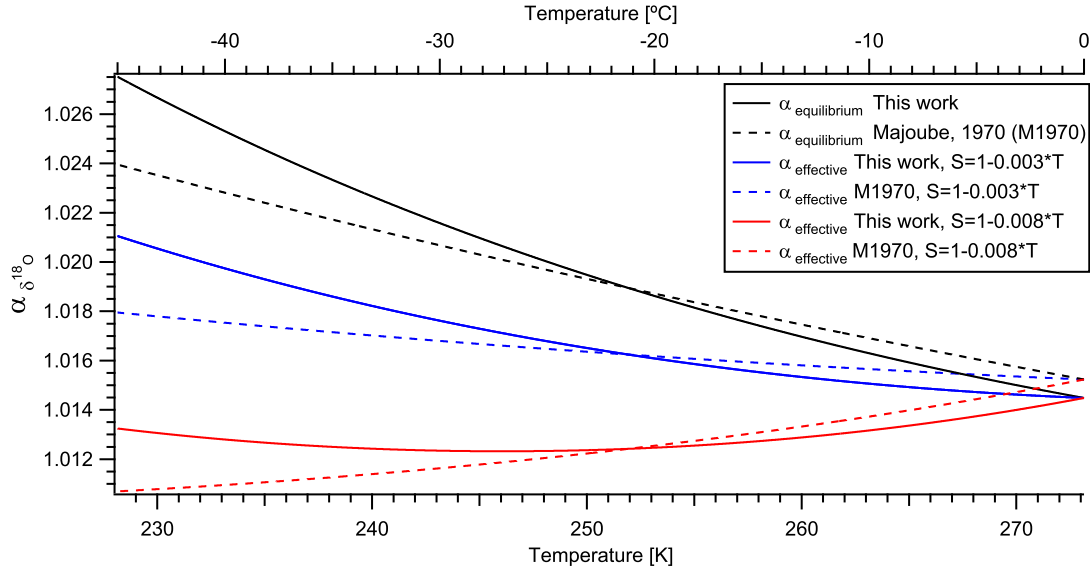


Figure 7.3: Effective fractionation of  $\delta^{18}\text{O}$  for two different super saturation functions compared to equilibrium fractionation. M1970 indicates the work of Majoube (1970) .

annual cycle through interpolation.

## 7.1 Effective fractionation factor

In this model the effective fractionation factor consists of contributions from both equilibrium and kinetic fractionation factors ( $\alpha_{eff} = \alpha_{eq}/\alpha_{kin}$ ) during condensation. Since the kinetic fractionation factor also depends on the equilibrium fractionation factor (see equation (7.0.3)) we need to investigate the effective fractionation factor separately to properly understand the model results. Figures 7.2 and 7.3 show the solid-vapor equilibrium fractionation factors for  $\delta\text{D}$  and  $\delta^{18}\text{O}$  along with the effective fractionation factors with super saturation functions  $S = 1 - 0.003 * T$  and  $S = 1 - 0.008 * T$  respectively. Here we can see that with kinetic effects the fractionation factors are significantly lower than the equilibrium values as expected. The curvature of the temperature dependency is kept but the slope becomes smaller with higher amount of super saturation since the super saturation minimizes the differences between the equilibrium and molecular diffusion fractionation factors. Interestingly enough the Merlivat and Nief (1967) equilibrium fractionation factor for  $\delta\text{D}$  and the effective fractionation factor with  $S = 1 - 0.003 * T$  based on the fractionation factor from this work are almost equal. For  $\delta^{18}\text{O}$  the same relationship is seen as the effective fractionation factors have a smaller temperature dependency. In the extreme case with  $S = 1 - 0.008 * T$  the effective fractionation factor actually becomes smaller with decreasing temperature down to  $-25^\circ\text{C}$ .

From equation (7.0.1) and Figures 7.3 and 7.3 we can see that deuterium excess for

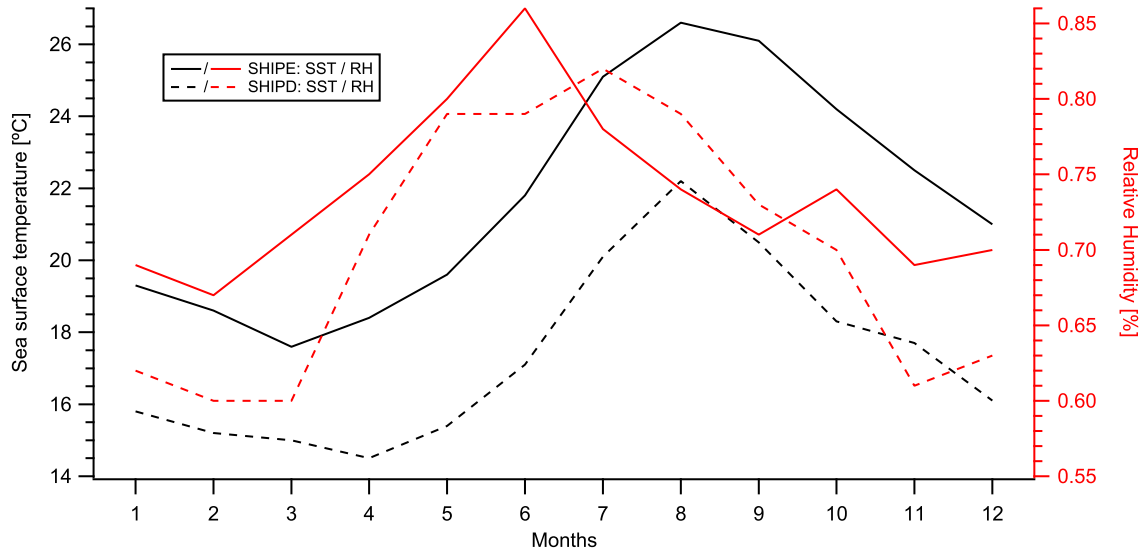


Figure 7.4: Moisture sources SHIP D and SHIP E sea surface temperature and relative humidity.

results based on this work will be lower than results based on the work of Merlivat and Nief (1967) and Majoube (1970) between  $0^{\circ}\text{C}$  and  $-20^{\circ}\text{C}$  due to the higher fractionation for  $\delta\text{D}$  and the lower fractionation for  $\delta^{18}\text{O}$  here. For temperatures lower than  $-20^{\circ}\text{C}$  the fractionation for  $\delta^{18}\text{O}$  is higher for this work and the deuterium excess is likely to be higher depending on the isotope values. Of course, these differences depends on the temperature and the phase change history of the vapor.

## 7.2 Investigating precipitation

For this investigation we make use of data from two model runs. One with the solid-vapor fractionation factors from Majoube (1970) and Merlivat and Nief (1967) and one with the results from this work. We use the mean NEEM  $\delta^{18}\text{O}$  cycle (read off Figure 2 in Steen-Larsen et al. (2010), approximated with a cosine curve) as input in the distillation model (Johnsen et al., 1989). This can be seen on Figure 7.5. As moisture source we use Weathership E (SHIP E)(IAEA/WMO, 1979) which is found to be an appropriate moisture source for the precipitation in central Greenland (Johnsen et al., 1989). SHIP E (and SHIP D) can be seen on Figure 7.4. As supersaturation function,  $S = 1 - 0.003 * T$  is used and the effective fractionation factor in this case can be seen on Figures 7.2 and 7.3. Since  $\delta^{18}\text{O}$  is the driving parameter in the model the model will find a different trajectory and  $T_{precip}$  corresponding to the input  $\delta^{18}\text{O}$  value when changing  $\alpha_{sv}$ . This will result in different  $\delta\text{D}$  values that do not reflect the change in  $\alpha$ . Therefore we need to find the isotope values for the same  $T_{precip}$  in both cases. This is done by finding the

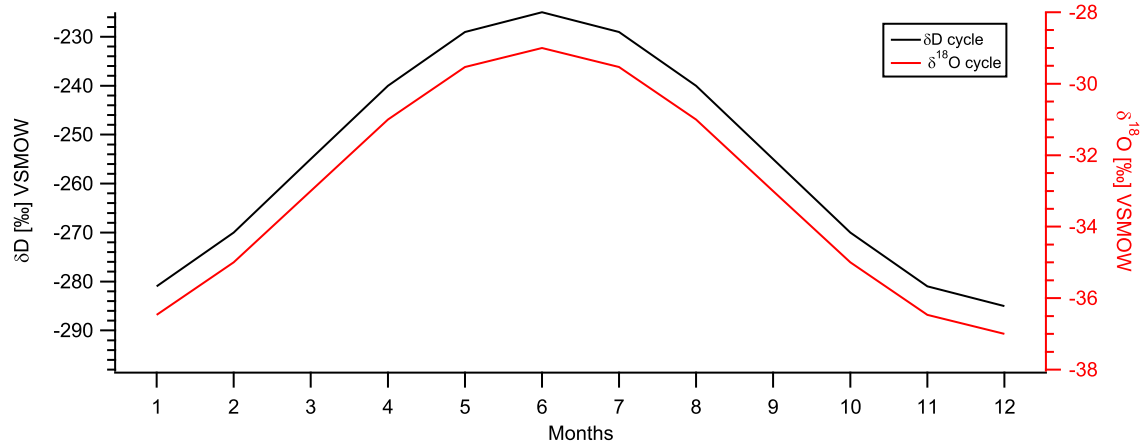


Figure 7.5: Approximated  $\delta\text{D}$  and  $\delta^{18}\text{O}$  cycle for the NEEM site from Steen-Larsen et al. (2010).

precipitation temperature  $T_{precip}$  for the run with the fractionation factors from Merlivat and Nief (1967) and Majoube (1970) and use this to find the  $\delta^{18}\text{O}$  and  $\delta\text{D}$  from the output of the run with the fractionation factors from this work by interpolation. As a check to see if the interpolation routine works, we perform runs only with a changed ice-vapor equilibrium fractionation factor for one of the isotopes,  $\delta^{18}\text{O}$ . In this case the isotopic composition of the precipitation should only change for  $\delta^{18}\text{O}$  while the values for  $\delta\text{D}$  should stay the same if the air parcel follows the same trajectory. This is confirmed.

### 7.2.1 Trajectories

Before we investigate the changes in the annual cycle we will investigate the trajectories for a selected run with initial conditions  $\text{SST} = 25^\circ\text{C}$ ,  $\text{RH} = 0.85$  and  $S = 1 - 0.003 * T$ . The run ends with values of  $\delta^{18}\text{O} = -23.81\text{‰}$  and  $\delta\text{D} = -278.65\text{‰}$ . The trajectories can be seen on Figures 7.6 and 7.7. The deuterium excess for these runs can be seen on Figure 7.2.1. These figures show the ongoing distillation of the vapor as a function of temperature during the transport from source to sink. The ice-vapor distillation begins at  $-5^\circ\text{C}$  which is set in the model and the kink occurring there is therefore expected. Between  $0^\circ\text{C}$  and  $-21^\circ\text{C}$ , the fractionation factor for  $\delta^{18}\text{O}$  from this work is smaller than from Majoube (1970) as seen on 7.3. The effect of this can be seen on Figure 7.6 where  $\delta^{18}\text{O}$  for the condensate starts out being less enriched for the curve based on this work compared to the curve based on Majoube (1970). The two curves indicating the isotope values for the vapor are almost the same here since only a relatively small fraction of the vapor has been removed. Here, the curve based on this work is less depleted as expected since the condensate is less enriched. This pattern continues for the vapor to the end of the distillation due to the initial conditions and during this process the difference between the two curves increases

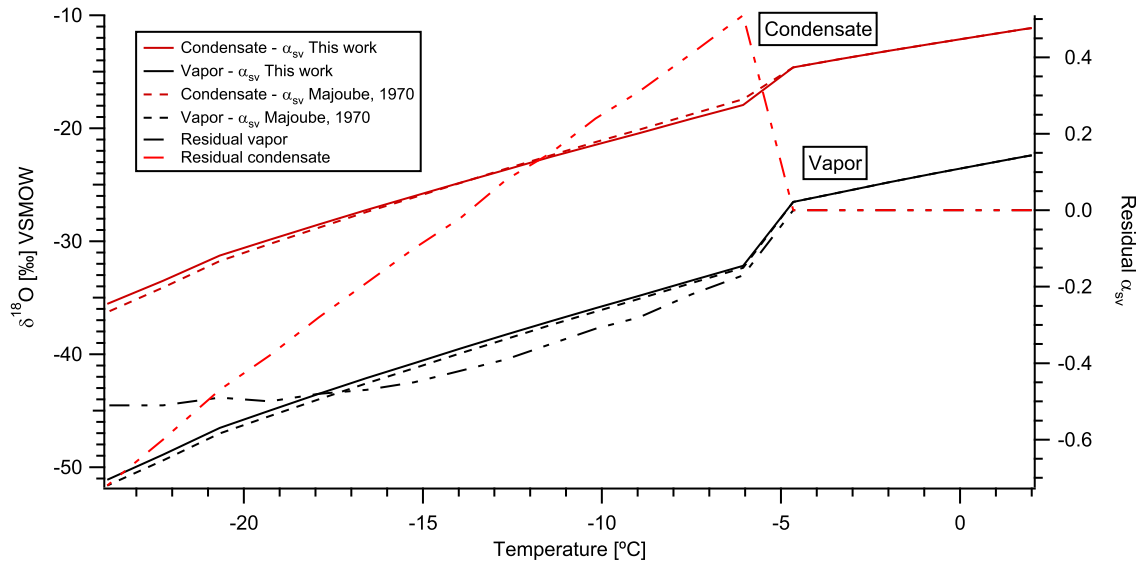


Figure 7.6: Vapor and condensate trajectories as a function of temperature for  $\delta^{18}\text{O}$  for a selected run with SST=25°C and RH=0.85 as initial conditions.

with lower temperatures down to -15°C as seen on the residual. Returning to the  $\delta^{18}\text{O}$  for the condensate, we can see that with lower temperatures, the two lines cross and the values based on this work becomes enriched compared to the values based on Majoube (1970). The residual increases to the end of the distillation. Both final condensate and vapor  $\delta^{18}\text{O}$  values are more enriched for the run based on the results from this work because of the distillation process (e.g. the slope of the fractionation factor of this work is different from the one of Majoube (1970)). For  $\delta\text{D}$  the fractionation factor from this work is larger for all temperatures and we see that the condensate values become more enriched (around 10‰) and the vapor values more depleted as expected. However, the residual for the condensate becomes smaller at the end of the process (starting around -15°C) and the values end up being similar since the stronger depletion of the vapor for the values based on this work affects the values of the condensate here.

Looking at the deuterium excess values on Figure 7.2.1 the above discussed processes are seen as expected. For the condensate the excess value starts out being larger when based on this work than with the values of Merlivat and Nief (1967) and Majoube (1970) since the fractionation of  $\delta^{18}\text{O}$  is not as large in the beginning of the process. As the distillation continues the two lines cross and the final value for the deuterium excess based on this work is lower than with the values of Merlivat and Nief (1967) and Majoube (1970) due to the different evolution of the isotope values of the condensate as discussed above. The changes in variations are of the order of up to 5‰. For the vapor we see the deuterium excess becomes lower at all times during the distillation due to the evolution of the vapor values, here up to 15‰. The final values of  $\delta\text{D}$  and  $\delta^{18}\text{O}$  are a product of the distillation

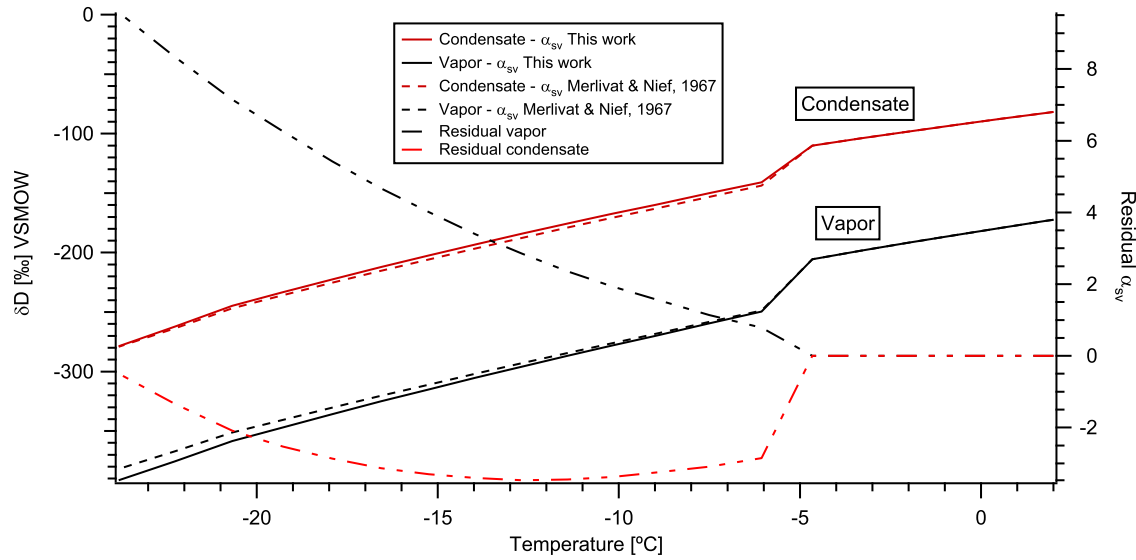


Figure 7.7: Vapor and condensate trajectories as a function of temperature for  $\delta D$  for a selected run with SST=25°C and RH=0.85 as initial conditions.

process. In this case we see that both the deuterium excess for both condensate and the vapor are lower with the values based on this work than with the values based on Majoube (1970) and Merlivat and Nief (1967). Of course this depends on the initial conditions and the temperature history of the air parcel and this result is hard to generalize but this is a typical case and the results from similar conditions will be similar.

### 7.2.2 Impact on the modeling of an annual cycle

With the results from the trajectories in mind we will now look at the values of  $\delta D$  and  $\delta^{18}O$  for an annual cycle as shown in Figure 7.5. As mentioned above this is approximated from the annual cycle on NEEM as seen in Steen-Larsen et al. (2010) along with initial conditions for SHIP E as seen on Figure 7.4. The results from the model runs can be seen on Figure 7.9. The top graphs show the isotopic composition of the vapor at the precipitation site. For  $\delta D$ , the vapor from the run based on the results from this work can be seen to be more depleted in heavy isotopes for all months whereas the opposite is seen for  $\delta^{18}O$ . This corresponds well to the patterns seen in the trajectories above. For the condensate the  $\delta^{18}O$  values have the same pattern as seen on Figure 7.2.1 with the final  $\delta^{18}O$  based on this work being more enriched due to the different slope. The  $\delta D$  curves are seen crossing each other due to different amounts of the compensation occurring in the last part of the distillation as seen on Figure 7.7. The differences in  $\delta D$  and  $\delta^{18}O$  values for the condensate and precipitation throughout the annual cycle are of course reflected in the deuterium excess. For the vapor we see a clear difference in magnitude with the values based on this work being between 10‰ and 15‰ lower in deuterium excess. Apart

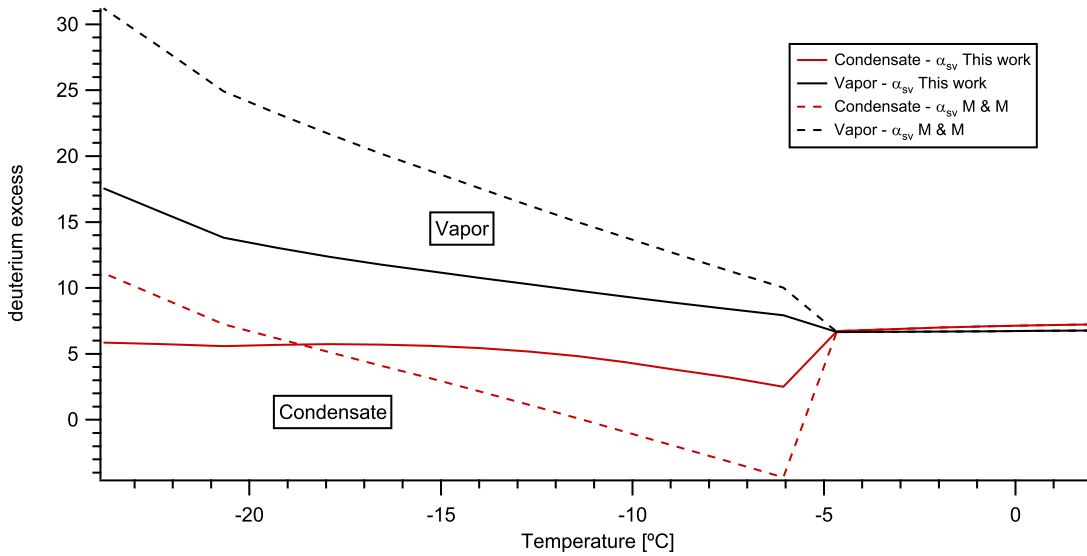


Figure 7.8: Vapor and condensate trajectories as a function of temperature for deuterium excess for a selected run with SST=25°C and RH=0.85 as initial conditions. M&M indicates the work of Merlivat and Nief (1967) and Majoube (1970) .

from small differences the overall shape of the deuterium excess cycle is maintained. For the condensate the deuterium excess is up to 10‰ lower in the first and last months while in the middle part of the cycle the values are similar. The shape is more flat the first six months after which it increases to a maximum around month 9 and decreases again. This annual cycle is significantly different in shape from the one based on the work of Merlivat and Nief (1967) and Majoube (1970) . The above results show that a changed fractionation factor has significant impact on both vapor and precipitation values and these differences are pronounced in the deuterium excess. Due to the combination of higher fractionation for  $\delta D$  and lower fractionation for  $\delta^{18}O$  for temperatures above -20°C the deuterium excess based on this work is in the shown cases generally lower compared to the one based on Merlivat and Nief (1967) and Majoube (1970) and the shape of the annual cycle for the condensate changes. These differences have in turn a significant impact for isotope modeling as shown since the value and shape of the deuterium excess annual cycle are key parameters in investigations of the condensation temperature and moisture source region for a certain sink, as e.g. the NEEM site on the Greenland ice cap.

### 7.3 Investigating the super saturation function

The above results were made with a fixed super saturation function of  $S = 1 - 0.003 * T$  and indicated significant differences in the shape of the deuterium excess for the annual cycle. In this section we make use of data from model runs with the fractionation factors

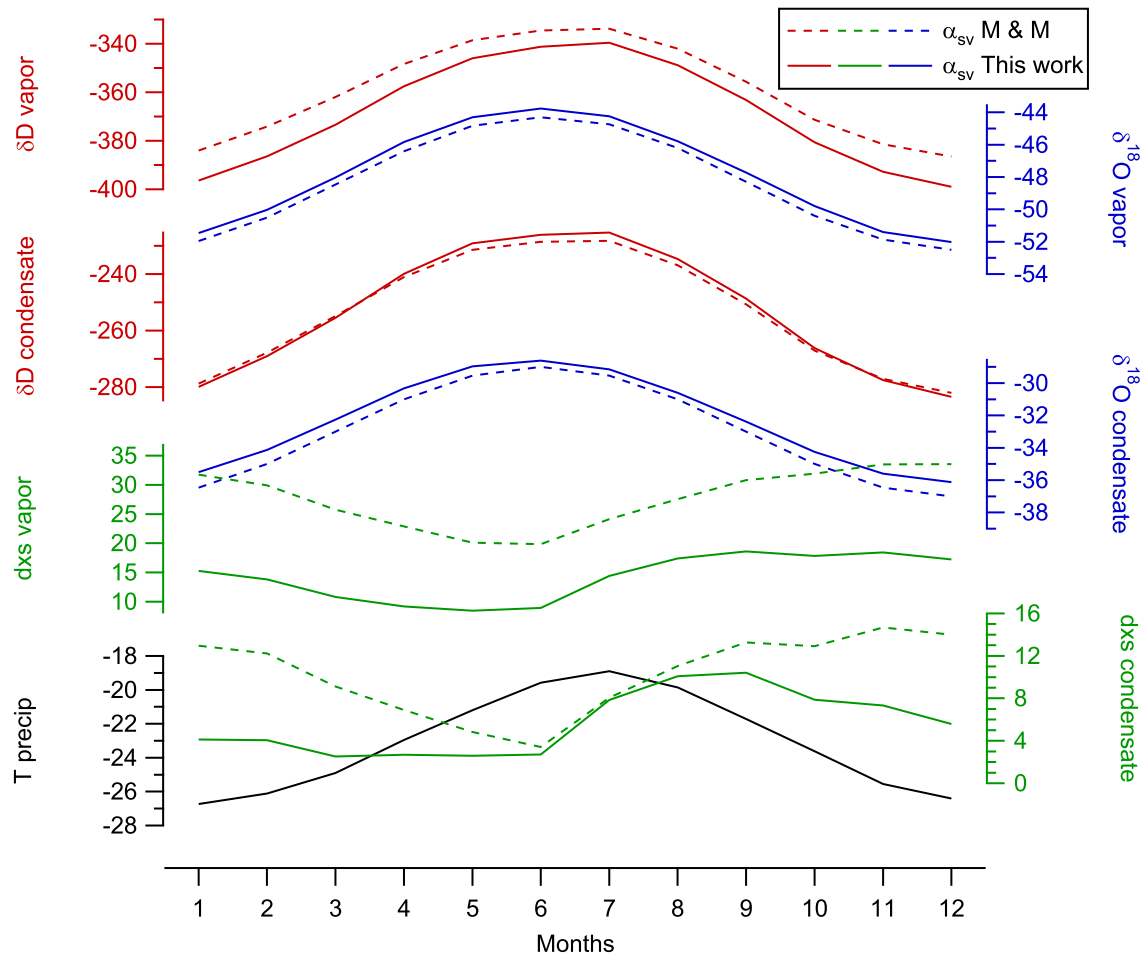


Figure 7.9: Output from the model runs. Solid lines are results with the ice-vapor equilibrium fractionation factors from this work and dashed lines are from the work of Merlivat and Nief (1967) and Majoube (1970) (M & M). Significant differences in both precipitation and condensate values change the deuterium excess values and shape.

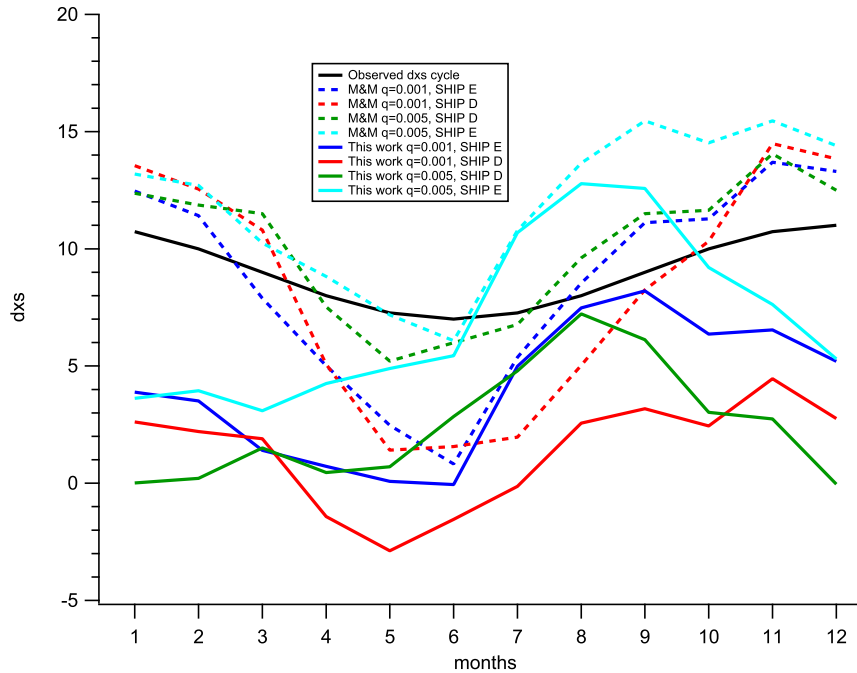


Figure 7.10: Annual deuterium excess cycle for model runs with different fractionation factors and different super saturation functions,  $SS = 1 - q \cdot T$ . M&M indicates the work of Merlivat and Nief (1967) and Majoube (1970) .

from Majoube (1970) and Merlivat and Nief (1967) as well as the ones from this work just as above. We use the same  $\delta^{18}\text{O}$  input for the NEEM annual cycle as above and investigate the annual deuterium excess cycle as a function of 4 different supersaturation functions ( $S = 1 - q \cdot T$  where  $q = 0.001, 0.003, 0.005$  and  $0.008$ ) and two initial conditions, SHIP D and SHIP E, as seen on Figure 7.4. Thus, in this case the trajectory is allowed to change and we will see how well the two frequently used moisture sources fit with the data for the different super saturation functions. This is inspired by the results of Steen-Larsen et al. (2010) and we will compare the results with these. Figure 7.10 shows model runs with  $q=0.001$  and  $q=0.005$  whereas Figure 7.11 shows the model runs with  $q=0.003$  and  $q=0.008$ . The dashed lines indicate model runs based on the fractionation factors of Majoube (1970) and Merlivat and Nief (1967) and the full lines are model runs based on this work. The black line indicate the observed deuterium excess (approximated from Steen-Larsen et al. (2010)). Compared to the work of Steen-Larsen et al. (2010) the deuterium excess here is 2-3 ‰ lower here (due to the approximation with a cosine function) but the overall shape is the same which makes it possible directly to compare Figure 7.11 with Figure 2 in Steen-Larsen et al. (2010). For the model runs based on Majoube (1970) and Merlivat and Nief (1967) the model run that fits the observed deuterium excess best is the one with  $q=0.008$  and SHIP D as moisture source and this is also one of the conclusions in Steen-Larsen et al. (2010). In their work the fit is even better due to the use of actual data. The

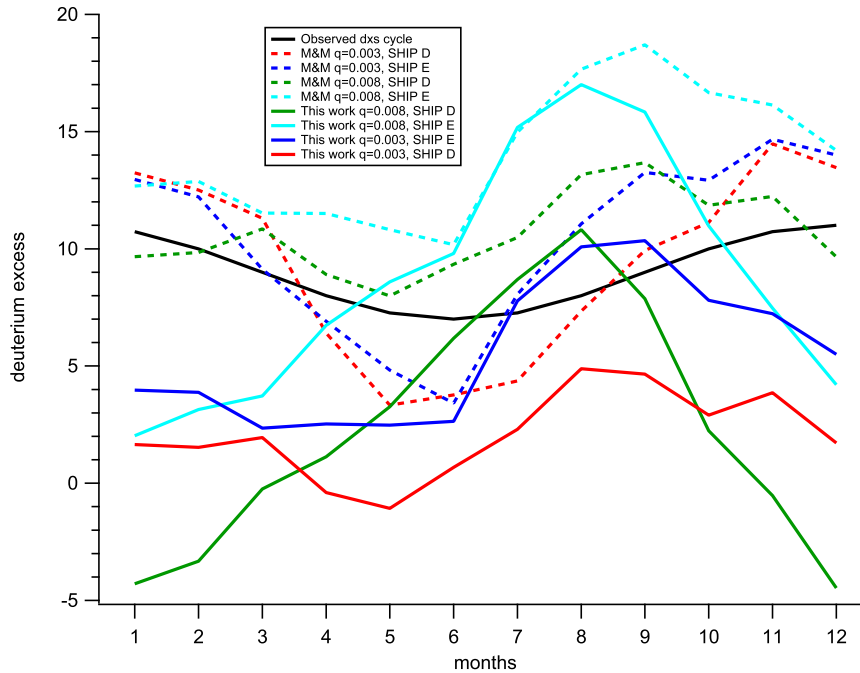


Figure 7.11: Annual deuterium excess cycle for model runs with different fractionation factors and different super saturation functions,  $SS = 1-q \cdot T$ . M&M indicates the work of Merlivat and Nief (1967) and Majoube (1970) .

model runs with  $q=0.001$ ,  $q=0.003$  and to some extent  $q=0.005$  generally have too large variations in the annual cycle and the SHIP E for  $q=0.008$  does not capture the observed cycle. Looking at the model runs based on this work we can see clear differences in the shape and magnitude of the deuterium excess. In this case the runs with  $q=0.005$  and  $q=0.008$  are more or less in anti-phase with the observed cycle. This shape is pronounced for large values of  $q$  due to the change in effective fractionation factor as seen on Figures 7.3 and 7.2. In the case of  $q=0.001$  and  $q=0.003$  this shape is less pronounced and despite an offset of roughly 5‰ in deuterium excess the best model run to fit the observed values would be SHIP D, probably with  $q=0.001$ . Thus in this case, with the results from this work (and not considering the offset), the super saturation function needed for the same moisture source is significantly lower.  $q=0.008$  is generally a high estimate for the super saturation function and most authors have used less, e.g.  $q=0.0017$  used by Landais et al. (2008). However, not much knowledge exist about this and many authors have used best fitting to find the appropriate coefficients in the super saturation function. Improving the knowledge of the ice-vapor equilibrium fractionation factor is therefore very important for constraining the contribution of kinetic fractionation in the above mentioned processes.

To summarize, the differences in equilibrium fractionation factor have a significant impact when trying to constrain the super saturation function and the moisture source for a given sink and this is of much relevance for investigations of the processes in the

hydrological cycle.

## 7.4 Conclusion

The above model results show significant changes in both magnitude and shape of the deuterium excess signal when using the results from this work, as compared to previous results. This underlines the fact that changes in basic components in such models can cause significant changes in the model output. Besides from the different shape of the annual deuterium excess cycle we observed offsets and variations of  $\sim 10\text{‰}$  in deuterium excess for both vapor and condensate. For comparison, the magnitude of variations in deuterium excess in Antarctic and Greenland ice cores is on the order of  $5\text{‰}$  (e.g. Steen-Larsen et al. (2010) and Uemura et al. (2004)). These changes are interpreted to indicate humidity and temperature variations in the moisture source region as shown above and are used to reconstruct the condensation temperature of the precipitation. Hence, since these variations are of the same magnitude as the variations observed above, this emphasizes the importance of the equilibrium fractionation factors in the interpretation of the processes in the hydrological cycle. Furthermore it underlines the significance of the differences between the results of this work and previous results.

## Chapter 8

# Conclusions

In this work we successfully designed and built an experimental setup with the purpose of investigating the temperature dependency of the ice-vapor equilibrium fractionation factor and to improve the temperature range of earlier work. Through some evolutionary cycles with testing and modifications, the experimental setup proved to work as intended with good reproducibility of the data. The main limitation of the setup was the time consuming data acquisition, mainly due to memory effects and the low vapor pressure, and as future improvements a different collection and measurement method could solve this.

By using both Picarro and IRMS instruments for the characterization and measurements, we were able to use the advantages of both techniques. The Picarro proved very valuable in the characterization of the system due to the ability of continuous monitoring the isotopes, but this technique had limitations for the actual measurements at low vapor pressures. The IRMS system on the other hand was limited in the characterization of the system due to the discrete measurements but this was the advantage for the measurements since here, the sampling time could just be increased. Besides for the Picarro  $\delta D$  calibrations, the calibrations and corrections performed well and did not introduce any significant uncertainties on the dataset. The IRMS dataset was the most extensive, covering a temperature range of  $-10^{\circ}\text{C}$  to  $-40^{\circ}\text{C}$  while the Picarro dataset was more sparse with a temperature range between  $-5^{\circ}\text{C}$  and  $-20^{\circ}\text{C}$  due to limited time allocation and humidity limitations.

### 8.1 Equilibrium conditions in the setup

Investigations of the equilibrium conditions for the vapor source and the equilibrium chamber were made. The vapor source performed well, delivering vapor with a stable isotopic composition at stable temperature and humidities, suitable for our needs. Some differences between observed and expected isotope values were seen but these were explained

by uncertainties and weak humidity calibration of the instrument. Kinetic effects were not present during evaporation but some long term enrichment of the vapor source was seen. The magnitude of this was characterized and the resulting changes in  $\delta D$  and  $\delta^{18}O$  of the vapor were are close to the measurement uncertainties of the instrumentation and were neglected. Surface cooling is most likely not an issue in the vapor source but a cooling effect of  $0.4^{\circ}C$  is possible within the uncertainties of the measurements. This was also neglected. The Picarro and IRMS vapor measurements were performed with two different carrier gases, and since the vapor measurements with both instruments are in agreement with each other, this confirms the performance of the setup. The main limitation of the vapor source characterization was the low amount of water and vapor samples. Higher sampling frequency here could have improved the investigation of the enrichment of the vapor source.

Investigations of the changes in the isotope ratios during a typical measurement run strongly indicated that equilibrium conditions are obtained in the equilibrium chamber. Furthermore, the small scale changes in isotope ratios and humidity due to temperature fluctuations in the equilibrium chamber could be predicted to a high detail by models assuming equilibrium. Kinetic effects do not seem to be present and the response of the equilibrium chamber indicate proper exchange between the vapor and ice phases for temperatures above  $-40^{\circ}C$ . For temperatures below this, ice crystals began growing towards the vapor flow and kinetic effects disturbed the equilibrium conditions. This was the main limitation of the equilibrium chamber and along with the memory effects in the TC/EA this effect limited the temperature range.

## 8.2 Experimental results

The performances of the vapor source and equilibrium chamber confirmed the assumptions of the system and allowed for the calculation of the ice-vapor equilibrium fractionation factor. The results of the experiments show fractionation factors for  $\delta D$  and  $\delta^{18}O$ , with a temperature dependency well in accordance with theory for equilibrium fractionation, for temperatures between  $0^{\circ}C$  and  $-40^{\circ}C$ . The best fit was found with the relationship of  $\ln \alpha = C_1 + C_2/T + C_3/T^2$ , giving the following expressions for the results:

$$\ln(\alpha_{\delta D}) = 0.2133 - \frac{203.10}{T} + \frac{48888}{T^2} \quad (8.2.1)$$

$$\ln(\alpha_{\delta^{18}O}) = 0.0831 - \frac{49.192}{T} + \frac{8312.5}{T^2} \quad (8.2.2)$$

Compared to the reference works of Majoube (1970) and Merlivat and Nief (1967), a significantly larger fractionation factor for  $\delta D$  is obtained while for  $\delta^{18}O$  the fractionation

factor is larger for temperatures below  $-20^{\circ}\text{C}$  and slightly lower for temperatures above this. Due to the similarities between our  $\delta^{18}\text{O}$  results and previous results and since the same method were used to measure  $\alpha$  for  $\delta\text{D}$ , this supports our  $\delta\text{D}$  results. Most errors in the experimental setup would reduce the fractionation factor while the few errors increasing it are argued to be unlikely to occur. The observed differences between this work and the work of Merlivat and Nief (1967) and Majoube (1970) could be due to the differences in the experimental setups, with their system possibly being influenced by backdiffusion effects.

With the results from this work the ice-liquid fractionation factor was found with values of  $\alpha_{ice-liquid} = 1.0187$  for  $\delta\text{D}$  and  $\alpha_{ice-liquid} = 1.00277$  for  $\delta^{18}\text{O}$  and these results agree very well with previously published results.

### 8.3 Impacts on processes in the hydrological cycle and future work

D/H in the martian climate is an important indicator for the vapor fluxes between the different water reservoirs on a seasonal scale and the key to understand the evolution and size of previous and present water reservoirs on Mars. These are subjects where fundamental knowledge about the governing processes is still missing and where investigations with isotope models use the equilibrium fractionation factor at temperatures down to 200K. To investigate this, a case study of condensation in the martian atmosphere showed that the differences between Mars temperature (202 K) extrapolated  $\alpha$  from Merlivat and Nief (1967) and from this work not surprisingly cause significant changes in model output. To some extent, the results of this work can help constrain the isotope models used to interpret and understand the above mentioned processes. But it is clear that more knowledge about the equilibrium fractionation factor at martian temperatures is needed for these purposes. This will also be of high relevance in the future where seasonal investigations of the D/H in the martian atmosphere, as well as a D/H record from an ice core from the ice caps or the subsurface ice, hopefully will be available.

The impact of the differences between the results of Merlivat and Nief (1967) and Majoube (1970) and this work were investigated with a Rayleigh distillation model (Johnsen et al., 1989; Steen-Larsen et al., 2010). The model results show significant changes in both magnitude and shape of the annual deuterium excess signal when using the results from this work, as compared to earlier work. This underlines the fact that changes in basic components in such models can cause significant changes in the model output. Here, offsets and variations of 5-10‰ in deuterium excess were seen for both vapor and condensate. For comparison, the magnitude of variations in deuterium excess in Antarctic and Greenland ice cores is on the order of 5‰ (e.g. Steen-Larsen et al. (2010) and Uemura et al. (2004)). These variations are interpreted to indicate humidity and temperature variations in the

moisture source region as shown above, and are used to reconstruct the condensation temperature of the precipitation. Hence, since these variations are of the same magnitude as the variations observed with these results, this emphasizes the importance of the fractionation factor for accurate studies of the processes in the hydrological cycle. Furthermore it underlines the significance of the differences between the results of this work and earlier work. We therefore conclude that the results of this work should be considered in future evaluations of the ice-vapor processes in the hydrological cycle.

The results presented in this work emphasize the need for better characterization and validation of the basic parameters in the models used to investigate the present and past climates on Earth and Mars. Some of these parameters depend on the ice-vapor equilibrium fractionation factor or can be better constrained with accurate knowledge of this. Examples of these parameters are the ice-liquid fractionation factors (Arnason, 1969; O'Neil, 1968), the liquid-water fractionation factors (Majoube, 1971b), the kinetic fractionation effects under condensation and the super saturation function (Jouzel and Merlivat, 1984), the possible temperature dependency of the diffusion fractionation factor (Luz et al., 2009) and  $\alpha$  for  $^{17}\text{O}$  (Landais et al., 2009).

# List of Figures

1.1	Rayleigh distillation in the vapor source (see next Chapter) with $T=1.41^{\circ}\text{C}$ and initial composition of $\delta\text{D} = -62.08\%$ . $f$ is the fraction of the remaining water. Liquid-vapor equilibrium fractionation factors from Majoube (1971b).	8
1.2	Previous work on the ice-vapor equilibrium fractionation factor for $\delta\text{D}$	13
1.3	Previous work on the ice-vapor equilibrium fractionation factor for $\delta^{18}\text{O}$	14
2.1	Sketch illustrating the principles of the experiments.	16
2.2	A chart of the flow lines in the experimental setup. A VICI 8-port valve is used to change the flow line (sample/purge) through the cryofocus. All tubing is heated with rope heaters.	17
2.3	A picture of the experimental setup with indications of the different units.	18
2.4	A picture of the VICI valve connecting the different parts of the experimental setup. The valve is heated with rope heaters and the location of the different connections are indicated.	20
2.5	Sketch of the connection between the experimental setup, the TC/EA and the IRMS. (Modified figure from ThermoScientific TC/EA brochure)	22
2.6	$\delta\text{D}$ as a function of peak area for injections of two different standards. Some peak area dependencies on the resulting $\delta\text{D}$ can be seen.	24
2.7	$\delta\text{D}$ and $\delta^{18}\text{O}$ as a function of injection number for three different standards. The memory effect of the system is stronger for $\delta^{18}\text{O}$ than for $\delta\text{D}$	25
2.8	The experimental setup is connected to the TC/EA injection port through a fitting with a conical head attached to a needle. Rope heaters keep a high temperature to limit adsorption/condensation, Vacuum grease on and around the fitting head ensures leak tightness.	26
2.9	Left: Kovar glass-metal connection connected to a Swagelok fitting. Right: the NiCr heating wire inside and outside the cryofocus ensure quick heating of the collected sample during sample injection. Rope heaters are always on to limit adsorption and condensation in the tubing.	27

---

2.10	The cryofocus in purge mode (A) and sampling mode (B). The rope heaters can be seen heat a part of the cryofocus and the tubing permanently, while the NiCr heating wire is only on during sample injection. . . . .	28
2.11	The vapor source water cylinder with three connections, mounted on a stainless steel stand. . . . .	30
2.12	Freezer with the vapor source submerged and attached to the rest of the setup. . . . .	31
2.13	Left: Inlet fitting with diffuser mounted on the vapor source cylinder. Right: Diffuser mounted on the inlet fitting. . . . .	32
2.14	Temperature control unit. Right: PVC housing. Left: The different components inside the unit. . . . .	33
2.15	The equilibrium chamber is custom made (right) of several spheres to increase the ice-vapor exchange (left). When mounted in the cooling bath the parts above the liquid level are heated and the addition of an outlet tube results in the vapor condensing out below the liquid level (middle). . . . .	34
2.16	Diffusion coefficient of H <sub>2</sub> O in Helium and Nitrogen as a function of temperature at 1 atm . . . . .	35
2.17	Left: Dismantled standard injection port which shows the septum and the modified nut. Right: Manual injections of 0.2 $\mu$ L standard water is done with a SGE syringe. . . . .	36
3.1	Collection time for 0.2E-6 kg water as a function of temperature in the equilibrium chamber. The calculations are based on vapor pressure differences. The mass of condensate can be seen approaching the total mass of the vapor entering the equilibrium chamber (dashed) as the temperature decreases. . .	39
3.2	Typical examples of the Picarro dataset (absolute humidity, $\delta$ D and $\delta^{18}$ O as a function of time) for the vapor source and vapor from the equilibrium chamber. Note that the sensitivity decreases with decreasing temperature. The temperature of the samples are within 0.2 $^{\circ}$ C of the temperature in the legend. . . . .	40
3.3	Allan variance as a function of integration time for $\delta$ D for measurements of the vapor source directly as well as for vapor from the equilibrium chamber at different temperatures. . . . .	42
3.4	Allan variance as a function of integration time for $\delta^{18}$ O for measurements of the vapor source directly as well as for vapor from the equilibrium chamber at different temperatures. . . . .	43

3.5	The vapor pressure or absolute humidity in ppmv as a function of temperature based on 1 atm (101325 Pa) in the system. . . . .	44
3.6	A section of the H <sub>2</sub> O Picarro humidity calibration measurements. There are between 6 and 8 seconds between each data point. The reference humidity is 18150 ppmv and the humidity is being varied from ~12800 ppmv to ~4000 ppmv in this section. . . . .	45
3.7	H <sub>2</sub> O Picarro humidity calibration fit for $\delta^{18}\text{O}$ . The graph shows the difference in isotope value caused by a change in humidity. A seven degree polynomial is used for fitting and this performs well for the range needed. . . . .	46
3.8	Picarro humidity calibration fit for $\delta\text{D}$ . The graph shows the difference in isotope value caused by a change in humidity. A double exponential function is used for fitting and this performs very well for the range needed. . . . .	47
3.9	H <sub>2</sub> O Picarro VSMOW calibration for $\delta^{18}\text{O}$ performed around 6100 ppm humidity. A clear linear relationship is seen. . . . .	48
3.10	H <sub>2</sub> O Picarro VSMOW calibration for $\delta\text{D}$ performed around 6100 ppm humidity. A clear linear relationship is seen. . . . .	48
3.11	Picarro results for $\delta\text{D}$ and $\delta^{18}\text{O}$ as a function of temperature. All measurements are shown including tests and non-stable measurements which create some deviation in the distributions. The data points can be seen in Table 3.3	50
3.12	Typical IRMS mass chromatogram of $m/z = 2$ and $3$ and $m/z = 28, 29$ and $30$ . Top: The isotope ratios of the different species. Middle: Peaks with intensity in mV. Bottom: Results from Isodat routine. The different peaks denoted by numbers are: 1: H <sub>2</sub> reference gas peak, 2: H <sub>2</sub> sample peak, 3: CO reference peak, 4: CO sample peak. . . . .	53
3.13	A typical IRMS sample run consisting of 9 measurements. The first measurements are affected by the memory effect of the system and are discarded when calculating the mean values. The ‰ values are uncalibrated. . . . .	54
3.14	$\delta\text{D}$ VSMOW calibration lines based on run numbers from Table 3.5: A = 278-304, B = 305-317, C = 318-335, D = 336-359, E = 360-385, F = 386-400.	57
3.15	$\delta^{18}\text{O}$ VSMOW calibration lines based on run numbers from Table 3.5: A = 278-304, B = 305-317, C = 318-335, D = 336-359, E = 360-385, F = 386-400.	58
3.16	IRMS results for $\delta\text{D}$ and $\delta^{18}\text{O}$ as a function of temperature. All measurements are shown including tests and non-stable measurements. The deviation in the distributions can be seen to grow as a function of lower temperature. The limits of the setup can be seen below -40°C. The data points can be seen in Table 3.7 . . . . .	61

---

4.1	Vapor source measurements over 12 hours showing temperature measured in vapor source water, absolute humidity, $\delta D$ and $\delta^{18}O$ as measured by the Picarro. Smoothed versions of $\delta D$ and $\delta^{18}O$ are shown, as is expected humidity and isotopic composition assuming equilibrium. . . . .	64
4.2	Measured humidity versus modelled (calibrated) humidity based on temperature measurements. Fit 1 is based on measured data below 5000 ppmv and Fit 2 is based on all datapoints . . . . .	65
4.3	Test for kinetic fractionation in the vapor source. The carrier gas flow rate was varied to check for changes in $\delta D$ and $\delta^{18}O$ as a function of this. No significant changes can be seen. . . . .	67
4.4	The Rayleigh model (full) for MQ1 based on $\delta D = -60.73 \pm 0.15\%$ with the propagated uncertainties (dashed) along with the values from Table 4.1. $f$ is the fraction of the initial water left in the vapor source. . . . .	70
4.5	The Rayleigh model (full) for MQ2 based on $\delta D = -62.08 \pm 0.14\%$ with the propagated uncertainties (dashed) along with the values from Table 4.1. $f$ is the fraction of the initial water left in the vapor source. . . . .	71
4.6	Rayleigh model (full) with uncertainties (dashed) and vapor source measurements as a function of time for MQ1. . . . .	72
4.7	Rayleigh model (full) with uncertainties (dashed) and vapor source measurements as a function of time for MQ2. . . . .	72
4.8	A typical Picarro run starting out with measurements of the vapor source. After this the equilibrium chamber is dried out and the tubing is humidified. Then vapor is allowed to enter the equilibrium chamber and the experiment starts. After being in non-equilibrium the system reaches an equilibrium state. . . . .	77
4.9	The part of Figure 4.8 containing the experiment start, the non-equilibrium and the equilibrium parts. . . . .	78
4.10	Picarro absolute humidity, $\delta D$ and $\delta^{18}O$ for $-10^\circ C$ vapor measurements from the equilibrium chamber along with the temperature in the Multi-Cooler, measured separately. . . . .	80
4.11	Response of the equilibrium chamber as a function of flow rate. No significant changes are seen in neither absolute humidity or in the isotope values. . . . .	81
4.12	$\alpha$ for $\delta D$ and $\delta^{18}O$ as a function of temperature with and without outlet tube in the equilibrium chamber. In general, a stronger fractionation is seen with the outlet tube, confirming the theory that the outlet tube will limit diffusion effects in the equilibrium chamber. . . . .	83

5.1	The difference ( $\Delta\alpha$ ) for $\delta\text{D}$ and $\delta^{18}\text{O}$ between $\alpha$ with $\delta_{v0}$ based on the average vapor measurements and $\alpha$ with $\delta_{v0}$ based on the Rayleigh model. . . . .	89
5.2	The difference ( $\Delta\alpha$ ) for $\delta\text{D}$ and $\delta^{18}\text{O}$ between $\alpha$ with $\delta_{v0}$ based on the average vapor measurements and $\alpha$ with $\delta_{v0}$ based on conditions with a surface cooling effect of $0.41^\circ\text{C}$ . . . . .	90
5.3	Equilibrium fractionation factor $\alpha$ results for $\delta\text{D}$ . All data for Picarro and IRMS measurements are shown. . . . .	92
5.4	Equilibrium fractionation factor $\alpha$ results for $\delta^{18}\text{O}$ . All data for Picarro and IRMS measurements are shown. . . . .	94
5.5	$\ln\alpha$ for $\delta\text{D}$ and $\delta^{18}\text{O}$ as a function of $T^{-1}$ , fitted with $\ln\alpha = C_1 + C_2/T$ . The dashed line indicate $0^\circ\text{C}$ . The fitting result can be seen in Table 5.5. . . . .	95
5.6	$\ln\alpha$ for $\delta\text{D}$ and $\delta^{18}\text{O}$ as a function of $T^{-2}$ , fitted with $\ln\alpha = C_1 + C_3/T^2$ . The dashed line indicate $0^\circ\text{C}$ . The fitting result can be seen in Table 5.5. . . . .	96
5.7	$\ln\alpha$ for $\delta\text{D}$ and $\delta^{18}\text{O}$ as a function of $T$ , fitted with $\ln\alpha = C_1 + C_2/T + C_3/T^2$ . The dashed line indicate $0^\circ\text{C}$ . The fitting result can be seen in Table 5.5. . . . .	96
5.8	Residual between the average $\alpha$ values and the different fit types, as seen in Table 5.6. . . . .	98
5.9	Comparison of the different fits and the previous published data for $\delta\text{D}$ when extrapolating outside the measurement range. . . . .	99
5.10	Comparison of the different fits and the previous published data for $\delta^{18}\text{O}$ when extrapolating outside the measurement range. . . . .	100
5.11	$\alpha$ for $\delta\text{D}$ for this work compared with previously published results. . . . .	101
5.12	$\alpha$ for $\delta^{18}\text{O}$ for this work compared with previously published results. . . . .	103
5.13	Figure 1 from Merlivat and Nief (1967) showing their experimental setup. . . . .	104
6.1	Column abundance of water vapor in the martian atmosphere as a function of $L_s$ (time) and latitude as observed by MGS-TES (Smith, 2004). MY indicates Mars year. . . . .	113
6.2	$\delta\text{D}$ as a function of precipitable water content in the martian atmosphere. Figure from Fisher (2007), data reproduced from Mumma et al. (2003) . . . . .	114
6.3	Fractionation of the atmospheric vapor as a function of precipitable water content with the different cloud models as described in Fisher et al. (2008). . . . .	118
7.1	Illustration of the moisture transport from the evaporation site to the Greenland ice sheet. Here, $R_h$ is the relative humidity, $T_s$ is the surface temperature, $h_p$ is elevation above the ice sheet and $H_s$ is the site height. Figure from Sjolte (2005), adapted from Johnsen et al. (1989). . . . .	121

7.2	Effective fractionation of $\delta D$ for two different super saturation functions compared to equilibrium fractionation. M&N indicates the work of Merlivat and Nief (1967).	122
7.3	Effective fractionation of $\delta^{18}O$ for two different super saturation functions compared to equilibrium fractionation. M1970 indicates the work of Majoube (1970)	123
7.4	Moisture sources SHIP D and SHIP E sea surface temperature and relative humidity.	124
7.5	Approximated $\delta D$ and $\delta^{18}O$ cycle for the NEEM site from Steen-Larsen et al. (2010).	125
7.6	Vapor and condensate trajectories as a function of temperature for $\delta^{18}O$ for a selected run with SST=25°C and RH=0.85 as initial conditions.	126
7.7	Vapor and condensate trajectories as a function of temperature for $\delta D$ for a selected run with SST=25°C and RH=0.85 as initial conditions.	127
7.8	Vapor and condensate trajectories as a function of temperature for deuterium excess for a selected run with SST=25°C and RH=0.85 as initial conditions. M&M indicates the work of Merlivat and Nief (1967) and Majoube (1970)	128
7.9	Output from the model runs. Solid lines are results with the ice-vapor equilibrium fractionation factors from this work and dashed lines are from the work of Merlivat and Nief (1967) and Majoube (1970) (M & M). Significant differences in both precipitation and condensate values change the deuterium excess values and shape.	129
7.10	Annual deuterium excess cycle for model runs with different fractionation factors and different super saturation functions, $SS = 1-q*T$ . M&M indicates the work of Merlivat and Nief (1967) and Majoube (1970)	130
7.11	Annual deuterium excess cycle for model runs with different fractionation factors and different super saturation functions, $SS = 1-q*T$ . M&M indicates the work of Merlivat and Nief (1967) and Majoube (1970)	131

# List of Tables

2.1	Molecular radii of different species assuming hard elastic spheres. . . . .	35
3.1	Working standards in ‰ for VSMOW calibrations as well as measured values for ~6100 ppm in ‰. SDOM is the standard deviation of the mean of the intervals used (typically 60 data points) . . . . .	49
3.2	H <sub>2</sub> O Picarro VSMOW calibration line fits with $y = ax + b$ . . . . .	49
3.3	Picarro results for $\delta D$ and $\delta^{18}O$ . All values are humidity and VSMOW calibrated. SDOM is the standard deviation of the mean of the integration interval and $\sigma$ indicates the deviation of the integration interval. $T$ is the temperature, $\sigma T$ is the deviation on $T$ , $hum_{av}$ is the average absolute humidity and $\delta^{18}O$ and $\delta D$ error are the propagated errors. . . . .	52
3.4	Working standard values vs. VSMOW in ‰ used for IRMS VSMOW calibrations. Uncertainties are $\pm 0.1\%$ for $\delta D$ ‰ and 0.05 for $\delta^{18}O$ unless otherwise noted. . . . .	55
3.5	VSMOW calibration injection results for the IRMS measurements. The calibration runs are divided into several sections to account for long term changes. Subscripts $m$ and $t$ indicates measured and true (VSMOW) values respectively. $n$ is the amount of values and $\sigma_{\bar{x}}$ indicates standard deviation of the mean. . . . .	56
3.6	IRMS VSMOW calibration line fits $y = ax + b$ with uncertainties ( $\pm 1\sigma$ ) for the different calibration lines A-F. . . . .	59
3.7	IRMS measurement results for $\delta D$ and $\delta^{18}O$ . All values are VSMOW calibrated. SDOM is the standard deviation of the mean based on $n$ measurements. . . . .	60
4.1	Measurements of vapor source water isotopic composition. Sampling days are estimated assuming the amount of vapor removed for each measurement run. SDOM is the standard deviation of the mean based on $n$ samples. . . .	69

---

5.1	$\Delta\alpha$ investigations for $\alpha_{\delta D}$ . Typical values of $\delta D \pm 0.5\%$ for each temperature are used. . . . .	87
5.2	$\Delta\alpha$ investigations for $\alpha_{\delta^{18}O}$ . Typical values of $\delta^{18}O \pm 0.2\%$ for each temperature are used. . . . .	87
5.3	Equilibrium fractionation factor $\alpha$ results from the Picarro measurements. Data points flagged as bad are shown below the line. . . . .	91
5.4	Equilibrium fractionation factor $\alpha$ results from the IRMS measurements. Data points flagged as bad are shown below the line. $n$ is the amount of samples. . . . .	93
5.5	Fitting results for the three different temperature dependencies. . . . .	97
5.6	Weighted average values of the IRMS measurements as well as the values from the $\ln \alpha = C_1 + C_2/T + C_3/T^2$ fit. . . . .	98

# Bibliography

- D.W. Allan. Statistics of atomic frequency standards. *Proceedings of the IEEE*, 54 (Issue:2):221 – 230, 1966. URL [http://ieeexplore.ieee.org/xpl/freeabs\\_all.jsp?arnumber=1446564](http://ieeexplore.ieee.org/xpl/freeabs_all.jsp?arnumber=1446564).
- B. Arnason. Equilibrium constant for fractionation of deuterium between ice and water. *Journal of Physical Chemistry*, 73(10):3491–&, 1969. E3547 Times Cited:33 Cited References Count:11.
- S. S. Assonov and C. A. M. Brenninkmeijer. A redetermination of absolute values for r-17(vpdb-co2) and r-17(vsmow). *Rapid Communications In Mass Spectrometry*, 17(10):1017–1029, 2003a. doi: 10.1002/rcm.1011.
- S. S. Assonov and C. A. M. Brenninkmeijer. On the o-17 correction for co2 mass spectrometric isotopic analysis. *Rapid Communications In Mass Spectrometry*, 17(10):1007–1016, 2003b. doi: 10.1002/rcm.1012.
- Eugeni Barkan and Boaz Luz. High precision measurements of 17o/16o and 18o/16o ratios in h2o. *Rapid Communications in Mass Spectrometry*, 19(24):3737–3742, 2005. URL <http://dx.doi.org/10.1002/rcm.2250>.
- Eugeni Barkan and Boaz Luz. Diffusivity fractionations of h216o/h217o and h216o/h218o in air and their implications for isotope hydrology. *Rapid Communications in Mass Spectrometry*, 21(18):2999–3005, 2007. URL <http://dx.doi.org/10.1002/rcm.3180>.
- G. Berden, R. Peeters, and G. Meijer. Cavity ring-down spectroscopy: Experimental schemes and applications. *International Reviews in Physical Chemistry*, 19(4):565–607, 2000. 381VZ Times Cited:334 Cited References Count:179.
- J. Bigeleisen, M. W. Lee, and F. Mandel. Equilibrium isotope-effects. *Annual Review of Physical Chemistry*, 24:407–440, 1973. ISI Document Delivery No.: R6788 Times Cited: 37 Cited Reference Count: 259 Annual reviews inc Palo alto.
- Jacob Bigeleisen. Statistical mechanics of isotope effects on the thermodynamic properties of condensed systems. *J. Chem. Phys.*, 34(5):1485–1493, May 1961. URL <http://link.aip.org/link/?JCP/34/1485/1>.

- Jacob Bigeleisen and Maria Goeppert Mayer. Calculation of equilibrium constants for isotopic exchange reactions. *The Journal of Chemical Physics*, 15(5):261–267, 1947.
- T Blunier and EJ Brook. Timing of millennial-scale climate change in antarctica and greenland during the last glacial period. *Science*, 291(5501):109112, 2001.
- G. Boato, G. Casanova, and A. Levi. Isotope effect in phase equilibria. *The Journal of Chemical Physics*, 37(1):201–202, 1962. URL <http://dx.doi.org/10.1063/1.1732963>.
- Y. Bottinga and M. Javoy. Comments on oxygen isotope geothermometry. *Earth and Planetary Science Letters*, 20(2):250–265, October 1973. ISSN 0012-821X. URL <http://www.sciencedirect.com/science/article/B6V61-47260NF-3H/2/5ff2546b252df3c5532bb54bbff8acae>.
- et al. Boynton, W. V. Distribution of hydrogen in the near surface of mars: Evidence for subsurface ice deposits. *Science*, 297:81–85, 2002. doi: doi:10.1126/science.1073722.
- W. V. Boynton, D. W. Ming, S. P. Kounaves, S. M. M. Young, R. E. Arvidson, M. H. Hecht, J. Hoffman, P. B. Niles, D. K. Hamara, R. C. Quinn, P. H. Smith, B. Sutter, D. C. Catling, and R. V. Morris. Evidence for calcium carbonate at the mars phoenix landing site. *Science*, 325(5936):61–64, July 2009. URL <http://www.sciencemag.org/cgi/content/abstract/325/5936/61>.
- W. A. Brand, S. S. Assonov, and T. B. Coplen. Correction for the o-17 interference in delta(c-13) measurements when analyzing co2 with stable isotope mass spectrometry (iupac technical report). *Pure and Applied Chemistry*, 82(8):1719–1733, August 2010. doi: 10.1351/PAC-REP-09-01-05.
- Willi A. Brand, Heike Geilmann, Eric R. Crosson, and Chris W. Rella. Cavity ring-down spectroscopy versus high-temperature conversion isotope ratio mass spectrometry; a case study on d2h and d18o of pure water samples and alcohol/water mixtures. *Rapid Communications in Mass Spectrometry*, 23(12):1879–1884, 2009.
- C. D. Cappa, M. B. Hendricks, D. J. DePaolo, and R. C. Cohen. Isotopic fractionation of water during evaporation. *Journal of Geophysical Research-Atmospheres*, 108(D16): –, 2003. 720GA Times Cited:71 Cited References Count:40.
- T. Chacko, D. Cole, and J. Horita. Equilibrium oxygen, hydrogen and carbon isotope fractionation factors applicable to geologic systems. *Reviews in Mineralogy and Geochemistry*, 43:1–81, 2001.
- S. Chapman and T. Cowling. *The Mathematical Theory of Non-Uniform Gases*. 3rd ed., Cambridge Univ. Press, New York., 1970.

- Robert N Clayton and Toshiko K Mayeda. Isotopic composition of carbonate in eeta 79001 and its relation to parent body volatiles. *Geochimica et Cosmochimica Acta*, 52(4):925–927, April 1988. ISSN 0016-7037. URL <http://www.sciencedirect.com/science/article/B6V66-488Y210-R/2/4c56a442249f15c279af44918a274b86>.
- H Craig and LI. Gordon. Deuterium and oxygen-18 variations in the ocean and marine atmosphere. In *Stable Isotopes in Oceanographic studies and Paleo-Temperatures*, ed. E Tongiorgi, pages 9–130, 1965.
- Harmon Craig. Isotopic standards for carbon and oxygen and correction factors for mass-spectrometric analysis of carbon dioxide. *Geochimica Et Cosmochimica Acta*, 12(1-2): 133–149, 1957.
- Harmon Craig. Standard for reporting concentrations of deuterium and oxygen-18 in natural waters. *Science*, 133(3467):1833–1834, 1961.
- R. E. Criss. *Principles of Stable Isotope Distribution*. Oxford University Press, USA (June 3, 1999), 1999.
- E. R. Crosson. A cavity ring-down analyzer for measuring atmospheric levels of methane, carbon dioxide, and water vapor. *Applied Physics B-Lasers and Optics*, 92(3):403–408, 2008. 341HA Times Cited:6 Cited References Count:8.
- Fabian Czerwinski, Andrew C. Richardson, and Lene B. Oddershede. Quantifying noise in optical tweezers by allan variance. *Opt. Express*, 17(15):13255–13269, July 2009. URL <http://www.opticsexpress.org/abstract.cfm?URI=oe-17-15-13255>.
- W. Dansgaard. The abundance of 18o in atmospheric water and water vapor. *Tellus*, 5: 461–469, 1953.
- W. Dansgaard. *The isotopic composition of natural waters*. PhD thesis, University of Copenhagen, 1961.
- W. Dansgaard. Stable isotopes in precipitation. *Tellus*, 16(4):436–468, 1964. Xf689 Times Cited:1976 Cited References Count:30.
- W. Dansgaard, S. J. Johnsen, J. Möller, and C.C. Langway. Oxygen isotope analysis of an ice core representing a complete vertical profile of a polar ice sheet. *ISAGE Symposium*, page 9394, 1968.
- H Fischer, M Wahlen, J Smith, D Mastroianni, and B Deck. Ice core records of atmospheric co2 around the last three glacial terminations. *Science*, 293(5408):1712–1714, 1999.
- K. Fishbaugh and C. Hvidberg. Martian north polar layered depository stratigraphy: Implications for accumulation rates and flow. *Journal of Geophysical Research*, 111 (E06012), 2006.

- D. Fisher. Mars' water isotope (d/h) history in the strata of the north polar cap: Inferences about the water cycle. *Icarus*, 187:430–441, 2007. doi: doi:10.1016/j.icarus.2006.10.032.
- D Fisher, R. Novak, and M. J. Mumma. D/h ratio during the northern polar summer and what the phoenix mission might measure. *J. Geophys. Res.*, 113:E00A15, 2008. doi: doi:10.1029/2007JE002972.
- Thierry Fouchet and Emmanuel Lellouch. Vapor pressure isotope fractionation effects in planetary atmospheres: Application to deuterium. *Icarus*, 144(1):114–123, March 2000. ISSN 0019-1035. URL <http://www.sciencedirect.com/science/article/B6WGF-45FC19C-6P/2/70b769d1e6a8e22d1caabc5478a86ff2>.
- Irving Friedman. Deuterium content of natural waters and other substances. *Geochimica Et Cosmochimica Acta*, 4(1-2):89–103, 1953.
- M. Gehre, H. Geilmann, J. Richter, R. A. Werner, and W. A. Brand. Continuous flow h-2/h-1 and and(18)o/o-16 analysis of water samples with dual inlet precision. *Rapid Communications in Mass Spectrometry*, 18(22):2650–2660, 2004. 875WU Times Cited:49 Cited References Count:18.
- V. Gkinis, T. J. Popp, Johnsen S. J., and T. Blunier. A continuous stream flash evaporator for the calibration of an ir cavity ring down spectrometer for isotopic analysis of water vapour. *Rapid Communications In Mass Spectrometry*, Submitted:–, 2010.
- J. A. Goff. Saturation pressure of water on the new kelvin scale. *Trans. Am. Soc. Heating Air-Cond. Eng.*, 63:347–354, 1957.
- J. A. Goff. *Saturation pressure of water on the new Kelvin scale. In Humidity and moisture: Measurement and control in science and industry.* Reinhold Publishing, New York, USA, 1965.
- R. Gonfiantini. Standards for stable isotope measurements in natural compounds. *Nature*, 271(5645):534–536, February 1978. URL <http://dx.doi.org/10.1038/271534a0>.
- P. Gupta, D. Noone, J. Galewsky, C. Sweeney, and B. H. Vaughn. Demonstration of high-precision continuous measurements of water vapor isotopologues in laboratory and remote field deployments using wavelength-scanned cavity ring-down spectroscopy (ws-crds) technology. *Rapid Communications in Mass Spectrometry*, 23(16):2534–2542, 2009. 480HN Times Cited:0 Cited References Count:22.
- J. H. Hoffman, R. C. Chaney, and H. Hammack. Phoenix mars mission-the thermal evolved gas analyzer. *Journal of the American Society For Mass Spectrometry*, 19(10):1377–1383, October 2008. doi: 10.1016/j.jasms.2008.07.015.

- Juske Horita, Kazimierz Rozanski, and Shabtai Cohen. Isotope effects in the evaporation of water: a status report of the craigâgordon model. *Isotopes in Environmental and Health Studies*, 44(1):23–49, 2008. ISSN 1025-6016. URL <http://www.informaworld.com/10.1080/10256010801887174>.
- C. Hvidberg. Relationship between topography and flow in the north polar cap on mars. *Annals of Glaciology*, 37:363–369, 2003.
- IAEA/WMO. Environmental isotope data no. 1-6. world survey of isotope concentration in precipitation. Technical reports series 96, 117, 129, 147, 165 and 192., -, 1979.
- Gyorgy Jakli and D. Staschewski. Vapour pressure of h218o ice (-50 to 0[degree]c) and h218o water (0 to 170[degree]c). *J. Chem. Soc., Faraday Trans. 1*, 73:1505–1509, 1977. ISSN 0300-9599. URL <http://dx.doi.org/10.1039/F19777301505>.
- B. M. Jakosky. The role of seasonal reservoirs in the mars water cycle: 1. seasonal exchange of water with the regolith. *Icarus*, 55:1–18, 1983. doi: doi:10.1016/0019-1035(83)90046-5.
- Bruce M. Jakosky. Mars volatile evolution: Evidence from stable isotopes. *Icarus*, 94(1):14–31, November 1991. ISSN 0019-1035. URL <http://www.sciencedirect.com/science/article/B6WGF-4731FBY-11G/2/28af6dae776bf458fdfbf605dc0eef1a>.
- Gabor Jancso and W. Alexander Van Hook. Condensed phase isotope effects. *Chemical Reviews*, 74(6):689–750, 1974. doi: 10.1021/cr60292a004.
- Gabor Jancso, Jovan Pupezin, and W. Alexander Van Hook. Vapour pressure of h218o ice (i) (-17[deg] c to 0[deg] c) and h218o water (0[deg] c to 16[deg] c). *Nature*, 225(5234):723–723, 1970a. 10.1038/225723a0.
- Gabor Jancso, Jovan Pupezin, and W. Alexander Van Hook. Vapor pressure of ice between +10-2 and -1020. *The Journal of Physical Chemistry*, 74(15):2984–2989, July 1970b. ISSN 0022-3654. URL <http://dx.doi.org/10.1021/j100709a025>.
- M. Johansson and K. E. Holmberg. Separation of heavy water in phase equilibria involving pure water or salt-water systems. *Acta Chemica Scandinavica*, 23(3):765–&, 1969.
- S. J. Johnsen, W. Dansgaard, and J. W. C. White. The origin of arctic precipitation under present and glacial conditions. *Tellus Series B-Chemical and Physical Meteorology*, 41B(4):452–468, 1989.
- S.J. Johnsen, H.B. Clausen, W. Dansgaard, F. Fuhrer, N. Gundestrup, C.U. Hammer, P. Iversen, J. Jouzel, B. Stauffer, and J.P. Steffensen. Irregular glacial interstadials recorded in a new greenland ice core. *Nature*, 359, 1992.

- S.J. Johnsen, D. Dahl-Jensen, N. Gundestrup, J.P. Steffensen, H.B. Clausen, H. Miller, V. Masson-Delmotte, A.E. Sveinbjörndottir, and J. White. Oxygen isotope and palaeotemperature records from six greenland ice-core stations: Camp century, dye-3, grip, gisp2, renland and northgrip. *J. Quat. Sci.*, 16:299–307, 2001.
- J. Jouzel, V. Masson-Delmotte, O. Cattani, G. Dreyfus, S. Falourd, G. Hoffmann, B. Minster, J. Nouet, J. M. Barnola, J. Chappellaz, H. Fischer, J. C. Gallet, S. Johnsen, M. Leuenberger, L. Loulergue, D. Luethi, H. Oerter, F. Parrenin, G. Raisbeck, D. Raynaud, A. Schilt, J. Schwander, E. Selmo, R. Souchez, R. Spahni, B. Stauffer, J. P. Steffensen, B. Stenni, T. F. Stocker, J. L. Tison, M. Werner, and E. W. Wolff. Orbital and millennial antarctic climate variability over the past 800,000 years. *Science*, 317(5839):793–796, August 2007. URL <http://www.sciencemag.org/cgi/content/abstract/317/5839/793>.
- Jean Jouzel and Liliane Merlivat. Deuterium and oxygen 18 in precipitation: Modeling of the isotopic effects during snow formation. *J. Geophys. Res.*, 89(D7):11749–11757, 1984.
- H. Kieffer. *Mars*. University of Arizona Press, Tucson, Arizona, 1992.
- V. A. Krasnopolsky, G. L. Bjoraker, M. J. Mumma, and D. E. Jennings. High-resolution spectroscopy of mars at 3.7 and 8 micrometer: A sensitive search for h<sub>2</sub>o<sub>2</sub>, h<sub>2</sub>co, hcl, and ch<sub>4</sub>, and detection of hdo. *J. Geophys. Res.*, 102(E3):6525–6534, 1997. ISSN 0148-0227. URL <http://dx.doi.org/10.1029/96JE03766>.
- V. A. Krasnopolsky, M. J. Mumma, and G.R. Gladstone. Detection of atomic deuterium in the upper atmosphere on mars. *Science*, 280:1576–1580, 1998.
- V. A. Krasnopolsky, J. P. Maillard, T. C. Owen, R. A. Toth, and M. D. Smith. Oxygen and carbon isotope ratios in the martian atmosphere. *Icarus*, 192(2):396–403, December 2007. doi: 10.1016/j.icarus.2007.08.013.
- Vladimir A. Krasnopolsky and Paul D. Feldman. Detection of molecular hydrogen in the atmosphere of mars. *Science*, 294(5548):1914–1917, November 2001. URL <http://www.sciencemag.org/cgi/content/abstract/294/5548/1914>.
- A. Landais, E. Barkan, and B. Luz. Record of delta o-18 and o-17-excess in ice from vostok antarctica during the last 150,000 years. *Geophysical Research Letters*, 35(2):L02709, January 2008. doi: 10.1029/2007GL032096.
- A. Landais, E. Barkan, F. Vimeux, V. Masson-Delmotte, and B. Luz. Combined analysis of water stable isotopes (h<sub>2</sub>16o, h<sub>2</sub>17o, h<sub>2</sub>18o, hd16o) in ice cores. *Physics of Ice Core Records 2, Supplement Issue of Low Temperature Science*, 68, 2009.

- D. F. LaPorte, C. Holmden, W. P. Patterson, T. Prokopiuk, and B. M. Eglinton. Oxygen isotope analysis of phosphate: improved precision using tc/ea cf-irms. *Journal of Mass Spectrometry*, 44(6):879–890, 2009. URL <http://dx.doi.org/10.1002/jms.1549>.
- R.B. Leighton and B.C. Murray. Behavior of carbon dioxide and other volatiles on mars. *Science*, 153:136–144, 1966.
- D. R. Lide. *CRC Handbook of Chemistry and Physics (70th Edn.)*. CRC Press, 1990.
- G. Lis, L. I. Wassenaar, and M. J. Hendry. High-precision laser spectroscopy d/h and 18o/16o measurements of microliter natural water samples. *Analytical Chemistry*, 80(1):287–293, 2008. doi: 10.1021/ac701716q. URL <http://pubs.acs.org/doi/abs/10.1021/ac701716q>. PMID: 18031060.
- Boaz Luz, Eugeni Barkan, Ruth Yam, and Aldo Shemesh. Fractionation of oxygen and hydrogen isotopes in evaporating water. *Geochimica Et Cosmochimica Acta*, 73(22):6697–6703, 2009.
- M. Majoube. Fractionation factor of 18o between water vapour and ice. *Nature*, 226(5252):1242–1242, 1970. 10.1038/2261242a0.
- M. Majoube. Fractionation in o-18 between ice and water vapor. *Journal De Chimie Physique Et De Physico-Chimie Biologique*, 68(4):625–&, 1971a. J2318 Times Cited:51 Cited References Count:37.
- M. Majoube. Oxygen-18 and deuterium fractionation between water and steam. *Journal De Chimie Physique Et De Physico-Chimie Biologique*, 68(10):1423–&, 1971b. K7956 Times Cited:214 Cited References Count:56.
- S. Matsuo and O. Matsubaya. Vapour pressure of h218o ice. *Nature*, 221(5179):463–464, 1969. 10.1038/221463a0.
- Sadao Matsuo, Hideko Kuniyoshi, and Yasuo Miyake. Vapor pressure of ice containing d2o. *Science*, 145(3639):1454–1455, 1964.
- Michael B. Mcelroy and Yuk Ling Yung. Oxygen isotopes in the martian atmosphere: Implications for the evolution of volatiles. *Planetary and Space Science*, 24(12):1107–1113, December 1976. ISSN 0032-0633. URL <http://www.sciencedirect.com/science/article/B6V6T-472SR5N-G/2/a10aaf27e5487bce60d3efde19bc7dd9>.
- C. R. McKinney, J. M. Mccrea, S. Epstein, H. A. Allen, and H. C. Urey. Improvements in mass spectrometers for the measurement of small differences in isotope abundance ratios. *Review of Scientific Instruments*, 21(8):724–730, 1950. Uk558 Times Cited:351 Cited References Count:5.

- L. Merlivat and J. Jouzel. Global climatic interpretation of the deuterium-oxygen-18 relationship for precipitation. *Journal of Geophysical Research-Oceans and Atmospheres*, 84(Nc8):5029–5033, 1979. Hj772 Times Cited:326 Cited References Count:12.
- L. Merlivat and G. Nief. Fractionnement isotopique lors des changements de état solide-vapeur et liquide-vapeur de leau a des temperatures inferieures a 0 degres c. *Tellus*, 19(1):122–&, 1967. 90282 Times Cited:78 Cited References Count:8.
- Liliane Merlivat. Molecular diffusivities of h<sub>2</sub><sup>16</sup>o, hd<sup>16</sup>o, and h<sub>2</sub><sup>18</sup>o in gases. *The Journal of Chemical Physics*, 69(6):2864–2871, 1978. URL <http://dx.doi.org/10.1063/1.436884>.
- Merlin Méheut, Michele Lazzeri, Etienne Balan, and Francesco Mauri. Equilibrium isotopic fractionation in the kaolinite, quartz, water system: Prediction from first-principles density-functional theory. *Geochimica et Cosmochimica Acta*, 71(13):3170–3181, July 2007. ISSN 0016-7037. URL <http://www.sciencedirect.com/science/article/B6V66-4NJ0TNF-1/2/100d403f0e395e1d05ab3de6ba5ff4a8>.
- F. Montmessin, T. Fouchet, and F. Forget. Modeling the annual cycle of hdo in the martian atmosphere. *J. Geophys. Res.*, 110:E03006, 2005. doi: doi:10.1029/2004JE002357.
- W. G. Mook. Environmental isotopes in the hydrological cycle. *IHP-V, Technical Documents in Hydrology*, 1(39):–, 2000.
- M. J. Mumma, R. E. Novak, M. A. DiSanti, B. Bonev, N. Dello Russo, and K. Magee-Sauer. Seasonal mapping of hdo and h<sub>2</sub>o. *Sixth International Conference on Mars Atmosphere, Jet Propul. Lab., Pasadena, Calif.*, Abstract 3186:–, 2003.
- D. M. Murphy and T. Koop. Review of the vapour pressures of ice and supercooled water for atmospheric applications. *Quarterly Journal of the Royal Meteorological Society*, 131(608):1539–1565, 2005.
- A.O. Nier. A mass-spectrometer for isotope and gas analysis. *Rev. Sci. Instrum.*, 18:398–404, 1947.
- Paul B. Nilcs, William V. Boynton, John H. Hoffman, Douglas W. Ming, and Dave Hamara. Stable isotope measurements of martian atmospheric co<sub>2</sub> at the phoenix landing site. *Science*, 329(5997):1334–1337, September 2010. URL <http://www.sciencemag.org/cgi/content/abstract/329/5997/1334>.
- R. E. Novak, M. J. Mumma, S. Lee, L. Ivanov, B. Bonev, and G. Villanueva. Mapping of d/h and ozone in the martian atmosphere near perihelion. *Bull. Am. Astron. Soc.*, 35(3):669, 2005.

- R. E. Novak, G. M. J. Mumma, B. Villanueva, Bonev, and M. DiSanti. Mapping of hdo and h2o in the martian atmosphere. *Seventh International Conference on Mars, Jet Propul. Lab., Pasadena, Calif., -:-*, 2007.
- Anthony O'Keefe and David A. G. Deacon. Cavity ring-down optical spectrometer for absorption measurements using pulsed laser sources. *Rev. Sci. Instrum.*, 59(12):2544–2551, December 1988. URL <http://link.aip.org/link/?RSI/59/2544/1>.
- James R. O'Neil. Hydrogen and oxygen isotope fractionation between ice and water. *The Journal of Physical Chemistry*, 72(10):3683–3684, 1968. doi: 10.1021/j100856a060.
- James R. O'Neil. Theoretical and experimental aspects of isotopic fractionation. *Reviews in Mineralogy and Geochemistry*, 16(1):1–40, 1986.
- T. Owen. *Composition and early history of the atmosphere on Mars*. University of Arizona Press, Tucson, Arizona, 1992.
- T. Owen, K. Biemann, D.R. Rushneck, J.E. Biller, D.W. Howarth, and A.L. Lafleur. The composition of the atmosphere at the surface of mars. *J. Geophys. Res.*, 82:4635–4639, 1977.
- T. Owen, J. P. Maillard, C. de Bergh, and B. L. Lutz. Deuterium on mars -the abundance of hdo and the value of d/h. *Science*, 240:1767–1770, 1988.
- C. V. Paganelli and F. K. Kurata. Diffusion of water-vapor in binary and ternary gas-mixtures at increased pressures. *Respiration Physiology*, 30(1-2):15–26, 1977. Dj579 Times Cited:18 Cited References Count:14.
- C. A. Paulson and T. W. Parker. Cooling of a water surface by evaporation, radiation, and heat transfer. *J. Geophys. Res.*, 77(3):491–495, 1972. ISSN 0148-0227. URL <http://dx.doi.org/10.1029/JC077i003p00491>.
- J. R. Petit, J. W. C. White, N. W. Young, J. Jouzel, and Y. S. Korotkevich. Deuterium excess in recent antarctic snow. *J. Geophys. Res.*, 96(D3):5113–5122, 1991. ISSN 0148-0227. URL <http://dx.doi.org/10.1029/90JD02232>.
- J. R. Petit, J. Jouzel, D. Raynaud, N. I. Barkov, J.-M. Barnola, I. Basile, M. Bender, J. Chappellaz, M. Davis, G. Delaygue, M. Delmotte, V. M. Kotlyakov, M. Legrand, V. Y. Lipenkov, C. Lorius, L. PEpin, C. Ritz, E. Saltzman, and M. Stievenard. Climate and atmospheric history of the past 420,000 years from the vostok ice core, antarctica. *Nature*, 399(6735):429–436, June 1999. ISSN 0028-0836. URL <http://dx.doi.org/10.1038/20859>.
- Jovan D. Pupezin, Gyorgy Jakli, Gabor Jancso, and W. Alexander Van Hook. Vapor pressure isotope effect in aqueous systems. i. water-water-d2 (-64.deg. to 100.deg.) and

- water-water18-0 (-17.deg. to 16.deg.). ice and liquid. ii. alkali metal chloride solution in water and water-d2 (-5.deg. to 100.deg.). *The Journal of Physical Chemistry*, 76(5):743–762, March 1972. ISSN 0022-3654. URL <http://dx.doi.org/10.1021/j100649a025>.
- K. Rankama. *Isotope Geology*. Pergamon Oxford, 1954.
- L. Rayleigh. On the distillation of binary mixtures. *Philosophical Magazine*, 4(19-24):521–537, 1902. V42ej Times Cited:8 Cited References Count:3.
- J. Santrock, S. A. Studley, and J. M. Hayes. Isotopic analyses based on the mass-spectrum of carbon-dioxide. *Analytical Chemistry*, 57(7):1444–1448, 1985.
- F. A. Schwertz and Jeanne E. Brow. Diffusivity of water vapor in some common gases. *The Journal of Chemical Physics*, 19(5):640–646, 1951. URL <http://dx.doi.org/10.1063/1.1748306>.
- Alex L. Sessions, Thomas W. Burgoyne, and John M. Hayes. Determination of the h3 factor in hydrogen isotope ratio monitoring mass spectrometry. *Analytical Chemistry*, 73(2):200–207, 2000. doi: 10.1021/ac000488m.
- J. Sjolte. Interpretation of the isotopic composition of the greenland ice cores using simple modeling. Masters thesis, Niels Bohr Institute, University of Copenhagen, 2005.
- M. D. Smith. The annual cycle of water vapor on mars as observed by the thermal emission spectrometer. *J. Geophys. Res.*, 107(E11):5115, 2002. doi: doi:10.1029/2001JE001522.
- Michael D. Smith. Interannual variability in tes atmospheric observations of mars during 1999-2003. *Icarus*, 167(1):148–165, January 2004. ISSN 0019-1035. URL <http://www.sciencedirect.com/science/article/B6WGF-4B1SGYB-1/2/913198761c55214891ba8734e92d04da>.
- P. H. Smith, L. Tamppari, R. E. Arvidson, D. Bass, D. Blaney, W. Boynton, A. Carswell, D. Catling, B. Clark, T. Duck, E. DeJong, D. Fisher, W. Goetz, P. Gunnlaugsson, M. Hecht, V. Hipkin, J. Hoffman, S. Hviid, H. Keller, S. Kounaves, C. F. Lange, M. Lemmon, M. Madsen, M. Malin, W. Markiewicz, J. Marshall, C. McKay, M. Mellon, D. Michelangeli, D. Ming, R. Morris, N. Renno, W. T. Pike, U. Staufer, C. Stoker, P. A. Taylor, J. Whiteway, S. Young, and A. Zent. Introduction to special section on the phoenix mission: Landing site characterization experiments, mission overviews, and expected science. *Journal of Geophysical Research-Planets*, 113:–, 2008. 362DY Times Cited:8 Cited References Count:47.
- P. H. Smith, L. K. Tamppari, R. E. Arvidson, D. Bass, D. Blaney, W. V. Boynton, A. Carswell, D. C. Catling, B. C. Clark, T. Duck, E. DeJong, D. Fisher, W. Goetz, H. P. Gunnlaugsson, M. H. Hecht, V. Hipkin, J. Hoffman, S. F. Hviid,

- H. U. Keller, S. P. Kounaves, C. F. Lange, M. T. Lemmon, M. B. Madsen, W. J. Markiewicz, J. Marshall, C. P. McKay, M. T. Mellon, D. W. Ming, R. V. Morris, W. T. Pike, N. Renno, U. Staufer, C. Stoker, P. Taylor, J. A. Whiteway, and A. P. Zent. H<sub>2</sub>O at the phoenix landing site. *Science*, 325(5936):58–61, July 2009. URL <http://www.sciencemag.org/cgi/content/abstract/325/5936/58>.
- H. C. Steen-Larsen, V. Masson-Delmotte, J. Sjolte, S. J. Johnsen, B. M. Vinther, F-M Bréon, H. B. Clausen, D. Dahl-Jensen, S. Falourd, X. Fettweis, H. Gallée, J. Jouzel, M. Kageyama, H. Lerche, B. Minster, G. Picard, H. J. Punge, C. Risi, D. Salas, J. Schwander, K. Steffen, A. E. Sveinbjörnsdóttir, A. Svensson, and J. White. Understanding the climatic signal in the water stable isotope records from the neem shallow firn/ice cores in north-west greenland. *submitted, Journal of Geophysical Research, Atmospheres*, -:-, 2010.
- Hans Christian Steen-Larsen. Personal communication. -, 2010.
- John S. Steinhart and Stanley R. Hart. Calibration curves for thermistors. *Deep Sea Research and Oceanographic Abstracts*, 15(4):497–503, August 1968. ISSN 0011-7471. URL <http://www.sciencedirect.com/science/article/B757H-48B0V8F-18W/2/6dfd12c92edb07a2061d04b46ff053d8>.
- J. Szydłowski. Isotope effects on phase-equilibria in hydrogen-bonded systems, especially vapor-pressure and miscibility isotope effects. *Journal of Molecular Structure*, 321(1-2): 101–113, May 1994.
- JR Taylor. *An introduction to error analysis*. University Science Books Mill Valley, CA, 2nd edition, 1997.
- Peter A. Taylor, Henrik Kahanpää, Wensong Weng, Ayodeji Akingunola, Clive Cook, Mike Daly, Cameron Dickinson, Ari-Matti Harri, Darren Hill, Victoria Hipkin, Jouni Polkko, and Jim Whiteway. On pressure measurement and seasonal pressure variations during the phoenix mission. *J. Geophys. Res.*, 115:E00E15–, March 2010. ISSN 0148-0227. URL <http://dx.doi.org/10.1029/2009JE003422>.
- R. Uemura, N. Yoshida, N. Kurita, M. Nakawo, and O. Watanabe. An observation-based method for reconstructing ocean surface changes using a 340,000-year deuterium excess record from the dome fuji ice core, antarctica. *Geophys. Res. Lett.*, 31(13):L13216–, July 2004. ISSN 0094-8276. URL <http://dx.doi.org/10.1029/2004GL019954>.
- H. C. Urey. The thermodynamic properties of isotopic substances. *J. Chem. Soc.*, pages 562–581, 1947.
- W. Alexander Van Hook. Vapor pressures of the isotopic waters and ices. *The Journal of Physical Chemistry*, 72(4):1234–1244, 1968. doi: 10.1021/j100850a028.

- E. H. Wahl, B. Fidric, C. W. Rella, S. Koulikov, B. Kharlamov, S. Tan, A. A. Kachanov, B. A. Richman, E. R. Crosson, B. A. Paldus, S. Kalaskar, and D. R. Bowling. Applications of cavity ring-down spectroscopy to high precision isotope ratio measurement of  $c\text{-}13/c\text{-}12$  in carbon dioxide. *Isotopes In Environmental and Health Studies*, 42(1):21–35, March 2006. doi: 10.1080/10256010500502934.
- C. A. Ward and D. Stanga. Interfacial conditions during evaporation or condensation of water. *Physical Review E*, 64(5):051509, November 2001. doi: 10.1103/PhysRevE.64.051509.
- P. Werle, R. Mücke, and F. Slemr. The limits of signal averaging in atmospheric trace-gas monitoring by tunable diode-laser absorption spectroscopy (tdlas). *Applied Physics B: Lasers and Optics*, 57(2):131–139–139, 1993. ISSN 0946-2171. URL <http://dx.doi.org/10.1007/BF00425997>.
- J. A. Whiteway, L. Komguem, C. Dickinson, C. Cook, M. Illnicki, J. Seabrook, V. Popovici, T. J. Duck, R. Davy, P. A. Taylor, J. Pathak, D. Fisher, A. I. Carswell, M. Daly, V. Hipkin, A. P. Zent, M. H. Hecht, S. E. Wood, L. K. Tamppari, N. Renno, J. E. Moores, M. T. Lemmon, F. Daerden, and P. H. Smith. Mars water-ice clouds and precipitation. *Science*, 325(5936):68–70, July 2009. URL <http://www.sciencemag.org/cgi/content/abstract/325/5936/68>.
- Y.L. Yung and D.M. Kass. Deuteronomy? a puzzle of deuterium and oxygen on mars. *Science*, 280:1545–1546, 1998.
- Yuk L. Yung, Jun-Shan Wen, Joseph P. Pinto, Mark Allen, Kathryn K. Pierce, and Suzanne Paulson. H<sub>2</sub>O in the martian atmosphere: Implications for the abundance of crustal water. *Icarus*, 76(1):146–159, October 1988. ISSN 0019-1035. URL <http://www.sciencedirect.com/science/article/B6WGF-4731F53-103/2/01d502d17eed6c9a3be5028612002170>.